

## Topological aspects of non-centrosymmetric magnets

Présentée le 15 décembre 2022

Faculté des sciences de base  
IPHYS - Gestion  
Programme doctoral en physique

pour l'obtention du grade de Docteur ès Sciences

par

**Priya Ranjan BARAL**

Acceptée sur proposition du jury

Prof. R. Houdré, président du jury  
Dr A. Magrez, Prof. O. Yazyev, directeurs de thèse  
Prof. A. Isaeva, rapporteuse  
Dr J. White, rapporteur  
Prof. A. Kis, rapporteur



There's Plenty of Room at the Bottom.  
— Richard P. Feynman

To my loving parents...





# Acknowledgements

The last four and half years has been a wonderful phase of my life, and the credit goes to many people. This section is an understatement for the gratitude I owe to all of you.

Starting academically, I was constantly rebounding between three groups. But first and foremost, I would like to thank my supervisor, Dr. Arnaud Magrez, for unlimited number of things. He has been more than a supervisor, a wonderful colleague and a great friend. For my EPFL tenure, the number of exciting stories we have together is just unimaginable. Thank you for giving me the freedom I needed to pursue all these crazy projects. This would not have been possible without you. And yes, I am really sorry for our last ESRF trip. I hope now you don't mind what happened. Also, I would like to thank my co-supervisor, Prof. Oleg Yazyev, for the discussions we had over the years and the helpful advices.

I would also like to take this opportunity to thank someone who was not my formal supervisor, but whose role in my scientific career has been no less than one, Prof. Henrik Rønnow. I do not recollect a time when I was stuck with a problem and Henrik has not suggested a way out of it. He was always full of ideas to make things work, and I have learnt a great deal from your ever-positive attitude. Thank you so much for making me feel like part of your group. One more person who needs to be acknowledged is Ivica Živković. He was always available for any kind of discussion, even when I text him at (really) odd hours. Thank you for teaching me the essential tricks needed for a great quality measurement.

Next, I would like to thank two other not only awesome physicists, but great human beings, Dr. Jonathan White and Dr. Victor Ukleev. Jon has been a wonderful collaborator and teacher for the whole time. Thank you for your patience and awesome advice on many topics. Victor has been a shadow-mentor for most of my work. You introduced me to the wonderful world of resonant x-ray scattering. Thank you so much for answering all the silly questions I had over the years, even during holidays and weekends. I want to you both know that the thesis would not have been possible without you two.

I have been fortunate enough to have access to many beamlines in different countries. The support I have received from the local contacts is simply tremendous. I would like to thank Dr. Pascal Manuel at WISH (ISIS), Dr. Diego Alba Venero at SANS2D (ISIS), Dr. Robert Cubitt at D33 (ILL), Dr. Sonia Francoual at P09 (DESY), Dr. Florin Radu at VEKMAG (BESSY-II), Dr. Manuel Valvidares, Dr. Pierluigi Gargiani at BOREAS (ALBA), Dr. Vladimir Pomjakushin at HRPT (PSI), Dr. Lukas Keller at DMC (PSI), and Dr. Oksana Zaharko at ZEBRA (PSI). Last but not the least Dr. Chennan Wang from the GPS beamline ( $S\mu S$ , PSI). You have been a lot of help regarding the experiment, analysis and interpretations (even during weekends!). Thank you

## Acknowledgements

---

so much!

I was lucky to have wonderful colleagues around me from LQM, Dr. Virgile Favre, Dr. Luc Testa, Dr. Peter Babkevich, Dr. Thomas Schönenberger, Dr. Nagabhushan Hegde and Dr. Jian-Rui Soh. You guys are wonderful, and I will always remember the great time we have had together. I was surrounded by many like-minded people (almost always) thinking about skyrmions. They would be Dr. Ping Che, Dr. Anna Kúkol'ová, Dr. Simon Phillip (University of Basel), Dr. Thomas Schönenberger and Dr. Le Yu. Benoît Truc has been more than a colleague, and a dear friend, to say the least. Thank you for being the constant source of ideas.

Mithilesh has been a great friend over the last few years. The number of discussions we have had over I don't remember how many topics, is simply amazing. I wish you all the best in life. Two collaborators need to be given extra credits in this section, Dr. Vamshi Katukuri and Dr. Ravi Yadav. Thank you for your patience with explaining me the calculations and sharing your passions. Also thank you Vamshi for the lunch boxes.

All the group members of the crystal growth facilities have been really welcoming to me over the years, especially David, Yong and Laure. Thank you for making all of my crazy ideas work. I enjoyed our outings so so much, especially the curling. Thank you very much.

Special thanks to all the friends from my undergraduate years, who I am still in contact with. Especially, Avirup, Utkarsh, and Pranshu. I should also mention Linta and Brinda for the funny discussions we have had.

Collaborators are the key to the success I have had over the years. The list includes, Dr. Thomas LaGrange, Dr. Victor Boureau, Prof. Patrick Maletinsky, Dr. Martino Poggio, Dr. Oleg Utesov and many more.

A big thank you goes to the administrative assistants, Ms. Carlin Laurence, Ms. Patricia Byron, Ms. Annick Evequo, Ms. Tanya Castellino and last but not the least Ms. Anh Eymann for all your support over the last few years.

My family members have been my backbone. Staying so far away is never easy. But thank you for your understanding and support.

Finally, one big thank you goes to the one who has been a constant support over the last few years, PCCP and her family. Life is so much more eventful and colourful around you. The overwhelming welcome I have received from you is simply not describable. Together we form a topological knot.

I thank the PSI, ESRF, ISIS, ALBA, BESSY, DESY, and ILL facilities for approving my scientific proposals. Also, the Swiss National Science Foundation for the financial support through Sinergia network NanoSkyrmionics (Grant no. CRSII5\_171003). Finally, I would like to thank my jury members for their effort into reviewing this thesis.

I sincerely apologise if I have missed anyone in this list. But you will always have a special spot in my heart.

*Lausanne, September 26, 2022*

PRB.

# Abstract

The concept of chirality has been influencing many branches of physics for centuries. On the other hand, study of topology and related concepts have recently been introduced to the physics community. Exotic quasiparticles, such as magnetic skyrmions emerge when these two elegant topics merge with each other. Among the many skyrmion hosts,  $\text{Cu}_2\text{OSeO}_3$  is one of the very few insulators to host a skyrmion lattice to date. Being finite size objects, the ease of formation, stabilization as well as manipulation of skyrmions strongly depend on the boundary conditions imposed by the crystal geometry. Thus leading to the so-called *Geometrical Confinement Effects*. In the first part of the thesis, this effect is explored in fine details, starting with synthesis of  $\text{Cu}_2\text{OSeO}_3$  particles in their relevant length scales. As a function of their size, the emergent behaviour in this system of particles, is explored with help of a number of sophisticated tools. Moreover, our experimental results are well-verified using micromagnetic simulations. We find distinct yet correlated signatures combining three of the most used frequency domains in physics. Our results will serve as the guiding principle for exploration of geometrical confinement effects in insulator-based application paradigms.

The latter chapter deals with a higher dimensional multi-spin object, the so-called *Hedgehog lattice*. Discovery of a Hedgehog lattice in a novel inorganic crystal is reported in this chapter. We have combined solid-state synthesis with various bulk property measurement probes to properly characterize this system. True magnetic configuration has been determined through many experiments performed at large scale facilities. Our results will not only spark research interest among experimentalists, but also theorists working on emergent properties of topological materials.

**Keywords:** Noncentrosymmetry, Chirality, Topology, Magnetic Skyrmions, Hedgehogs, Geometrical Confinement Effects, Chemical Vapor Transport, Hydrothermal Growth, Reflux Growth, Resonant Elastic X-ray Scattering, Small Angle Neutron Scattering, Magnetometry, Williamson-Hall, Chemical Kinetics, Neutron Diffraction, Heat Capacity, Muon Spin Relaxation, Micromagnetic Simulations, Quantum Chemistry Calculations



# Résumé

Depuis des siècles, le concept de chiralité a influencé de nombreuses branches de la physique. Plus récemment, l'étude de la topologie et des concepts relatifs à celle-ci ont été introduits en physique. Sur la base de ces deux concepts, l'existence de quasi-particules exotiques, telles que les skyrmions magnétiques, a été prédite. À ce jour,  $\text{Cu}_2\text{OSeO}_3$  est l'un des très rares matériaux isolants au sein duquel se forme un réseau ordonné de skyrmions dans des conditions de température et de pression particulières. Les skyrmions sont des objets de taille finie pour lesquels la formation, la stabilisation ainsi que la manipulation dépendent fortement des conditions limites imposées par la géométrie du cristal. Ils sont donc sensibles à un effet de confinement géométrique. Cet effet est étudié en détail dans la première partie de la thèse. Pour cette étude, une méthode innovante de synthèse de nano- et micro-cristaux de  $\text{Cu}_2\text{OSeO}_3$  a été développée. Les mécanismes chimiques ont été étudiés en détail afin d'obtenir des échantillons ayant des tailles de cristaux précises et contrôlées. Le comportement et la signature des skyrmions et d'autres particules topologiques apparaissant dans  $\text{Cu}_2\text{OSeO}_3$  sont explorées à l'aide d'un certain nombre d'outils sophistiqués dans les trois domaines de fréquence les plus utilisés en physique. De plus, ce travail expérimental est consolidé par des résultats théoriques obtenus par simulation micromagnétique. En conclusion, nos résultats sur les effets de confinement géométrique pourront servir de référence à des applications futures de particules topologiques dans des matériaux isolants.

Le dernier chapitre traite d'un objet multi-spins de plus grande dimension, appelé Hedgehog. La découverte d'un réseau de Hedgehog dans un cristal inorganique,  $\text{Co}_5\text{TeO}_8$ , est présentée dans ce chapitre. Les cristaux de  $\text{Co}_5\text{TeO}_8$  ont été obtenus par synthèse à l'état solide. Les propriétés macroscopiques de ces cristaux ont été caractérisées par différentes techniques expérimentales. La configuration magnétique réelle a été déterminée suite à de nombreuses expériences réalisées dans des grandes installations. Cette découverte va non seulement susciter l'intérêt des expérimentateurs mais aussi des théoriciens travaillant sur les propriétés émergentes des matériaux topologiques.

**Mots-clés :** Noncentrosymétrie, Chiralité, Topologie, Skyrmions Magnétiques, Hedgehog Magnétiques, Effets de Confinement Géométrique, Transport Chimique en Phase Vapeur, Croissance Hydrothermale, Croissance par Reflux, Résonance élastique des Rayons X, Diffusion des Neutrons Aux Petits Angles, Magnétométrie, Williamson-Hall, Cinétique Chimique, Diffraction des Neutrons, Chaleur Spécifique, Relaxation du Spin des muons, Simulations Micromagnétiques, Calculs de Chimie Quantique.



# Contents

Acknowledgements	i
Abstract	iii
List of Figures	ix
<b>I Introduction</b>	<b>1</b>
1 Chirality Of Matter And Exotic Phenomena	3
2 Structure Of The Thesis	7
3 The Physics Of Magnetic Skyrmions: Theoretical Background	9
3.1 The Non-linear Sigma Model ( $NL\sigma M$ ) and Skyrme Field . . . . .	9
3.2 Skyrmion Hosting $P2_13$ Helimagnets . . . . .	10
3.3 Theoretical Treatment Of Magnetic Skyrmions Based On $NL\sigma M$ . . . . .	11
4 Experimental Techniques	15
4.1 Material Growth . . . . .	15
4.1.1 Chemical Vapor Transport (CVT) . . . . .	15
4.2 Characterizations Of Long-period Incommensurate Structures . . . . .	18
4.2.1 Resonant Elastic X-ray Scattering (REXS) . . . . .	18
4.2.2 Small Angle Neutron Scattering (SANS) . . . . .	28
<b>II Magnetic Skyrmions And Related Phases In Chiral Cubic <math>Cu_2OSeO_3</math></b>	<b>35</b>
5 <i>Geometrical Confinement Effects In <math>Cu_2OSeO_3</math> (Nano)Particles</i>	37
5.1 $Cu_2OSeO_3$ : The Magneto-Electric Insulating Skyrmion Host . . . . .	38
5.2 Controlled Chemical Synthesis Of Nanostructures . . . . .	40
5.3 Structural Characterizations . . . . .	42
5.4 Reaction Kinetics And Mechanism Of Chemical Transformation Between $CuSeO_3 \cdot 2H_2O$ and $Cu_2OSeO_3$ . . . . .	47
5.5 Magnetic Phase Diagram Of All Particles Derived From Magnetization & Susceptibility Measurements . . . . .	57
	vii

## Contents

---

5.6	Dynamics Of Different Parts Of The Magnetic Phase Diagram Probed By Muon Spin Relaxation ( $\mu$ SR) Technique . . . . .	64
5.7	Heat Capacity Studies Of $\text{Cu}_2\text{OSeO}_3$ System At Different Particle Sizes . . . . .	68
5.8	Magnetic Structure Determination Through Powder Neutron Diffraction . . . . .	72
5.9	Small Angle Neutron Scattering Investigations Of $\text{Cu}_2\text{OSeO}_3$ Particles . . . . .	74
5.10	Micromagnetic Simulations On $\text{Cu}_2\text{OSeO}_3$ Particles Based On Landau-Lifshitz-Gilbert equation . . . . .	80
<b>6</b>	<b>Anisotropic Exchange Interaction</b>	<b>87</b>
6.1	Significance Of AEI in Skyrmion Hosting Helimagnets . . . . .	87
6.2	High-resolution $t$ -REXS Experiments at BESSY-II . . . . .	89
6.3	Results And Discussions . . . . .	93
<b>7</b>	<b>Surface Spiral State With Doubled Periodicity: An Open Question</b>	<b>97</b>
7.1	Description Of The High-resolution $r$ -REXS Experiments . . . . .	97
7.2	Results And Discussions . . . . .	100
<b>III</b>	<b>Higher Order Spin Texture In A Complex Cubic Magnet</b>	<b>103</b>
<b>8</b>	<b><math>\text{Co}_5\text{TeO}_8</math>: Structural Complexity Meets Topology</b>	<b>105</b>
8.1	Topological Hedgehog Magnetic Structures . . . . .	105
8.2	Micro Crystal Synthesis And Characterizations . . . . .	107
8.3	Magnetic Phase Diagram Construction Through Magnetization & Susceptibility Measurements . . . . .	110
8.4	Heat Capacity Of $\text{Co}_5\text{TeO}_8$ . . . . .	117
8.5	Powder Neutron Diffraction . . . . .	120
8.6	Reciprocal Space Magnetic Structure Using SANS . . . . .	125
8.7	Estimation Of Exchange Couplings Through Quantum Chemical Approaches . . . . .	140
<b>IV</b>	<b>Summary &amp; Conclusions</b>	<b>145</b>
<b>9</b>	<b>Conclusions &amp; Future Work</b>	<b>147</b>
	<b>Bibliography</b>	<b>151</b>
	<b>Curriculum Vitae</b>	<b>171</b>



# List of Figures

1.1	Sohncke type classification of space groups. . . . .	4
1.2	List of Sohncke space groups. . . . .	5
1.3	Two of the many skyrmion types. . . . .	6
4.1	Principle of Chemical Vapor Transport technique.. . . .	16
4.2	Chemical Vapor Transport growth of $\text{Cu}_2\text{OSeO}_3$ . . . . .	19
4.3	Two main scattering processes involving x-rays. . . . .	20
4.4	Crystal structure and reciprocal space map of $\text{Cu}_2\text{OSeO}_3$ . . . . .	25
4.5	Reciprocal space map of $\text{Cu}_2\text{OSeO}_3$ for different magnetic phases. . . . .	27
5.1	Skyrmion lattice in two different particle size limits for $\text{Cu}_2\text{OSeO}_3$ . . . . .	38
5.2	Phase diagram of $\text{Cu}_2\text{OSeO}_3$ with magnetic field applied along either of the three high symmetry directions. . . . .	39
5.3	Overview of $\text{Cu}_2\text{OSeO}_3$ synthesis. . . . .	40
5.4	X-ray diffraction analysis of all $\text{Cu}_2\text{OSeO}_3$ particles. . . . .	41
5.5	Representative particles used for studying the <i>geometrical confinement effects</i> . . . . .	42
5.6	Williamson-Hall analysis of all particles based on x-ray diffraction data. . . . .	44
5.7	Secondary particle size determination from dynamic light scattering measurements. . . . .	44
5.8	High resolution TEM image of grown $\text{Cu}_2\text{OSeO}_3$ particles. . . . .	45
5.9	Structural homogeneity in $\text{Cu}_2\text{OSeO}_3$ particles probed by Raman spectroscopy and XRF . . . . .	46
5.10	The complex crystal structure of $\text{CuSeO}_3 \cdot 2\text{H}_2\text{O}$ . . . . .	48
5.11	Linearized JMAK equation for kinetics analysis. . . . .	51
5.12	Chemical mechanism of transformation between $\text{CuSeO}_3 \cdot 2\text{H}_2\text{O}$ & $\text{Cu}_2\text{OSeO}_3$ . . . . .	53
5.13	Reaction activation energy for various bases. . . . .	54
5.14	Schematic representation of proton acidity in $\text{CuSeO}_3 \cdot 2\text{H}_2\text{O}$ . . . . .	56
5.15	Temperature scans at constant magnetic fields for grown $\text{Cu}_2\text{OSeO}_3$ particles. . . . .	57
5.16	DC magnetization and AC susceptibility magnetic field scans of 338 nm particles at both 5 K and 53 K. . . . .	58
5.17	Magnetic isotherms across the phase diagram for three different sized $\text{Cu}_2\text{OSeO}_3$ particle sizes. . . . .	60

## List of Figures

---

5.18	Determination of magnetic phase diagram of $\text{Cu}_2\text{OSeO}_3$ particles from AC susceptibility. . . . .	61
5.19	Magnetic phase diagram of all particles as inferred from AC susceptibility measurements . . . . .	62
5.20	Effects of finite particle size on magnetic susceptibility. . . . .	63
5.21	Experimental conditions for our $\mu\text{SR}$ experiment at GPS beamline, $S\mu\text{S}$ . . . . .	65
5.22	Local field broadening and fluctuation rate obtained as a function fo temperature. . . . .	66
5.23	Magnetic field scan close to $T_c$ for both particles. . . . .	67
5.24	$C_p$ measured with short heat pulses. . . . .	69
5.25	Phase transitions in Bulk $\text{Cu}_2\text{OSeO}_3$ probed by long heat pulses. . . . .	70
5.26	$C_p$ vs $T$ for $\text{Cu}_2\text{OSeO}_3$ at different magnetic fields as obtained using long heat pulses. . . . .	71
5.27	Zero field magnetic structure of $\text{Cu}_2\text{OSeO}_3$ probed by wide angle neutron diffraction. . . . .	73
5.28	Experimental setup and proposed magnetic textures in real and reciprocal space. . . . .	75
5.29	Probing 338 nm $\text{Cu}_2\text{OSeO}_3$ particles using SANS. . . . .	77
5.30	Length of incommensurate modulation in 338 nm particles. . . . .	78
5.31	Magnetic modulation in 73 nm particles. . . . .	79
5.32	FFT of an octahdeon possessing a single helix. . . . .	80
5.33	Finite size effect in reciprocal space. . . . .	81
5.34	Micromagnetic simulations on isolated octahedral $\text{Cu}_2\text{OSeO}_3$ particles. . . . .	82
5.35	Size dependent phase diagram of octahedral $\text{Cu}_2\text{OSeO}_3$ particles. . . . .	83
5.36	Magnetization ( $M$ ) and $dM/dB$ as obtained from the micromagnetic simulations. . . . .	84
5.37	FFT of the magnetic texture within each octahedron. . . . .	85
6.1	Lamella preparation and initial characterisations at $\text{Cu-L}_3$ edge. . . . .	90
6.2	Response of conical peaks due to the in-plane magnetic field. . . . .	91
6.3	Summed up intensity profile of the conical peaks in 2D reciprocal space at various temperatures. . . . .	92
6.4	Anisotropic exchange interaction constant for $\text{Cu}_2\text{OSeO}_3$ at $T = 20$ K. . . . .	93
6.5	AEI constant as a function of temperature. . . . .	94
7.1	Setup of the $r$ -REXS experiment at BL29 BOREAS. . . . .	98
7.2	Observation of SS-state in a field-driven sequence. . . . .	99
7.3	$H - T$ phase diagram of the surface spiral state. . . . .	100
8.1	Cubic and tetrahedral hedgehog lattice in $\text{MnSi}_{1-x}\text{Ge}_x$ . . . . .	106
8.2	Solid state synthesis of $\text{Co}_5\text{TeO}_8$ . . . . .	108
8.3	XRD analysis of $\text{Co}_5\text{TeO}_8$ . . . . .	109
8.4	Static magnetization of $\text{Co}_5\text{TeO}_8$ at a constant applied magnetic field. . . . .	110
8.5	Subtle variations in the temperature induced transitions in $\text{Co}_5\text{TeO}_8$ for a few selected magnetic fields. . . . .	111

8.6	Temperature dependent static magnetization for $\text{Co}_5\text{TeO}_8$ under various strength of magnetic fields. . . . .	112
8.7	Static isothermal magnetization measured above and below $T_N$ for $\text{Co}_5\text{TeO}_8$ . . .	112
8.8	$dM/dH$ for $\text{Co}_5\text{TeO}_8$ signalling field-induced metamagnetic-type phase transitions. . . . .	113
8.9	Magnetic field-induced metamagnetic phase transitions at selected temperatures below $T_N$ . . . . .	114
8.10	Probing zero-field magnetic transitions in $\text{Co}_5\text{TeO}_8$ using AC susceptibility measurements. . . . .	114
8.11	Behaviour of various temperature driven transitions probed by $\chi_{AC}$ . . . . .	115
8.12	All AC susceptibility temperature scans at different applied DC fields for $\text{Co}_5\text{TeO}_8$	116
8.13	Electrical capacitance as a function of magnetic field for $\text{Co}_5\text{TeO}_8$ . . . . .	117
8.14	Magnetic phase diagram of $\text{Co}_5\text{TeO}_8$ as inferred from magnetization and susceptibility measurements. . . . .	118
8.15	Heat capacity of $\text{Co}_5\text{TeO}_8$ measured with short heat pulses and zero magnetic field. . . . .	119
8.16	Low temperature thermodynamic quantities of $\text{Co}_5\text{TeO}_8$ . . . . .	119
8.17	$\text{Co}_5\text{TeO}_8$ specific heat extracted from short heat pulses for increasing magnetic fields. . . . .	120
8.18	Probing various temperature-driven transitions using long heat pulses. . . . .	121
8.19	Further probing of the transitions using long heat pulses. . . . .	122
8.20	Magnetic field dependent specific heat of $\text{Co}_5\text{TeO}_8$ measured using long pulses.	122
8.21	Powder neutron diffraction results obtained from $\text{Co}_5\text{TeO}_8$ . . . . .	123
8.22	Temperature evolution of the magnetic satellites as obtained via neutron diffraction measurements. . . . .	123
8.23	Analysis of (111) Bragg peak its incommensurate satellites in $\text{Co}_5\text{TeO}_8$ . . . . .	124
8.24	SANS experimental configuration for $\text{Co}_5\text{TeO}_8$ at the SANS-I instrument, PSI. .	125
8.25	SANS patterns for $\text{Co}_5\text{TeO}_8$ as a function of temperature. . . . .	127
8.26	Analysis of temperature dependent SANS patterns for $\text{Co}_5\text{TeO}_8$ . . . . .	128
8.27	High magnetic field-training of $\text{Co}_5\text{TeO}_8$ just below $T_N$ in transverse geometry.	129
8.28	Effects of Field-training procedure across the magnetic phase diagram of $\text{Co}_5\text{TeO}_8$ .	130
8.29	Magnetic field dependent SANS patterns of $\text{Co}_5\text{TeO}_8$ at $T = 44$ K. . . . .	132
8.30	Field evolution of incommensurate satellites at 44 K with zero-field state produced at 28 K. . . . .	133
8.31	Sector box analysis of scattering pattern at $T = 44$ K for $\text{Co}_5\text{TeO}_8$ . . . . .	134
8.32	Systematic magnetic field scan in transverse geometry at $T = 32$ K. . . . .	136
8.33	Detailed analysis of scattering pattern at $T = 32$ K for $\text{Co}_5\text{TeO}_8$ . . . . .	137
8.34	Arrangement of propagation vectors corresponding to the proposed spin structure in $\text{Co}_5\text{TeO}_8$ . . . . .	138
8.35	Wide angle rocking scan of $\text{Co}_5\text{TeO}_8$ without external magnetic field. . . . .	139
8.36	Magnetic structure of both hedgehog lattices. . . . .	140
8.37	Manifold of nearest-neighbor exchange interaction. . . . .	142



# Introduction **Part I**



# 1 Chirality Of Matter And Exotic Phenomena

The concept of “chirality” has deep significance at different length scales in the entirety of physics, starting from quantum mechanical structures derived at microscopic length scales till astronomical scale of cosmology. In general terms, chirality assigns a sense of handedness to the objects. That is evident from the Greek root of the word, “ $\chi\epsilon\iota\rho$ ”, which literally means *hand*. Examples of chiral structures include formation of whirlpool in water, massive hurricanes, last but not the least, spiral galaxies. Setting aside the early adventures from philosophers, Lord Kelvin was the first one to formally introduce the term “chirality” in 1884. According to him, the definition of chirality goes as follows: “*I call any geometrical figure, or group of points, chiral, and say it has chirality, if its image in a plane mirror, ideally realized, cannot be brought to coincide with itself*” [99]. Almost a century later, the modern definition of chirality came from Laurence Barron, which states: *True chirality is exhibited by systems that exist in two distinct enantiomeric states that are interconverted by space inversion (parity  $\mathcal{P}$ ), but not by time reversal ( $\mathcal{T}$ ) combined with any proper spatial rotation ( $\mathcal{R}$ )* [13]. In simpler words, an object is said to exhibit true chirality in case when it remains  $\mathcal{RT}$ -invariant, even if  $\mathcal{P}$  is broken. But if  $\mathcal{P}$  and  $\mathcal{T}$  are individually broken, while it still remain invariant under  $\mathcal{PT}$ , then it's assigned a false chirality [14]. Let us first describe the static space inversion symmetry in terms of something fundamental in condensed matter physics, the structure of crystals.

Solids are classified in terms of the symmetry of its fundamental building block, called unit cells, and these are categorized into space groups. According to group theory, infinitely many space groups exist. But if one considers a *crystallographic space group*, the choices are then restricted to 230 only [62]. For its point group symmetry, a chiral object is said to contain *operations of the first kind*. If it contains *operations of the second kind*, then it can be mirror imposed on each other, leading to an achiral structure. Here, the *operations of the first kind* are defined as the ones which preserve the orientation of the object, such as translation, rotation, and screw-rotation. Whereas *operations of the second kind* reverses the orientation of the object under transformation. Examples of this include inversions, roto-inversions, reflections, and glide reflections, etc. At this point a subtle but important difference has to be made clear. The chirality of a symmetry group is not the same as the chirality of an object. That would

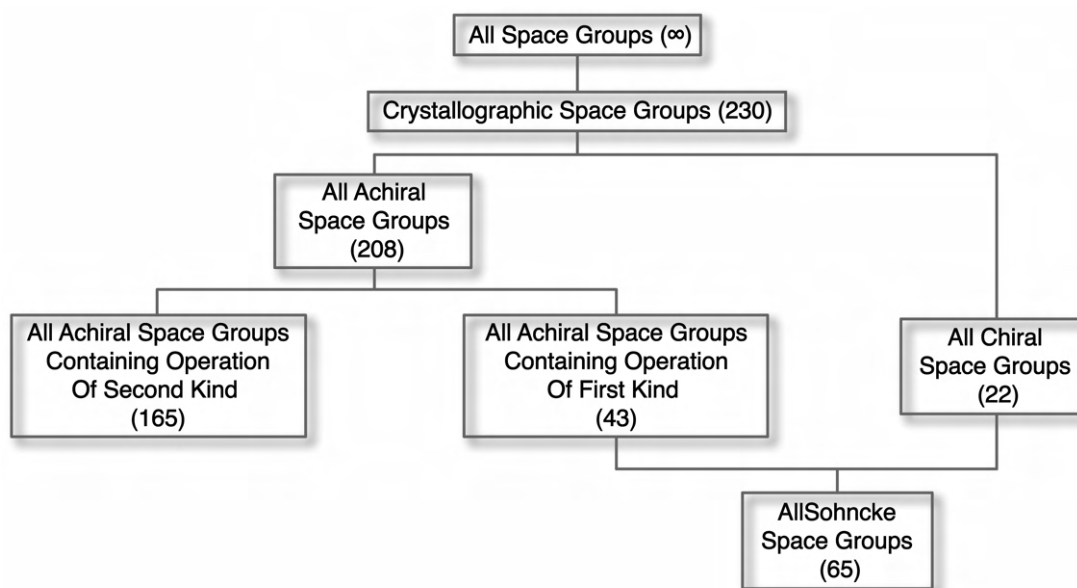


**Figure 1.1: Sohncke type classification of space groups.** Classification scheme for all 230 crystallographic space groups resulting in the final 65 Sohncke space groups.

mean inorganic structures crystallizing in one of the 22 chiral space groups are always chiral, whereas the reverse may not be true. As shown in Fig. 1.1, all chiral molecules will belong to one of the so called *Sohncke groups*. The 22 chiral space groups, coming in 11 pairs, are pairwise enantiomers. For example,  $P4_132$  (Number 213) and  $P4_332$  (Number 212) form an enantiomorphous pair, whereas  $P2_13$  (Number 198) does not have such a space group pair. Still all three of them belong to the list of *Sohncke groups*. In this thesis, most of our discussions will be based on inorganic compounds belonging to the *Sohncke groups*. The list of these space groups have been listed in Fig. 1.2.

Some of these chiral structures together with non-trivial *topological* properties are one of the most researched topics of recent condensed matter physics [64]. Topology is the branch of mathematics dealing with smooth transformation of geometric objects, without breaking or tearing it. New classes of topological materials have been discovered in the last few decades. The excitement in these materials is due to the condensed matter realization of phenomena previously only known in high energy physics, mainly fermionic excitations (such as Dirac, Weyl or Majorana) [84, 119, 204, 212, 213], topological surface states [118], and the last but not the least localized topological objects, the so called *Magnetic Skyrmions* [134, 169, 220]. Note that entirely new fermionic excitations have been proposed in condensed matter physics, without any analogy with high energy physics [28]. In chiral systems, new type of quasiparticles have been observed as well [163, 165]. But we will focus mainly on theory and experiments on magnetic skyrmions.

If we include magnetic moment of atoms in chiral crystals, we add another aspect of chirality within. Chiral magnetism is not only intriguing from a theoretical point of view, but is





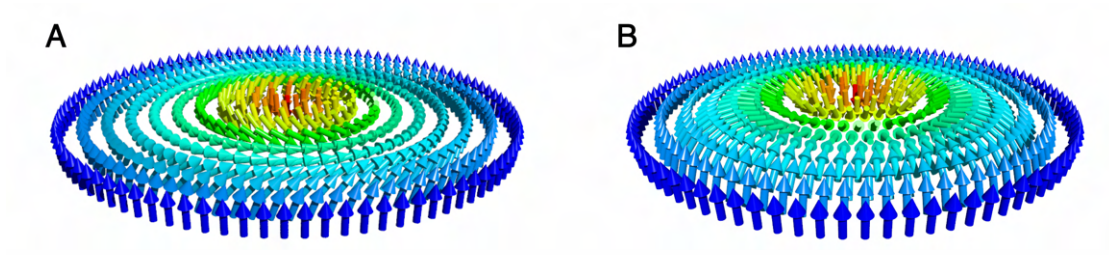


**Figure 1.3: Two of the many skyrmion types.** The stereographic projection of 3D hedgehogs resulting in two main types of magnetic skyrmions, (A) Bloch-type, (B) Néel-type. The key difference between these two is the *helicity* (the angle between the in-plane magnetization component and position vector). This turns out to be  $\pm\pi/2$  for Bloch-type and 0 for a Néel-type skyrmions.

quadrupole)  $q$ -hedgehogs [54], or finally a skyrmion lattice phase (SkL) [95, 134, 169, 220]. Magnetic skyrmions are topologically protected vortex-like objects which also have an analogy with High energy physics. In the last decade or so, there has been an explosive interest emerged in the field of skyrmions. The DMI-driven magnetic skyrmions are usually Bloch-type, whereas the interface-stabilized [strong spin-orbit coupling (SOC)] skyrmions are Néel-type (as shown in Fig. 1.3) <sup>1 2</sup>.

---

<sup>1</sup>These are not the only types of skyrmions which exist. For an extensive classifications of skyrmions-like quasiparticles, see Ref. [58].

<sup>2</sup>Néel-type skyrmion lattice have also been discovered in bulk polar crystals, such as  $\text{GaV}_4\text{S}_8$  [100], and  $\text{VOSe}_2\text{O}_5$  [112].

## 2 Structure Of The Thesis

The structure of this thesis is as follows: In chapter- 3, we give a short introduction to skyrmions from the perspective of The Non-linear Sigma Model, followed by few words for all the skyrmion hosting magnets belonging to  $P2_13$  space group. We will further go into the details of *magnetic* skyrmions in the framework of chiral magnets. We will end this chapter with a brief introduction to geometrical phases and their relevance in skyrmion-hosting chiral magnets. In chapter 4, we will give details about Chemical Vapor Transport growth of  $\text{Cu}_2\text{OSeO}_3$  single crystals. Also, we will give explicit derivation for the form factor resulting from various incommensurate magnetic phases from two scattering processes, (I) Resonant Elastic X-ray Scattering and (II) Small Angle Neutron Scattering. Next, in chapter 5, we will go into the details of novel *Geometrical Confinement effects* arising in  $\text{Cu}_2\text{OSeO}_3$  particles. Followed by, results from high resolution  $t$ -REXS experiments for estimation of Anisotropic Exchange Interaction in  $\text{Cu}_2\text{OSeO}_3$ . An open question concerning a newly discovered twice-modulated surface state will be addressed in chapter 7. In the following chapter, we will introduce a novel cubic chiral insulator,  $\text{Co}_5\text{TeO}_8$ , hosting a higher dimensional  $4q$  magnetic structure, characterized by various sophisticated experimental probes, including small angle neutron scattering. In the final chapter, we will provide the conclusions drawn from the studies included in this thesis and outline some of the unanswered questions as well as future directions.



## 3 The Physics Of Magnetic Skyrmions: Theoretical Background

The experimental manifestation of magnetic skyrmions as well as the exact theory behind them are equally fascinating. In this chapter, we briefly introduce the concept of magnetic skyrmions from a field theory point of view, followed by providing a short discussion about energy landscape in  $P2_13$  helimagnets. Finally, we also provide an introduction to geometrical phases and their relevance in topic of chiral magnetism.

### 3.1 The Non-linear Sigma Model (NL $\sigma$ M) and Skyrme Field

The original skyrmion solution was provided by Tony Skyrme in 1962, but for nucleons, in a completely different subject than condensed matter physics [172]. With  $SU(2)$  symmetry on the non-linear sigma model, Skyrme field can be written as  $\varphi(\mathcal{X})$ , where  $\mathcal{X}$  is a four-vector. In equation form  $\varphi(\mathcal{X})$  can then be written as

$$\varphi(\mathcal{X}) = \begin{pmatrix} \sigma + i\pi_3 & i\pi_1 + \pi_2 \\ i\pi_1 - \pi_2 & \sigma - i\pi_3 \end{pmatrix} \quad (3.1)$$

where,  $\pi_1$ ,  $\pi_2$  and  $\pi_3$  are three almost massless pion fields satisfying  $SO(3)$  symmetry [136]. Whereas,  $\sigma(\mathcal{X})$  is introduced in order for  $SO(3)$  symmetry to hold [29]. Ignoring time dependence, the Lagrangian density of the system can be written as:

$$\mathcal{L} = -\frac{1}{2}\text{Tr}R_\mu R^\mu + \frac{1}{16}\text{Tr}([R_\mu, R_\nu][R^\mu, R^\nu]) + m^2\text{Tr}(\phi - 1). \quad (3.2)$$

The first two terms, that is the kinetic term and the Skyrme term preserve the chiral symmetry, whereas the third term involving dimensionless pion mass parameter breaks it. And so, we can write the energy density of the system in the following manner:

$$W = -\frac{1}{2}\text{Tr}R_i R_i - \frac{1}{16}\text{Tr}([R_i, R_j][R_i, R_j]) - m^2\text{Tr}(\phi - 1). \quad (3.3)$$

The consequence of it is that the Baryon number  $\mathcal{N}$  exists in a way to impose a solitonic solution. This  $\mathcal{N}$  takes the following form:

$$\mathcal{N} = -\frac{1}{24\pi^2} \int \epsilon_{ijk} \text{Tr}(R_i R_j R_k) d^3 \mathbf{r} \quad (3.4)$$

Few points about Eqn. 3.4 has to be pointed out. First, the field solution given above for Baryon number guarantees that nucleons behave like particles. Second, the number  $\mathcal{N}$  signifies the number of times parameter space ( $\varphi$ ) is wrapped around by real-space. And thus is a topological invariant, called the *topological charge* of the system. Now in order to derive different classes of topological objects, let us use the polar coordinates to express  $\varphi$  as

$$\varphi(\rho, Z) = \begin{pmatrix} \cos f(\rho) + i \sin f(\rho) \left( \frac{1 - |R|^2}{1 + |R|^2} \right) & i \sin f(\rho) \left( \frac{2|R|}{1 + |R|^2} \right) \\ -i \sin f(\rho) \left( \frac{2|R|}{1 + |R|^2} \right) & \cos f(\rho) - i \sin f(\rho) \left( \frac{1 - |R|^2}{1 + |R|^2} \right) \end{pmatrix} \quad (3.5)$$

Where,  $f(\rho)$  is the polar function which determines the radial behaviour of  $\varphi$ . For a specific  $\mathcal{N}$ , Eqn. 3.5 can be minimized in order to produce the corresponding profile function. A number of solutions, along with the corresponding isosurfaces have been shown in Ref. [136]. From their Figure.1, it is clear that there is an obvious huge energy cost to go from  $\mathcal{N}=3$  to  $\mathcal{N}=4$  Skyrmion configuration. With actual analogy to experiments, these processes will manifest as dissipative first-order type transitions. All possible Skyrmionic configurations shown in Figure.1 of Ref [136] form a *homotopy group*, where each class of object is distinguished from each other by the *winding number*. Each Skyrmion configuration has their energy landscape determined from the radial as well as angular functions, whereas the their stability is caused by the winding number.

### 3.2 Skyrmion Hosting $P2_13$ Helimagnets

After introducing the concept of skyrmions from the field theoretical point of view, in this section we will discuss the actual experimental manifestation of these in magnetic systems. The first ever experimental realization of magnetic skyrmions came to picture in 2009 on archetypal itinerant helimagnet MnSi [134]. Small angle neutron scattering (SANS) technique was utilized in order to observe the symmetric six-fold scattering pattern due to the skyrmion lattice in reciprocal space. Afterwards, SkL was also observed in Co-doped FeSi via the Lorentz transmission electron microscopy (LTEM) method [220].  $\text{Cu}_2\text{OSeO}_3$  was the first insulator found to host skyrmions [169]. Whereas, in MnGe and Ge-doped MnSi, higher order topological spin textures were observed, such as a  $3q$  and a  $4q$ -Hedgehog lattice, respectively [54, 182]. Over the years, there have been reports of many bulk materials hosting different kind of topological spin structures. They are listed in Table. 3.1.

### 3.3. Theoretical Treatment Of Magnetic Skyrmions Based On $NL\sigma M$

**Table 3.1:** List of Bulk materials hosting topological spin textures. HL: Hedgehog Lattice, SkL: Skyrmion Lattice. **RED**: Centrosymmetric, **BLUE**: Non-centrosymmetric, **GREEN**: Enantiomorphic, and **CYAN**: Polar.

Material	Space Group	Point Group	Electrical Behaviour	Topological Spin Texture
<b>SrFeO<sub>3</sub></b>	$Pm\bar{3}m$ (221)	$O_h$	Conductor	4q-HL [76, 77]
<b>Co<sub>x</sub>Zn<sub>y</sub>Mn<sub>z</sub></b> ( $x + y + z = 20$ , $z \leq 6$ )	$P4_332/P4_132$ (212/213)	$O$	Conductor	Bloch SkL [93, 94, 95, 186, 219]
<b>Co<sub>8-x</sub>Fe<sub>x</sub>Zn<sub>8</sub>Mn<sub>4</sub></b>	$P4_132$ (213)	$O$	Conductor	Bloch SkL [93]
<b>FeCo<sub>0.5</sub>Rh<sub>0.5</sub>Mo<sub>3</sub>N</b>	$P4_132$ (213)	$O$	Semiconductor	Bloch SkL [116]
<b>MnSi</b>	$P2_13$ (198)	$T$	Conductor	Bloch SkL [134]
<b>Fe<sub>1-x</sub>Co<sub>x</sub>Si</b> ( $0.05 \leq x \leq 0.7$ )	$P2_13$ (198)	$T$	Conductor	Bloch SkL [21, 220]
<b>FeGe</b>	$P2_13$ (198)	$T$	Conductor	Bloch SkL [218]
<b>Cu<sub>2</sub>OSeO<sub>3</sub></b>	$P2_13$ (198)	$T$	Insulator	Bloch SkL [3, 169]
<b>EuPtSi</b>	$P2_13$ (198)	$T$	Conductor	Bloch SkL [86, 91, 178]
<b>MnGe</b>	$P2_13$ (198)	$T$	Semiconductor	3q-HL [89, 182]
<b>MnSi<sub>1-x</sub>Ge<sub>x</sub></b> $0 \leq x \leq 0.25$ $0.3 \leq x \leq 0.6$ $0.7 \leq x \leq 1$	$P2_13$ (198) $P2_13$ (198) $P2_13$ (198)	$T$ $T$ $T$	Conductor Conductor Conductor	Bloch SkL 4q-HL 3q-HL [54]
<b>Mn<sub>1-x</sub>Fe<sub>x</sub>Ge</b> ( $0 \leq x \leq 0.3$ )	$P2_13$ (198)	$T$	Conductor	HL [60, 170]
<b>Gd<sub>3</sub>Ru<sub>4</sub>Al<sub>12</sub></b>	$P6_3/mmm$ (194)	$D_{6h}$	Conductor	Bloch-SkL [71]
<b>Gd<sub>2</sub>PdSi<sub>3</sub></b>	$P6/mmm$ (191)	$D_{6h}$	Conductor	Bloch-SkL [111]
<b>GaV<sub>4</sub>S<sub>8</sub></b>	$R3m$ (160)	$C_{3v}$	Insulator	Néel-SkL [100]
<b>GaV<sub>4</sub>Se<sub>8</sub></b>	$R3m$ (160)	$C_{3v}$	Insulator	Néel-SkL [26, 52]
<b>GdRu<sub>2</sub>Si<sub>2</sub></b>	$I4/mmm$ (139)	$D_{4h}$	Conductor	Bloch-SkL [101]
<b>EuAl<sub>4</sub></b>	$I4/mmm$ (139)	$D_{4h}$	Conductor	Bloch-SkL [179]
<b>Mn<sub>1.4</sub>Pt<sub>0.9</sub>Pd<sub>0.1</sub>Sn</b>	$I\bar{4}2m$ (121)	$D_{2d}$	Conductor	Anti-SkL [137, 149]
<b>VOSe<sub>2</sub>O<sub>5</sub></b>	$P4cc$ (103)	$C_{4v}$	Insulator	Néel-SkL [112]

Along with these bulk materials, there have been numerous reports of skyrmions in thin film heterostructures (mainly stabilized by large spin-orbit coupling due to heavy  $5d$  metals) [66, 124, 129, 159, 202, 216]. But from the point of this thesis, we will restrict ourselves to only bulk materials, especially those belonging to  $P2_13$  space group.

### 3.3 Theoretical Treatment Of Magnetic Skyrmions Based On $NL\sigma M$

The presence of weak spin-orbit coupling (SOC) in  $P2_13$  helimagnets (except for MnGe and its related compounds), makes it attractive from the theoretical point of view, since the magnetic moment density can be described rather well with an effective model. This SOC

### Chapter 3. The Physics Of Magnetic Skyrmions: Theoretical Background

also directly influences the strength of Dzyaloshinskii-Moriya interaction constant ( $\mathbb{D}$ ) [48, 132]. Competition between leading order Heisenberg exchange ( $\mathbb{J}$ ) and next order  $\mathbb{D}$  forces the ground state of these magnets to adapt a long-periodically modulated magnetization configuration with  $q_h \propto \mathbb{D}/\mathbb{J}$ . In the frame work of NL $\sigma$ M, the Lagrangian density of the system can be written in the following form:

$$\mathcal{L} = \frac{\mathbb{J}}{2}(\nabla \mathbf{m})^2 + \mathbb{D} \mathbf{m}(\nabla \times \mathbf{m}) - \mathbf{m} \cdot \mathbf{B} \quad (3.6)$$

Minimising this equation gives the free energy of the system. Together with the Ginzburg-Landau theory, we find the more general free energy of the system as [134]:

$$\mathcal{E}_F = \frac{\mathbb{J}}{2}(\nabla \mathbf{m})^2 + \mathbb{D} \mathbf{m}(\nabla \times \mathbf{m}) - \mathbf{m} \cdot \mathbf{B} + \frac{a}{2} \mathbf{m}^2 + \frac{b}{4!} \mathbf{m}^4 + \xi_{\text{cubic}}. \quad (3.7)$$

Here,  $a$ , and  $b$  are constants. Then the total energy is given as,  $E_{\text{total}} = \int \mathcal{E}_F d^3 \mathbf{r} + E_{\text{dipolar}}$ . Away from phase transitions, 4<sup>th</sup> and 5<sup>th</sup> term in Eqn. 3.7 can in principle be neglected, which reduces the free energy expression to the more simplified version shown in Eqn. 3.6. Without loss of generality, for a two-dimensional system, we can write the following topological number density:

$$\varkappa = (\partial_j \mathbf{m} \times \partial_i \mathbf{m}) \cdot \mathbf{m} \quad (3.8)$$

In connection with the Baryon number density introduced in the previous section, Eqn. 3.8 describes the number of times the 2D real space completely wraps a unit sphere in parameter space. In real space,  $\varkappa$  would represent the solid angle between neighbouring spins, which will have a corresponding value of  $4\pi$  in the order parameter space. Thus for a 2D system, we can write the following.

$$\mathcal{N} = \frac{1}{4\pi} \int \varkappa d^2 \mathbf{r} = \frac{1}{4\pi} \int (\partial_j \mathbf{m} \times \partial_i \mathbf{m}) \cdot \mathbf{m} d^2 \mathbf{r} \quad (3.9)$$

In this case, the set of all  $\mathcal{N}$ s form the  $\pi_2(S)^2$  homotopy group. We are now ready to implement the functional form of  $\mathbf{m}(\mathbf{r})$  in order to find the exact magnetization configuration for different  $\mathcal{N}$ s. In 2D polar coordinates, it is sufficient to assume the following form of  $\mathbf{m}[m_1(\rho, \psi), m_2(\rho, \psi), m_3(\rho, \psi)]$  as [135]:

$$\begin{aligned} m_1(\rho, \psi) &= M_S \sin[\theta(\rho)] \cos[\mathcal{N}(\psi + \chi_h)], \\ m_2(\rho, \psi) &= M_S \sin[\theta(\rho)] \sin[\mathcal{N}(\psi + \chi_h)], \\ m_3(\rho, \psi) &= M_S \Lambda \sin[\theta(\rho)]. \end{aligned} \quad (3.10)$$



### 3.3. Theoretical Treatment Of Magnetic Skyrmions Based On NL $\sigma$ M

In these expressions,  $M_S$  is the saturation magnetization,  $\theta(\rho)$  is responsible for the radial profile of the field, whereas  $\cos[\mathcal{N}(\psi + \chi)]$  and  $\sin[\mathcal{N}(\psi + \chi)]$  terms determine the angular behaviour of magnetization.  $\chi_h$  is known as the helicity angle. Finally,  $\Lambda$  determines the sign of  $m_3$  component of the central spin. It is easy to check that  $\theta(\rho)$  satisfies the Euler-Lagrange equation [23, 160]. Also, plugging in the 2D polar functional form of  $\mathbf{m}$  in equation. 3.9, we recover exactly  $\mathcal{N}$ . This guarantees the topological protection of field configurations rising from therein. Thus for a spontaneous symmetry breaking process in SO(2) (for 2D systems) or SO(3) (for 3D systems), the NL $\sigma$ M encodes the main features and produces a stable soliton-like solution. Since we discuss actual 3D bulk materials in this thesis, the magnetization configuration can be expressed as the following [134, 160]:

$$\begin{aligned} m_1(\mathbf{r}) &= M_S \cos \zeta, \\ m_2(\mathbf{r}) &= M_S \sin \zeta \cos(q_h \cdot \mathbf{r}), \\ m_3(\mathbf{r}) &= M_S \sin \zeta \sin(q_h \cdot \mathbf{r}). \end{aligned} \quad (3.11)$$

Here  $\zeta$ , the cone angle depends on sample parameters as  $\cos \zeta \propto B/M_S q_h \mathbb{D}$ . Thus, as the strength of external magnetic field increases, the cone angle gradually goes to zero, resulting in a field-polarized state. Whereas, without any magnetic field,  $\zeta$  acquires a value of  $90^\circ$ . This is exactly the helical ground state observed in the  $P2_13$  helimagnets. Away from  $T_c$ , this perfectly reproduces the hierarchy of different phases in  $P2_13$  helimagnets (except for MnGe), especially in the intermediate temperature range of  $\text{Cu}_2\text{OSeO}_3$ . Just below  $T_c$ , the thermal Gaussian fluctuations add one more extra term to Eqn. 3.7 and the free energy becomes [134]:

$$\mathcal{E}_{\text{GF}} \approx \mathcal{E}_{\text{F}} + \frac{1}{2} \log \left[ \det \left( \frac{\partial^2 \mathcal{E}_{\text{F}}}{\partial \mathbf{m} \partial \mathbf{m}} \right) \right] \quad (3.12)$$

Due to this new term, now the SkL phase has lower energy compared to the conical phase and becomes stable. Thus the NL $\sigma$ M appropriately reproduces all the magnetic phases observed in the  $P2_13$  helimagnets.



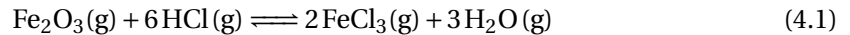
## 4 Experimental Techniques

After introducing the theory of magnetic skyrmions and related incommensurate phases, we give a short introduction about their experimental aspects in this chapter. The long list of bulk materials hosting these topological spin textures have been grown via different synthetic routes. We will provide a short introduction to the most common crystal growth method for  $\text{Cu}_2\text{OSeO}_3$ , that is the chemical vapor transport technique. In view of the topics included in this thesis, we will provide a short introduction to the single crystal growth under non-ambient conditions, such as the hydrothermal route. Finally, we will briefly cover the growth method for nanoparticles in a reflux technique. We will then give experimental insight into detecting skyrmion lattice phase in reciprocal space using two widely-used techniques, small angle neutron scattering and resonant elastic x-ray scattering, along with some theoretical argument behind them.

### 4.1 Material Growth

#### 4.1.1 Chemical Vapor Transport (CVT)

*Historical background:* Chemical vapor transport reactions have been taking place under naturally occurring environments for millennia. Bunsen was the first to identify one of these reactions at a volcanic site [30]. What Bunsen observed was the prototypical reaction to purify  $\text{Fe}_2\text{O}_3$  from an impure ore, using gaseous species such as  $\text{HCl}$ .



The whole process of growth can be divided into few key steps. During the first step, known as *dissolution*, gaseous phase of impure  $\text{Fe}_2\text{O}_3$  forms, as the forward reaction in the equation shown above. Usually this part of the process takes place in the hotter side, known as *source*. This is followed by a *backward reaction*, when pure  $\text{Fe}_2\text{O}_3$  phase is recrystallized. These pure

crystals form away from the hot zone, known as the *sink*. The underlying chemical equation describing the crystal growth process is known as the *transport equation*. In the early 1920s, Van Arkel and de Boer successfully employed this technique under laboratory conditions to grow metal iodides [196]. The method was mainly used to produce pure metals. In the 1960s, Schäfer established the first systematic approach towards the understanding of such chemical reactions and slowly this technique expanded to enable the growth of many different families of crystals [164].

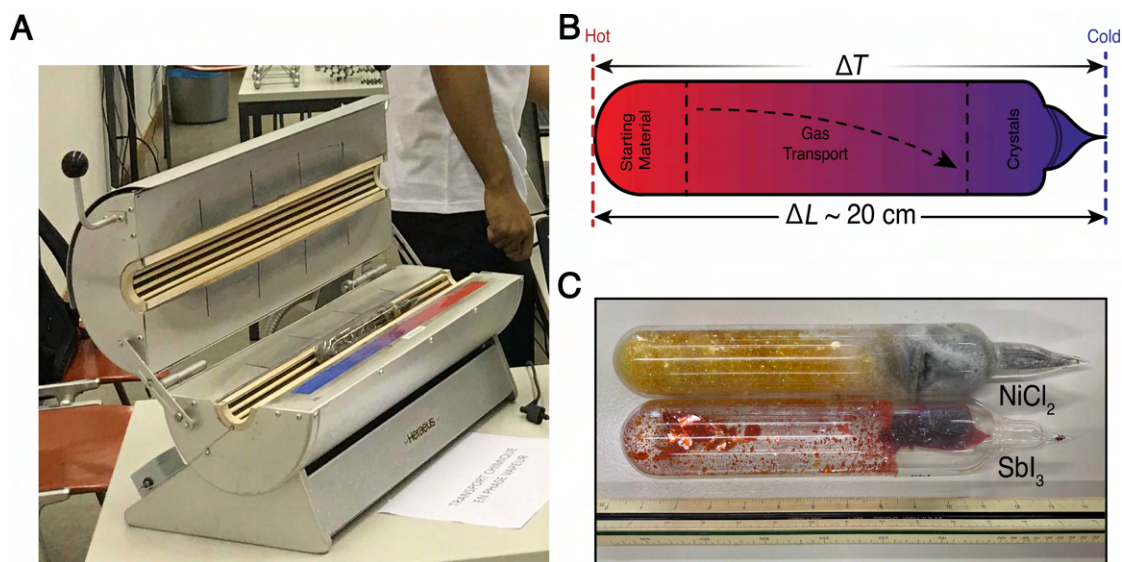
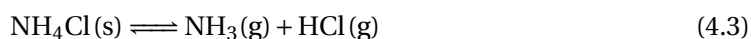


**Figure 4.1: Principle of Chemical Vapor Transport technique.** (A) Optical image of a table-top CVT furnace. The actual growth furnace is almost twice as large. (B) Schematics of the transport mechanism resulting in single crystal growth. (C) Two examples of metal halides grown using this method.

*Different dissolution processes:* Dissolution can take place in many different ways. During *sublimation*, a solid substance directly converts to a gaseous phase. One of the simplest example of this is  $\text{AlCl}_3$ . After sublimation,  $\text{AlCl}_3$  is found to exist in a dimerized form,  $\text{Al}_2\text{Cl}_6$ .



As the name suggests, compounds undergoing *decomposition sublimation* go through sublimation via decomposing into two or more gaseous species. The parent phase is recovered while cooling.



But this process could get more complicated in case there are more than two reactive gaseous species involved. Finally, under *self transport*, there is no need to add any extra transport

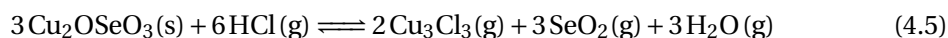
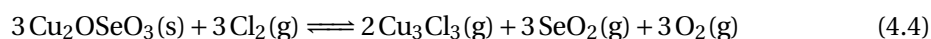
agent. The starting material undergoes either sublimation or decomposition sublimation to form the transport agent, which finally transfers the material to the sink.

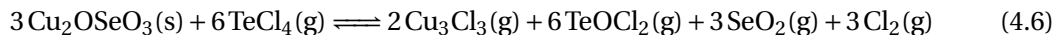
*Growth setup:* In an open system, a long glass or ceramic tube is used. The dissolution takes place for the source material and with help of a constant flow of transport agent, the vapor is recrystallized in a colder part of the tube. But most of the laboratory reactions proceed in a closed system. Typical example includes glass/quartz tubes. Length of these tubes are kept between 10 and 20 cm, whereas diameter is about 10-20 mm. In order to compensate for the rising vapor pressure from the transport agent (as well as source material), usually the transport tube is sealed under vacuum.

*Transport agent:* If the material intended for single crystal growth does not self-transport across the quartz tube, one needs to use a separate transport agent. In this context halogens or halogen containing compounds are most widely used. One of the most basic prerequisites for the choice of the transport agent is that it should be reactive enough to form gaseous species with the source material, which can then be transported to the sink. The second aspect while choosing a transport agent is the difference observed in the partial pressure of the transport agent between source and sink temperature. If the difference in partial pressure is low, then effective transport becomes unfeasible.

*Thermodynamic considerations:* The CVT method produces pure single crystals of the source material, if the right transport agent is chosen. But even so, transport of the target phase to the sink side is not guaranteed. There are certain thermodynamic conditions which are supposed to be satisfied before the reaction can take place. First, all target phase species have to be in a gaseous phase under the reaction conditions. Thus depending upon if the transport reaction is exothermic or endothermic, the crystallization takes place on either source or sink side, respectively. Second is the reaction kinetics affecting the transport of gaseous species. In between the forward reaction from dissolution and backward reaction from recrystallization, there is the actual *gas motion*, where the transient reactive species transport across the reaction tube. In most of the cases, this is the slowest, and thus the rate determining step. The equilibrium reaction constant ( $K$ ) has to be close to unity in order for the transport reaction to take place.

$\text{Cu}_2\text{OSeO}_3$ : The bulk single crystals used in this thesis (for example, in Chapter 7) are grown via the CVT technique. For our growth, CuO and SeO<sub>2</sub> (or Cu<sub>2</sub>OSeO<sub>3</sub> powder) are used as precursors while mostly HCl [47], Cl<sub>2</sub>, TeCl<sub>4</sub>, NH<sub>4</sub>Cl [146] are used as transport agents. And the growth proceeds chemically by the following reactions:





The presence of several gaseous species makes the energy landscape of this reaction incredibly complex. Also, the temperature of the sink end of the ampoule never exceeds 823 K to prevent the thermal decomposition of  $\text{Cu}_2\text{OSeO}_3$  crystals into  $\text{CuO} + \text{SeO}_2$ , but is preferably higher than 803 K to prevent the undesired co-crystallization of copper selenates with Cu:Se ratio different from 2:1. This results in only a 20 K temperature range to produce single crystals. Apart from the small temperature window, the high vapor pressure of the gaseous species makes the reaction even more complicated.

Figure 4.2 shows the representative examples of grown  $\text{Cu}_2\text{OSeO}_3$  using HCl as the transport agent. After the completion of the growth, lasting for about 3-4 weeks, we obtain several large single crystals (~500 mg). Clean Laue patterns from three of the principal axes ( $\langle 100 \rangle$ ,  $\langle 110 \rangle$ , and  $\langle 111 \rangle$ ) show the good quality of the crystals. Magnetic characterization was also performed on some of these single crystals. Figure 4.2F shows the real part of the ac susceptibility as a function of temperature. The extracted  $T_c$  agrees quite well with the reported literature [230]. In Fig. 4.2G near to  $T_c$ , we observe quite sharp peaks in the  $\chi''$  signalling the transitions in and out of the SkL phase. Thus, the grown  $\text{Cu}_2\text{OSeO}_3$  crystals have excellent quality and the magnetic properties are in well accordance with previous reports.

## 4.2 Characterizations Of Long-period Incommensurate Structures

The zoology of compounds shown in Table. 3.1 host incommensurate magnetic structures whose modulation in real space range between 3 nm and 200 nm. In real space, there also exist Lorentz Transmission Electron Microscopy (LTEM) [75, 218, 220], Magnetic Force Microscopy (MFM) [126, 173], as well as Spin(-polarized) Scanning Tunnelling Microscopy (SP-STM) [66, 74, 159] to name a few, which can provide details about the magnetic structure. There exists only few experimental techniques which can probe this correlation length scale in reciprocal space. From the point of view of this thesis, we will focus on two main techniques: Resonant elastic X-ray scattering and Small angle neutron scattering. We will give a detailed account of the process followed by analytical expression for structure factors arising due to different magnetic phases.

### 4.2.1 Resonant Elastic X-ray Scattering (REXS)

*Background information:* Since the discovery of x-rays by Wilhelm Röntgen, the x-ray diffraction (XRD) technique has become an integral part of research in condensed matter physics. The laboratory XRD techniques work on the principle of interaction between electromagnetic waves and the charge density of the electrons, known as *Thomson scattering* (Fig. 4.3) [7]. Since the scattering takes place between the electronic charge cloud and the photon, in principle, x-rays also become sensitive to the spin and orbital degrees of freedom. Thus leading to mag-



## 4.2. Characterizations Of Long-period Incommensurate Structures

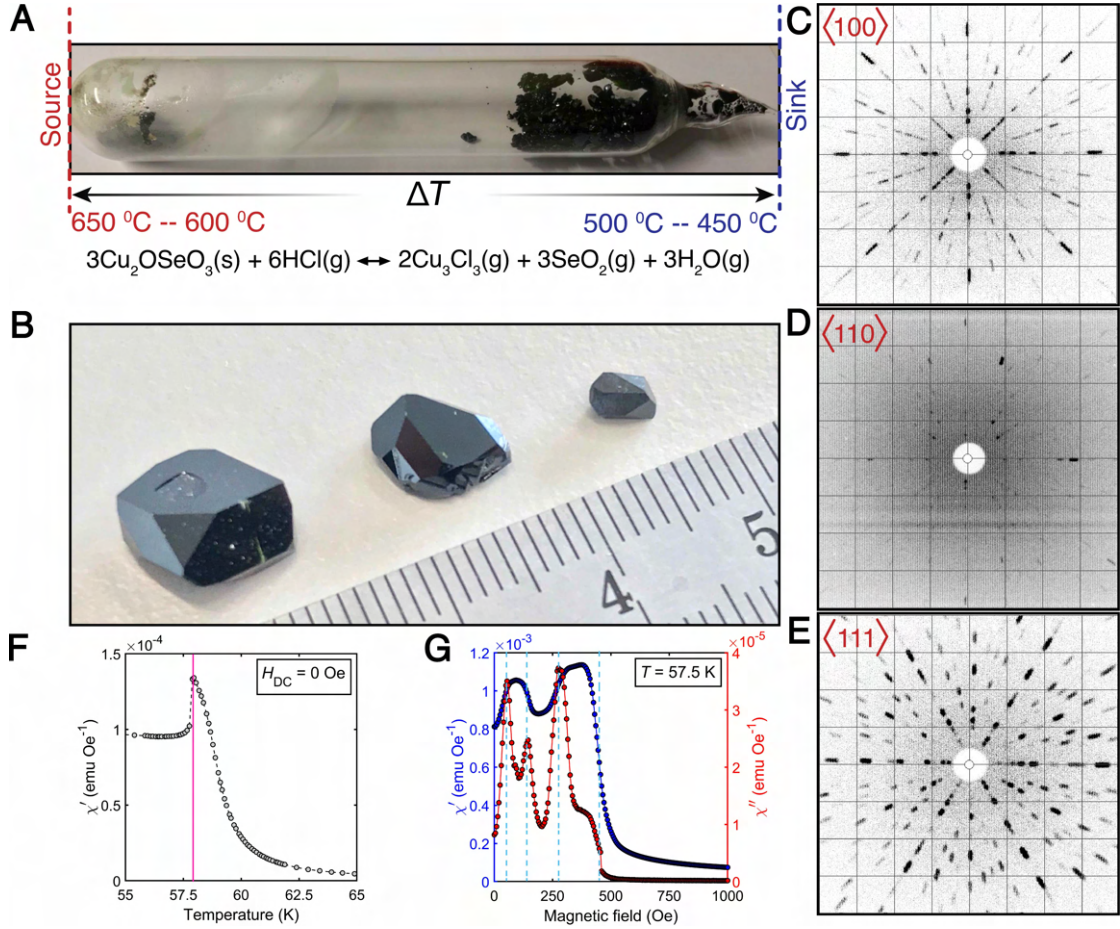


**Figure 4.2: Chemical Vapor Transport growth of  $\text{Cu}_2\text{OSeO}_3$ .** (A) Shows post-growth optical image of a quartz ampoule with crystallized  $\text{Cu}_2\text{OSeO}_3$  on the sink side. The chemical equation describes the underlying forward and backward reaction for the growth of these crystals while using HCl as the transport agent. (B) Optical image of some of the well-faceted single crystals. Mass of these crystals are 928 mg, 380 mg and 81 mg, respectively. (C), (D), (E) Show Laue patterns for  $\langle 100 \rangle$ ,  $\langle 110 \rangle$ , and  $\langle 111 \rangle$  axes in  $\text{Cu}_2\text{OSeO}_3$ . AC susceptibility temperature scans were performed as function of both temperature and magnetic field. Results are shown in panel-F and G. We thus confirm the value  $T_c$  as well as the phase boundaries for various magnetic-field induced phases.

netic scattering, known as *non-resonant magnetic scattering* [37, 152]. This scattering process involves photon energy away from the resonant edge of the target atom. Since the scattering mainly takes place between the incident photon and the outermost electronic orbitals close to the Fermi level, it has a much lesser strength compared to that of the *Thomson scattering*. But when the incident photon energy is tuned to the resonance edge of the target atom, *resonant magnetic scattering*, with a much higher scattering strength, takes place. The summary of this process is as follows. A core electron of the target atom absorbs the incident photon energy and makes a transition into one of the empty valence shells close to the Fermi level. The strong dependence of this transition on the inherent nature of the valence shell, ensures enhanced

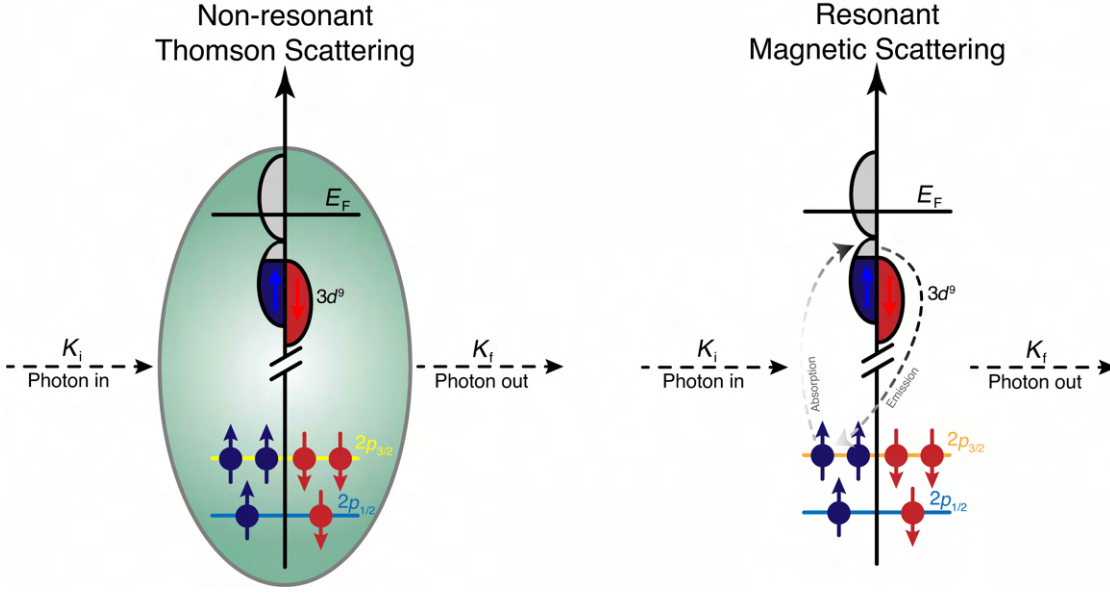


**Figure 4.3: Two main scattering processes involving x-rays.** For illustration purposes  $\text{Cu}^{2+}$  ions ( $3d^9$  valence shell configuration) are shown. (A) The most widely used x-ray scattering technique, that is the (non-resonant) Thomson scattering. As shown in the figure, The scattering takes place between the photon and the electronic charge cloud of the atom, without distinguishing between the filled core orbitals and empty valence orbitals. (B) Shows the two-step process underlying the resonant elastic x-ray scattering. There is also the third kind of scattering process involving x-rays called non-resonant magnetic scattering, where only the valence  $3d^9$  orbital acts as the scattering centre. But the scattering cross-section for this process is quite small. See text for more details.

sensitivity of x-rays to electronic ordering. This process is followed by the decay of this excited state back into the initial configuration, while emitting a photon with the same energy. This two-step process combining spectroscopy and diffraction is what constitutes the heart of Resonant Elastic X-ray Scattering (REXS). Thus at the resonance edge, x-rays become a highly sensitive tool towards probing magnetic moment density, since the cross-section becomes comparable to that of the Thomson scattering [184, 197]. Although lab-based diffractometers are limited in their energy ranges, modern synchrotron sources are capable of producing x-rays over an extended energy regime. At present, many synchrotrons in the world are able to routinely provide x-rays both in the soft (0.4-2 keV) and hard (>2 keV) regime for user-base operations. All the REXS experiments outlined in this thesis utilize the  $L_{2,3}$  (from here on, it will be denoted as  $L_3$ ) dipole transition of Cu.

*About the scattering centre,  $\text{Cu}_2\text{OSeO}_3$ :* The wavelength carried by the x-rays in the soft x-ray regime is usually in the range of 6-30 Å. Due to this, accessible Bragg peaks are quite limited. The unit cell length of  $\text{Cu}_2\text{OSeO}_3$  is 8.925 Å [47, 49], which is higher compared to the  $B20$  materials listed in Table 3.1 [135]. At the Cu  $L_3$  edge, the x-ray wavelength is about 13.3 Å. Thus making the [001] of  $\text{Cu}_2\text{OSeO}_3$  the only Bragg peak which can be probed by reflection-REXS



(or  $r$ -REXS for short) experiments ( $\theta - 2\theta \simeq 48-96^\circ$ ). As discussed later in the thesis, this issue can be overcome by switching to transmission-REXS ( $t$ -REXS) geometry. Interestingly enough, due to selection rules,  $\{001\}$  are forbidden Bragg peaks for  $P2_13$  space group. But because of the anisotropic third rank tensor arising from dipole-quadrupole terms, these forbidden peaks in non-centrosymmetric crystals appear in the actual experiment. This is known as anomalous Templeton scattering (ATS) [183]. One more aspect of the REXS process becomes crucial in the course of this thesis, that is the surface sensitivity. Below  $L_3$  and above  $L_2$  edges, x-rays probe a greater depth of the material. As shown by G. van der Laan *et al.*, at resonance edges, the sample penetration depth is limited to about 100 nm from the surface [198]. This makes  $r$ -REXS an invaluable tool as discussed in Chapter 7.

*Resonant scattering from charge and spin:* In order to derive the scattering form factor associated with the REXS process, and finally the intensity observed on the detectors, we will derive the same for a single atom, followed by extending that for an periodic array of atoms. In the case of a single free electron, the propagating x-rays can be represented as plane waves using Maxwell's electromagnetic equations in the following way:

$$\begin{aligned}\mathbf{E}(\mathbf{r}, t) &= -i\omega\mathbf{A}_0 \left[ ae^{i(\mathbf{k}\cdot\mathbf{r}-\omega t)}\epsilon - a^\dagger e^{-i(\mathbf{k}\cdot\mathbf{r}-\omega t)}\epsilon^* \right], \\ \mathbf{B}(\mathbf{r}, t) &= iA_0 \left[ ae^{i(\mathbf{k}\cdot\mathbf{r}-\omega t)}\mathbf{k} \times \epsilon - a^\dagger e^{-i(\mathbf{k}\cdot\mathbf{r}-\omega t)}\mathbf{k} \times \epsilon^* \right], \\ \mathbf{A}(\mathbf{r}, t) &= A_0 \left[ ae^{i(\mathbf{k}\cdot\mathbf{r}-\omega t)}\epsilon + a^\dagger e^{-i(\mathbf{k}\cdot\mathbf{r}-\omega t)}\epsilon^* \right].\end{aligned}\tag{4.7}$$

Where, the symbols carry the following meaning.  $\mathbf{k}$ ,  $\mathbf{E}$ ,  $\mathbf{B}$ ,  $\mathbf{A}$ , and  $\epsilon$  represent wavevector, electric field, magnetic field, vector potential, and polarization vector for the incident x-ray beam, whereas  $\mathbf{r}$  is the real space coordinate of the electron. For a single photon interacting with one electron, the non-relativistic Hamiltonian reads as the following.

$$H_{\text{int}} = \frac{e}{m}\mathbf{p} \cdot \mathbf{A} + \frac{e}{m}\mathbf{S} \cdot \mathbf{B} + \frac{e^2}{2m}\mathbf{A}^2\tag{4.8}$$

Where,  $\mathbf{p}$  is the momentum operator. We also define the coupled initial and the final state of the system as  $|\Psi_{\text{IS}}\rangle (\equiv |\Phi_{\text{IS}}, (\epsilon_i, \mathbf{k}_i)\rangle)$  and  $|\Psi_{\text{FS}}\rangle (\equiv |\Phi_{\text{FS}}, (\epsilon_f, \mathbf{k}_f)\rangle)$ , respectively.  $|\Phi_{\text{IS}}\rangle$  and  $|\Phi_{\text{FS}}\rangle$  are the initial and final state of the electron. Only the first two terms in Eqn 4.8 involve interaction between x-ray and electron, thus have relevance for REXS process, whereas the third term becomes dominant in non-resonant processes, such as Thomson scattering. We write the transition process between  $|\Psi_{\text{IS}}\rangle$  and  $|\Psi_{\text{FS}}\rangle$  using a matrix  $T_{\text{M}} (\approx H_{\text{int}} + H_{\text{int}}G_0(\epsilon_i)H_{\text{int}})$ , such that the transition probability becomes  $|\langle\Psi_{\text{FS}}|T_{\text{M}}|\Psi_{\text{IS}}\rangle|^2$ .

$$T_M = T_1 + T_2^a + T_2^b$$

$$= \frac{e}{m}(\mathbf{p} \cdot \mathbf{A} + \mathbf{S} \cdot \mathbf{B}) + \frac{e^2}{2m} \mathbf{A}^2 + \left(\frac{e}{m}\right)^2 (\mathbf{p} \cdot \mathbf{A} + \mathbf{S} \cdot \mathbf{B}) G_0(\epsilon_i) (\mathbf{p} \cdot \mathbf{A} + \mathbf{S} \cdot \mathbf{B}) \quad (4.9)$$

Where,  $G_0$  is the Green function for the non-interacting Hamiltonian. Analysing equation 4.9, we find that  $T_1$  is linear in  $\mathbf{A}$  or  $\mathbf{B}$ , corresponding to one-photon processes such as an absorption or an emission. While  $T_2^a$  and  $T_2^b$  are responsible for two-photon processes, for example non-resonant Thomson scattering and anomalous scattering, respectively [59]. The intensity of the scattered x-rays is expressed as the double differential,  $d^2\sigma/d\Omega d\omega$ . For elastic processes,  $d\sigma/d\Omega$  is found to be proportional to  $|f|^2$ , with  $f$  being the scattering form factor, and takes the following form [59].

$$f = \frac{C_s}{r_0} \langle \Psi_{FS} | (T_2^a + T_2^b) | \Psi_{IS} \rangle \quad (4.10)$$

The factor  $C_s/r_0$  is the normalization constant and can be calculated readily. Eqn. 4.10 is the master equation for any scattering processes involving photons. Now adding more electrons into the scattering system, the form factor picks up an overall phase,  $e^{i\mathbf{q} \cdot \mathbf{r}}$ . Now, each of the three contributions of  $T_M$  will be examined separately.

1. *Non-interaction term,  $T_2^a$* : Plugging in  $T_2^a$  into Eqn. 4.10, and summing over all occupied states, we obtain:

$$f_T^a = \epsilon_f^* \cdot \epsilon_i \sum_{IS} \langle \Phi_{IS} | e^{i\mathbf{q} \cdot \mathbf{r}} | \Phi_{IS} \rangle = \epsilon_f^* \cdot \epsilon_i \int \rho(\mathbf{r}) e^{i\mathbf{q} \cdot \mathbf{r}} d^3\mathbf{r} \quad (4.11)$$

As one can expect, in forward scattering ( $\mathbf{q} = 0$ ),  $f_T^a$  becomes exactly equal to  $\epsilon_f^* \cdot \epsilon_i Z$ , with  $Z$  being the atomic number. Thus Thomson scattering purely depends on the electronic charge distribution of the scattering centre (shown in Fig. 4.3).

2. *First interaction term,  $T_1$* : Following the same procedure as before, one notices that the structure of  $|\Phi_{IS}\rangle$  now becomes important. In  $\text{Cu}_2\text{OSeO}_3$ , all Cu atoms are in  $\text{Cu}^{2+}$  state, with the same electronic configuration of  $1s^2 2s^2 2p^6 3s^2 3p^6 3d^9$ . After summing over all the electronic states within a magnetic ion, the atomic form factor is found to be proportional to the spin (polarized) density of states in the valence shell. Thus, this is responsible for magnetic scattering off the atom both at and away from resonance. But since the typical amplitude for this kind of scattering is in the range of  $0.01 r_0$ , the corresponding intensity is orders of magnitude smaller than charge scattering.
3. *Second interaction term,  $T_2^b$* : This results in the two step model shown in Fig. 4.3. By absorbing a photon, the electronic ground state,  $|\Psi_{IS}\rangle (\equiv |\Phi_{IS}, (\epsilon_i, \mathbf{k}_i)\rangle)$ , first gets excited

## 4.2. Characterizations Of Long-period Incommensurate Structures

into an intermediate state,  $|\Psi_n\rangle (\equiv |\Phi_n, 0\rangle)$ , followed by an immediate decay into the final state,  $|\Psi_{FS}\rangle (\equiv |\Phi_{FS}, (\epsilon_f, \mathbf{k}_f)\rangle)$ . And finally we obtain the form factor as:

$$f_T^{\text{res}} \propto \sum_{\text{IS}} \sum_n \frac{\langle \Phi_{\text{IS}} | \hat{O}_f^* | \Phi_n \rangle \langle \Phi_n | \hat{O}_i | \Phi_{\text{IS}} \rangle}{\epsilon_n - \epsilon_{\text{IS}} - \hbar\omega - i\Gamma_b/2}. \quad (4.12)$$

Here,  $\Gamma_b$  represents the lifetime of the intermediate state. As one can expect, the sum over  $n$  goes on all valence holes, whereas the sum over IS spans all  $2p$  electronic states. The operator  $\hat{O}$  takes the following form:

$$\hat{O} = [\mathbf{p} \cdot \epsilon + i\mathbf{S} \cdot (\mathbf{k} \times \epsilon)] e^{i\mathbf{q} \cdot \mathbf{r}} \quad (4.13)$$

With the electric and magnetic dipole approximations on  $\mathbf{A}$  and  $\mathbf{B}$ , respectively, we obtain

$$\langle \Phi_n | \hat{O} | \Phi_{\text{IS}} \rangle = i \frac{m}{\hbar} (\epsilon_n - \epsilon_{\text{IS}}) \langle \Phi_n | \hat{O}_{E1} + \hat{O}_{M1} + \dots | \Phi_{\text{IS}} \rangle \quad (4.14)$$

where,

$$\begin{aligned} \hat{O}_{E1} &= \epsilon \cdot \mathbf{p} \\ \hat{O}_{M1} &= \frac{\hbar}{2m(\epsilon_n - \epsilon_{\text{IS}})} (\mathbf{k} \times \epsilon) \cdot (\mathbf{L} + 2\mathbf{S}) \end{aligned} \quad (4.15)$$

Here, compared to  $E1$ , the  $M1$  term can be neglected. Thus finally for an atom at site  $i$ , Eqn. 4.12 can be rewritten as:

$$f_T^{\text{res}} = f_0(\epsilon_f^* \cdot \epsilon_i) - i f_1(\epsilon_f^* \cdot \epsilon_i) \cdot \mathbf{m}_i + f_2(\epsilon_f^* \cdot \mathbf{m}_i)(\epsilon_i \cdot \mathbf{m}_i) \quad (4.16)$$

The quadratic term in the above equation is usually a higher order effect and thus very small. The final form of the form factor equation is reached.

$$f_T^{\text{res}} = f_0(\epsilon_f^* \cdot \epsilon_i) - i f_1(\epsilon_f^* \cdot \epsilon_i) \cdot \mathbf{m}_i. \quad (4.17)$$

After calculating the form factor of a single atom with many electrons, in the next step, the same procedure can be repeated for many atoms arranged periodically in a crystal, at positions  $\mathbf{R}_i$ s. The total form factor,  $\mathcal{F}$  becomes a combination of three terms shown in Eqn. 4.9, but now summed over all atoms in the unit cell. We can also ignore non-resonant scattering.

$$\begin{aligned}\mathcal{F}^{\text{tot}} &= \sum_{i,j} \left( f_{T(i)}^{(j)} + f_{(i)}^{\text{res}(j)} \right) e^{i\mathbf{q} \cdot \mathbf{R}_i^j} \\ &= \mathcal{F}_T + \mathcal{F}_0^{\text{res}} + \mathcal{F}_1^{\text{res}}.\end{aligned}\tag{4.18}$$

The  $f_0$  term essentially overlaps with the Thomson scattering term  $f_T^a$ , and scales with incident photon energy. This would result in order of magnitude increase of diffraction intensities with photon energy corresponding to the resonant energy of the atom, even making forbidden peaks appear [183]. Beautiful examples of this are the  $\{001\}$  [in general  $(0,0,2n+1)$  peaks, where  $n = 0,1,2,\dots$  (shown in Fig. 4.4)] peaks of  $\text{Cu}_2\text{OSeO}_3$ , extensively studied using REXS [221, 222, 223, 224].

In addition to structural (nuclear) peaks, if  $\mathbf{q}$  also corresponds to magnetic atoms,  $\mathcal{F}_1^{\text{res}}$  terms have to be considered. For commensurate magnetic structures such as a ferromagnetic compounds at resonance, each Bragg peak contains information from all the three phases. Whereas, for an antiferromagnetic material, an extra purely magnetic Bragg peak appears at half of the structural peak position. While for incommensurate magnets, where magnetic periodicity is completely decoupled from lattice periodicity, additional Bragg peaks emerge. As an obvious consequence of Fourier transformation of Eqn 4.18, a set of magnetic satellites flank each structural peak.

$$\begin{aligned}\mathcal{F}_0^{\text{res}}(\mathbf{q}) &= f_0 \sum_i (\epsilon_f^* \cdot \epsilon_i) e^{i\mathbf{q} \cdot \mathbf{R}_i^{\text{Cu}}} = F_0(\epsilon_f^* \cdot \epsilon_i) \bar{\rho}(\mathbf{q}), \\ \mathcal{F}_1^{\text{res}}(\mathbf{q}) &= -i f_1 \sum_i (\epsilon_f^* \times \epsilon_i) \cdot \mathbf{m}_i e^{i\mathbf{q} \cdot \mathbf{R}_i^{\text{Cu}}} = -i F_1(\epsilon_f^* \times \epsilon_i) \cdot \mathbf{M}(\mathbf{q}).\end{aligned}\tag{4.19}$$

Looking at Eqn 4.19 closely, it is immediately realised that in a certain crystal, if there exist two spectroscopically distinct magnetic sites, for example  $\text{Cu}^{1+}$  and  $\text{Cu}^{2+}$ , then  $F_0$  and  $F_1$  replace  $f_0$  and  $f_1$ , respectively. But since in  $\text{Cu}_2\text{OSeO}_3$ , there are 16  $\text{Cu}^{2+}$  ions (Fig. 4.4B),  $f_0$  and  $f_1$  turn out to be the same for all of them. And the transition we probe using resonant x-rays is the  $2p \rightarrow 3d$  electric dipole transitions. By summing over all Cu atoms inside the unit cell, we obtain  $\bar{\rho}(\mathbf{q})$  and  $\mathbf{M}(\mathbf{q})$ , the Fourier transform of charge density and real space magnetic moment, respectively. Finally we arrive at the expression for scattering intensity stemming from REXS process.

$$I(\mathbf{q}) = I_C(\mathbf{q}) + I_M(\mathbf{q}) + I_{\text{Int}}(\mathbf{q})\tag{4.20}$$

where, the charge  $[I_C(\mathbf{q})]$ , magnetic  $[I_M(\mathbf{q})]$  and interference  $[I_{\text{Int}}(\mathbf{q})]$  terms are defined as:

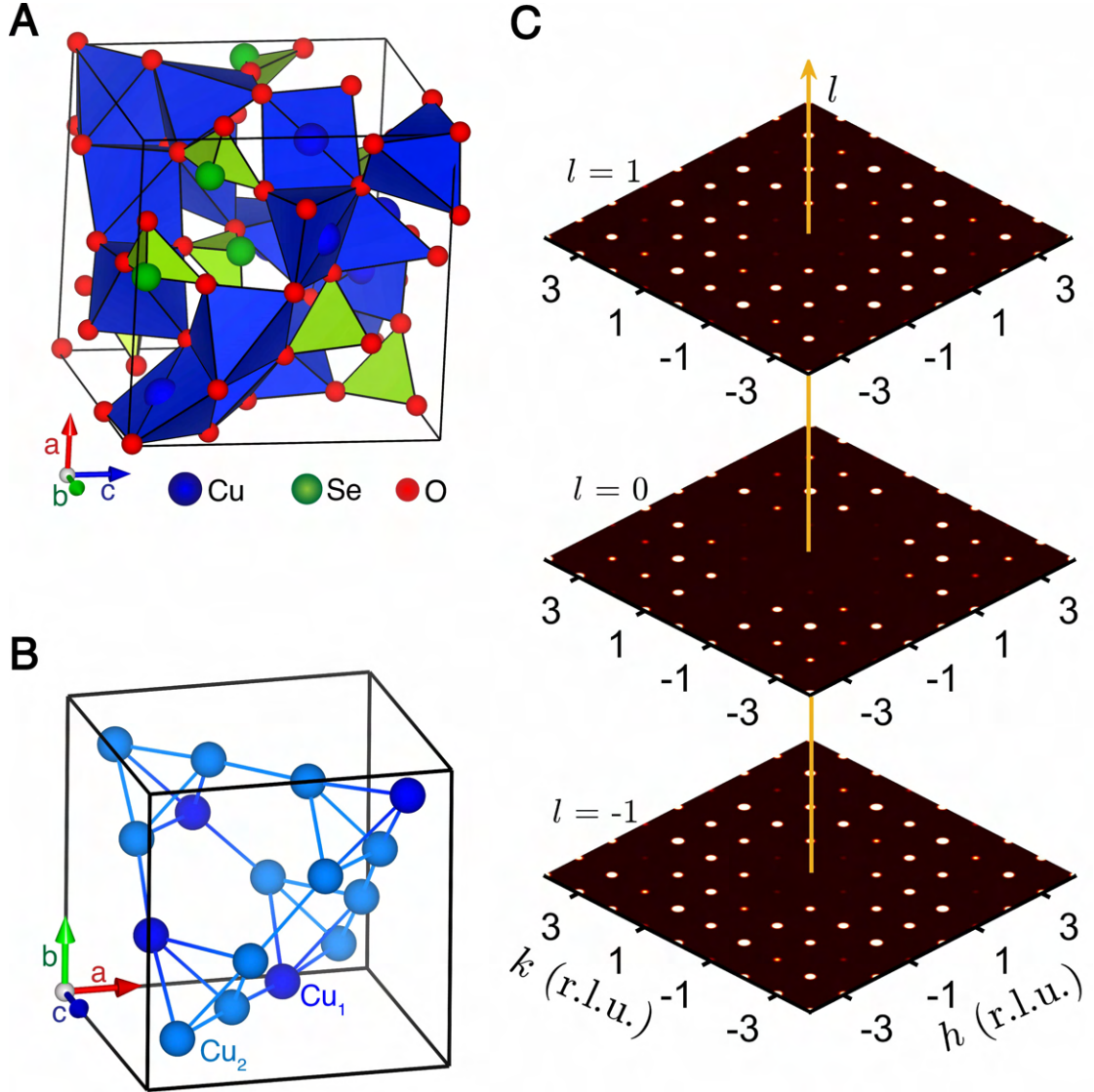


**Figure 4.4: Crystal structure and reciprocal space map of  $\text{Cu}_2\text{OSeO}_3$ .** (A) Chiral cubic crystal structure of  $\text{Cu}_2\text{OSeO}_3$ . Cu-O atoms in  $\text{Cu}_2\text{OSeO}_3$  form either a square pyramid or trigonal bipyramid structure (blue polyhedra), whereas Se-O form only trigonal bipyramid units (green polyhedra). (B)  $\text{Cu}_2\text{OSeO}_3$  unit cell showing only the magnetic atoms. The two crystallographically inequivalent Cu-sites are labelled accordingly. Each of these inequivalent  $\text{Cu}^{2+}$  ions carries a  $S = 1/2$ , while being oriented anti-parallel to each other. Therefore, each tetrahedron has an effective spin of 1 ( $S_{\text{eff}} = 1$ ) [27]. (C) The reciprocal space map of  $\text{Cu}_2\text{OSeO}_3$  for three constant  $\ell$ s. Since all three  $\ell$  planes have the same intensity scale, the size of each reciprocal space point corresponds to its structure factor.

$$\begin{aligned}
 I_{\text{C}}(\mathbf{q}) &= |\mathcal{F}_0^{\text{res}}(\mathbf{q})|^2, \\
 I_{\text{M}}(\mathbf{q}) &= |\mathcal{F}_1^{\text{res}}(\mathbf{q})|^2, \\
 I_{\text{Int}}(\mathbf{q}) &= \mathcal{F}_1^{\text{res}}(\mathbf{q})[\mathcal{F}_0^{\text{res}}(\mathbf{q})]^* - \mathcal{F}_0^{\text{res}}(\mathbf{q})[\mathcal{F}_1^{\text{res}}(\mathbf{q})]^*.
 \end{aligned}
 \tag{4.21}$$

We now define the following convention.  $\pi$  and  $\sigma$  polarizations are set to be as parallel and perpendicular to the scattering plane, respectively. And the following identities are realized. We follow the convention used by *Hill and McMorro* [70]:

$$\begin{aligned}\sigma_f \cdot \sigma_i &= 1 \quad , \quad \sigma_f \times \sigma_i = 0, \\ \pi_f \cdot \pi_i &= \hat{k}_f \cdot \hat{k}_i \quad , \quad \pi_f \times \pi_i = \hat{k}_f \times \hat{k}_i, \\ \sigma_f \times \pi_i &= \hat{k}_i \quad \text{and} \quad \pi_f \times \sigma_i = -\hat{k}_f.\end{aligned}\tag{4.22}$$

Plugging these identities in Eqn 4.21, Bragg peak intensity for any polarization can easily be calculated. It has also to be noted that only magnetic scattering changes the polarization of scattered photon, not charge scattering. Thus, if the incident x-ray has  $\sigma$  polarization, one should expect  $\sigma_f$  for  $\mathcal{F}_0^{\text{res}}$ , while  $\pi_f$  for  $\mathcal{F}_1^{\text{res}}$ . And the scattered intensity becomes,  $I_C^\sigma(\mathbf{q}) = 1/2|F_0\bar{\rho}(\mathbf{q})|^2$ ,  $I_M^\sigma(\mathbf{q}) = 1/2|F_1|^2|\hat{\mathbf{k}}_f \cdot \mathbf{M}(\mathbf{q})|^2$ , and  $I_{\text{Int}}(\mathbf{q}) = 0$ . It can be readily proved that  $I_{\text{Int}}(\mathbf{q}) = 0$  term does not vanish for both  $\pi$  or circular polarization. Two aspects of incommensurate magnetic modulations hold elegant simplifications to the total form factor at resonance. Since for these purely magnetic modulations (that is  $\mathbf{q} = \mathbf{q}_m$ ),  $I_C(\mathbf{q}_m) = 0$ . As a consequence, the interference term,  $I_{\text{Int}}(\mathbf{q}_m)$ , also goes to zero. From Eqn 4.19, we can already see that only  $\mathbf{M}(\mathbf{q})$  and polarization of the incident (and scattered x-ray) determine the amplitude of magnetic scattering.

*Form factor for various incommensurate magnetic phases:* Now we can write down the explicit formula for total form factor from different magnetic phases. First for the helical phase, we go back to Eqn. 3.11 and put  $\varsigma = 90^\circ$  to generate the zero-field helical structure. So the magnetization takes the following form:

$$\mathbf{m}(\mathbf{r}) = M_S [\mathbf{n}_3 \cos(q_h \cdot \mathbf{r}) + \mathbf{n}_2 \sin(q_h \cdot \mathbf{r})], \tag{4.23}$$

where,  $\mathbf{m}(\mathbf{r}) = m_1(\mathbf{r})\mathbf{n}_1 + m_2(\mathbf{r})\mathbf{n}_2 + m_3(\mathbf{r})\mathbf{n}_3$ , as defined in Eqn. 3.11. With the length of a single helix denoted as  $\lambda_h$ , where  $\lambda_h = 2\pi/q_h$ , the structural form factor thus becomes:

$$F_h = f_h \left( 1 + e^{iq_h \cdot \lambda_h \hat{\mathbf{R}}} \right). \tag{4.24}$$

While,  $f_h$  is obtained by plugging the magnetization into Eqn. 4.19, and is represented as:

$$f_h = -iM_S f_1 \int_0^{\lambda_h} (\epsilon_f^* \times \epsilon_i) \cdot [\mathbf{n}_3 \cos(q_h \cdot \mathbf{r}) + \mathbf{n}_2 \sin(q_h \cdot \mathbf{r})] e^{i\mathbf{q} \cdot \mathbf{r}} d\mathbf{r}. \tag{4.25}$$

Next the magnetic field-induced conical phase is formed when  $\varsigma$  is set between  $0^\circ$  and  $90^\circ$ . The propagation direction is set by the direction of magnetic field. Proceeding in a similar



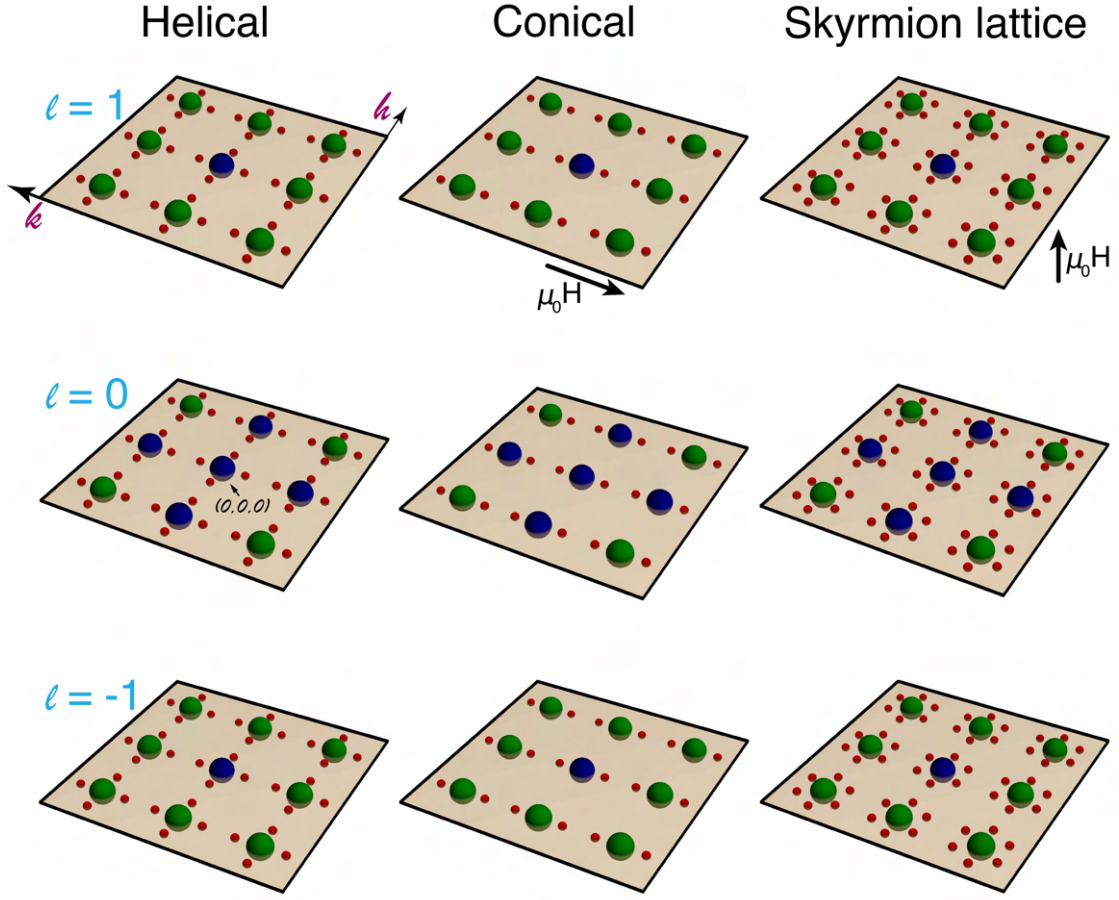


**Figure 4.5: Reciprocal space map of  $\text{Cu}_2\text{OSeO}_3$  for different magnetic phases.** Reciprocal space map of  $\text{Cu}_2\text{OSeO}_3$  for three constant  $\ell$ s, similar to Fig. 4.4, but also with magnetic Bragg peaks. Blue, green and red spheres represent forbidden charge reflections, allowed charge reflections, and incommensurate magnetic reflections, respectively. Note that magnetic field was applied along the  $k$ -direction for conical phase, whereas in out-of-plane  $\ell$ -direction for the skyrmion lattice phase. Small angle neutron scattering technique always probes the incommensurate magnetic satellites around (000) nuclear peak. While REXS is slightly more complicated than that. In the  $t$ -REXS experiment, again the Friedel pairs around the Brillouin zone centre are detected in the experiment. But for the  $r$ -REXS geometry, the (001) forbidden reflection (for  $\text{Cu}_2\text{OSeO}_3$ ) appears under resonant conditions, and the incommensurate Bragg peaks around it are detected.

manner, as done just before, we obtain the following expressions for the conical state:

$$\begin{aligned}
 F_c &= f_c \left( 1 + e^{i q_h \cdot \lambda_h \hat{\mathbf{R}}} \right) \\
 f_c &= -i M_S f_1 \int_0^{\lambda_h} (\epsilon_f^* \times \epsilon_i) \cdot [\cos \zeta \mathbf{n}_1 + \mathbf{n}_2 \sin \zeta \cos(q_h \cdot \mathbf{r}) + \mathbf{n}_3 \sin \zeta \sin(q_h \cdot \mathbf{r})] e^{i \mathbf{q} \cdot \mathbf{r}} d\mathbf{r}.
 \end{aligned} \tag{4.26}$$

Finally, for the skyrmion structure, we go back to Eqn. 3.10 and compute the form factor as:

$$F_{\text{sky}} = f_{\text{sky}} (1 + e^{i\mathbf{q}\cdot\mathbf{a}_1} + e^{i\mathbf{q}\cdot\mathbf{a}_2} + e^{i\mathbf{q}\cdot\mathbf{a}_3})$$

$$f_{\text{sky}} = -iM_S f_1 \int \int (\epsilon_f^* \times \epsilon_i) \left( m_1^{\text{sky}} \mathbf{n}_1 + m_2^{\text{sky}} \mathbf{n}_2 + m_3^{\text{sky}} \mathbf{n}_3 \right) e^{i\mathbf{q}\cdot\mathbf{r}} d\mathbf{r}, \quad (4.27)$$

where,  $a_1$ ,  $a_2$ , and  $a_3$  ( $a_1 = a_2 = a_3 = 2\lambda_h/\sqrt{3}$ ) are the three real space basis vectors rotated by  $120^\circ$  with respect to each other.

We can combine the results from Eqn. 4.25, 4.26, and 4.27 pictorially in Figure 4.5 for  $\text{Cu}_2\text{OSeO}_3$ . As shown there, four helical peaks decorate each lattice peak in zero field. Due to cubic anisotropy in  $\text{Cu}_2\text{OSeO}_3$ , the third helical domain is oriented along  $[001]$ , thus out of the constant  $\ell$ -planes. Next, applying a moderate magnetic field between  $B_{c1}$  and  $B_{c2}$  along  $k$ -direction, the system stays in conical phase with modulation along the same direction. Just below  $T_c$ , with the magnetic field along  $\ell$ -direction, hexagonal skyrmion lattice manifests in  $\text{Cu}_2\text{OSeO}_3$ , with six magnetic Bragg peaks around each nuclear peak. This is the basic principle of both scattering probes discussed in this thesis. Next, we will discuss small angle neutron scattering briefly.

### 4.2.2 Small Angle Neutron Scattering (SANS)

Neutron scattering is one of the most powerful techniques in condensed matter physics. There are a few inherent properties of neutrons which makes it a versatile tool for studying structural as well as magnetic properties of matter. First, the de-Broglie wavelength of thermal neutrons is of the order of few angstroms, suitable for studying most atomic and molecular structures. This wavelength is also in the same range for studying most of the elementary excitations using inelastic scattering processes, such as phonons, magnons etc. The advantage of neutron scattering in this context is that it probes the entirety of the Brillouin-zone, unlike other techniques involving photons. Second, the interaction between the charge-neutral neutrons and matter. This interaction is short ranged, and thus point-like scattering approximation will be valid. Unlike for x-rays, the neutron scattering cross-section is a non-monotonous function of atomic number, even for isotopes. Thus resulting in quite distinct scattering from different elements. This is extremely useful in case of light elements. Third, unlike x-ray based techniques, due to absence of the Coulomb interaction, neutron scattering can also be used to probe the bulk of the materials. Fourth, due to the weak dipolar interaction between the neutron moment and the internal moment of the magnetic atoms in the sample, neutron scattering becomes an elegant tool to study magnetism in condensed matter physics. We will give a short derivation for the cross-section in case of both nuclear and magnetic scattering involving neutrons. For more detailed derivations, readers are advised to follow classic textbooks such as *Squires* [174].



## 4.2. Characterizations Of Long-period Incommensurate Structures

*Nuclear scattering:* The de-Broglie wavelength of a neutron travelling at speed  $v$  is given as  $\lambda = 2\pi\hbar/m_n v$ , whereas wave vector and energy of the neutron can be written as  $k_n = m_n v/\hbar$  and  $E_n = \hbar^2 k_n^2/2m_n$ , respectively. For a neutron undergoing scattering from  $K_i(E_i)$  to  $K_f(E_f)$ , the momentum and energy conservation lead to the following identities:

$$\begin{aligned} \mathbf{q} &= K_i - K_f, \text{ and} \\ \hbar\omega &= E_i - E_f = \frac{\hbar^2}{2m_n} (|K_i|^2 - |K_f|^2) \end{aligned} \quad (4.28)$$

$\hbar\omega$  is the energy transfer in the inelastic process, whose sign stands for whether the scattering is energy absorbing or emitting. We will derive our expressions for an inelastic process. But the transformation of these identities from an inelastic to elastic process is quite trivial. We start by defining scattering cross section as the ratio between the number of neutrons scattered per second to the total flux, and written as:

$$\sigma = \frac{1}{\Psi} [\text{Number of neutrons scattered per second}] \quad (4.29)$$

We now introduce angular dependency into the scattering in the following form:

$$\frac{d\sigma}{d\Omega} = \frac{1}{\Psi} \frac{\text{Number of neutrons scattered per second into the solid angle } d\Omega}{d\Omega}, \quad (4.30)$$

where, the infinitesimal solid angle  $d\Omega$  while integrated over the whole space gives  $4\pi$ . Equation 4.30 is known as the *differential scattering cross section*. The energy dependence is then introduced into Eqn. 4.30, and called the *partial differential scattering cross section*. Mathematically, it can be expressed as:

$$\frac{d^2\sigma}{d\Omega dE_f} = \frac{1}{\Psi} \frac{\left( \frac{\text{Number of neutrons scattered per second} \cdots}{\cdots \text{into the solid angle } d\Omega \text{ within the interval } dE_f} \right)}{d\Omega dE_f}. \quad (4.31)$$

Since this term includes contributions from both coherent (sum of elastic scattering such as Bragg peaks, phonons, magnons etc) and incoherent (diffusion, fluctuations, etc) processes, we can further simplify it into:

$$\frac{d^2\sigma}{d\Omega dE_f} = \left( \frac{d^2\sigma}{d\Omega dE_f} \right)_{\text{coh}} + \left( \frac{d^2\sigma}{d\Omega dE_f} \right)_{\text{incoh}}. \quad (4.32)$$

Of course, during the topics discussed in this present thesis, we will be focused on the coherent part. We are now ready to include the neutron-matter interaction into the process. Let's

assume that the system (neutron + matter) makes the following transition from  $|\Phi_i\rangle (\equiv |\lambda_i, K_i\rangle)$  to  $|\Phi_f\rangle (\equiv |\lambda_f, K_f\rangle)$ .  $\lambda$  and  $K$  are the sample and neutron quantum states, respectively. The weak interaction can change the quantum state of the sample, and we can use Fermi's Golden Rule to express the *partial differential scattering cross section*.

$$\left. \frac{d^2\sigma}{d\Omega dE_f} \right|_{\lambda_i \rightarrow \lambda_f} = \frac{K_f}{K_i} \left( \frac{m_n}{2\pi\hbar^2} \right)^2 |\langle K_f \lambda_f | \mathcal{V} | K_i \lambda_i \rangle|^2 \delta(\hbar\omega + E_i - E_f) \quad (4.33)$$

Here, we have included the interaction potential,  $\mathcal{V}$ . Since the interaction is weak, using the Born approximation for both incoming and outgoing neutrons as plane waves we get,

$$\langle K_f \lambda_f | \mathcal{V} | K_i \lambda_i \rangle = \mathcal{V}(\mathbf{q}) \langle \lambda_f | \sum_j e^{i\mathbf{q} \cdot \mathbf{r}_j} | \lambda_i \rangle. \quad (4.34)$$

Here,  $\mathbf{r}_j$  is the position of the scatterer inside a unit cell with the nuclear pseudo-potential:

$$\mathcal{V}(\mathbf{q}) = \int \mathcal{V}(\mathbf{r}) e^{i\mathbf{q} \cdot \mathbf{r}} d\mathbf{r} \quad (4.35)$$

Since we are dealing with the short-range nature of the strong nuclear force, this potential can effectively be described by the delta function (*Fermi pseudo-potential*) in position space as:

$$\mathcal{V}(\mathbf{r}) = \frac{2\pi\hbar^2}{m_n} \sum_j b_j \delta(\mathbf{r} - \mathbf{R}_j), \quad (4.36)$$

where,  $b_j$  is the element-specific scattering length. Plugging this into the left side of Eqn. 4.34, we arrive at the following conclusion.

$$\langle \Phi_f | \mathcal{V} | \Phi_i \rangle = \frac{2\pi\hbar^2}{m_n} b_j e^{i\mathbf{q} \cdot \mathbf{r}_j} \quad (4.37)$$

Finally, for coherent elastic scattering from a sample, we can have the following expression for the *differential scattering cross section*.

$$\left. \frac{d\sigma}{d\Omega} \right|_{\text{coh,el}} = \int \frac{d^2\sigma}{d\Omega dE_f} dE_f = N \frac{(2\pi)^3}{V_0} \sum_j |S_n(\mathbf{q})|^2 \delta(\mathbf{q} - \mathbf{G}) \quad (4.38)$$

$V_0$  is the volume of unit cell. Equation. 4.38 guarantees that scattering only takes place when the momentum transfer ( $\mathbf{q}$ ) matches the reciprocal lattice vectors ( $\mathbf{G}$ ). The nuclear structure factor,  $S_n(\mathbf{q})$ , encodes information about atomic coordinates and their fluctuations, and

$$S_n(\mathbf{q}) = \bar{b}_j e^{i\mathbf{G} \cdot \mathbf{r}_j} e^{-W_j} \quad (4.39)$$

Here, the term  $e^{-W_j}$  is called the *Debye-Waller factor*.

*The small angle approximation:* Under these conditions, we make the assumption that the  $\mathbf{q}$  of the particles are so small that the phase factor of the summation in Eqn. 4.38 does not greatly vary between successive atoms. Assuming the interatomic distance to be  $a$ , we have  $\mathbf{q}a \ll 2\pi$ . Therefore, we can replace the summation in Eqn. 4.38 to an integral. And finally, we have

$$\left. \frac{d\sigma}{d\Omega} \right|_{\text{SANS}} = N |S_n(\mathbf{q})|^2 \left| \int \rho_b(\mathbf{r}) e^{i\mathbf{q} \cdot \mathbf{r}} dV \right|^2. \quad (4.40)$$

Here,

$$\rho_b = \frac{1}{V_0} \sum_d b_d \quad (4.41)$$

is known as the *effective scattering length density* of the material. Assuming mono-dispersed spherical particles (radius  $R$ ), there exists two important approximations. For **(I)** small  $\mathbf{q}$ s, ( $\mathbf{q}R \ll 1$ ) and **(II)** large  $\mathbf{q}$ s, ( $\mathbf{q}R \gg 1$ ). These two cases are called the *Guinier approximation* and the *Porod's approximation*, respectively. The particle form factor arising in these two cases have quite distinct signatures in the resultant scattering. But since main focus of this thesis is the magnetic neutron scattering, this part will not be explained in details here.

*Magnetic neutron scattering:* Since neutrons possess a magnetic moment, they become sensitive to the local magnetism arising due to the ions in a crystal. The Zeeman interaction of a neutron in a magnetic field is given as:

$$E_z = -\boldsymbol{\mu} \cdot \mathbf{B} = -\gamma \mu_n \hat{\sigma} \cdot \mathbf{B} \quad (4.42)$$

Here,  $\hat{\sigma}$  represents the three Pauli spin matrices for the neutron. Within the dipole approximation, the magnetic field from each atom can be approximated by:

$$\mathbf{B} = \frac{\mu_0}{4\pi} \left( \nabla \times \left( \boldsymbol{\mu} \times \frac{\mathbf{r}}{r^3} \right) \right) \quad (4.43)$$

Thus, the Zeeman energy becomes,

$$E_z = \frac{\mu_0}{4\pi} g \mu_B \gamma \mu_n \hat{\sigma} \cdot \nabla \times \left( \frac{\mathbf{s} \times (\mathbf{r} - \mathbf{r}_j)}{|\mathbf{r} - \mathbf{r}_j|^3} \right) \quad (4.44)$$

The Zeeman interaction term will act as our potential  $\mathcal{V}$ . So in order to obtain the *partial differential scattering cross section*, we introduce Eqn. 4.44 into Eqn. 4.33, and thus find

$$\frac{d^2\sigma}{d\Omega dE_f} = \frac{K_f}{K_i} \left( \frac{\mu_0}{4\pi} \right)^2 \left( \frac{m_n}{2\pi\hbar^2} \right)^2 (g\mu_B\gamma\mu_n)^2 \sum_{\lambda_i, \lambda_f, \sigma_i, \sigma_f} p_{\lambda_i} p_{\sigma_i} \times \left| \left\langle K_f \lambda_f \sigma_f \left| \sum_j \sigma \cdot \nabla \times \left( \frac{\mathbf{s}_j \times (\mathbf{r} - \mathbf{r}_j)}{|\mathbf{r} - \mathbf{r}_j|^3} \right) \right| K_i \lambda_i \sigma_i \right\rangle \right|^2 \delta(\hbar\omega + E_{\lambda_i} - E_{\lambda_f}) \quad (4.45)$$

Here,  $p$  denotes the probability of the neutron to be in the initial state, which means  $p_{\uparrow}=p_{\downarrow}=1/2$ . The matrix element in Eqn. 4.45, contains a  $\hat{\mathbf{q}} \times (\mathbf{s}_j \times \hat{\mathbf{q}})$  term, which we will denote as  $\mathbf{s}_{\perp}$ . Also, we immediately realise that the  $\mathbf{s}_{\parallel}$  term vanishes, implying that neutrons are invisible to the spin component parallel to  $\mathbf{q}$ . So the spin part of the matrix after summing over all final states becomes

$$\sum_{\sigma_i, \sigma_f, \lambda_f} p_{\sigma_i} |\langle \sigma_f \lambda_f | \sigma \cdot \mathbf{s}_{\perp} | \sigma_i \lambda_i \rangle|^2 = \langle \lambda_i | \mathbf{s}_{\perp} \cdot \mathbf{s}_{\perp} | \lambda_i \rangle. \quad (4.46)$$

Including the orbital magnetic contribution, the total *partial differential scattering cross section* becomes [171, 174],

$$\begin{aligned} \frac{d^2\sigma}{d\Omega dE_f} = & (\gamma r_0)^2 \frac{K_f}{K_i} \left[ \frac{g}{2} F(\mathbf{q}) \right]^2 \sum_{\alpha\beta} (\delta_{\alpha\beta} - \hat{q}_{\alpha} \hat{q}_{\beta}) \\ & \times \sum_{\lambda_i, \lambda_f} p_{\lambda_i} \sum_{j, j'} \langle \lambda_i | e^{-i\mathbf{q} \cdot \mathbf{r}_j} \mathbf{s}_j^{\alpha} | \lambda_f \rangle \langle \lambda_f | e^{i\mathbf{q} \cdot \mathbf{r}_{j'}} \mathbf{s}_{j'}^{\beta} | \lambda_i \rangle \times \delta(\hbar\omega + E_{\lambda_i} - E_{\lambda_f}) \end{aligned} \quad (4.47)$$

The magnetic form factor,  $F_M(\mathbf{q})$  can be written as:

$$F_M(\mathbf{q}) = \int e^{i\mathbf{q} \cdot \mathbf{r}} \mathbf{s}(\mathbf{r}) d^3\mathbf{r}. \quad (4.48)$$

Here,  $\mathbf{s}(\mathbf{r})$  is the normalized spin density. For  $\mathbf{q} \rightarrow 0$ ,  $F_M(\mathbf{q}) \rightarrow 1$ , whereas it vanishes for large  $\mathbf{q}$ s. Now, if we consider only the elastic scattering, the delta function vanishes, and we end up with the following expression:

$$\left. \frac{d\sigma}{d\Omega} \right|_{\text{Mag, el}} = (\gamma r_0)^2 \left[ \frac{g}{2} F(\mathbf{q}) \right]^2 e^{-2W} \left| \sum_j e^{-i\mathbf{q} \cdot \mathbf{r}_j} \langle \mathbf{s}_{j, \perp} \rangle \right|^2 \quad (4.49)$$

In the above expression,  $\langle \mathbf{s}_{j,\perp} \rangle$  denotes the thermal averaged perpendicular spin component (with respect to  $\mathbf{q}$ ) of the magnetic atom. If we sum over all magnetic atoms, we end up with the final expression as:

$$\left. \frac{d\sigma}{d\Omega} \right|_{\text{Mag,el}} = (2\pi)^3 \frac{N}{V_0} (\gamma r_0)^2 \left[ \frac{g}{2} F(\mathbf{q}) \right]^2 e^{-2W} |F_M(\mathbf{q})|^2 \sum_{\mathbf{G}_M} \delta(\mathbf{q} - \mathbf{G}_M). \quad (4.50)$$

For a magnetically ordered lattice, for example a SkL phase, we need to write down the magnetization vectors. But we have already done this in Eqn. 3.10. It means except for a different form factor between resonant x-rays and neutrons, the final scattering pattern remains the same for both. We can use Fig. 4.5 to describe the magnetic plus nuclear reciprocal space in case of neutron scattering too. The only difference concerning the scattering geometry is that SANS is *always* performed around (000) reciprocal lattice vector, which is the same as transmission-REXS. Whereas in case of reflection-REXS, magnetic satellites around (001) structural peak are probed. Now we are ready to go deeper into the details of the various results described in this thesis.



# **Magnetic Skyrmions And Related Phases In Chiral Cubic $\text{Cu}_2\text{OSeO}_3$**

## **Part II**





## 5 Geometrical Confinement Effects In $\text{Cu}_2\text{OSeO}_3$ (Nano)Particles

In condensed matter physics, elucidation of the physical properties of novel materials in low dimensions is crucial from the viewpoint of fundamental physics as well as novel applications such as imaging, catalysis, and information devices, among others [20, 56, 107, 123, 147, 211]. In these materials, the reduction of at least one of the physical dimensions below a certain critical length results in *geometrical confinement effects*. The effect of surface symmetry breaking, due to an absence of neighbouring atoms or the presence of defects, together with geometrically confined magnetic spin textures may give rise to other exotic phenomena and different physics as compared to bulk single crystals [15, 50, 105]. A fertile ground to discover such unusual modifications is low dimensional samples of compounds hosting skyrmions [81]. The geometrical confinement effects in regular-shaped samples with dimensions approaching the nanoscale appear to modify the magnetic phase diagrams of chiral magnets drastically [36, 139]. Skyrmions have been imaged while confined in FIB-shaped nanowires and nanodisks of the itinerant  $B20$  chiral magnets MnSi or FeGe [45, 46, 85, 181, 217, 227]. It is found that the phase diagram of MnSi nanowires differs from those of both thin plate and bulk samples, thus illustrating an effect of particle morphology. More recently, isolated skyrmionic vortex have been discovered in tetrahedral (nano)particles of FeGe [139]. As a consequence of the 0D chiral geometric frustration, the skyrmionic vortex appears with an increased robustness against temperature variation. In this thesis, we provide a systematic study of the particle size-dependent thermodynamic properties of skyrmion hosting chiral magnet,  $\text{Cu}_2\text{OSeO}_3$ . These studies are essential not only for understanding the emergent physics from the novel geometrical confinement effects, but also controlling these behaviour in other chiral systems for future technological applications. We will first provide a short introduction to  $\text{Cu}_2\text{OSeO}_3$ , followed by the synthesis and structural characterizations of regular shaped octahedral particles in varying sizes. Next we will focus on the magnetic and thermodynamic properties of these systems based on various probes such as AC susceptibility, heat capacity and  $\mu\text{SR}$ , followed by size-dependent magnetic structure as obtained from neutron scattering experiments. In the final section, we will connect the experimental findings with those obtained from micromagnetic simulations based on Landau-Lifshitz-Gilbert equations<sup>1</sup>.

---

<sup>1</sup> Part of the results presented in this chapter is published in Ref. [11]

### 5.1 $\text{Cu}_2\text{OSeO}_3$ : The Magneto-Electric Insulating Skyrmion Host

Magnetic skyrmions are topologically protected multi-spin objects that can have a size between a few to hundreds of nanometers and that are stable in both metals and insulators alike [203]. Among the few known insulator skyrmions hosts,  $\text{Cu}_2\text{OSeO}_3$  is the archetype with a chiral cubic crystal structure. In the bulk, the skyrmions form a triangular SkL phase that is stable over a region that extends over a few Kelvin directly below the magnetic ordering temperature  $T_c \approx 58$  K. With an applied magnetic field along [111], the HT-SkL phase appears among all skyrmion-hosting  $B20$  magnets as well as  $\text{Cu}_2\text{OSeO}_3$ . Whereas, in thin plates (typically below 150 nm thick) prepared from FIB milling (shown in panel-B of Fig. 5.1), due to increased dipolar interaction, skyrmion lattice was found to be stable till the lowest temperatures. This was the first evidence of particle size dependent magnetic phase diagram in this chiral cubic insulator.

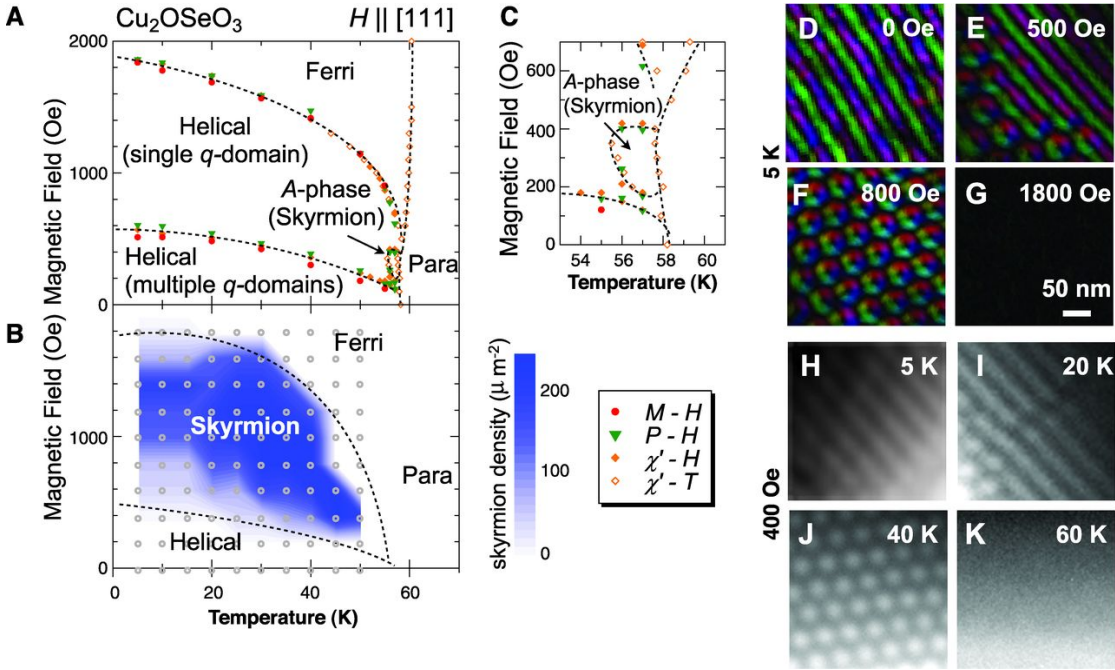


**Figure 5.1: Skyrmion lattice in two different particle size limits for  $\text{Cu}_2\text{OSeO}_3$ .** Magnetic phase diagram of  $\text{Cu}_2\text{OSeO}_3$  as obtained for  $H \parallel [111]$ . (A) bulk single crystals, (B) thin plates prepared by FIB milling. (C) Shows the zoomed-in view of boundaries of the HT-SkL phase in  $\text{Cu}_2\text{OSeO}_3$ . (D)-(G) Show the real space magnetization distribution as obtained at 5 K, as a function of applied magnetic field. At zero magnetic field, the stripy patterns due to helical phase slowly changes to six-spot pattern, characteristic of a SkL phase. (H)-(K) Show the Lorentz TEM images as a function of temperature, at a constant magnetic field. This figure has been adapted from Ref. [169].

Below  $T_c$ , the system further display magneto-electric (ME) coupling due to simultaneously broken  $\mathcal{P}$  and  $\mathcal{T}$  [144, 167]. Owing to this ME coupling, skyrmion manipulation by an electric field (EF) has been shown experimentally, including EF-driven skyrmion creation and

annihilation [110, 142, 205, 207]. Apart from this ME-coupling,  $\text{Cu}_2\text{OSeO}_3$  is also different from other  $P2_13$  skyrmion hosts in another aspect as well. Around the HT-SkL phase,  $\text{Cu}_2\text{OSeO}_3$  behaves isotropically in all crystallographic directions. But as the temperature is lowered, increased cubic magneto-crystalline anisotropy energy gives rise to a stable LT-SkL phase as well as a metastable tilted conical phase, only along  $\langle 100 \rangle$  [33, 63]. Thus, the phase diagram for a bulk crystal changes drastically when magnetic field is applied along either of the three high symmetry directions ( $\langle 100 \rangle$ ,  $\langle 110 \rangle$ , or  $\langle 111 \rangle$ ). This is shown in figure 5.2. One key aspect of the LT-SkL phase is that it does not require the usual thermal fluctuations energy to be stabilized, unlike all the chiral cubic skyrmion hosts. The well-known single domain conical phase follows the direction of applied magnetic field. Whereas, in the tilted conical phase, the modulation deviates from the magnetic field direction at a finite angle (also known as the tilt angle), which gradually increases with higher magnetic fields. While the outcome from 0D confinement will be discussed in the current chapter, results relevant to the LT-SkL phase will be outlined in the later part of this thesis (mainly chapter 6 and 7).

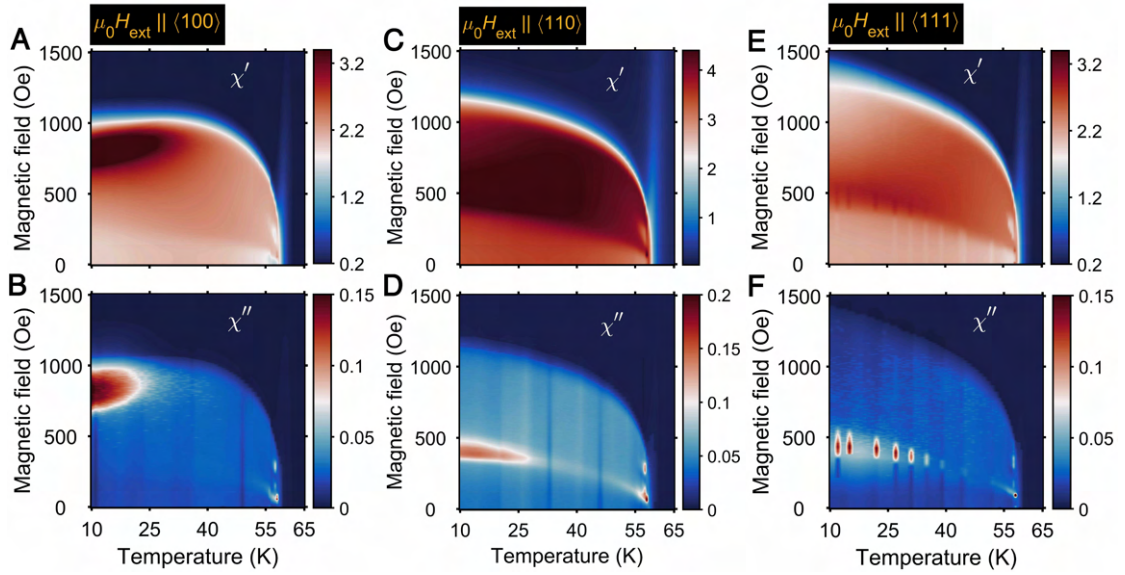


**Figure 5.2: Phase diagram of  $\text{Cu}_2\text{OSeO}_3$  with magnetic field applied along either of the three high symmetry directions.** Magnetic phase diagram of  $\text{Cu}_2\text{OSeO}_3$  single crystals measured with AC susceptibility field scans. Magnetic field was applied along  $\langle 100 \rangle$  (panel-A and B),  $\langle 110 \rangle$  (panel-C and D), or  $\langle 111 \rangle$  (panel-E and F) crystallographic directions. AC excitation field and frequency were fixed at 1 Oe and 911 Hz, respectively. As discussed in the text, the HT-SkL is present along all the three crystallographic directions shown in all six panels. Whereas, at lowest temperatures, a huge dissipative region can be seen existing only along  $\langle 100 \rangle$  axes. This is a clear signature of tilted conical phase. Just above the tilted conical phase, presence of LT-SkL phase is confirmed via a hysteretic region (not shown in the contour plot).

## 5.2 Controlled Chemical Synthesis Of Nanostructures

*Chemical process resulting in “Macro” to “Nano” crystals:* In order to observe the *geometrical confinement effects*, we need to have precise control over the particle size in the relevant length scale. In  $\text{Cu}_2\text{OSeO}_3$ , this is about the pitch length of a single helix ( $\sim 62$  nm) and slightly more [3, 206]. From the synthesis point of view, there is a lack of proper literature describing particle size control, in any length scale, let alone around a single helix. Currently the existing reports describe synthesis of  $\text{Cu}_2\text{OSeO}_3$  particles with size either below a magnetic helix pitch length (about 35 nm in Ref. [41]) or a broad size distribution resulting due to thermal decomposition of starting material [122]. Thus one needs a systematic chemical approach in order to fine tune the particle size and morphology, resulting in tunable magnetic properties.

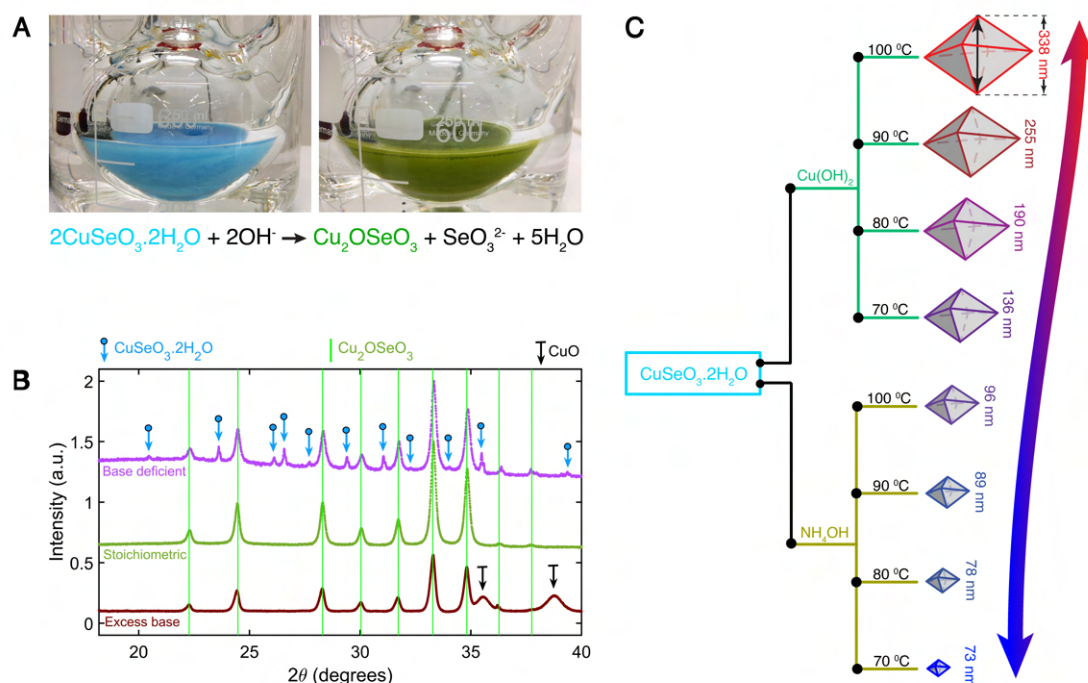


**Figure 5.3: Overview of  $\text{Cu}_2\text{OSeO}_3$  synthesis.** (A) Optical images of the starting solution containing  $\text{CuSeO}_3 \cdot 2\text{H}_2\text{O}$  on the left, and the final product,  $\text{Cu}_2\text{OSeO}_3$  on the right. In a 250 ml round bottom flask, about 1.5 g of  $\text{Cu}_2\text{OSeO}_3$  particles are produced in about 5 hours at 100 °C. The chemical equation describes the solid-to-solid transformation between the initial and final products in presence of a basic medium. (B) X-ray diffractograms of the final products as obtained from the reaction when stoichiometric and off-stoichiometric mixture of  $\text{CuSeO}_3 \cdot 2\text{H}_2\text{O}$  and base were used. Using an excess of base results in the presence of CuO formed by the decomposition of  $\text{Cu}_2\text{OSeO}_3$  ( $\text{Cu}_2\text{OSeO}_3 + 2\text{OH}^- \rightarrow 2\text{CuO} + \text{SeO}_3^{2-} + \text{H}_2\text{O}$ ). When the base is deficient, part of  $\text{CuSeO}_3 \cdot 2\text{H}_2\text{O}$  remains unreacted. (C) Schematic illustration linking synthesis protocol and the final average particle size as obtained from X-ray analysis.



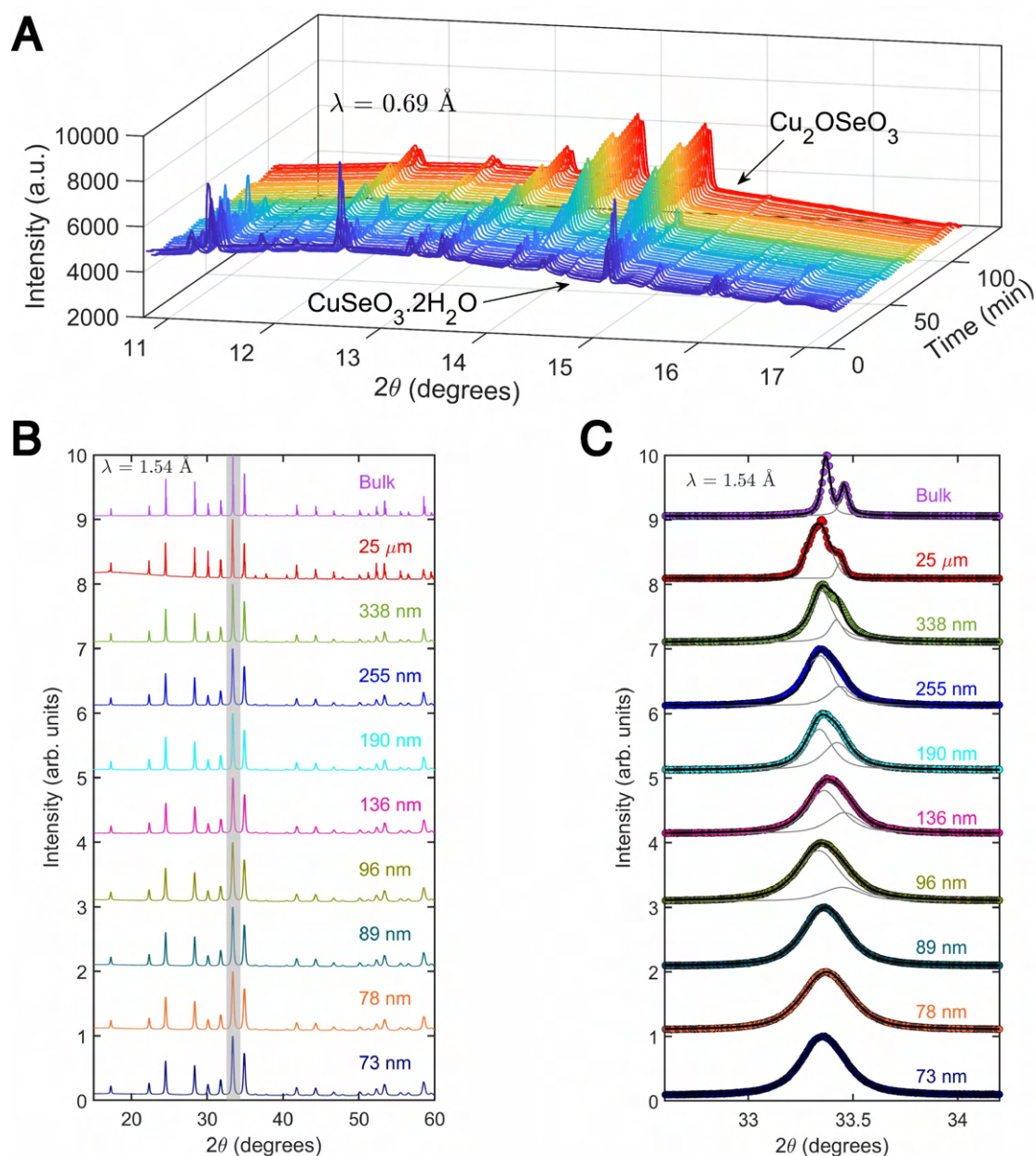


**Figure 5.4: X-ray diffraction analysis of all  $\text{Cu}_2\text{OSeO}_3$  particles.** (A) High resolution synchrotron XRD patterns of *in situ* transformation between the precursor  $\text{CuSeO}_3 \cdot 2\text{H}_2\text{O}$  and final product  $\text{Cu}_2\text{OSeO}_3$ , performed at SNBL, ESRF. This solid-solid transformation excludes the possibility of having any impurity phases throughout the whole process including the final  $\text{Cu}_2\text{OSeO}_3$  phase. (B) High-resolution room temperature lab XRD patterns of all the particles, compared with that of the bulk sample. All specimens appear to be phase pure. (C) From the complete  $2\theta$  range, one peak at  $2\theta \sim 33.4^\circ$  has been singled out for all the particles

The synthesis of  $\text{Cu}_2\text{OSeO}_3$  particles proceeded during a low-temperature reflux treatment performed in a round bottom flask at temperature ranging from 70 to 100 °C (Fig. 5.3A).

The solution was kept under constant stirring for homogeneous distribution of particles and temperature throughout.  $\text{CuSeO}_3 \cdot 2\text{H}_2\text{O}$ , used as a selenite precursor, was obtained by instantaneous precipitation when highly concentrated  $\text{CuSO}_4 \cdot 5\text{H}_2\text{O}$  and  $\text{SeO}_2$  solutions were mixed. Bases used during reflux are  $\text{NH}_4\text{OH}$  or  $\text{Cu}(\text{OH})_2$ . As shown in Figures 5.3 and 5.5, nanoparticles with a size smaller than 100 nm were obtained with  $\text{NH}_4\text{OH}$  while the use of  $\text{Cu}(\text{OH})_2$  yielded particles larger than 100 nm.  $\text{Cu}(\text{OH})_2$  was prepared by reaction between  $\text{Cu}(\text{NO}_3)_2 \cdot 3\text{H}_2\text{O}$ ,  $\text{NH}_4\text{OH}$ , and  $\text{NaOH}$  [138]. Using high temporal resolution synchrotron X-ray diffraction (XRD), the transformation of  $\text{CuSeO}_3 \cdot 2\text{H}_2\text{O}$  into  $\text{Cu}_2\text{OSeO}_3$  was followed *in situ*, as shown in Fig. 5.4A. The low temperatures ensure restrictive growth of the nucleation centres, resulting in a direct correlation with the size of the crystallites in Fig. 5.4C. The room temperature XRD patterns of Fig. 5.4B confirm not only the phase purity of these samples but also the excellent crystallinity. In order to compare the emerging magnetic order in the as-grown particles, throughout this chapter, we will make comparison with the more established studies performed on single crystals  $\text{Cu}_2\text{OSeO}_3$ . The “Bulk” sample mentioned throughout this chapter was obtained by crushing few single crystals of  $\text{Cu}_2\text{OSeO}_3$ , similar to the one seen in figure. 5.5A, which is grown by chemical vapor transport, as described in section 4.1. Crystals larger than 20 microns were obtained when the reaction between  $\text{CuSeO}_3 \cdot 2\text{H}_2\text{O}$  and  $\text{NH}_4\text{OH}$  proceeds in an autoclave at 150 °C (figure. 5.5B).

### 5.3 Structural Characterizations

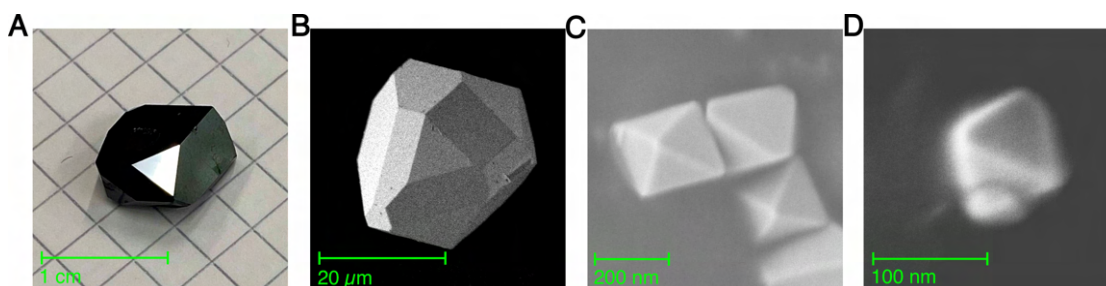


**Figure 5.5: Representative particles used for studying the *geometrical confinement effects*.** (A) Optical image of  $\text{Cu}_2\text{OSeO}_3$  bulk crystal grown via CVT technique. Similar crystals were crushed to make the sample labelled as “Bulk” in this chapter. (B)-(D) SEM images of different particles discussed in the text.

All the in-house XRD measurements were carried out on a PANalytical Empyrean diffractometer with the  $\text{Cu-K}\alpha$  radiation. The *in situ* XRD measurements were carried out at the Swiss-Norwegian Beamline (SNBL) at the European Synchrotron Radiation Facility (ESRF), Grenoble, France. The x-ray wavelength used for these experiments was  $\lambda = 0.69 \text{ \AA}$ . In the presence of a basic medium as  $\text{NH}_4\text{OH}$ ,  $\text{CuSeO}_3 \cdot 2\text{H}_2\text{O}$  transforms completely to  $\text{Cu}_2\text{OSeO}_3$ , with no trace of any other impurity phases, as shown in Fig. 5.4A. It provides us with great insight into the microscopic mechanism of formation of the final product. This part will be discussed in more details in later section 5.4 of this chapter. Powder XRD data reveals the

synthesized  $\text{Cu}_2\text{OSeO}_3$  samples to display excellent purity and crystallinity. The crystallization of the particles is inferred from the peak broadening in the XRD patterns data (see Fig. 5.4) and from scanning electron microscopy images, see Fig. 5.5C,D, which reveal all particles to display an octahedral morphology. The first insight into the size control of the particles is evident from the room-temperature XRD patterns (Fig. 5.4B & C). The evidence of peak broadening is obvious from here. In theory, this peak broadening can be a result of various factors, such as dislocations, twinning, coherency strain, chemical heterogeneity and, finally, small crystallite sizes. If these factors, other than the final reason, were responsible for the observations, it would also be evident from other local characterization tools (Fig. 5.9). And finally, since the instrumental contribution was fixed for all the patterns, the broadening of diffraction peaks is thus attributed to average coherent size of the particles. Refinement of the powder XRD patterns, as shown in Figure 5.6C, confirms that the unit cell length for all particle sizes remains essentially unchanged from the bulk value [49].

*Particle size determination:* In our work, the particle size was determined by using a combination of dynamic light scattering (DLS), SEM imaging and Williamson-Hall analysis. Figure. 5.6 shows a Williamson-Hall (W-H) analysis of the XRD data, from which the average coherent particle size is determined and the nanoparticle strain is estimated. The various samples of  $\text{Cu}_2\text{OSeO}_3$  particles have octahedral heights ( $h$ ) ranging from 73 to 338 nm and negligible strain ( $<0.2\%$ ). As shown in the SEM image in Fig. 5.7, the as-grown sample is typically synthesized as agglomerates of well faceted and highly crystalline particles. Thus, the size determination procedure was divided into two steps. In the first step, the secondary particle size was determined by DLS technique. The powder sample was suspended in a water + surfactant solution (SDS-Sodium Dodecyl Sulfate), followed by thorough sonication. The measurement was performed in a Zetasizer and for consistency check, 10-15 repetitions were performed for each sample size.

As can be seen from Fig. 5.7, the DLS technique correctly measures the secondary particle sizes, for all samples. The example shown below corresponds to the one with mean size of  $1324 \pm 5$  nm. The measurements confirm the very narrow distribution of the secondary particle size as opposed to the distribution reported so far in Ref. [72].

But from the perspective of skyrmion physics, the size of the primary particles is much more relevant. Although the distribution appears to be narrow in panel B of fig. 5.7, an accurate particle size measurement cannot be obtained from the SEM images because particles are tilted, overlapping and/or partially embedded in the agglomerates. So, the 3D particle size distribution cannot not be obtained from SEM. We chose to determine the primary particle size by performing Williamson-Hall (W-H) analysis. A large  $2\theta$  range is used such that the 3D particle size can be accurately obtained. As shown in the Fig. 5.6, the primary particle size corresponding to the sample in panel B of fig. 5.7 is determined to be  $136 \pm 2$  nm. Together with all the measurement protocols described above, we achieved a tight distribution of the particle sizes, which correlates directly with the systematic behaviour observed in the experimental magnetic properties described in section. 5.5. In order to confirm the narrow size distribution,

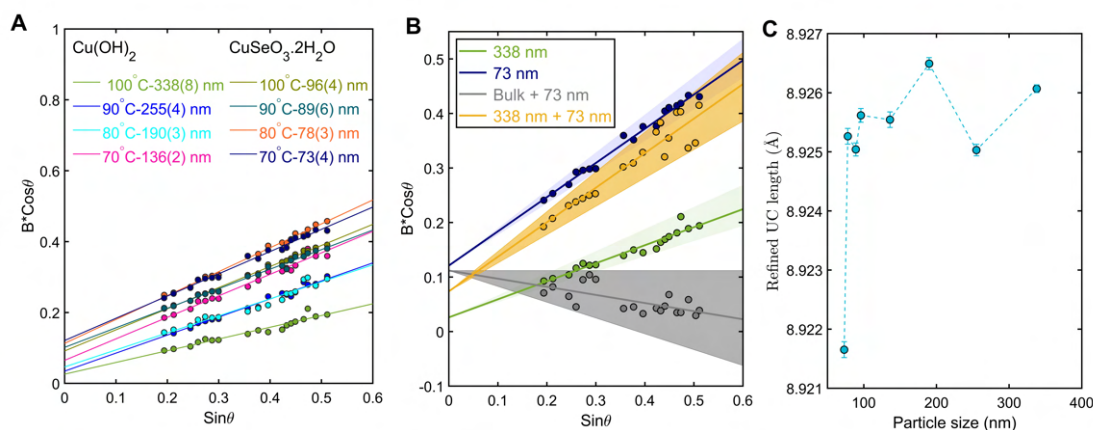


**Figure 5.6: Williamson-Hall analysis of all particles based on x-ray diffraction data.** (A) Particle size obtained from the Williamson-Hall analysis of all XRD data. The instrumental contribution of the peak broadening was determined in the XRD pattern recorded with the bulk  $\text{Cu}_2\text{OSeO}_3$  powder. The slope and intercept of the fits are representative of the average particle size and strain, respectively. The different particle sizes obtained are given with the corresponding reflux temperatures and bases used during the synthesis. (B) W-H measurements performed on a mixture of two particle sizes. Data for 338 nm and 73 nm have been shown for reference. (C) Refined lattice parameter for all particles shown in panel-A.

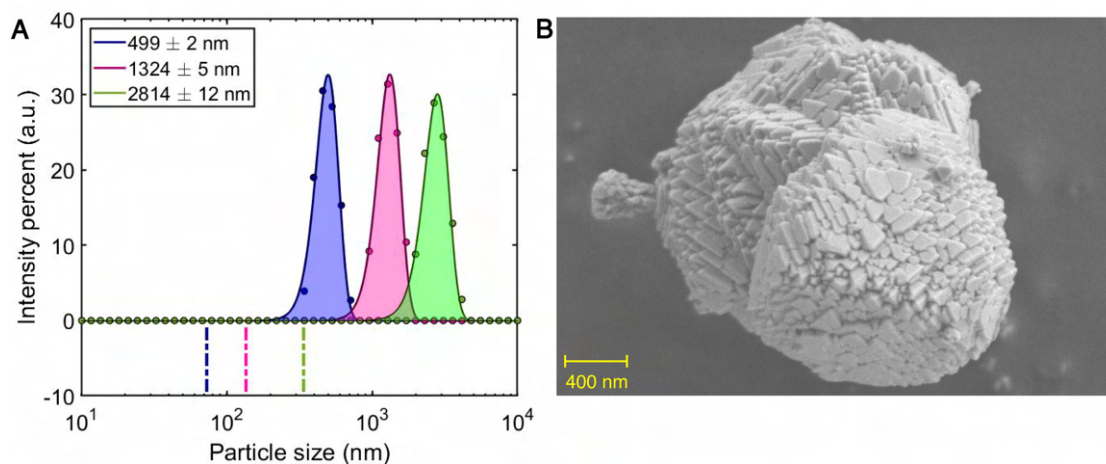


**Figure 5.7: Secondary particle size determination from dynamic light scattering measurements.** (A) Particle size determination from DLS measurements. The maximum of the shaded region corresponds to the average secondary size as determined from the experiments. The dashed lines are the average primary particle sizes, as obtained from W-H analysis (shown in Fig. 5.6A). (B) An example SEM image representing both the primary as well as secondary particle sizes for the batch coloured in magenta in Panel-A.

we performed some additional W-H measurements on a mixture made of 73 nm particles with 338 nm particles such that the size distribution becomes broad. Fig. 5.6B shows that while the W-H plot for pure 73 nm and 338 nm samples are perfectly linear, a strong scattering is



obtained at high  $2\theta$  angles for the mixture of 73 nm and 338 nm. Same broadening in the W-H plot is seen when the 73 nm particles are mixed with a powder obtained by crushing a  $\text{Cu}_2\text{OSeO}_3$  single crystal. These additional measurements confirm the primary particle size distribution is narrow.

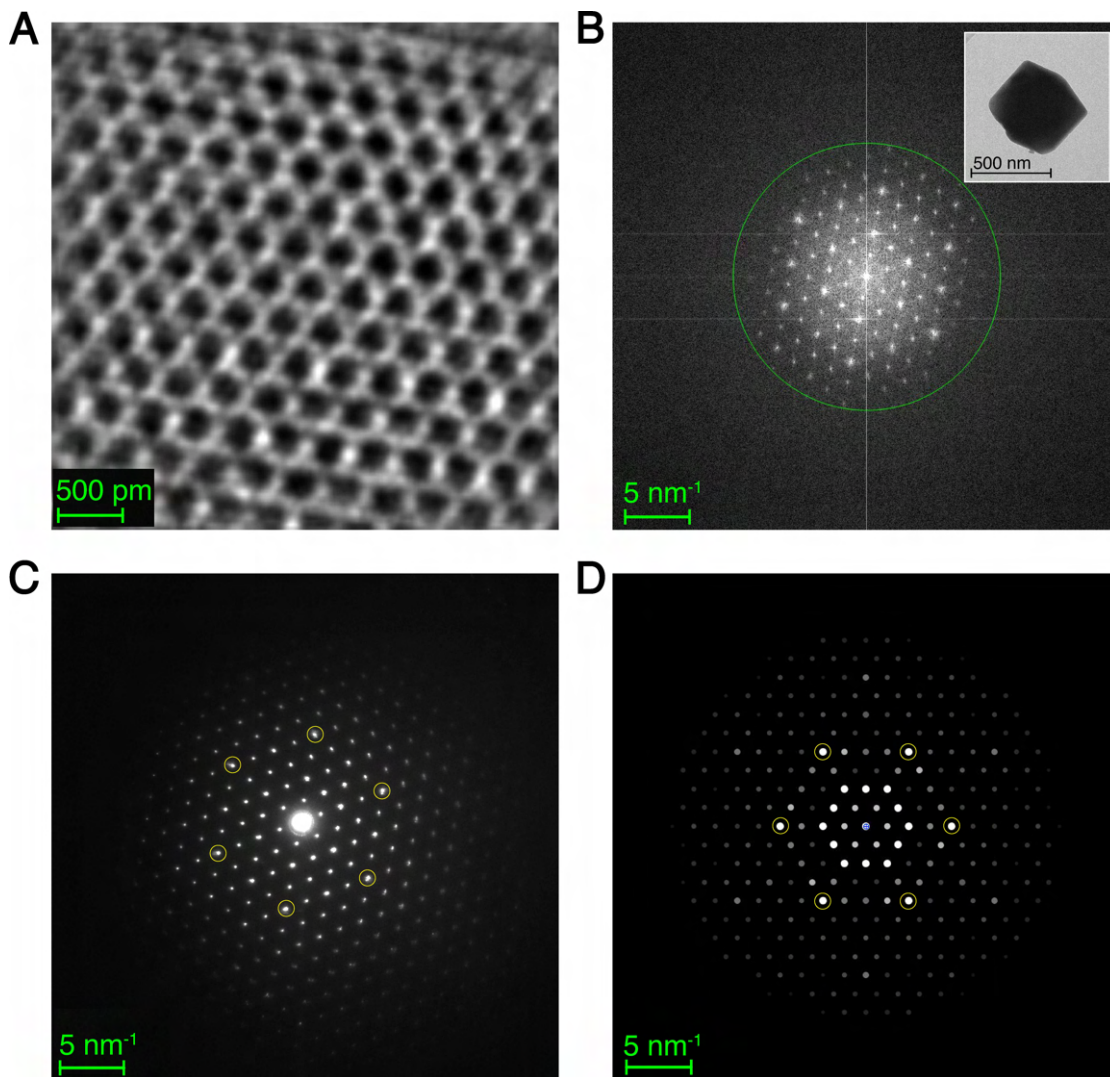


**Figure 5.8: High resolution TEM image of grown  $\text{Cu}_2\text{OSeO}_3$  particles.** (A) High resolution TEM image of grown  $\text{Cu}_2\text{OSeO}_3$  viewed along  $\langle 111 \rangle$  zone axis. The hexagonal pattern is formed due to the arrangement of Cu and Se atoms in the structure. Since a non-aberration corrected microscope was used, oxygen atomic positions were difficult to be resolved. (B) Fast Fourier transform (FFT) pattern of the HRTEM image shown in (A). The green circle indicates the information limit of the microscope (0.1 nm). Inset shows a TEM image of a particle. (C) Small angle electron diffraction (SAED) pattern of the same crystallite obtained under diffraction mode. (D) Simulated diffraction pattern for a 300 nm thick particle along the  $\langle 111 \rangle$  zone axis showing good agreement with the experimental pattern.

*Additional characterizations:* To probe the structural matrix at an atomic scale, high resolu-

tion transmission electron microscopy (HRTEM) investigations were performed on several crystallites<sup>2</sup>. The HRTEM picture of  $\text{Cu}_2\text{OSeO}_3$  atomic structure viewed from the  $\langle 111 \rangle$  zone axis, is shown in figure 5.8A. With the non-aberration corrected microscope, even though oxygen atomic positions are quite difficult to resolve, the emergence of a clear hexagonal pattern is the consequence of Cu and Se atoms in the structure. Together with the clean fast Fourier transform (FFT) image of this pattern (figure 5.8B), it is sufficient to conclude the excellent quality and structural homogeneity of the grown  $\text{Cu}_2\text{OSeO}_3$ . These results are also corroborated by the small angle electron diffraction (SAED) pattern shown in figure 5.8C. In order to check the validity of the SAED analysis, the diffraction pattern was simulated for a 300 nm thick sample using the JEMS software. As shown in figure 5.8D, the result obtained from the simulation is equivalent to the experimental SAED pattern. For further information about HRTEM analysis from a different zone axis, refer to Baral *et al.* [11].

Raman scattering measurements were performed on a Renishaw inVia Raman spectroscope equipped with a 532 nm wavelength laser. The incident power on the sample was kept fixed at 0.05 mW (spectral resolution of  $0.8 \text{ cm}^{-1}$ ). Pellets were made from each sample, and 10 repetitions were performed (at different positions), each with 100s exposure time. This data shown in Figure 5.9A provides us with additional information about the structural equivalence between the grown materials and bulk  $\text{Cu}_2\text{OSeO}_3$ .

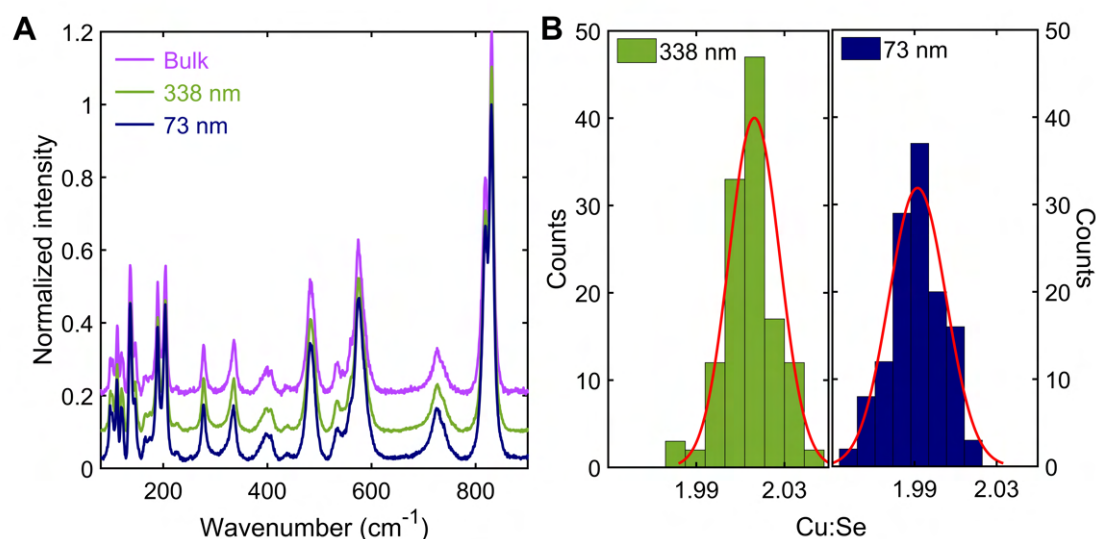


**Figure 5.9: Structural homogeneity in  $\text{Cu}_2\text{OSeO}_3$  particles probed by Raman spectroscopy and XRF.** (A) Raman spectrum of selected particles showing distinct modes consistent with the ones obtained from the bulk sample. These results are representative of those from the remaining sizes of particles. (B) XRF analysis of the same selected  $\text{Cu}_2\text{OSeO}_3$  particles showing the atomic ratio of Cu and Se being very close to an expected stoichiometric value of 2.

X-ray fluorescence (XRF) measurements were performed on an ORBIS PC with an applied

<sup>2</sup>This work was performed in collaboration with Dr. Thomas LaGrange from the Laboratory for Ultrafast Microscopy and Electron Scattering (LUMES), EPFL.

#### 5.4. Reaction Kinetics And Mechanism Of Chemical Transformation Between $\text{CuSeO}_3 \cdot 2\text{H}_2\text{O}$ and $\text{Cu}_2\text{OSeO}_3$

voltage of 26 kV and with a current of 1000  $\mu\text{A}$ . The quantification was done using the  $K\alpha$  line of both Cu and Se. For a good statistical distribution, measurements were performed at 128 different points for each sample. the Cu and Se stoichiometries of the particles were also investigated. Figure 5.9B shows that the average Cu/Se atomic ratios are determined to be 1.99(2) and 2.01(1) for the 73 and 338 nm particles, respectively. The negligible deviation will have little to no consequences on the physical properties. In summary, volume aside, the synthesized particles are essentially chemically and structurally equivalent to bulk  $\text{Cu}_2\text{OSeO}_3$ . We now have all the ingredients ready to explore the *geometrical confinement effects* in these size-varying particles.

#### 5.4 Reaction Kinetics And Mechanism Of Chemical Transformation Between $\text{CuSeO}_3 \cdot 2\text{H}_2\text{O}$ and $\text{Cu}_2\text{OSeO}_3$

But before we explore that, we take a small deviation to discuss a different aspect arising from this whole process, that is the chemical principles behind the transformation between the starting and the final products. Precise control over rate kinetics, mostly in a wide range of external parameters such as temperature and pressure, is essential for an in-depth understanding of inherent chemical processes, and thus helps with more efficient observation and manipulation of the physical chemistry of materials. We already have a glimpse of the incredibly complex mechanism of  $\text{Cu}_2\text{OSeO}_3$  synthesis via the CVT route (see Eqn. 4.4- 4.6). The temperature of the sink end of the ampoule never exceeds 823 K to prevent the thermal decomposition of  $\text{Cu}_2\text{OSeO}_3$  crystals into  $\text{CuO} + \text{SeO}_2$ , but is preferably higher than 803 K to prevent the undesired co-crystallization of copper selenates with Cu:Se ratio higher from 2:1. Thus, resulting in only a 20 K temperature range to produce single crystals. Apart from the small temperature window, high vapor pressure and presence of other gaseous species makes the reaction even more complicated.  $\text{Cu}_2\text{OSeO}_3$  particles can in principle be grown via other techniques such as supercritical hydrothermal method [40] and thermal decomposition of  $\text{CuSeO}_3 \cdot 2\text{H}_2\text{O}$  [122]. But a detailed knowledge about the reaction mechanism is essential for controlling various functional properties of the grown material, such as the particle size, composition, homogeneity etc.

*Structure of  $\text{CuSeO}_3 \cdot 2\text{H}_2\text{O}$  and binding energy of protons:* Since the crystal structure at the atomic scale plays the pivotal role in the underlying chemical transformation, we begin by giving a detailed account of  $\text{CuSeO}_3 \cdot 2\text{H}_2\text{O}$ , the starting material used for synthesis of  $\text{Cu}_2\text{OSeO}_3$ . As shown in Figure 5.10A, the unit cell of  $\text{CuSeO}_3 \cdot 2\text{H}_2\text{O}$  contains four inequivalent proton sites. Hydrogen bonding among these protons and the corresponding oxygen atoms form pseudo two-dimensional ring like structures in the *ab*-plane. These rings are stacked forming proton containing channels propagating along *c*-direction, as shown in figure 5.10A. Anisotropic expansion of the  $\text{CuSeO}_3 \cdot 2\text{H}_2\text{O}$  unit cell is evident from Fig. 5.10C. Concomitantly, the dihedral angle of the two water molecules (at  $109^\circ$  for  $H1\text{-O-H}2$ , and  $106^\circ$  for  $H3\text{-O-H}4$ ) gets significantly modified compared to naturally occurring water ( $104.5^\circ$ ). This is one of the most crucial points about the complete transformation, since growth of  $\text{Cu}_2\text{OSeO}_3$  from

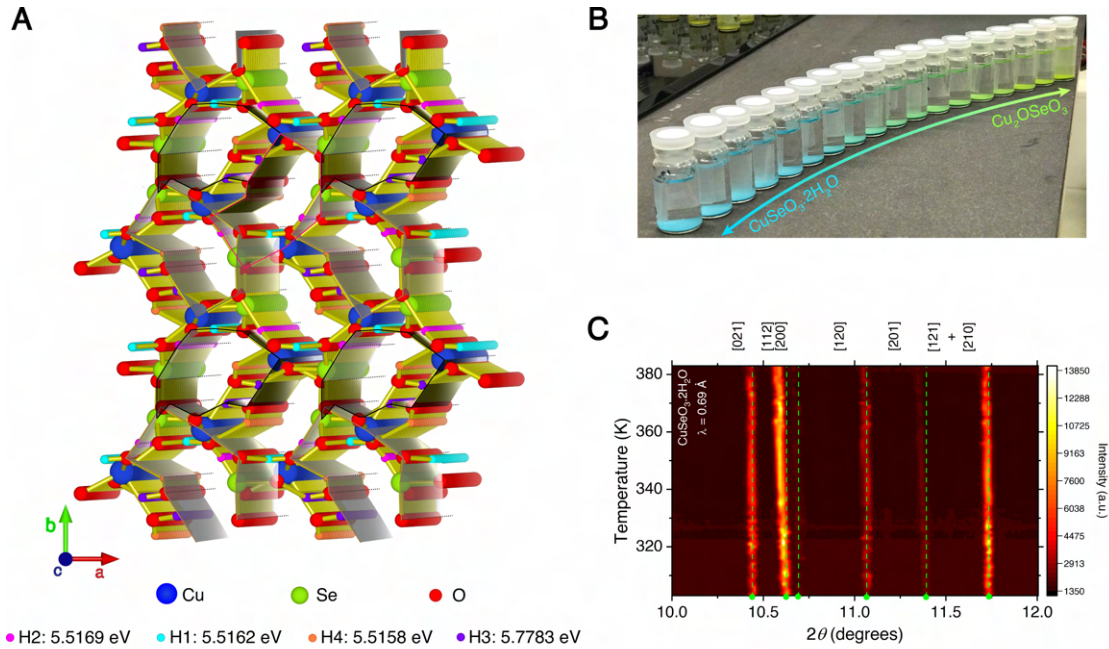


**Figure 5.10: The complex crystal structure of  $\text{CuSeO}_3 \cdot 2\text{H}_2\text{O}$ .** (A) Crystal structure of  $\text{CuSeO}_3 \cdot 2\text{H}_2\text{O}$ , as visualized with a slight tilt from the crystallographic  $c$ -axis. The dark gray colored polygons have been drawn in order to emphasize on the *channels* formed in the  $ab$ -plane of the structure. Note that many unit cells have been included, along all three crystallographic axes, to make the structure visually more appealing. The number shown against each proton site is the binding energy obtained from the DFT calculations. (B) Optical images of specimen collected at various stages throughout the transformation between  $\text{CuSeO}_3 \cdot 2\text{H}_2\text{O}$  and  $\text{Cu}_2\text{OSeO}_3$ . (C) Intensity evolution of few of the  $\text{CuSeO}_3 \cdot 2\text{H}_2\text{O}$  Bragg peaks obtained during thermal treatment between room temperature and 383 K.

$\text{CuSeO}_3 \cdot 2\text{H}_2\text{O}$  is based on the principle of extraction of these protons. While one (or more) of these acidic protons are being neutralized, the leaching of  $\text{SeO}_2$  from the structural matrix of  $\text{CuSeO}_3 \cdot 2\text{H}_2\text{O}$  takes place simultaneously. Thus in order to know the exact strength of basic medium required to remove each of these protons successively, one needs to know the corresponding  $\text{p}K_a$  values. Thus we calculated an equivalent physical property of the system, the binding energy of the protons.

Density functional theory (DFT) calculations were performed on periodic models with the Vienna Ab Initio Simulation Package (VASP) [108, 109]<sup>3</sup>. Electron-core interactions were described with the projector-augmented wave method, while the Kohn-Sham wave-functions for the valence electrons were expanded in a plane wave basis with a cutoff of 500 eV on the kinetic energy. We used a mesh of  $11 \times 11 \times 11$   $k$ -points for the PBE variant of the GGA functional and allowed atomic coordinates to be optimized along with the unit cell shape and volume in the structure relaxation process [151]. Atomic coordinates used for calculations

<sup>3</sup>This work was performed in collaboration with Dr. Ravi Yadav from the group of Chair of Computational Condensed Matter Physics (C3MP) at EPFL.



#### 5.4. Reaction Kinetics And Mechanism Of Chemical Transformation Between $\text{CuSeO}_3 \cdot 2\text{H}_2\text{O}$ and $\text{Cu}_2\text{OSeO}_3$

were obtained by performing a single crystal XRD experiment at 100 °C.

As a model system, we first performed DFT calculations on a similar Se-containing biprotic acid,  $\text{H}_2\text{SeO}_3$ , which has rather well-known acidity of  $\text{p}K_{\text{a}1} = 2.62$  and  $\text{p}K_{\text{a}2} = 8.32$  [98]. In order to calculate the binding energies of the protons, first, the crystal structure was relaxed and total energy of the  $\text{H}_2\text{SeO}_3$  unit cell was obtained using periodic boundary conditions. In the second step, one  $H$  atom was removed while adding an extra electron to the system (in order to maintain charge neutrality). By choosing which  $H$  atom to remove, two different configurations were obtained, corresponding to the two inequivalent  $H$  atoms present in the unit cell. The total energy was obtained by relaxing the crystal structure for each of these two configurations. The binding energy for each inequivalent  $H$  ion is then calculated as the difference between the total energy of the configuration obtained after removing the  $H$  atom and adding an electron with respect to the total energy of the parent system. Thus the  $H$  ion with minimum binding energy is found. For  $H1$ , the binding energy is 6.71 eV, whereas for  $H2$  it is 7.82 eV. Removal of  $H1$  in a basic medium corresponds to  $\text{p}K_{\text{a}1}$  of  $\text{H}_2\text{SeO}_3$ . The next configuration is set via removing this specific H-ion. Binding energy associated with the remaining proton is estimated by following the previous step. After removal of  $H1$ , the binding energy of  $H2$  reduces to 4.8 eV. And thus roughly corresponds to  $\text{p}K_{\text{a}2}$ . Thus we know that if  $\text{p}K_{\text{b}}$  of the basic medium is between 11.38 ( $E_{\text{B}} = 6.71$  eV,  $H1$ ), and 5.68 ( $H2$ ), then a single proton will be removed and thus making  $\text{HSeO}_3^-$  anion. Whereas, for  $\text{p}K_{\text{b}}$  lesser than 5.68, both protons will be removed producing  $\text{SeO}_3^{2-}$  ions in the solution.

Now for  $\text{CuSeO}_3 \cdot 2\text{H}_2\text{O}$ , by performing the same process three times iteratively, the energetically favourable sequence in which all the  $H$  ions can be removed is found (see table 5.1 for details). At  $T = 373$  K, the relative differences in the energy between the four protons are smaller compared to the ones at  $T = 298$  K. Due to the anisotropic expansion in the unit cell between these two temperatures,  $H4$  is found to possess the least binding energy at the latter temperature, instead of  $H2$ . Thus becoming the most energetically favourable site to be de-protonated first. But after removal of  $H4$ , the binding energy of  $H3$  is enhanced and it becomes energetically favourable for  $H2$  to be removed. With successful removal of one proton from each site, the parent structure becomes increasingly unstable and finally starts transforming into  $\text{Cu}_2\text{OSeO}_3$  matrix.

Thus we know that the  $\text{H}_2\text{O}$  molecule containing  $H1$  and  $H2$  will be removed first.  $\text{CuSeO}_3 \cdot 2\text{H}_2\text{O}$  will also follow similar behaviour as compared with  $\text{H}_2\text{SO}_3$ . But since the precise  $\text{p}K_{\text{a}}$  for  $\text{CuSeO}_3 \cdot 2\text{H}_2\text{O}$  is not known, different bases with accurate strength were selected. Our experiments include NaOH ( $\text{p}K_{\text{b}} = 0.2$ ), Methylamine ( $\text{p}K_{\text{b}} = 3.34$ ), Ammoniac ( $\text{p}K_{\text{b}} = 4.77$ ), Pyridine ( $\text{p}K_{\text{b}} = 8.77$ , not shown but discussed), Urea ( $\text{p}K_{\text{b}} = 13.9$ , not shown but discussed) as well as one Cu-containing base  $\text{Cu}(\text{OH})_2$  ( $\text{p}K_{\text{b}} = 2.43$ ).

*Analysis of the phase fraction:* During the reflux growth of  $\text{Cu}_2\text{OSeO}_3$ , a few milliliters of the solution containing  $\text{Cu}_2\text{OSeO}_3$  and  $\text{CuSeO}_3 \cdot \text{H}_2\text{O}$  is collected and quenched in a vial at room temperature. As can be seen in the figure. 5.10, the solution stays transparent during the

Proton site	$T = 298 \text{ K}$			$T = 373 \text{ K}$		
	Original configuration	After removal of 1 <sup>st</sup> H	After removal of 2 <sup>nd</sup> H	Original configuration	After removal of 1 <sup>st</sup> H	After removal of 2 <sup>nd</sup> H
H1	6.7037 eV	7.1522 eV	6.9519 eV	5.5162 eV	5.3356 eV	6.1527 eV
H2	6.6839 eV	–	–	5.5169 eV	5.3018 eV	–
H3	7.3012 eV	6.5294 eV	7.4078 eV	5.7783 eV	6.3394 eV	6.4078 eV
H4	7.1681 eV	6.3818 eV	–	5.5158 eV	–	–

**Table 5.1:** Binding energies for four-inequivalent protons obtained from DFT calculations at room temperature and  $T = 373 \text{ K}$ .

process illustrating the absence of dissolved Cu. On the other hand, blue  $\text{CuSeO}_3 \cdot 2\text{H}_2\text{O}$  solid progressively converts into light green  $\text{Cu}_2\text{OSeO}_3$ . The filtered sample was dried (not washed in order not to lose the soluble species potentially formed during the reaction), followed by measuring their XRD pattern. A zero background holder was used for collecting all patterns, to detect amorphous phase(s) present, if any. The whole solid-to-solid transformation between the two phases can be effectively tracked using high resolution XRD measurements. One Bragg peak is chosen from each of the participating phases in such a way that there is no overlap of intensity between them and with other peaks. The phase fraction of each of the participating phases can then be calculated as the ratio of the intensity of the particular Bragg peak with respect to the total intensity of all considered peaks. Our Bragg peaks of choice here are [101] ( $2\theta = 17.92^\circ$ ) and [222] ( $2\theta = 34.79^\circ$ ) for  $\text{CuSeO}_3 \cdot 2\text{H}_2\text{O}$  and  $\text{Cu}_2\text{OSeO}_3$ , respectively [shown in Fig 5.11A-C]. This isothermal  $\text{Cu}_2\text{OSeO}_3$  phase growth is then treated with the modified Johnson-Mehl-Avrami-Kolmogorov (JMAK) equation:

$$\alpha = 1 - e^{-[kt(1-t_0/t)]^n}, \quad (5.1)$$

where,  $\alpha$ ,  $k$ , and  $t_0$  represent phase fraction of  $\text{Cu}_2\text{OSeO}_3$ , rate constant and reaction initiation time, respectively. The Avrami exponent,  $n$ , controversial in its own terms, stands for dimensionality of the final product. In theory,  $n$  can have a maximum value of 4 in case of a three-dimensional crystallization. Compared to this simple scenario, there are many more complicated mechanisms giving rise to a value of  $n$  more than 4. From the mathematical form of the JMAK equation itself, it can be seen that critical information is lost while trying to fit phase fraction evolution. As shown in Fig 5.11D, a linearized JMAK equation expressed as:

$$\ln(-\ln(1 - \alpha)) = n(\ln t) + n(\ln k), \quad (5.2)$$

uncovers finer details of fundamental importance, such as the crossover time ( $t_{\text{CO}}$ ). We define  $t_{\text{CO}}$  as the time when the overall reaction kinetics switches between two unique Avrami regions. As discussed later, this is the consequence of a two-step chemical reaction with

#### 5.4. Reaction Kinetics And Mechanism Of Chemical Transformation Between $\text{CuSeO}_3 \cdot 2\text{H}_2\text{O}$ and $\text{Cu}_2\text{OSeO}_3$

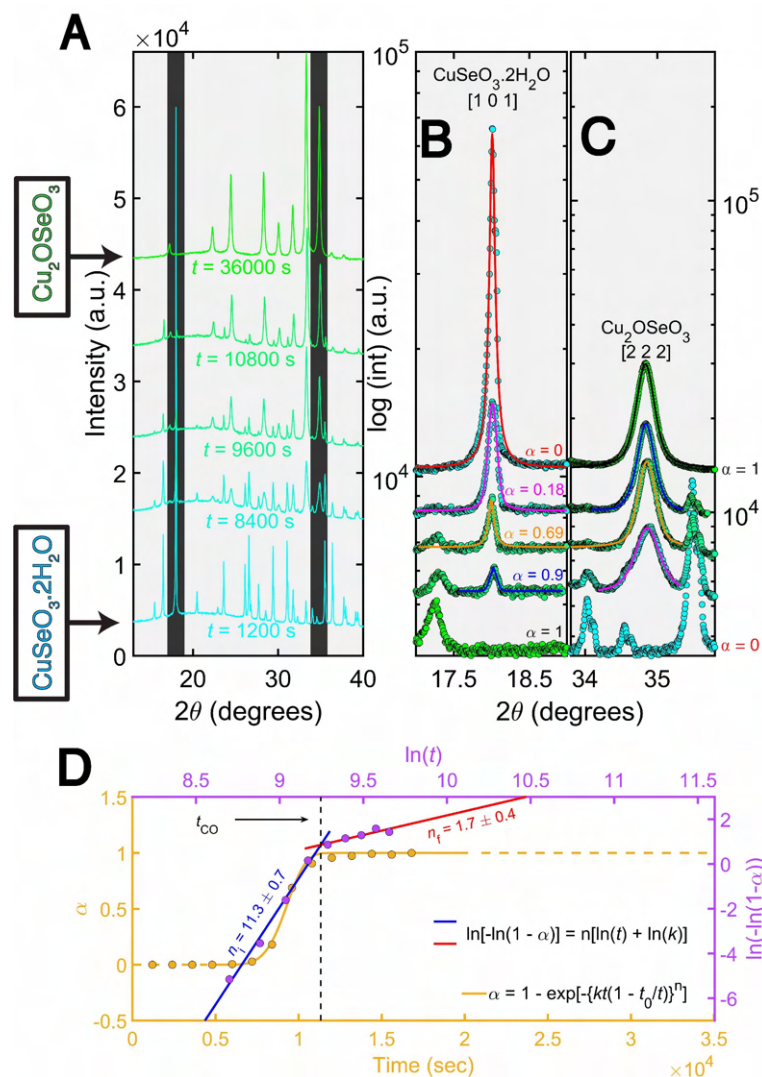


**Figure 5.11: Linearized JMAK equation for kinetics analysis.** (A) XRD patterns of the samples collected during the transformation between  $\text{CuSeO}_3 \cdot 2\text{H}_2\text{O}$  and  $\text{Cu}_2\text{OSeO}_3$ . For the phase fraction analysis, we considered the absolute height of two separate Bragg peaks, one from each of the participating phases. These two peaks are highlighted in black. The only requirement while choosing the peaks was not to have an overlap between them. This process was cross-checked with other sets of Bragg peaks. (B) and (C) focus on the same regions shown in panel-(A), along with Pseudo-Voigt fits to the diffraction peaks. Parameter  $\alpha$  is defined as the ratio between the intensity of  $[222]$  peak of  $\text{Cu}_2\text{OSeO}_3$  to the  $[101]$  peak of  $\text{CuSeO}_3 \cdot 2\text{H}_2\text{O}$ . (d) The  $\alpha$  values thus obtained were fitted using the JMAK equation (see text for more details) in both linear and logarithmic time scales. Analysis of the phase fraction using the linearized JMAK equation reveals finer details about the growth kinetics. The crossover time,  $t_{CO}$  is defined as when the rate of the reaction switches between two distinct values, resulting in two different Avrami coefficients,  $n$ .

distinct kinetics. The second variable from the JMAK equation is the reaction rate constant,  $k$ , which when plugged into the well-known Arrhenius equation (see below, Eqn. 5.3), produces the activation energy of the reaction.

$$k = A \exp(-E_a/RT), \quad (5.3)$$

where,  $R$  is the universal gas constant. As discussed in the next section, we find a trend in the activation energy dependency on the strength of basic medium. We provide a step-by-step mechanism for the same as well. In order to illustrate this in more details, we start with a thorough explanation of the analysis of the XRD data.

*Kinetics and mechanism:* The Avrami plots reveal the growth mechanism to depend on the strength of the base. While trying to neutralize  $\text{CuSeO}_3 \cdot 2\text{H}_2\text{O}$  with pyridine, the reaction never produces pure phase  $\text{Cu}_2\text{OSeO}_3$ . The reaction medium stays in a state of dynamic equilibrium between  $\text{CuSeO}_3 \cdot 2\text{H}_2\text{O}$  and  $\text{Cu}_2\text{OSeO}_3$ , giving rise to an oscillatory phase fraction between the two. Thus the  $\text{p}K_b$  of pyridine (8.77) is not strong enough to deprotonate even a single  $\text{H}^+$ -ion of  $\text{CuSeO}_3 \cdot 2\text{H}_2\text{O}$ . This provides us with an estimate of the lower bound of  $\text{p}K_{a1}$  for the starting material, which is approximately around 5.23. For the other bases, we find four distinct growth mechanisms.

- I.  *$\text{NH}_4\text{OH}$  at high temperatures:* Using  $\text{NH}_4\text{OH}$  at high temperatures (for example, 371 K) only takes up half the stoichiometric amount necessary to complete the transformation (that is  $\text{NH}_4\text{OH}:\text{CuSeO}_3 \cdot 2\text{H}_2\text{O}=1:2$ ) between  $\text{CuSeO}_3 \cdot 2\text{H}_2\text{O}$  and  $\text{Cu}_2\text{OSeO}_3$ . Thus making the final reaction medium to contain  $\text{HSeO}_3^-$ , instead of  $\text{SeO}_3^{2-}$ . A similar comparison can be drawn with respect to dissociation of selenous acid,  $\text{H}_2\text{SeO}_3$ . Therefore it hints towards the acidity of the first proton leaving the  $\text{CuSeO}_3 \cdot 2\text{H}_2\text{O}$  matrix, that is  $\text{H}_4$  (See table. 5.1). Our estimation puts the upper bound of  $\text{p}K_{a1}$  to be around 9.23. Finally, together with the results from neutralization using pyridine, we conclude that  $\text{p}K_{a1}$  of  $\text{CuSeO}_3 \cdot 2\text{H}_2\text{O}$  lies in-between 5.23 and 9.23. From the chemical reactions leading to neutralization of  $\text{CuSeO}_3 \cdot 2\text{H}_2\text{O}$  using  $\text{NH}_4\text{OH}$ , we can write the following equation:



- II.  *$\text{NH}_4\text{OH}$  at low temperatures:* While if the same base is used at lower temperatures, the reaction proceeds via a different route. The evidence for this is three-fold. 1. The reaction medium turns slightly bluish, instead of completely transparent, as shown in Fig. 5.10B. 2. The appearance of an unknown peak low  $2\theta$ , which can not be indexed to any one of the two participating solid phases. We hypothesize this unknown intermediate to be an ammoniacal salt of Se and Cu. That would also be corroborated from the distinct bluish colour of the reaction medium. 3. The Avrami coefficient obtained from the reaction kinetics. Unlike all other examples shown in this section,  $n_i$  for  $\text{NH}_4\text{OH}$  at lower growth temperatures, has a value of 3.4 ( $\pm 0.5$ ). This signifies a rather well-documented form of



#### 5.4. Reaction Kinetics And Mechanism Of Chemical Transformation Between $\text{CuSeO}_3 \cdot 2\text{H}_2\text{O}$ and $\text{Cu}_2\text{OSeO}_3$

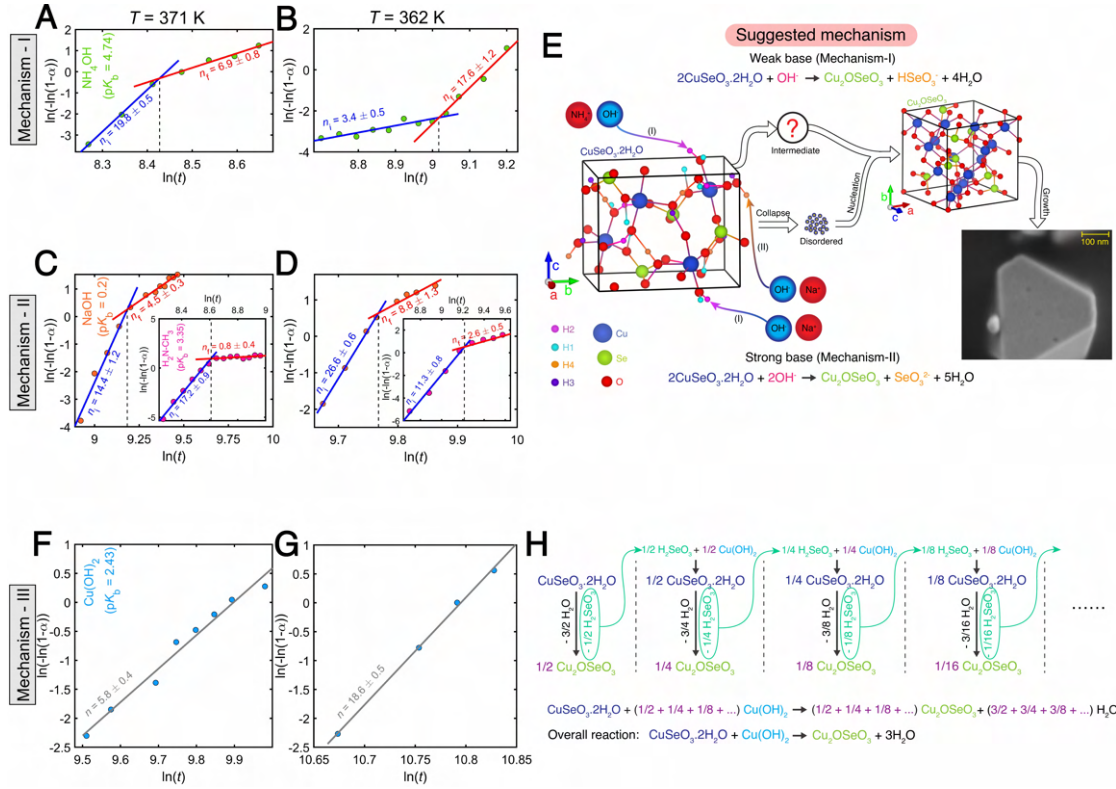


**Figure 5.12: Chemical mechanism of transformation between  $\text{CuSeO}_3 \cdot 2\text{H}_2\text{O}$  &  $\text{Cu}_2\text{OSeO}_3$ .** Linearized Avrami equation [as shown in Figure.5.11 (d)] was fitted to the phase fraction of  $\text{Cu}_2\text{OSeO}_3$  during the growth period in  $\text{NH}_4\text{OH}$  basic medium at (a)  $T = 371 \text{ K}$  and (b) at  $T = 362 \text{ K}$ . Similar fitting procedure was followed when  $\text{CuSeO}_3 \cdot 2\text{H}_2\text{O}$  was neutralized with  $\text{NaOH}$  and  $\text{H}_2\text{N}-\text{CH}_3$  (insets), as shown in (c) and (d). The vertical dashed lines represent  $t_{CO}$  for each reaction. Panel-(e) shows the mechanism of transformation between  $\text{CuSeO}_3 \cdot 2\text{H}_2\text{O}$  and  $\text{Cu}_2\text{OSeO}_3$ , in the non Cu-containing basic mediums. The SEM picture stands for the complex topology of the grown  $\text{Cu}_2\text{OSeO}_3$ , and is representative of final products obtained in each pathway.  $\text{CuSeO}_3 \cdot 2\text{H}_2\text{O}$  was also tried to be neutralized with a Cu-containing base,  $\text{Cu(OH)}_2$ . Panels-(f) and (g) show the results of similar fitting procedure using the JMAK equation. The clear absence of a  $t_{CO}$  necessitates for a different reaction mechanism, which is outlined in (h).

low dimensional growth kinetics. Though the overall chemical equation describing the transformation remains the same as Eqn. 5.4.

III. *NaOH and Methylamine:* Strong bases such as  $\text{NaOH}$  ( $pK_{b,\text{NaOH}} = 0.2$ ), and methylamine ( $pK_{b,\text{H}_3\text{CNH}_2} = 3.34$ ), are capable of completely removing both protons from the  $\text{CuSeO}_3 \cdot 2\text{H}_2\text{O}$  structural matrix. And therefore, with the actual stoichiometry [ $\text{NaOH}$ (or  $\text{H}_3\text{CNH}_2$ ): $\text{CuSeO}_3 \cdot 2\text{H}_2\text{O}$ =1:2], the following chemical reaction is realised:



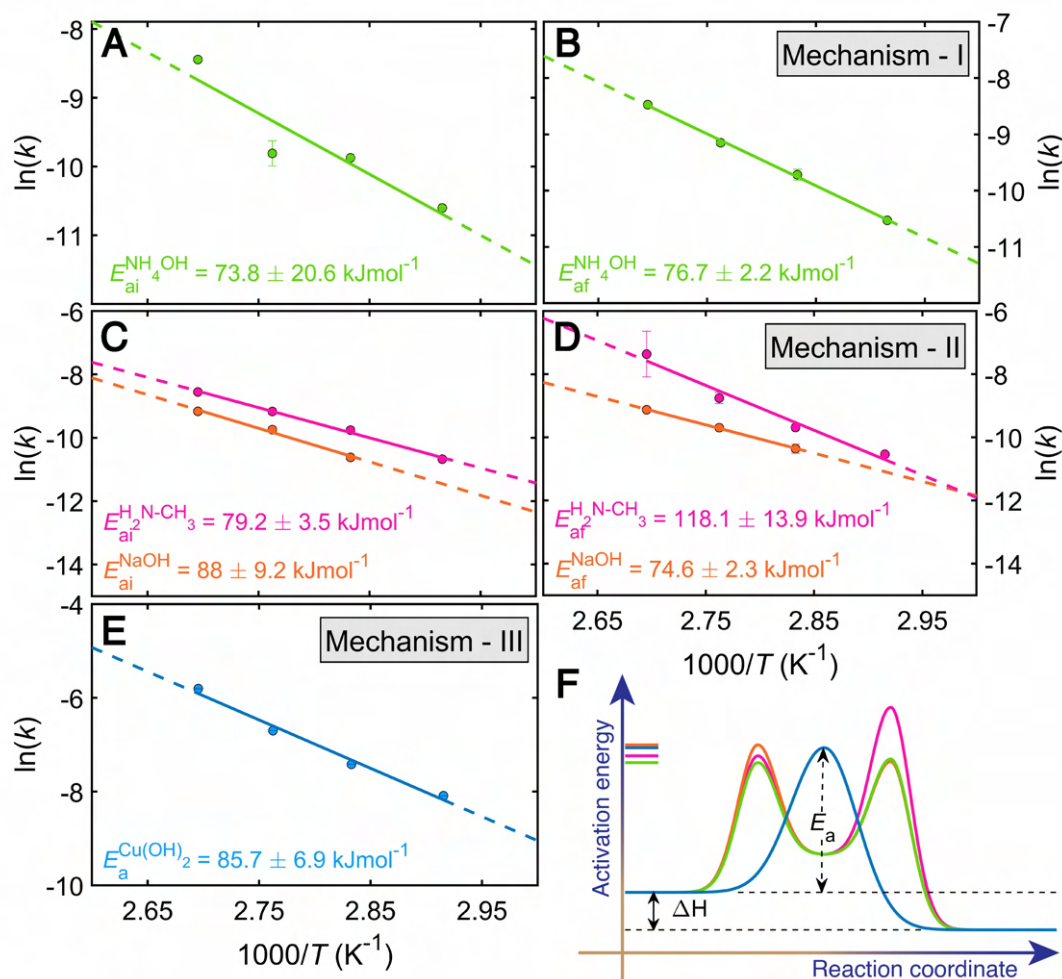


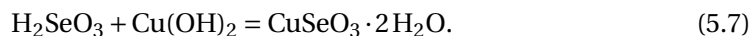
**Figure 5.13: Reaction activation energy for various bases.** Activation energy of the kinetics of transformation between  $\text{CuSeO}_3 \cdot 2\text{H}_2\text{O}$  and  $\text{Cu}_2\text{OSeO}_3$  in presence of  $\text{NH}_4\text{OH}$  [panels (a) and (b)],  $\text{NaOH}$  and  $\text{H}_2\text{N}-\text{CH}_3$  [panels (c) and (d)] as obtained using the Arrhenius equation.  $E_{\text{ai}}$  and  $E_{\text{af}}$  correspond to the observed kinetics before and after  $t_{\text{CO}}$ , as shown in Figure 5.11(d). Absence of  $t_{\text{CO}}$  in case of  $\text{Cu(OH)}_2$  results in a single activation energy as shown in (e). A schematic activation energy diagram has been shown in panel (f).  $E_a$  (or  $E_{\text{ai}}$ ) was found to be inversely proportional to  $\text{p}K_{\text{b}}$ . For more details, refer to the main text.

Consequently, we now have an estimation of the acidity of the second proton (labelled as  $H_2$  in Fig. 5.10 and Table. 5.1) exiting the  $\text{CuSeO}_3 \cdot 2\text{H}_2\text{O}$  structural matrix. Since methylamine can deprotonate  $\text{CuSeO}_3 \cdot 2\text{H}_2\text{O}$  twice, the experimental value of  $\text{p}K_{\text{a}2}$  lies in-between 9.23 and 10.66. The summary of these findings can be found in Fig. 5.14.

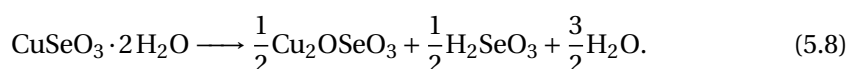
- IV.  $\text{Cu(OH)}_2$ : Unlike the bases discussed above, here  $\text{CuSeO}_3 \cdot 2\text{H}_2\text{O}$  is not used as the starting material directly. But rather it is formed as an instantaneous precipitate while mixing  $\text{SeO}_2$  into an aqueous solution containing  $\text{Cu(OH)}_2$ . Two moles of  $\text{Cu(OH)}_2$  is required for the complete transformation into phase pure  $\text{Cu}_2\text{OSeO}_3$ . In the first step,

#### 5.4. Reaction Kinetics And Mechanism Of Chemical Transformation Between $\text{CuSeO}_3 \cdot 2\text{H}_2\text{O}$ and $\text{Cu}_2\text{OSeO}_3$

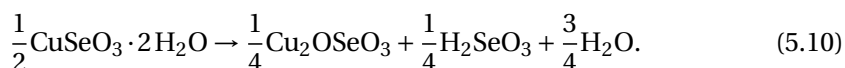
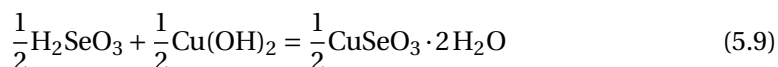
half of the  $\text{Cu}(\text{OH})_2$  produces mole equivalent amount of  $\text{CuSeO}_3 \cdot 2\text{H}_2\text{O}$ . The reaction proceeds as follows:



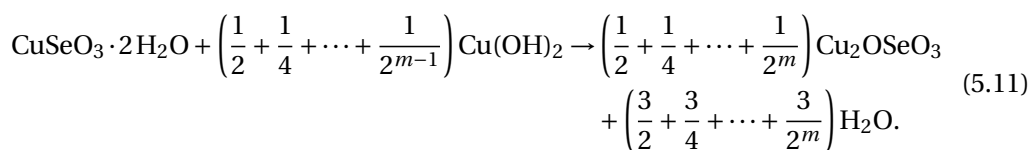
The  $\text{CuSeO}_3 \cdot 2\text{H}_2\text{O}$  produced reacts with the remaining mole of  $\text{Cu}(\text{OH})_2$  to produce 0.5mol of  $\text{Cu}_2\text{OSeO}_3$ , along with 0.5mol of  $\text{H}_2\text{SeO}_3$  and 1.5mol of  $\text{H}_2\text{O}$ , which can be written as:



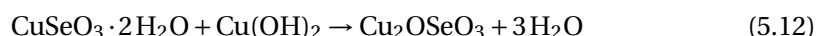
But the selenous acid produced in this step immediately reacts with the mole equivalent quantity of  $\text{Cu}(\text{OH})_2$  (as shown in equation 5.7) to produce half the quantity of  $\text{CuSeO}_3 \cdot 2\text{H}_2\text{O}$ , which ultimately produces half the quantity of  $\text{Cu}_2\text{OSeO}_3$  compared to the previous step (equation 5.8), that is 0.25mol. Chemically this step can be written as the following:



This process continues iteratively, and at the  $m$ -th step  $1/2^{m-1}$  mole of  $\text{Cu}(\text{OH})_2$  is consumed, while producing  $1/2^m$  mole of  $\text{Cu}_2\text{OSeO}_3$ . Summing these  $m$ -steps, the expression looks as the following:



At long enough time scale (for example, about 6 hours at 371 K), that is when  $m \rightarrow \infty$ , the overall equation finally has the following form:



This mechanism is also shown in figure. 5.12H. Unlike the non Cu-containing bases, here the  $\text{CuSeO}_3 \cdot 2\text{H}_2\text{O}$  is synthesised in the solution medium. Due to its higher reactivity, originating from the temperature-induced instability in the transient structure in the

reaction medium, is more susceptible to being de-protonated compared to the more stable structure mentioned earlier. Since the reaction kinetics would be dominated by formation of  $\text{Cu}_2\text{OSeO}_3$  as the rate determining step, it would result in a single activation energy as clearly found in our experiments (shown in Fig. 5.12F&G, and Fig 5.13E).

The large values of  $n$  are characteristic of the transient nucleation processes during which the nucleation rate as well as the velocity of the crystal growth do not remain constant. For all the non-Cu containing bases used in this work, except for  $\text{NH}_4\text{OH}$  at lower temperatures, we observe similar behaviour from the isothermal phase fraction evolution and subsequently the trend in  $n$ . In addition to strong bases such as  $\text{NaOH}$  and  $\text{H}_2\text{C}-\text{NH}_2$ ,  $\text{NH}_4\text{OH}$  at 371 K also have  $n_i$ s which are higher than the ones while approaching completion,  $n_f$ . We ascribe this initial phase of the growth kinetics to the leaching of Se atoms through the structural matrix of  $\text{CuSeO}_3 \cdot 2\text{H}_2\text{O}$ , right after removal of the proton(s) from the surface of the precursor. Fast diffusion of Se atoms (in the form of  $\text{SeO}_3^{2-}$ ) during this step makes the whole process to have a relatively higher growth rate. At the same time removal of  $\text{SeO}_3^{2-}$  is also limited by the strength of the base being used. Transfer of either one (for bases with  $8.77 \geq \text{p}K_b \geq 4.77$ ) or two  $\text{H}^+$  (for bases with  $\text{p}K_b \leq 3.34$ ) ions from  $\text{CuSeO}_3 \cdot 2\text{H}_2\text{O}$  structure introduces a net negatively charged species, that is  $\text{CuSeO}_3 \cdot 2\text{H}_2\text{O} \cdot \text{OH}^-$  in the case of  $\text{NH}_4\text{OH}$  and  $\text{CuSeO}_3 \cdot 2(\text{OH})^-$  in the case of  $\text{NaOH}$ . This negative charge cloud hinders the movement of another negatively charged ion  $\text{SeO}_3^{2-}$  from the core. Thus slowing down the rate of Se-leaching in the presence of a stronger base, and ultimately giving rise to a higher activation energy, as shown in figure. 5.13C and E. Our results point towards careful manipulation of functional properties of not only  $\text{CuSeO}_3 \cdot 2\text{H}_2\text{O}$ , but other selenates and selenites.

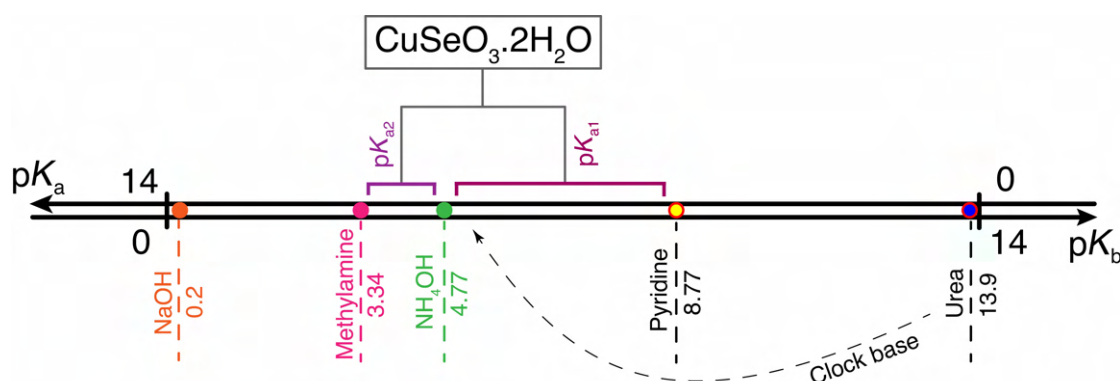


**Figure 5.14: Schematic representation of proton acidity in  $\text{CuSeO}_3 \cdot 2\text{H}_2\text{O}$ .** Summary of  $\text{CuSeO}_3 \cdot 2\text{H}_2\text{O}$  neutralization in various basic medium and the  $\text{p}K_a$ s of relevant protons. The hydrolysis of urea produces ammonia and carbon dioxide making  $\text{p}K_b$  the reaction medium close to that containing  $\text{NH}_4\text{OH}$ .

## 5.5 Magnetic Phase Diagram Of All Particles Derived From Magnetization & Susceptibility Measurements

In this section, we will elucidate the consequences of particle size control on the corresponding magnetic phase diagrams. But first, we would like to discuss the magnetic properties of one particle size alone (338 nm), followed by extending our results to all particle sizes. We will compare them with the results from bulk particles. For this purpose, DC as well as AC magnetic measurements were performed using the VSM and ACMS-II option of a commercial Quantum Design (QD) 14T Physical Property Measurement System (PPMS).

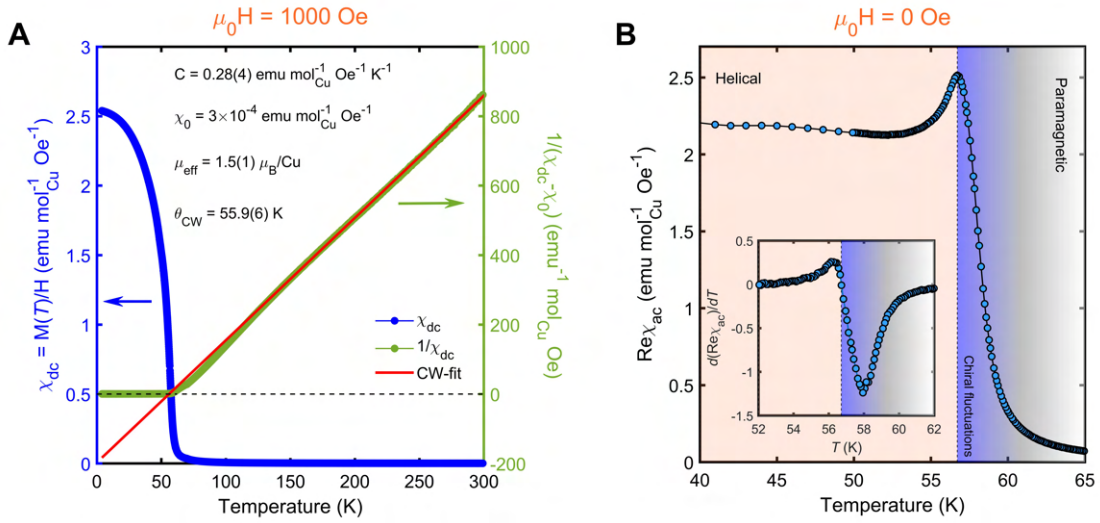


**Figure 5.15: Temperature scans at constant magnetic fields for grown  $\text{Cu}_2\text{OSeO}_3$  particles.** (A) DC magnetization measurements for the grown  $\text{Cu}_2\text{OSeO}_3$  particles in presence of 1000 Oe of external magnetic field. Result of a Curie-Weiss type fitting is also shown. (B) AC susceptibility temperature scan for the same particles close to  $T_c$ .  $H_{AC}$  and  $\omega_{AC}$  were fixed at 1 Oe and 1011 Hz, respectively.

Being a Mott insulator, the macroscopic magnetism of  $\text{Cu}_2\text{OSeO}_3$  is equally as fascinating as the chemical processes behind its synthesis. Away from its helimagnetic ordering temperature ( $T_{HM}$ ), in the paramagnetic regime, the magnetism is governed by  $S = 1/2$   $\text{Cu}^{2+}$  ions that are oxygen anion coordinated in square pyramids or trigonal bipyramids. A Curie-Weiss fit to the high temperature magnetization data for the 338 nm particles yields an effective moment of  $1.5(1) \mu_B/\text{Cu}$ , which is higher than the reported value, but still lower than what is expected for the spin-only value of  $\text{Cu}^{2+}$  ions [27]. The obtained Curie-Weiss temperature ( $\theta_{CW}$ ) slightly underestimates  $T_{HM}$ . The Curie constant ( $C$ ) also matches the one reported earlier for polycrystalline  $\text{Cu}_2\text{OSeO}_3$  [27]. These results are closely reminiscent of mean field behaviour on isolated  $\text{Cu}^{2+}$  ions on the 3D lattice of  $\text{Cu}_2\text{OSeO}_3$ . But as  $T_{HM}$  approaches (between 150 K and 200 K), the superexchange interaction among four neighboring Cu ions on a tetrahedron start to become increasingly stronger, resulting in a peculiar “3-up,1-down” spin configuration [189]. This ferrimagnetic arrangement ( $S_{eff} = 1$ ) is the basic building block



for all incommensurate magnetic phases appearing in  $\text{Cu}_2\text{OSeO}_3$  [83]. From  $\chi'$ , we extract  $T_{\text{HM}}$  to be slightly lower than that of the bulk single crystals [230]. The explanation for this will be given when we compare different particle sizes later in this section. As the temperature is lowered further, in the vicinity of  $T_{\text{HM}}$ , chiral fluctuations start to manifest before the system settles down to the multi-domain helimagnetic ground state. These chiral fluctuations play a significant role in suppressing the ordering temperature compared to what is expected for a conventional ferromagnet, not only in  $\text{Cu}_2\text{OSeO}_3$ , but also in other chiral helimagnets [82, 230]. Various parameters obtained from our temperature scans outlines a great match with the reported literature.

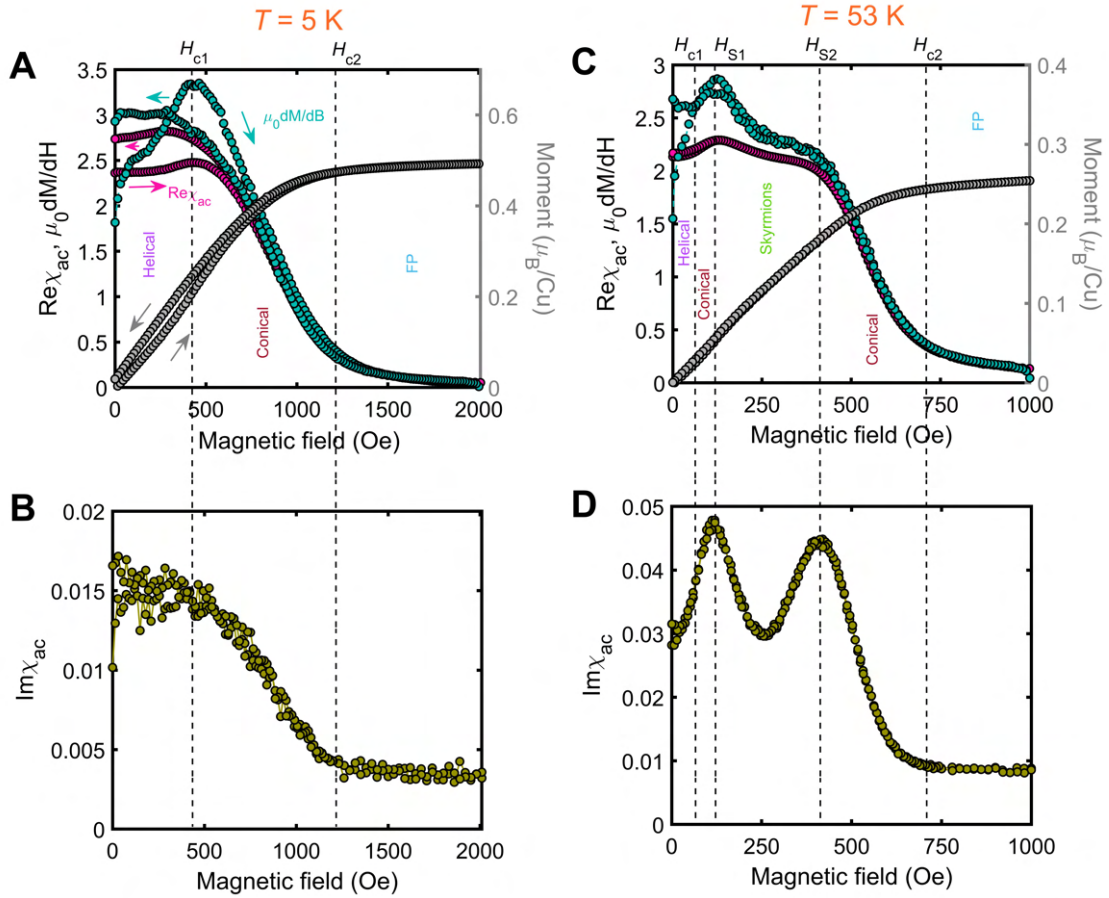


**Figure 5.16: DC magnetization and AC susceptibility magnetic field scans of 338 nm particles at both 5 K and 53 K.** (A) Shows the magnetic field dependence of DC magnetization along with the real part of AC susceptibility measured at 5 K.  $\text{Re}\chi_{\text{AC}}$  has been compared with derivative of dc magnetization ( $\mu_0 dM/dH$ ). (B)  $\text{Im}\chi_{\text{AC}}$  measured at the same temperature. Even though there is a clear change of slope at  $H_{c1}$ , any peak signifying a helical  $\rightarrow$  conical phase transition is absent. (C) and (D) showcase similar measurements performed close to  $T_{\text{HM}}$ , at  $T = 53$  K. A “double-peak” feature observed in the imaginary part is the characteristic signature seen in numerous skyrmion-hosting bulk chiral magnets, with the “valley” region signalling the presence of a skyrmion lattice.

### 5.5. Magnetic Phase Diagram Of All Particles Derived From Magnetization & Susceptibility Measurements

---

Due to the chiral cubic lattice symmetry, the antisymmetric Dzyaloshinskii-Moriya interaction (DMI) is also active, and in combination with the symmetric exchanges, plays the key role leading to the formation of both the helical ground state and skyrmion phases. Each is characterized by a modulation period of 60 nm in the bulk, which is much larger than the cubic crystal lattice constant of 0.89 nm [3, 169, 206]. At the lowest temperatures, far away from  $T_{\text{HM}}$ , the hierarchy of energy scales in bulk cubic SkL hosts is as follows: at zero external magnetic field, the system settles down to a multidomain helical structure, where the helical domains equally populate the three cubic  $\langle 100 \rangle$  axes. This has been demonstrated with help of various experimental probes in the last decade [3, 169, 221]. With application of magnetic field, between  $H_{c1}$  and  $H_{c2}$ , the helices reorient to form a cone like structure oriented along the direction of applied magnetic field. As shown in figure 5.16A and B, the magnetic field induced change from helical  $\rightarrow$  conical phase is evidenced by the presence of a weak metamagnetic transition obtained at  $T = 5$  K. Though the phase boundaries probed by both  $\text{Re}\chi_{\text{ac}}$  and  $dM/dH$  remain the same, the qualitative differences appearing in both curves at the low field region have been observed in chiral magnets before [63, 19]. These differences are attributed to the dynamics of the participating incommensurate magnetic phases. For the reciprocal space determination of the said phases in these particles, please refer to Section 5.9. The saturation magnetization value obtained at  $T = 5$  K ( $0.52 \mu_{\text{B}}/\text{Cu}$ ) also agrees well with previous reports, thus proving the presence of “3-up,1-down” spin configuration. Ultimately, with stronger magnetic fields, above  $H_{c2}$ , the system enters into a forced field-polarized state.

Now moving to the region just below  $T_{\text{HM}}$ , in the presence of a finite magnetic field, thermal fluctuations stabilize the SkL phase [134]. In this region, the SkL lattice phase is surrounded by other non-topological phases. One of the best methods for probing the boundaries of SkL phase is via AC susceptibility magnetic field scans [19, 63, 115, 157]. Due to their topological nature, the dissipative transition to and from the SkL phase (from and to topologically trivial phases) appear as well-formed peaks in the imaginary part of the susceptibility ( $\text{Im}\chi_{\text{AC}}$ ), as shown in figure 5.16D. Also, the width of the “valley” region (between  $H_{S1}$  and  $H_{S2}$ ) was found be higher than that observed in the bulk samples. This phase also extends down to lower temperatures compared to that of bulk- $\text{Cu}_2\text{OSeO}_3$ . Increasing anisotropy in our samples could be one of the main reasons for this enhanced stability of skyrmions in phase space.

The samples discussed in this chapter display length-scales between slightly greater than one bulk helical pitch (73 nm) up to larger than five (338 nm), see Fig. 5.6. Shown in Figure 5.17, are the magnetic isotherms around and below  $T_{\text{HM}}$  for two particle sizes, compared with the standard bulk sample (prepared by crushing few single crystals as shown in Fig. 4.2). Here we observe the first evidence for the difference in the overall magnetic properties. First, the field-induced Helical $\rightarrow$ Conical phase transition is smeared as we reduce the particle size. Second, the overall  $H_{c2}$  also reduces with average particle size.

Figure 5.18 summarizes isothermal AC susceptibility data obtained on a bulk sample, along with particles with octahedral heights of 338 nm, and 73 nm. Data for other particle sizes are presented in Fig. 5.19. At 57 K in the bulk sample, shown in Fig. 5.18B, the standard sequence

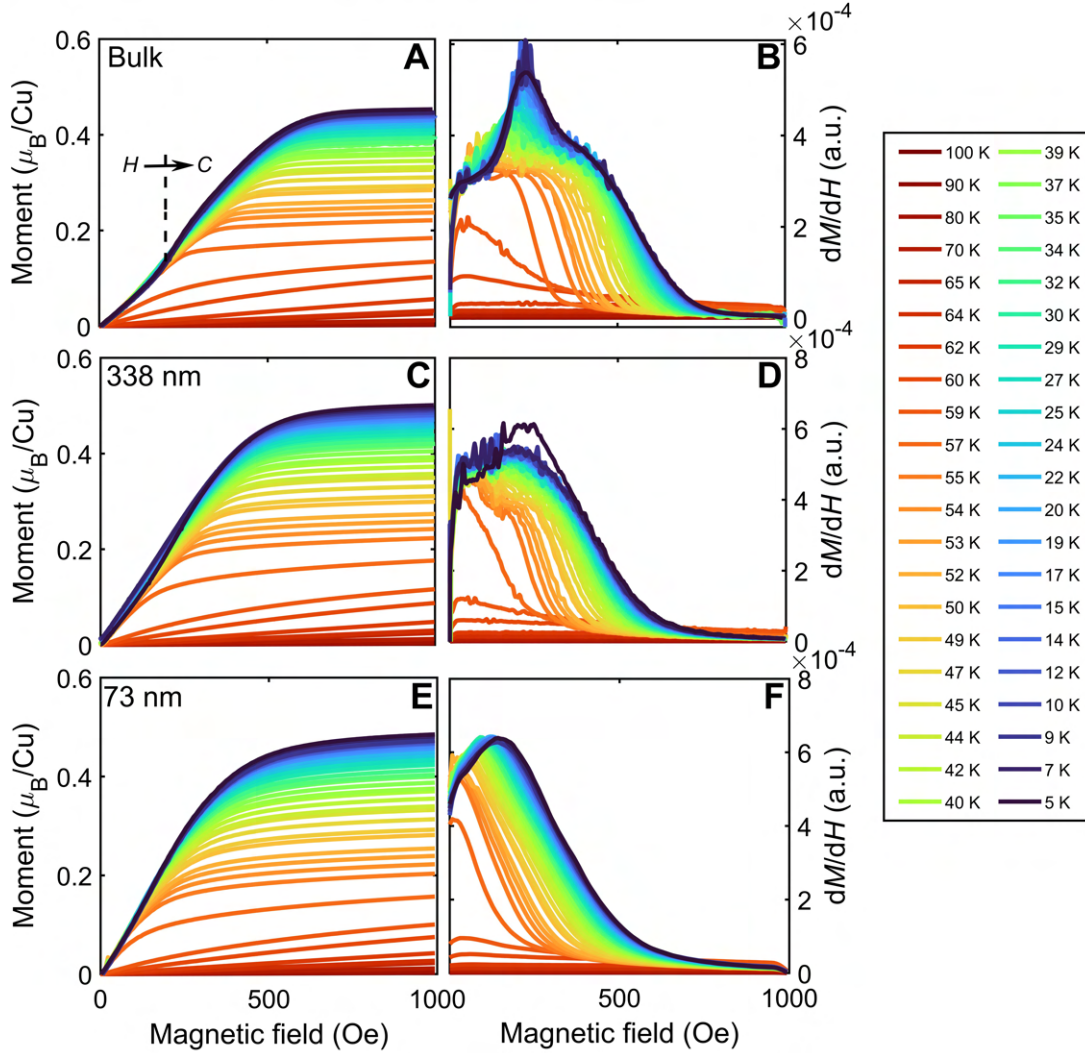


**Figure 5.17: Magnetic isotherms across the phase diagram for three different sized  $\text{Cu}_2\text{OSeO}_3$  particle sizes.** Static DC magnetization as a function of external magnetic field for all three particle sizes. In the bulk particles, the familiar Helical ( $H$ )  $\rightarrow$  Conical ( $C$ ) phase transition is detected via a metamagnetic-type transition around 350 Oe (panel-A), which clearly shows up in the derivative of magnetization with respect to magnetic field (panel-B). Also the “double-peak” feature is clearly seen at  $T = 57$  K, indicating a transition in and out of the skyrmion lattice phase. Panel-(C) and (D) In contrast, for the 338 nm particles at  $T = 5$  K, a clear yet broad transition is seen to be taking place around the similar field value, indicating the existence of more strongly pinned helices. (E) and (F) Finally for 73 nm particles, this transition moves towards lower field values. At higher temperatures, the  $dM/dB$  monotonically falls to zero without any signature of intermediate phase transitions.

of field-driven phase transitions from helical  $\rightarrow$  conical  $\rightarrow$  skyrmion lattice  $\rightarrow$  Conical  $\rightarrow$  field-polarized are observed in the data. A characteristic two-peak structure in the imaginary ( $\chi''$ ) part of the AC susceptibility is seen clearly between 180 and 300 Oe, signalling the range of



## 5.5. Magnetic Phase Diagram Of All Particles Derived From Magnetization & Susceptibility Measurements

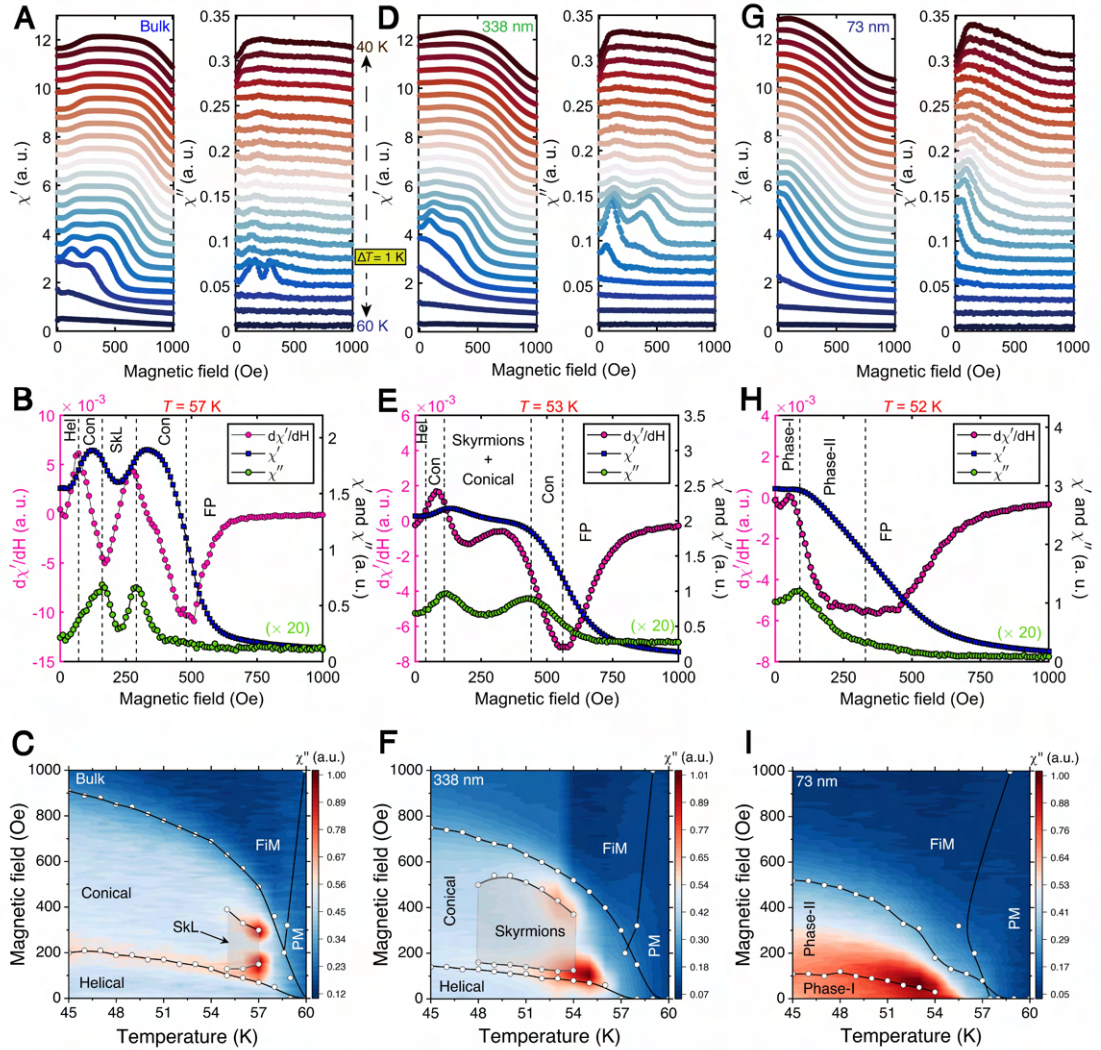


**Figure 5.18: Determination of magnetic phase diagram of  $\text{Cu}_2\text{OSeO}_3$  particles from AC susceptibility.** Panel (A), (D) and (G) show AC susceptibility field scans for three different particle sizes between 40 K and 60 K, with 1 K step. Clear differences can be observed between these particles from  $\chi''$ , especially the extended “valley” region in the 338 nm particles at 53 K. The same feature is entirely absent in the smallest particles, 73 nm. (B), (E), and (H) show the procedure of extracting the boundaries between different phases from both  $\chi'$  and  $\chi''$  of the total susceptibility. Note that in panel (B), (E), and (H),  $\chi''$  data has been scaled up in order to show all in the same graph. (C), (F), (I) represent the magnetic phase diagrams thus extracted from the  $\chi''$  data for the respective particle sizes.

SkL phase stability in analogy with other chiral magnets [17, 19, 157, 208]. The established bulk phase diagram, see Fig. 5.18C, shows that the SkL phase extends over a narrow temperature window of  $\sim 3$  K directly below  $T_c$ .

By tracking the two-peak feature in  $\chi''$  for in 338 nm particles (Fig. 5.18E), the thermal window

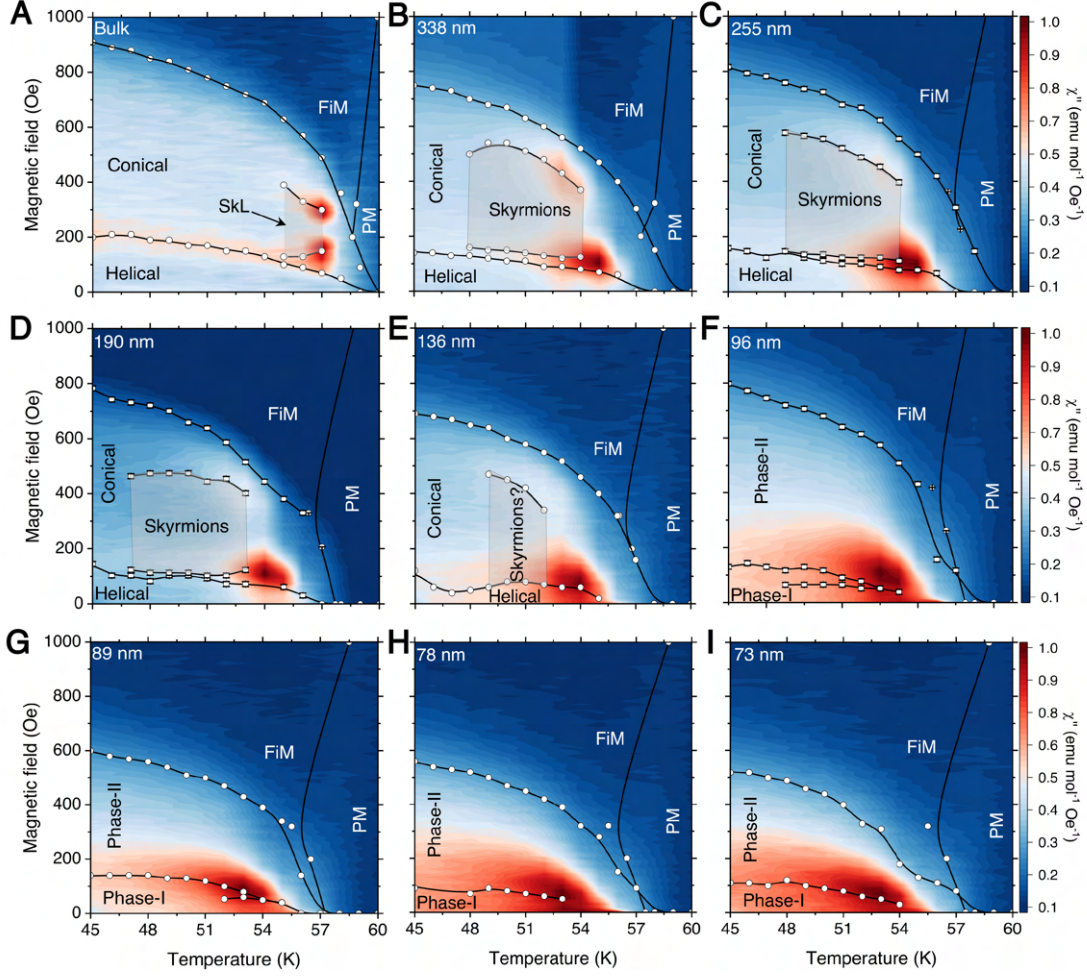


**Figure 5.19: Magnetic phase diagram of all particles as inferred from AC susceptibility measurements.** (A)-(I) display the magnetic phase diagrams of all synthesized particles discussed in this thesis. While the phase boundaries have been extracted from the combination of both real as well as imaginary part of the susceptibility, colorplot has been made only using the latter. All colorplots have been normalized with respect to the corresponding  $\chi''_{\max}$ . Enhancement of the dissipative region close to  $T_c$  is well evident from the increasing  $\chi''$ , as a function of reducing particle size.

of SkL phase stability is found to extend to 10 K below  $T_c$ , as shown in Fig. 5.18F. In the established absence of particle strain, the enhanced thermal stability is likely due to the onset of *geometrical confinement effects* analogous to those observed in thin layers of cubic chiral magnets [114, 218]. As additional evidence for confinement effects, further magnetometry data presented in Fig. 5.19 reveals the systematic suppression of  $T_c$  as  $h$  is reduced. In bulk  $\text{Cu}_2\text{OSeO}_3$ , it is established that pronounced paramagnetic spin fluctuations already suppress the onset of helical order at  $T_c$  to a slightly lower temperature than anticipated for a conventional ferromagnet [230]. The further reduction of  $T_c$  with  $h$  thus indicates geometrical

## 5.5. Magnetic Phase Diagram Of All Particles Derived From Magnetization & Susceptibility Measurements

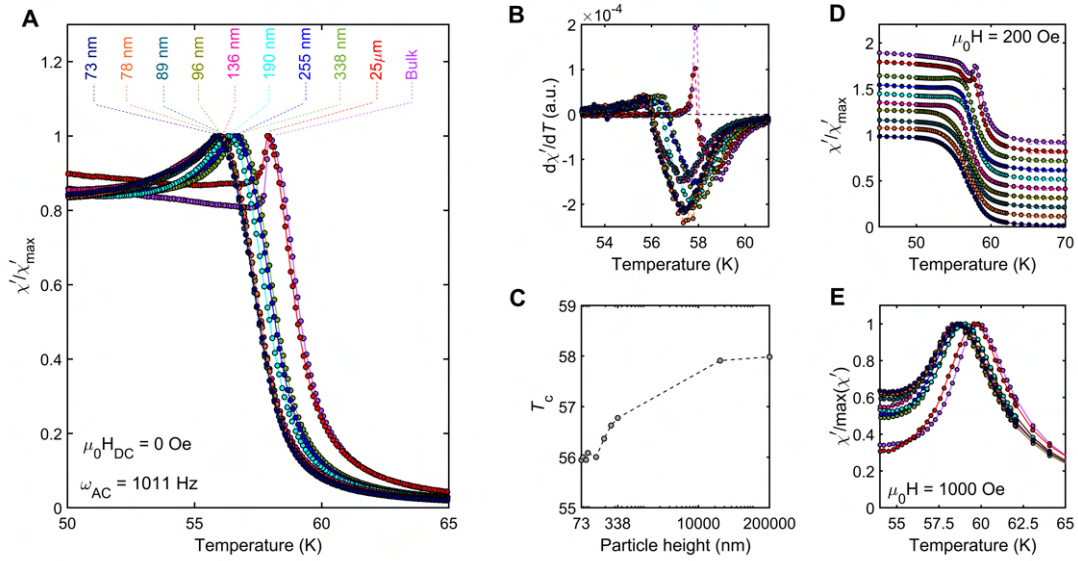


**Figure 5.20: Effects of finite particle size on magnetic susceptibility.** (A) AC susceptibility temperature scans for all the particles in presence of zero applied DC-field. All scans have been normalized with respect to their corresponding maximum value ( $\chi'_{\max}$ ), in order to highlight the reduction in  $T_c$ , as a function of lowering particle size. (B) Shows the differentiation with respect to temperature for all the scans shown in panel-(A), thus extracting the exact  $T_c$ . (C) The estimated  $T_c$  from the previous procedure compared with all particle sizes considered. AC susceptibility temperature scan in presence of (D) 200 Oe (going through the SkL phase in Bulk sample) and (E) 1000 Oe of DC magnetic field, also for all the particles. In panel-(D), a constant offset ( $0.1 \times \chi'/\chi'_{\max}$ ) has been applied to shift the curves with respect to each other, in order to better visualize the fine features.

confinement to aid the fluctuations even further. A similar behavior is also seen in FeGe nanoparticles, which suggests the phenomenon to be a generic feature of chiral magnets as their size approaches the nanoscale [139].

In the  $h = 73$  nm particles, no signatures in AC susceptibility delineating a skyrmion phase are observed. Instead, a differently structured phase diagram is found with a lower  $T_c$  and a single low field phase boundary giving a clear signal in  $\chi''$  [Fig. 5.18(H) and (I)]. The dissipative nature of the phase boundary may indicate a transformation between imperfect, large-scale spin configurations, which the simulations presented later (see section 5.10) suggest are unlikely to be due to skyrmions. According to the established phase diagrams for  $h$  ranging from 338 nm to 73 nm (Fig. 5.19), the threshold octahedral height ( $S_c$ ) for which standard signatures of the skyrmion are observed is 190 nm. For smaller sizes below  $S_c$ , the phase diagrams resemble that shown in Fig. 5.18I, hosting helical-like, but unestablished spin configurations labelled Phase-I and Phase-II.

The divergence in the susceptibility close to  $T_c$  for smaller particles signifies a direct consequence of finite-size effects. Similar results were obtained with 1000 Oe of applied magnetic



field (Fig. 5.20), suggesting the applicability of these finite-size effects not only in zero-field transitions, but also finite-field crossovers. In bulk- $\text{Cu}_2\text{OSeO}_3$ , temperature-cooling scan in presence of 200 Oe magnetic field drives the system through  $\text{PM} \rightarrow \text{SkL} \rightarrow \text{Conical}$  phase, represented by the cusp in the susceptibility data (Fig. 5.20D). In the absence of a well-defined lattice of skyrmions, this cusp vanishes in the particles. In the biggest particles (for example, 338 nm), a small change in the susceptibility can be seen. Since in these small particles, it's impossible to have a lattice of skyrmions, these changes are thus attributed to the presence of few isolated skyrmion tubes and/or other spin textures. Whereas, in the smallest particles, absence of this feature not only disfavours the possibility of having skyrmion tubes but also completely agrees with the SANS observations.

## **5.6 Dynamics Of Different Parts Of The Magnetic Phase Diagram Probed By Muon Spin Relaxation ( $\mu\text{SR}$ ) Technique**

After the AC susceptibility characterizations, we now study the  $\text{Cu}_2\text{OSeO}_3$  (nano)particles using another measurement technique which extracts information about magnetic order in a separate frequency regime. The muon spin relaxation ( $\mu\text{SR}$ ) technique gathers information about magnetic order from a MHz frequency regime, compared to the kHz regime probed by AC susceptibility [188]. Due to its unique property to probe local magnetic order,  $\mu\text{SR}$  has been widely used to detect long-range order in such systems which try to avoid magnetic ordering down to low temperatures, such as material(s) hosting a spin-liquid ground state [117]. In context of magnetic skyrmions, longitudinal-field muon-spin relaxation (LF- $\mu\text{SR}$ ) studies have been performed on few of the skyrmion hosting systems, such as  $\text{Cu}_2\text{OSeO}_3$  [69],  $\text{Cu}_{2-x}\text{Zn}_x\text{OSeO}_3$  [175],  $\text{GaV}_4\text{S}_{8-y}\text{Se}_y$  [51, 68], and  $\text{Co}_x\text{Zn}_y\text{Mn}_{20-x-y}$  [69, 191]. Even though in  $\text{Cu}_2\text{OSeO}_3$ , the skyrmion dynamics is reported in GHz frequency regime [166],  $\mu\text{SR}$  clearly identifies characteristic MHz dynamics from the skyrmion lattice and related phases [69]. Thus  $\mu\text{SR}$  becomes a useful tool to probe MHz dynamics in the  $\text{Cu}_2\text{OSeO}_3$  (nano)particles. The magnetic phase diagram probed by AC susceptibility (as shown in Fig. 5.19) measurements form the basis of further investigation in terms of  $\mu\text{SR}$  experiments. But due to scarcity of beamtimes, we will investigate only two particle sizes,  $h = 338$  nm and  $h = 73$  nm, as shown in Fig. 5.21.

LF- $\mu\text{SR}$  experiments were performed on these two particle sizes at the GPS beamline of the HIPA complex of the Paul Scherrer Institute. For this purpose, one pellet was prepared from each particle size, as shown in the inset of Fig. 5.21E. The magnetic phase diagram shown in panel-B and C of fig. 5.21 was probed with help of both temperature as well as magnetic field scans. First, a temperature scan was performed without any external magnetic field in order to check for the  $\text{PM} \rightarrow \text{Helical}$  ( $\text{PM} \rightarrow \text{Phase-I}$ ) phase transition in the 338 nm (73 nm) particles. Followed by one more temperature scan with 200 Oe constant DC magnetic field, in order to cut through the “skyrmions” phase in 338 nm particles. Finally, magnetic field scan at a constant temperature was performed at  $T = 54$  K, in order to probe the field-induced dynamics from different phases. With a Maxwellian distribution, the time dependence of the

## 5.6. Dynamics Of Different Parts Of The Magnetic Phase Diagram Probed By Muon Spin Relaxation ( $\mu$ SR) Technique

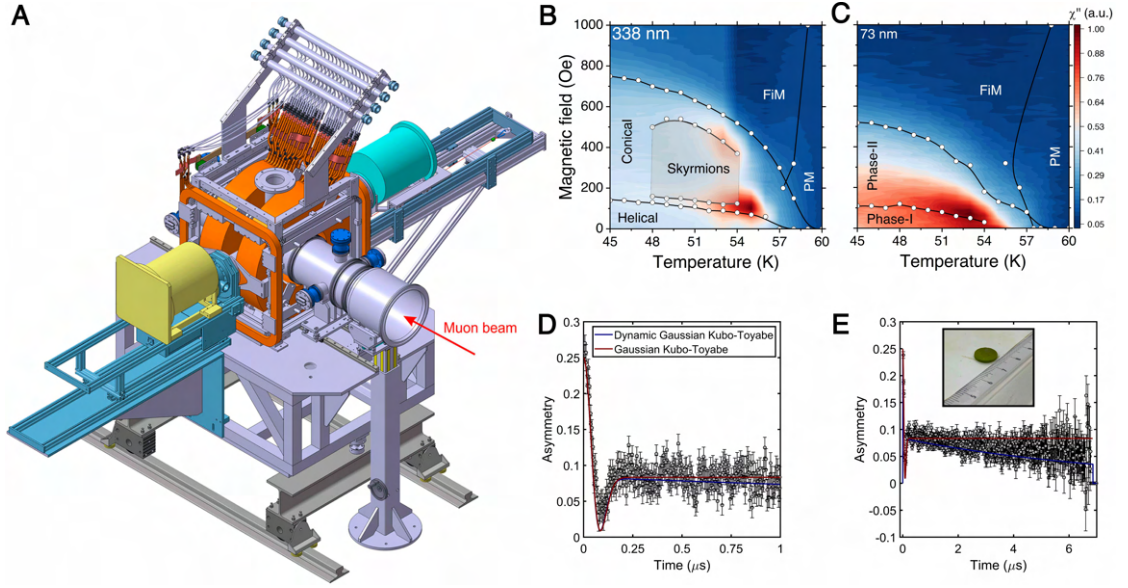


**Figure 5.21: Experimental conditions for our  $\mu$ SR experiment at GPS beamline, S $\mu$ S.** (A) schematics of the GPS instrument located at the Paul Scherrer Institute. The yellow and green parts are the cryostats, whereas the orange part is the Helmholtz coils capable of producing 0.5 T magnetic field. (B) and (C) represent the magnetic phase diagrams as obtained from the AC susceptibility measurements for two particles sizes, 338 nm and 73 nm, respectively. (D) and (E) show the fit results obtained using two different functions. The inset shows one of the pellets used for the actual experiment. Panel-A has been adapted from Ref. [8].

muon spin polarization becomes:

$$P_z^{\text{GKT}}(t) = \frac{1}{3} + \frac{2}{3}(1 - \sigma^2 t^2) \exp\left(-\frac{1}{2}\sigma^2 t^2\right) \quad (5.13)$$

Here  $\sigma$  is known as the local field broadening due to static magnetic moments as measured by the muons. Here,  $\sigma$  is related to the muon gyromagnetic ratio and the internal magnetic field as,  $\sigma^2 = \gamma_\mu^2 \langle B_\alpha^2 \rangle$  (and  $\alpha = x, y, z$ ). This is the well-known Gaussian Kubo-Toyabe function. Even though the obtained  $\mu$ SR spectrum at  $T = 54$  K is reasonably well-fitted with help of the Gaussian Kubo-Toyabe function (as shown in Fig. 5.21D), at larger time scale, it fails to do so (Fig. 5.21E). In order to account for the dynamics of the muon spin depolarization more accurately, we used the so called longitudinal field dynamic Gaussian Kubo-Toyabe (LF-DGKT) function, which can be expressed as the following:

$$P_z^{\text{LF-DGKT}}(t) = 1 - \frac{2\sigma^2}{(\gamma_\mu B_{\text{ext}})^2} \left[ 1 - \exp\left(-\frac{1}{2}\sigma^2 t^2\right) \cos(\gamma_\mu B_{\text{ext}} t) \right] + \frac{2\sigma^4}{(\gamma_\mu B_{\text{ext}})^3} \int_0^t \exp\left(-\frac{1}{2}\sigma^2 t'^2\right) \sigma(\gamma_\mu B_{\text{ext}} t') dt'. \quad (5.14)$$

Here, we define  $\nu = B_{\text{ext}} \times \gamma_\mu$ , as we extract this quantity from our fitting.  $\nu$  is known as the local field fluctuation rate, as measured by the muon spin.

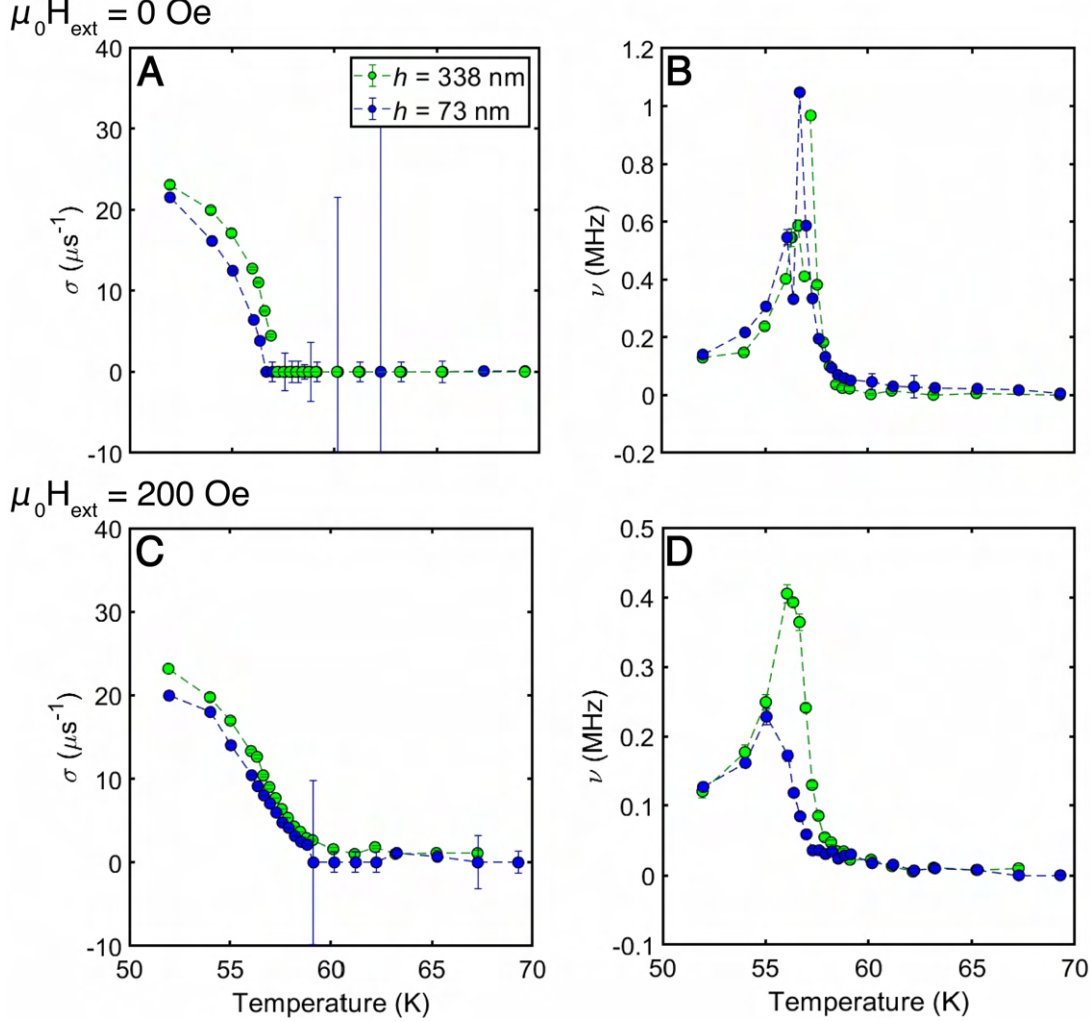


**Figure 5.22: Local field broadening and fluctuation rate obtained as a function of temperature.**  $\mu\text{SR}$  spectra were fitted using longitudinal field dynamic Gaussian Kubo-Toyabe (LF-DGKT). (A) shows the results of the local field broadening, while (B) shows the results of the local field fluctuation rate with zero applied external magnetic field. (C) and (D) show the same for 200 Oe external magnetic field.

Without applying any external magnetic field,  $\mu\text{SR}$  spectra were collected as a function of temperature. As shown in Fig. 5.22A, due to the long range nature of the magnetic order just below  $T_c$ , there is a finite broadening of the local field for both particles. A small change in  $T_c$  for both particle sizes is clearly seen from Fig. 5.22A, well-corroborated with our AC susceptibility data (see Fig. 5.20). Thus, providing more evidence towards suppression of magnetic order in smaller nanoparticles due to increased surface-induced density of fluctuations. The measured particles also possess an order of magnitude higher response in  $\nu$  close to  $T_c$ , which slowly decays with moving away from it (see Fig. 5.22B). As  $\sigma t \gg \nu$ , the muon depolarization lies in

## 5.6. Dynamics Of Different Parts Of The Magnetic Phase Diagram Probed By Muon Spin Relaxation ( $\mu$ SR) Technique

the so-called “slow fluctuation regime”. Here, the muon depolarization rate is proportional to the strength of the dynamics of the magnetic moment. Even though there is a clear change observed at  $T_c$ , the dynamics of muon spin depolarization can hardly be distinguished at zero magnetic field. The apparent difference observed in the exact form of the local field fluctuation rate may be related to the critical slowing down expected from a Heisenberg ferromagnet, with contributions from several other factors, such as DMI, finite-size effects, etc. But with 200 Oe external magnetic field, at the onset of long range ordered magnetic state, dramatic changes in the local field fluctuation rate is observed (see Fig. 5.22D). For the smallest nanoparticles,  $\nu$  is found to be reduced by nearly 44%, compared to the biggest nanoparticles. This points towards presence of more isotropic magnetic texture in the smallest nanoparticles, compared to the 338 nm particles. With the proposed formation of skyrmions in the 338 nm particles will generate a large internal magnetic field. This may result in a higher local field fluctuation rate compared to that generated from the non-trivial magnetic texture proposed in the smallest particles. As indicated in Fig. 5.22C, the 338 nm particles do show a larger (but not yet significant) local magnetic field, as probed by our experiments.

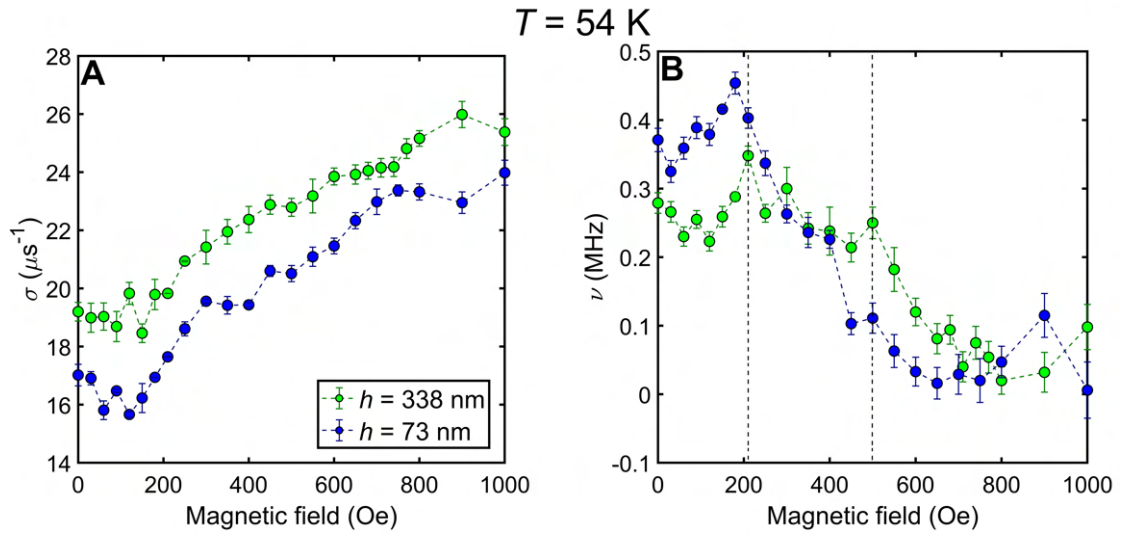


**Figure 5.23: Magnetic field scan close to  $T_c$  for both particles.** Local field parameters obtained for both particles as a function of magnetic field. Panel-A and B carry their usual meaning. The dashed lines in panel B shown the phase boundaries as obtain from AC susceptibility and  $\mu$ SR measurements.

Finally, with a magnetic field scan, at the lower field regime, the smallest nanoparticles show an elevated  $|\nu|$  value. With our previous reasoning, there could be formation of non-trivial spin texture at small enough magnetic fields in these nanoparticles. Upon application of magnetic field, these spin textures gradually rotate towards the forced ferromagnetic phase. Thus in the *slow fluctuation regime*, effectively quenching the electronic spin fluctuation. In the respective relevant length scales, skyrmion tubes have been found to be formed at zero magnetic field in FeGe tetrahedral particles [139]. Since the fluctuation scale observed in the nanoparticles is one order of magnitude smaller than the reported skyrmion lattice excitation in  $\text{Cu}_2\text{OSeO}_3$ ,

the observed data may point towards occurrence of low lying excitations of the established magnetic structure or emergence of novel spin texture without analogy to bulk- $\text{Cu}_2\text{OSeO}_3$ . Our data points towards emergent dynamics from the magnetic structure in the  $\text{Cu}_2\text{OSeO}_3$  nanoparticles, which should be resolved using real space imaging techniques, such as LTEM or electron holography.

### 5.7 Heat Capacity Studies Of $\text{Cu}_2\text{OSeO}_3$ System At Different Particle Sizes

The heat capacity of three different  $\text{Cu}_2\text{OSeO}_3$  particle sizes (I. Single crystal, II. 338 nm, and III. 73 nm) were studied by using the specific heat option of the PPMS. For the latter two cases, one pellet was made for each particle size, as shown in Fig. 5.24A. Single crystal  $\text{Cu}_2\text{OSeO}_3$  as well as the other two pellets were mounted onto a typical  $3 \times 3 \text{ mm}^2$  sapphire plate. Since all our measurements were carried out below room temperature, Apiezon N grease was used to make good thermal contact between the sample and the platform. As can be seen in Fig. 5.24A, the platform also contains platinum wires connecting it to a resistive heater as well as a thermometer.

Shown in Fig. 5.24B is the typical heat pulse method used to extract the sample heat capacity at a given temperature. The sample temperature is raised by this heat pulse, while system temperature remains the same. The PPMS system applies a constant power to raise the sample temperature, followed by removing this pulse. This results in the temperature-time curve shown in Fig. 5.24B. By analysing either of the two sides (or both) of temperature evolution, sample heat capacity is known. In the usual measurement protocol, first heat capacity of the platform together with grease is measured in the desired temperature range ( $C_{\text{total}}$ ), followed by measuring both sample and grease together. The difference between these two gives the actual sample heat capacity ( $C_p$ ).

In the case of perfect contact between the sample and the platform, the total heat capacity of the system evolves as the following.

$$C_{\text{total}} \frac{dT}{dt} = P(t) - K_W(T - T_b) \quad (5.15)$$

where,  $K_W$  is the thermal conductance of the supporting platinum wires. In the excited temperature regime, the sample heat capacity is assumed not to change drastically. Solution to this equation is an exponential function with a parameter,  $\tau$ , known as the *time constant*.  $\tau$  varies as the ratio between  $C_{\text{total}}$  and  $K_W$ , and determines the duration of the applied heat pulse. The fitting routine is known as the “ $1\tau$ ” method. As an extension of this procedure, if the sample-platform contact is not ideal, then one has to introduce the thermal conductance between the sample and the grease. This more sophisticated procedure is known as the “ $2\tau$ ” method. One crucial point to be mentioned here is that irrespective of the pulse size, the num-



## 5.7. Heat Capacity Studies Of $\text{Cu}_2\text{OSeO}_3$ System At Different Particle Sizes

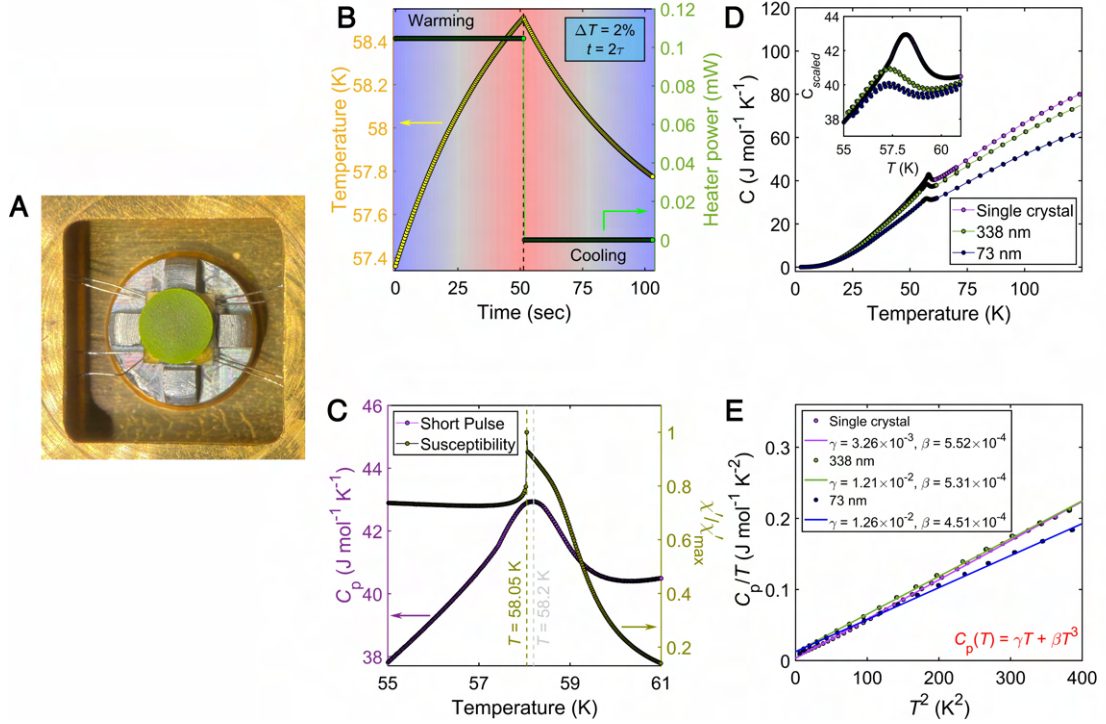


**Figure 5.24:  $C_p$  measured with short heat pulses.** Optical pictures of the mounted  $\text{Cu}_2\text{OSeO}_3$  (A) pellet made from 338 nm particles on the heat capacity puck. The single crystal was chosen in a such a way that the flat surface area is smaller than the platform. (B) shows an example of the heater power used and the corresponding heat pulse produced in the more widely used short-pulse method. (C) Shows the measured heat capacity as well as  $\chi'$  for the same single crystal  $\text{Cu}_2\text{OSeO}_3$  sample in the vicinity of  $T_c$ . Even with a 0.02 K step size, the short pulse method fails to detect the first-order transition. (D) Measured heat capacity ( $C_p$ ) between  $T = 2.1$  K and  $T = 145$  K for all three particle sizes using the short-pulse technique. The inset shows the scaled  $C_p$  (in the paramagnetic regime) around  $T_c$ . The low temperature electronic parameters extracted from  $C_p$  for all three particle sizes are shown in panel-E.

ber of data points for each pulse stays the same at 256. Since the sample-platform coupling strength was higher than 99% in our case, only  $1\tau$  method was employed. Correspondingly, the extracted heat capacity for the single crystal  $\text{Cu}_2\text{OSeO}_3$  at many temperatures is shown in panel-C of Fig. 5.24. While comparing the results with the AC susceptibility measurements, one does not fail to notice the absence of first order peak corresponding to PM→HM phase transition. This issue will be addressed later in this section.

Panel-D of Fig. 5.24 shows the comparison between the measured specific heat for all three particle sizes. The data measured for the single crystal  $\text{Cu}_2\text{OSeO}_3$  matches quite well with the reported values [3]. Also, the hump-like feature nicely correlates with the measured susceptibility of all particles (see fig. 5.20). Apart from the very low temperatures, we observe reduced heat capacity values for smaller particles. Analytical theory needs to be developed in order to explain this point further. The extracted Sommerfeld coefficients shown in panel-F

also agree well with a previous report [154].

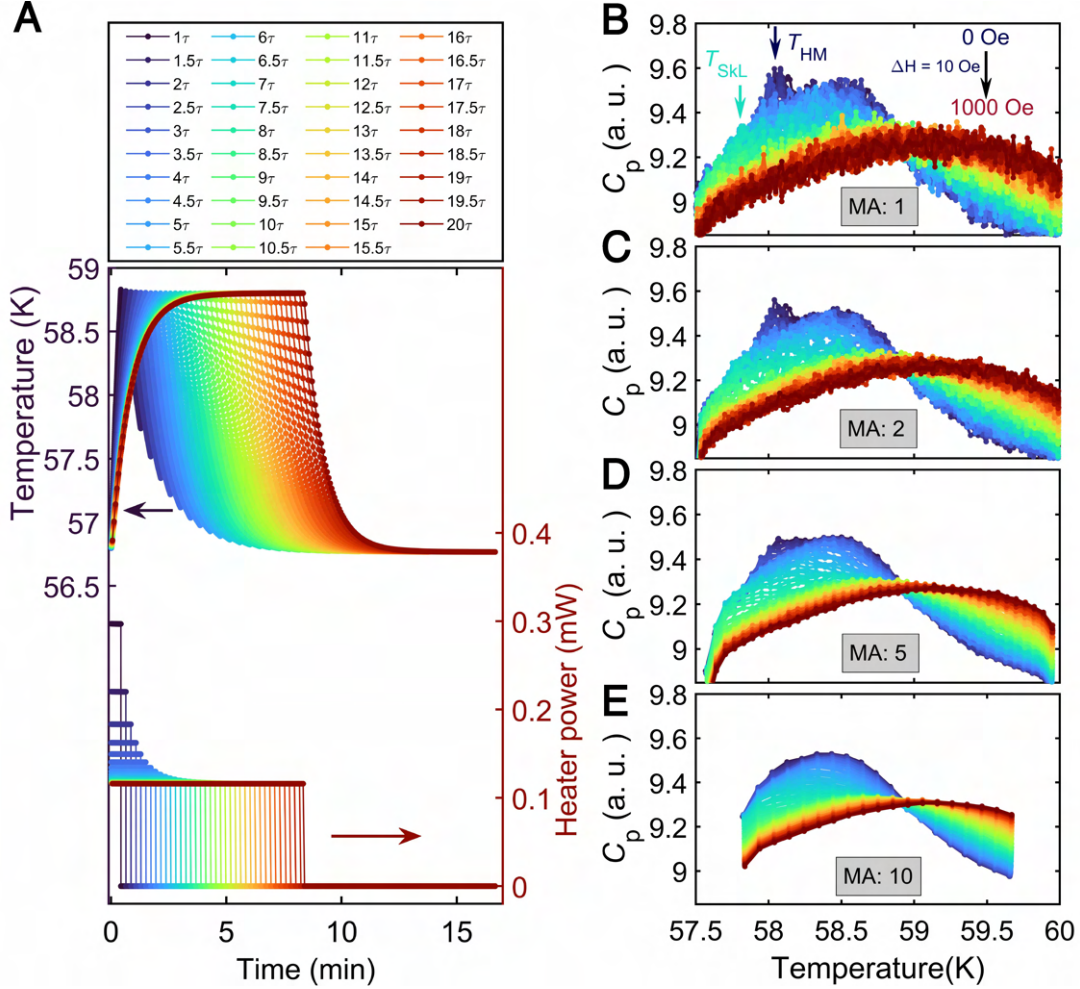


**Figure 5.25: Phase transitions in Bulk  $\text{Cu}_2\text{OSeO}_3$  probed by long heat pulses.** (A) Sample temperature,  $T$  and heater power ( $P$ ) as a function of temperature for various time constants ( $\tau$ ) for a zero-field scan crossing  $T_c$ . Heat capacity measurements were performed with long pulses in presence of a finite magnetic field varying between 0 and 1000 Oe. Extracted  $C_p$  for different moving average (MA) window are shown in panels-(B)-(E). As shown in panel-E, choosing a higher MA smoothens the data, thus losing valuable information about the sample behaviour. For panel-(B)-(E), all heat capacity data were taken with a 5% temperature rise.

Now for the second method, the *long pulse technique*, usually sample temperature is changed by 30-50% by using a single pulse. This is especially useful in case of first-order phase transitions, where the usual  $1\tau$  method fails to account for sharp change in heat capacity due to latent heat. Assuming an ideal contact between sample and grease (that is  $1\tau$  model) the total heat capacity is then extracted according to the following equation:

$$C_{\text{total}} = \frac{P(t) - K_W(T - T_b)}{dT/dt}. \quad (5.16)$$

### 5.7. Heat Capacity Studies Of $\text{Cu}_2\text{OSeO}_3$ System At Different Particle Sizes

Using this long-pulse technique the first order transition in the archetypal helimagnet MnSi has been well-resolved [16]. Now we apply the same principle to not only single crystal  $\text{Cu}_2\text{OSeO}_3$ , but nanoparticles as well. In order to probe the specific heat of  $\text{Cu}_2\text{OSeO}_3$  properly, we used heat pulses of various lengths, between  $1\tau$  and  $20\tau$  (as shown in Fig. 5.25A). For the  $\text{Cu}_2\text{OSeO}_3$  we used, each measurement lasted between  $\sim 1.5$  mins till  $\sim 18$  mins. For a heat pulse with smaller  $\tau$ , the power provided by the heater is high. This is due to the fact that the temperature of the sample has to be increased by the same amount in a really narrow time window. Post data acquisition, (either warming, or cooling or both) the Temperature-Time curve is analysed according to Eqn. 5.16. The typical example of the results look like the ones shown in Fig. 5.25(B)-(E). The total heat capacity of the single crystal  $\text{Cu}_2\text{OSeO}_3$  as a function of applied magnetic field appears like the behaviour observed in MnSi [16]. By choosing a specific moving average (MA), we select a corresponding interval of the 256 data points which we intend to use for analysing the Temperature-Time curve. As clearly seen between panels-(B) and (E) of Fig. 5.25, choosing a higher MA smears out the sharp transitions intrinsic to sample. Both short pulse as well as long pulse techniques have been shown to produce consistent results with respect to each other [16, 18].

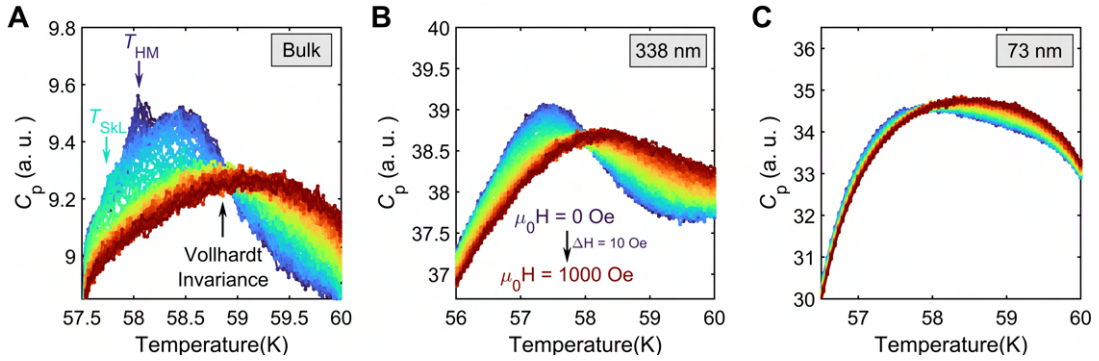


**Figure 5.26:  $C_p$  vs  $T$  for  $\text{Cu}_2\text{OSeO}_3$  at different magnetic fields as obtained using long heat pulses.** Heat capacity measurements were performed on all three particle sizes using the long pulse technique, as explained in the caption of Fig. 5.25. A sharp peak was observed for the bulk single crystal signalling the first order transition from Helimagnetic phase (HM) to the paramagnetic phase. This feature is clearly absent in the 338 nm as well as 73 nm particle, showing clear correspondence between heat capacity and susceptibility measurements. The sharp peak corresponding to the first order topological transition to the SkL phase is also detected for the bulk  $\text{Cu}_2\text{OSeO}_3$  crystal. Agreeing well with our previous AC susceptibility results, no such transitions were observed for both 338 nm and 73 nm particles.

Now we outline the next aspect of the geometrical confinement effects in  $\text{Cu}_2\text{OSeO}_3$  particles. As shown in Fig. 5.26, the magnetic field dependent heat capacity data for single crystal  $\text{Cu}_2\text{OSeO}_3$  correspond quite well with the  $\chi(T)$  data shown in Fig. 5.24C. As expected from the magnetic phase diagram of these three particle sizes (see fig. 5.18C, E, and I), the bulk crystal shows a sharp first order peak at the  $T_{\text{HM}}$  (panel-A of Fig. 5.26), which was absent from the heat capacity data measured with small pulses (Fig. 5.24C). We also observed sharp peaks corresponding to the conical  $\rightarrow$  SkL topological phase transition. For the remaining two particle

sizes, we observed rather smeared out transitions, in accord with the  $\chi(T)$  data. Similar to the broad field-induced transitions seen in the  $\chi(T)$  data,  $C_p(T)$  also shows no signature of any transition in and out of the SkL phase, for both particle sizes. The suppression on the hump-like feature in all three particles are as follows: 2.11% for the bulk particle, 1.02% for 338 nm particles whereas -0.869% in the 73 nm particles. These values roughly correspond to the changes observed in the magnetic entropy while crossing the phase diagram at various points.

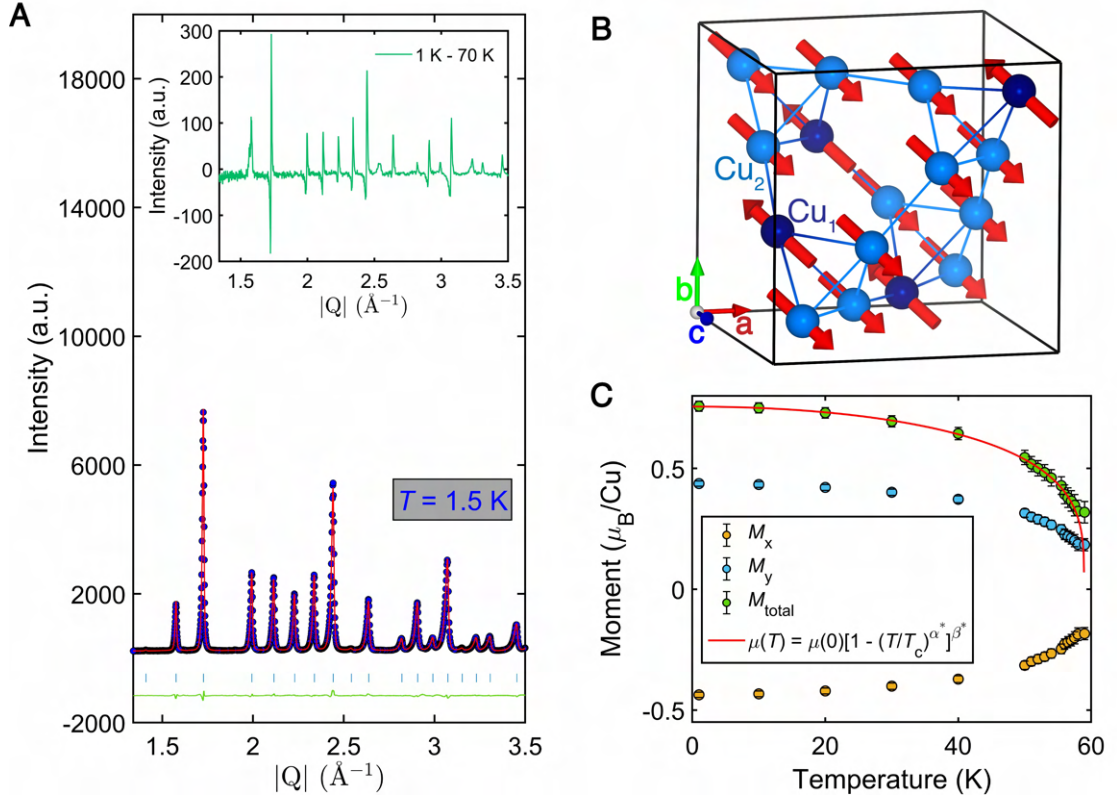
The *Vollhardt crossing point* is where specific heat curves cross almost at the same point for varying external parameters, such as magnetic field [201], and at which the system is argued to possess the Vollhardt invariance [18, 22]. Although it may seem the case, it is not an invariant point, since for high enough magnetic field, the specific heat curves do not pass through a single point anymore. For  $\text{Cu}_2\text{OSeO}_3$ , we find that a single crystal sample exhibits a Vollhardt crossing point for magnetic field values below 700 Oe. This signifies the energy scale over which the Dzyaloshinskii-Moriya interaction energy is dominant, and helps form the spiral ground state. Now for the 338 nm particles, the corresponding crossing point was found to be below 650 Oe. Finally, for the 73 nm particles, 330 Oe was found to be the Vollhardt crossing point. This illustrates a strong correspondence between the magnetic phases observed within these particles with their fundamental energy scales.

## **5.8 Magnetic Structure Determination Through Powder Neutron Diffraction**

Wide angle neutron diffraction measurement were performed to determine the ground state spin configuration. For this purpose, we performed two independent neutron diffraction experiments on the same  $\text{Cu}_2\text{OSeO}_3$  sample. One at a constant-wavelength instrument (DMC SINQ, PSI) and the second at a time-of-flight instrument (WISH ISIS, RAL). 4.506 Å cold neutrons were used at the DMC diffractometer. About 1g powder sample was enclosed in a vanadium can and sealed tight under He atmosphere. Each pattern was recorded for about one hour at WISH and for 2.5 hours at DMC. As the results of magnetic refinements from both data are almost identical with respect to each other, from here on discussion will be focused around the result obtained from the WISH data.

Out of the many possible models, the collinear one proposed by Bos *et al.* [27] is the simplest solution which agrees with the experimental data reasonably well. In this scenario, different groups are described in the so-called “parent setting”. In the cubic unit cell, symmetry does not constraint the values and orientation of the moments. Additionally, a symmetry lowering is essential in order to accommodate ferromagnetic/ferrimagnetic arrangement in the cubic parent setting. Thus in one of the subgroups for  $P2_13$ , the colourless (type 1)  $R3$  Shubnikov group, there are 6 independent Cu-sites. While one of them ( $\text{Cu}_2^I$ ) is constrained to be along the 3-fold axis, the others remain totally free (thus a total of  $3 \times 5 + 1 = 16$  free parameters). Due to lack of information in the powder pattern, this does not result in satisfactory fitting



338 nm,  $\mu_0 H = 0$  Oe


**Figure 5.27: Zero field magnetic structure of  $\text{Cu}_2\text{OSeO}_3$  probed by wide angle neutron diffraction.** (A) Refinement of neutron powder diffraction pattern obtained at  $T = 1$  K. Pattern measured in the paramagnetic phase at  $T = 70$  K was used for estimating the nuclear contribution. Inset shows the difference between these two patterns. (B) Shows the refined magnetic structure. For simplicity, other atoms in the unit cell have not been shown. Magnetic moment of the two inequivalent Cu atoms in each tetrahedron were found to be similar in magnitude but opposite in direction, ultimately resulting in a “3-up,1-down” ferrimagnetic arrangement. (C) Temperature dependent magnetic moment on Cu-sites obtained by Rietveld refinement. The red curve denotes a power law fit to the total moment.

of the data. In order to overcome this challenge, all moments have been constrained to be along the 3-fold axis (like the  $\text{Cu}_2^{\text{I}}$  site), with same amplitude. Thus, effectively reducing the problem to a single varying parameter: the moment amplitude. The value obtained within the  $R3$  group is  $0.73(1) \mu_B$ . In a modified approach, the moments can also be split up into two values corresponding to the two original Cu-sites in the cubic parent setting ( $\text{Cu}^{\text{I}}$  and  $\text{Cu}^{\text{II}}$ ). Two different moment amplitudes  $0.90(7)$  for  $\text{Cu}^{\text{I}}$  and  $0.57(7) \mu_B$  for  $\text{Cu}^{\text{II}}$  are obtained with similar goodness of fit.

Similar refinements were also carried out for Orthorhombic magnetic subgroup  $P2_1'2_1'2_1$ . But in this case, there are four Cu-sites (12 free parameters) and there is no constraint in the

orientation of the moments. When the moments are restricted to lie along the  $c$ -axis, we obtain similar results as for  $R3$  Shubnikov group, with the same values for the moments. From the temperature-dependent data, extracted moment values were fitted using the following power law equation.

$$\mu(T) = \mu_0 \left[ 1 - \left( \frac{T}{T_c} \right)^{\alpha^*} \right]^{\beta^*}. \quad (5.17)$$

The resultant  $T_c$  of 58.9(2) K from the fit is about 1 K lower compared to the value obtained from single crystals [229], but still higher than the one from  $\mu\text{SR}$  experiments [120]. This  $T_c$  agrees quite well with results obtained from the AC susceptibility measurements. The second parameter,  $\alpha^*$ , is known to dominate the power law behaviour in the magnetically ordered regime away from transition. Only dimensionality and spin quantum number influence the absolute value of  $\alpha^*$ . In a perfect case,  $\alpha^*$  has the value of 2. The  $\alpha^*$  obtained from our fit is 2.1(4) and thus very close to the behaviour expected from a perfect system. The Heisenberg parameter,  $\beta^*$  was found to be 0.27(2), and is somehow lower than the perfect 3D Heisenberg behaviour (where,  $\beta = 0.365$  [43]). A slightly different magnetic phase diagram was obtained for these particles with respect to the bulk single crystal [11]. The critical parameter could heavily be influenced by other instabilities in free energy arising due to finite particle size. Finally,  $\mu_0$  [ $0.75(1)\mu_B$ ] is slightly higher than the reported value [ $0.68\mu_B$ ], but still  $\sim 25\%$  lower than the expected spin-only value of  $1\mu_B$ . The ground state of  $\text{Cu}_2\text{OSeO}_3$  is known to be a long periodic helical state, with a propagation vector,  $|q_h| = 0.01 \text{ \AA}^{-1}$ . As discussed earlier, these helices populate three  $\langle 100 \rangle$  cubic axes equally. This small momentum transfer can hardly be resolved with a wide angle neutron diffraction instrument. A small angle neutron scattering (SANS) setup would be particularly useful for this analysis [11].

## 5.9 Small Angle Neutron Scattering Investigations Of $\text{Cu}_2\text{OSeO}_3$ Particles

Small angle neutron scattering (SANS) experiments were performed to elucidate the magnetic textures in  $\text{Cu}_2\text{OSeO}_3$  particles with  $h$  of 338 nm and 73 nm, bigger and smaller than  $S_c$ , respectively. For this purpose, the SANS-II instrument at the Swiss Spallation Neutron Source (SINQ), Paul Scherrer Institute (PSI), Switzerland and D33 instrument at the Institut Laue Langevin (ILL), Grenoble, France were used. Samples for experiments at both instruments were prepared as pressed pellets of 10 mm diameter and thickness  $< 0.5$  mm and installed into a horizontal field cryomagnet. The magnetic field was applied in the plane of the sample pellet, and perpendicular to the neutron beam. For the field-training procedure, the sample was first saturated to field-polarized state while collecting statistics at specific magnetic field values mentioned throughout the chapter. This was followed by ramping down the magnetic field to 0 Oe at a rate of 10 Oe per second. At SANS-II, neutrons with a wavelength of  $7.29 \text{ \AA}$  were used with a FWHM spread  $\Delta\lambda/\lambda = 10 \%$ . The incoming beam was collimated over a distance of 6 m

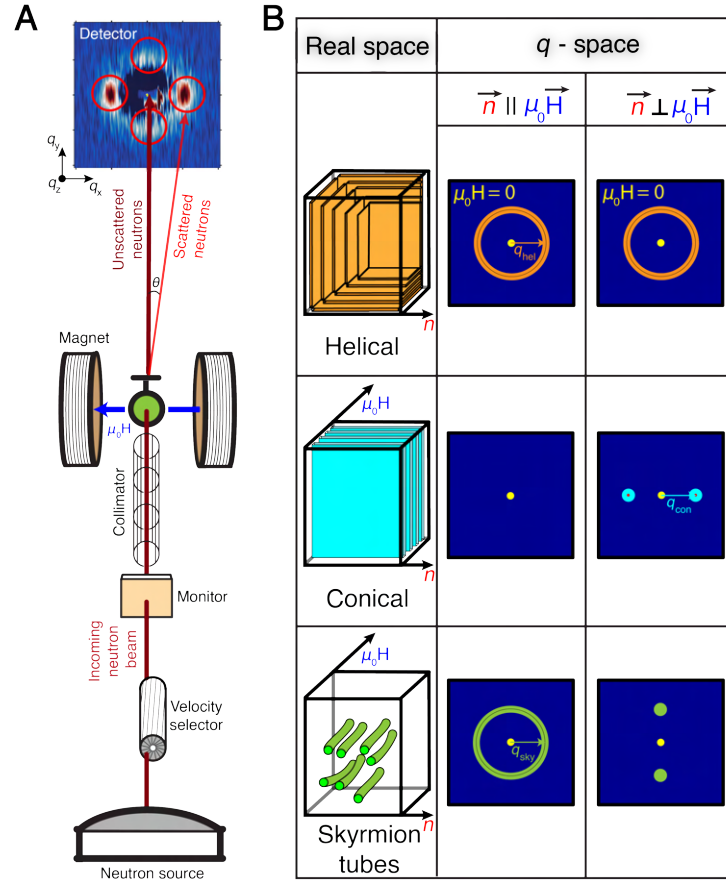


**Figure 5.28: Experimental setup and proposed magnetic textures in real and reciprocal space.** (A) Schematic illustration of the experimental geometry used in our SANS measurements. The applied magnetic field was always kept perpendicular to the incoming neutron beam. The detector image shown is the scattering pattern obtained for the 338 nm particles, in an external field of 200 Oe and a temperature of 52.4 K. (B) Left column: Proposed chiral magnetic textures that may be stable inside each 338 nm particle, such as multidomain helical phase, single domain conical phase and skyrmion phase. Their corresponding reciprocal space scattering patterns for a magnetic field aligned with the neutron beam (center column) and perpendicular to the neutron beam (right column) are given when such textures are stable inside a sample of unoriented particles. The central yellow spot is due to the unscattered neutrons. These have been masked in the real detector images (such as shown in A or Fig. 5.29). The helical phase stable in zero field shows up as a sphere of intensity in reciprocal space, and correspondingly always as a ring on the detector. In the conical phase, the magnetic order always propagates along the magnetic field, and so the scattering is concentrated into peaks that are observed only when the neutron beam is perpendicular to the field. Since skyrmion tubes align with the field direction, the scattering signal due to skyrmions in the sample of unoriented particles, manifests as a ring in the plane perpendicular to the applied field, and thus presents as two peaks at the north and south pole positions when the field is perpendicular to the neutron beam.

before the sample, with the scattered neutrons collected by a two-dimensional multidetector placed 6 m behind the sample. At D33, neutrons with a wavelength of 4.6 Å were used with a FWHM spread  $\Delta\lambda/\lambda = 10\%$ . Both the collimation distance and the sample-to-detector distance were 12.8 m. The data collected at D33 are available from the ILL [12]. All the data analysis was performed using the GRASP software [42].

The experimental setup is illustrated in Fig. 5.28A. Fig. 5.28B summarizes the connection between the real-space magnetic textures (left column) consistent with those found in bulk chiral magnets, and the corresponding SANS patterns (centre and right columns) when such textures are stable in particles that are unoriented with respect to one another. In the 338 nm particles at 52.4 K and after zero field cooling, Fig. 5.29A shows the appearance of a ring-like magnetic scattering around  $q = 0$  due to propagating helical spin correlations within a sample of the randomly oriented particles. From the intensity ring, the magnitude of the wavevector describing the magnetic modulation is determined as  $|q| = 0.1027(2) \text{ nm}^{-1}$  (Fig. 5.30). This gives a magnetic modulation periodicity ( $\lambda$ ) of 61.2(1) nm consistent with that due to helical order found in bulk samples as illustrated in Fig. 5.28B [3, 168, 206].

Fig. 5.29B-F show that a horizontal magnetic field applied perpendicular to the incident neutron beam drives a rearrangement of the SANS intensity in the 338 nm ( $> S_c$ ) particles. As indicated in Fig. 5.28B, a redistribution of the SANS intensity to regions aligned with the field (green boxes in Fig 5.29A-F) and perpendicular to the field (red boxes in Fig 5.29A-F) are hallmark signatures for the formation of conical and skyrmion orders, respectively [94]. The formation of both of these orders is most clearly seen in Fig. 5.29C, where peaks are observed due to co-existing conical and skyrmion orders consistent with those expected according to Fig. 5.28B. Fig 5.29G shows the field-dependence of the green box (helical and conical modulations) intensity to display a similar field-dependence and two-peak structure as that of  $\chi''$  determined from AC susceptibility. These are further clear signs for skyrmion formation in the “valley” field region  $150 < B < 350 \text{ Oe}$ . Concomitantly, over the same field region, Fig. 5.29H reveals a small, yet clear enhancement of the red box (skyrmion) SANS intensity above any residual ring intensity (white boxes in Fig. 5.29A-F) that remains undistributed by the field before saturation, presumably due to pinning. In the middle of the valley region shown in Fig. 5.29G, the intensity of the green boxes drops by roughly 35%, while a similar percentage increase of intensity in the red boxes compared with the white boxes is also observed in Fig. 5.29H. These results indicate that 35% of the particles in the sample undergo a transition to a skyrmion-like phase and that these coexist with particles that remain in unoriented helical-like and conical-like phases. Overall, these SANS data confirm microscopically the existence in the 338 nm particles of phases directly analogous to those found standardly in bulk chiral magnets.

In the 73 nm ( $< S_c$ ) nanoparticles at 52.4 K near to  $T_c$ , a ring of magnetic SANS intensity is again observed around  $q = 0$  after zero-field cooling (Fig. 5.31) from which the pitch length  $\lambda$ , was determined to be 72(1) nm, as shown in (Fig. 5.31I). The value of  $\lambda$  is longer than that of ~60 nm expected for helical order in bulk samples, and spans exactly the average octahedral height



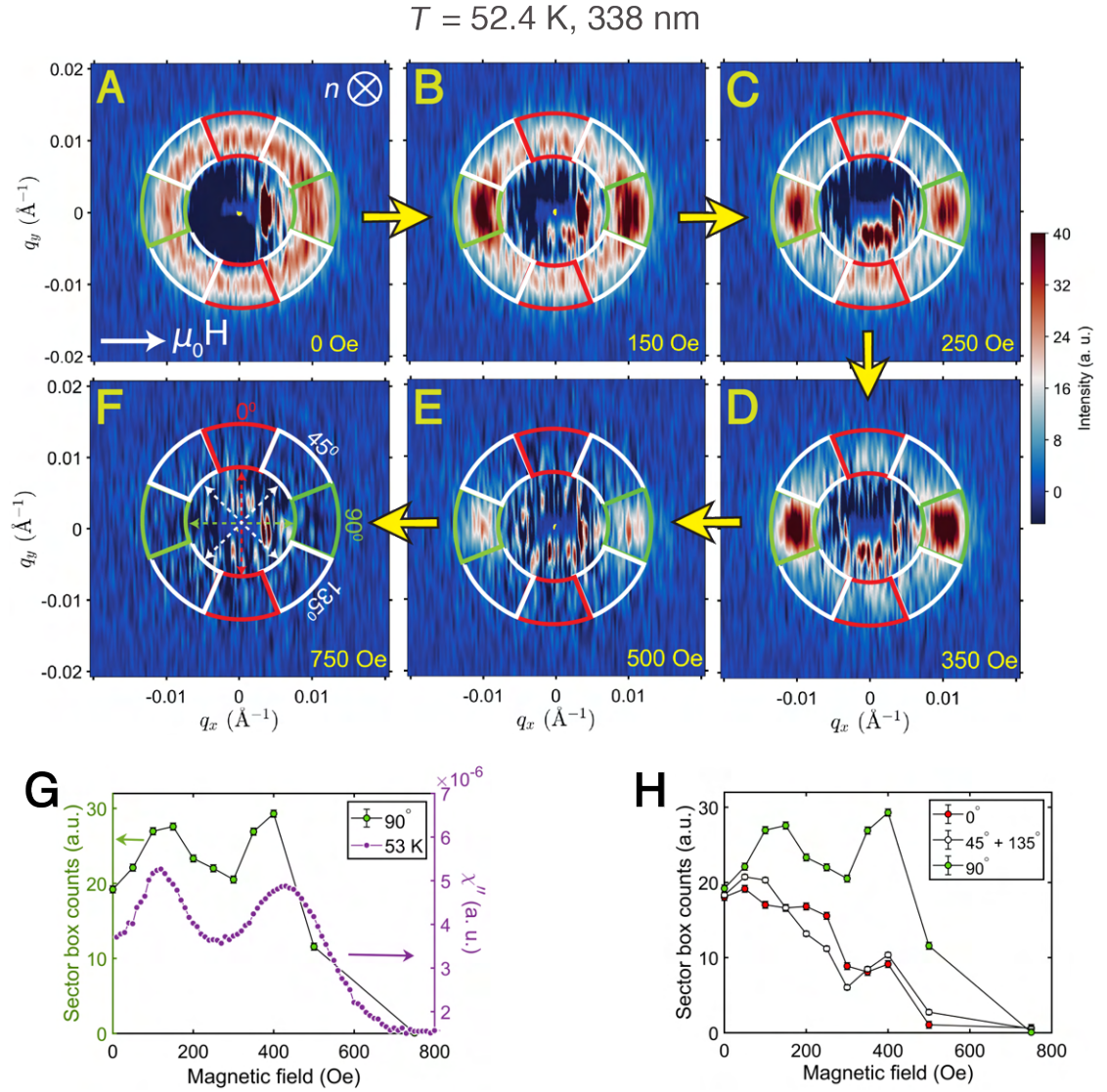


**Figure 5.29: Probing 338 nm  $\text{Cu}_2\text{OSeO}_3$  particles using SANS.** (A)-(F) SANS detector images from the  $h = 338 \text{ nm}$  particles measured at 52.4 K and as a function of the applied magnetic field. For simplicity, the intensity scale has been kept the same for all patterns. The angular positions of sector boxes indicated in panel F represent sector boxes corresponding to that particular position, as well as the one which is situated diametrically opposite to it. (G) shows the evolution of intensity in the sector boxes corresponding to the conical phase [green boxes in (A)-(F)], as a function of applied magnetic field. For a comparison,  $\chi''$  for the same particles measured at 53 K is also shown. (H) The dip in conical phase SANS intensity between 15 and 35 mT indicates a redistribution of the intensity due to the formation of skyrmion tubes.

of the nanoparticle. The adaptation of the ground state magnetic modulation in accordance with the geometry of the nanoparticles is a clear sign for a finite size effect. Furthermore, as shown in Fig. 5.32, a ring-like scattering pattern remains consistent with that expected from a sample of unoriented particles each hosting a single-period helical spiral structure that spans

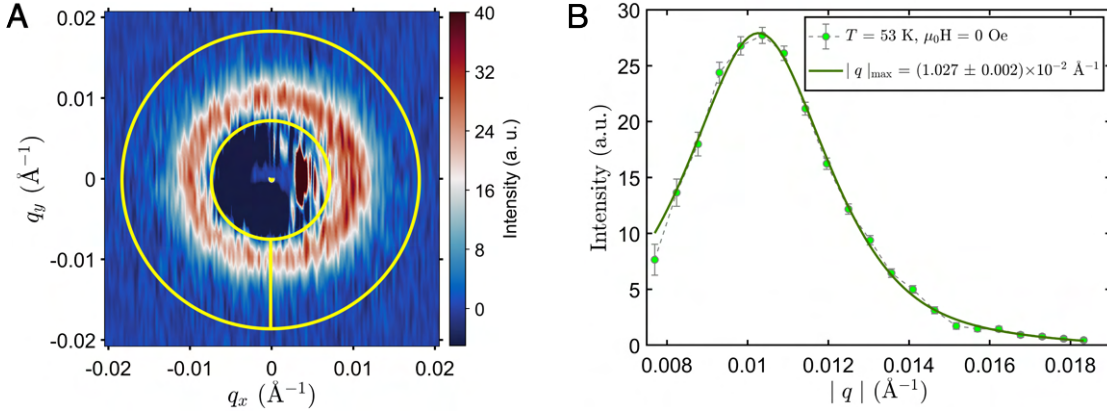


**Figure 5.30: Length of incommensurate modulation in 338 nm particles.** (A) SANS detector image for 338 nm particles at 53 K at zero magnetic field. In order to estimate the total radial intensity evolution as a function of  $|q|$ , an isotropic sector was chosen as shown in yellow. To ensure all magnetic scattering is considered for this analysis, the width of the sector was chosen such that it spans the maximum of the detector image. (B) Magnetic scattering as a function of  $q$  extracted from the sector box defined in (A). The green solid line represents a Pseudo-Voigt fit to the same.

the octahedral particle height. Under increasing magnetic field, the confinement effect on  $\lambda$  is relieved as it falls towards the bulk value for helical order on the approach to saturation, shown in Fig. 5.31I. In addition, there is no observed rearrangement of the intensity in the ring, and instead the SANS intensity falls monotonically on the approach to saturation, see Fig. 5.31H. This latter observation may be indicative of either a pinning effect on the magnetic modulations, or the realization of an unexpected spin configuration with more isotropic susceptibility that is without analogy to the standard chiral magnet phases realized in the bulk.

It is to be noted that a single period helical spiral can also produce a “two-spot” SANS pattern, as shown in Fig. 5.32. When a single 73 nm helical pitch embedded into the octahedron with the same height, the corresponding two-dimensional fast Fourier transform (FFT) of the  $M_z$ -component of the magnetization features a two-spots pattern. This FFT pattern can serve as a rough approximation of the SANS intensity map in the  $(yz)$  plane, where the neutron beam  $k_i$  is parallel to  $x$  and helical propagation axis is parallel to  $y$  [57]. Two bright spots seen in the FFT (Fig. 5.32), are results of the magnetic structure factor. The possible emergence of aperiodic arrangements of magnetic skyrmions, chiral bobbles, merons or other isolated textures embedded into ferromagnetic background should be manifested in form-factor small-angle scattering across the large  $q$ -range [200]. With the present dataset at hand it will not be able to discuss this weak effect due to the limited dynamic range, and predominance of the peaked scattering intensity.

Finite size-effects on  $\lambda$  are also observed far from  $T_c$  at 5 K in both the 73 nm and the 338 nm particle samples. Figure 5.33A and B each show two-spot SANS patterns indicative of helical-like spin-correlations existing in each sample at zero field after applying a standard field-

$T = 52.4 \text{ K}$ , 73 nm

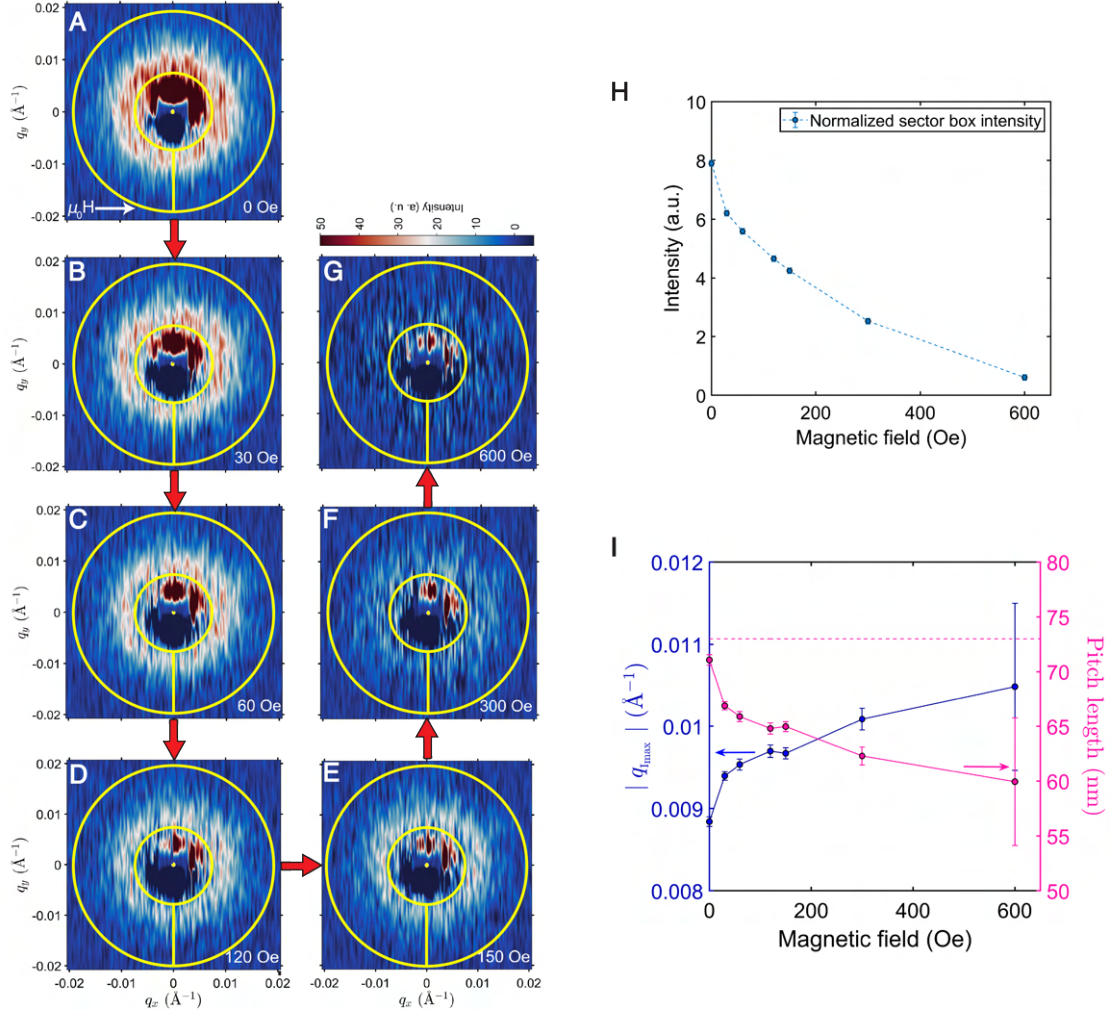


**Figure 5.31: Magnetic modulation in 73 nm particles.** (A)-(G) represent SANS detector images for the smallest nanoparticles (73 nm) measured in the same instrumental conditions as described previously in Fig. 5.29. In order to estimate the total intensity of magnetic scattering as a function of magnetic field, similar sector boxes were chosen as shown in Fig. 5.30. The resulting intensity evolution is shown in (H).  $|q|$  corresponding to the maximum of intensity was estimated for each of the detector images shown and is plotted in (I). It also shows the equivalent pitch length in real space for these incommensurately modulated phases. The dashed line in magenta signifies the height of each octahedron, as estimated from the W-H analysis presented in Fig. 5.6A previously.

training procedure performed at 5 K. As shown in Fig. 5.33K, the magnetic periodicity determined from the spot positions is  $\lambda = 72(2) \text{ nm}$  in the 73 nm nanoparticles, which is the same as close to  $T_c$  (Fig. 5.31I). For the 338 nm particles,  $\lambda = 65(1) \text{ nm}$  is larger than close to  $T_c$ , and has expanded so that exactly five magnetic modulations span the octahedral height. It's worthwhile noting that the observed enhancement of  $\lambda$  in the particles at low tempera-

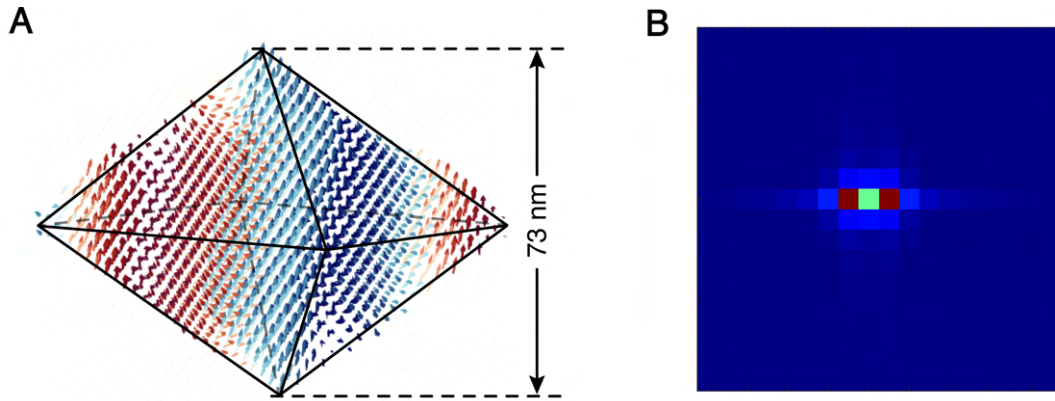


**Figure 5.32: FFT of an octahedron possessing a single helix.** (A) A single period of magnetic helix embedded into 73 nm nanoparticle. (B) Fast-Fourier transform of the  $z$ -component of the magnetization projected on the  $(yz)$  plane, showing characteristic “two-spot” pattern.

ture is an order of magnitude larger than the increase otherwise observed on cooling in bulk  $\text{Cu}_2\text{OSeO}_3$  [33].

While the quantization effect on helices has previously been reported in epitaxially grown thin samples of chiral magnets FeGe [90, 153] and MnSi [92, 210], this work is the first demonstration of such novel behaviour in 0D particles hosting magnetic helices. The observed modifications to the helices in the thin plate samples are attributed to surface-induced magnetic anisotropy together with boundary conditions arising due to reduced dimensionality. We propose a modified scenario in case of our 0D particles. As shown in the schematics (Fig. 5.33D & E), each magnetic helix can span the entire height of the octahedron or more generally, non-adjacent vertices. Each vertex of the octahedron, due to its natural symmetry breaking, form a type of topological defect. With reduced particle volume, role of these vertices become increasingly more important. The consequences of similar argument is recently reported experimentally in FeGe 0D particles [139]. The so-called “pot-belly”-type vortex state is observed, without any analogy with bulk chiral magnet of the same system. Within the framework of our results, with octahedral particles, we expect enhanced contribution from the increased number of vertices, compared to the tetrahedral particles studied by *Niitsu et al.* [139]. Due to this key role of the geometry in generating the interactions that underlie the confined magnetic configurations, the robust stability of these emergent magnetic states can be anticipated, particularly in the genuine nanoparticle limit.

## 5.10 Micromagnetic Simulations On $\text{Cu}_2\text{OSeO}_3$ Particles Based On Landau-Lifshitz-Gilbert equation

In order to simulate the emergent magnetic texture in octahedral  $\text{Cu}_2\text{OSeO}_3$  particles, micromagnetic simulations were used. Micromagnetic simulation is the most straightforward



### 5.10. Micromagnetic Simulations On $\text{Cu}_2\text{OSeO}_3$ Particles Based On Landau-Lifshitz-Gilbert equation

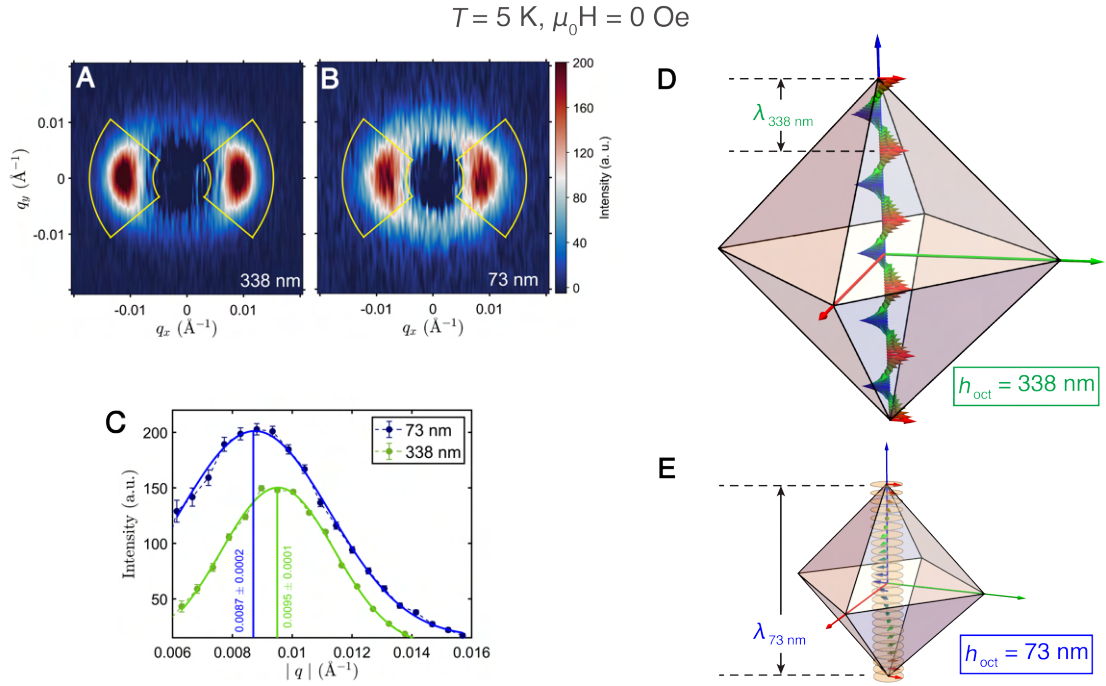


**Figure 5.33: Finite size effect in reciprocal space.** (A) and (B) show the detector images obtained in zero field and 5 K after performing a field training procedure for both particle sizes. Here the zero-field state was prepared by ramping the magnetic field down from saturation in an attempt to concentrate the SANS intensity into a smaller reciprocal space volume. This hysteretic effect of field training on the spiral propagation vector is typical for cubic chiral magnets at low temperatures [193, 102]. The wavevector-dependence of the resulting intensity indicated by the sectors in (A) and (B) is shown in (C), and the peak positions determined by solid lines. (D) and (E) represent the consequences of the finite size effects for both particles shown as the real space pitch length of the underlying incommensurate phase. For the 338 nm particles, exactly five periods span the entire height of the octahedron, whereas the same for 73 nm particles is found to be just one.

way of predicting the microscopic behaviour of magnetic systems. The simulation packages use either finite difference or finite element-based solvers to find the quasi-stationary and dynamic solutions by solving the Landau-Lifshitz-Gilbert (LLG) equations. All the energy terms are typically expressed as the effective fields,  $B_{\text{eff}} = -\delta E / \delta M$ , and evaluated at every cell. After each subsequent step the magnetization in every cell varies by  $\delta_{\text{m}} = -\lambda_{\text{m}} \times (\mathbf{m} \times B_{\text{eff}})$  up until the convergence is reached. Recently, micromagnetic simulations has been a way for correctly predicting the emergent phenomena in skyrmion hosting materials [139].

LLG simulations calculations were performed at  $T = 0 \text{ K}$  using the MuMax3 software package, based on finite difference discretization, and appropriate magnetic parameters for a  $\text{Cu}_2\text{OSeO}_3$  particle: exchange stiffness  $A_{\text{ex}} = 7\text{e}^{-13} \text{ Jm}^{-1}$  and Dzyaloshinskii-Moriya interaction constant  $D = 7.4\text{e}^{-5} \text{ Jm}^{-2}$  [83, 199, 222]. The size of the elementary unit of 4 nm was used. An initially random spin configuration was allowed to relax for 2.5 ns in each simulation. The magnetic

field was first applied along the top vertex of the octahedron shown in Fig. 5.35A. Similar calculations were performed for when the external magnetic field was applied perpendicular to one of the octahedron facets, the results of which are shown in Fig. 5.35B. Note that the various spin textures are identified by observation only, since the definition of topological charge breaks down in 3D [133]. The computation was performed using NVIDIA GPU 980Ti, and RTX 3080 Ti. The magnetic structure was visualized using the Paraview software [6].

## Results

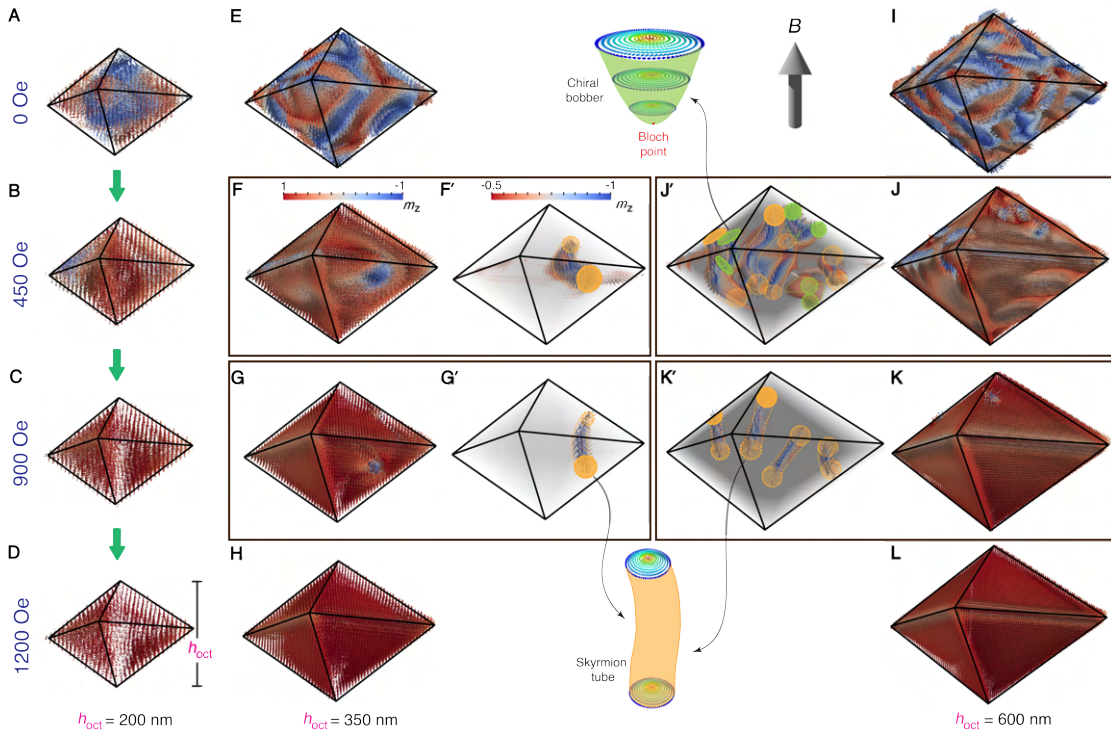


**Figure 5.34: Micromagnetic simulations on isolated octahedral  $\text{Cu}_2\text{OSeO}_3$  particles.** (A)-(D), (E)-(H) and (I)-(L) show magnetic textures obtained from the micromagnetic simulation performed on octahedrons of height 200 nm, 350 nm and 600 nm, respectively. Panels (F', G') and (J', K') elucidate the internal magnetic structures of 350 nm and 600 nm particles in magnetic fields of 450 Oe and 900 Oe, respectively. The colour scale represents the  $z$ -component of the magnetization. The black lines have been added in order to make the particle contours more obvious. The appearance of chiral bobbles and skyrmion tubes is highlighted by green and yellow ellipses, respectively. The direction of applied magnetic field was kept the same in all cases, which is along the top vertex of the octahedron.

To understand better the role of the particle geometry and size on the stability of different magnetic configurations, micromagnetic simulations were performed for a realistic octahedron-shaped particle, and exchange, DMI and magnetization constants typical for bulk  $\text{Cu}_2\text{OSeO}_3$ <sup>4</sup> [222]. The resulting variety of magnetic textures found by simulations of a

<sup>4</sup>This work was performed in collaboration with Dr. Victor Ukleev from the group of

### 5.10. Micromagnetic Simulations On $\text{Cu}_2\text{OSeO}_3$ Particles Based On Landau-Lifshitz-Gilbert equation

single particle are expected to be representative for our samples, since the dipolar interaction is shown to be negligible for these systems, as pointed out recently by means of finite-element simulations [148]. In the absence of an external magnetic field, the initially random spin configuration relaxes to a state with randomly-oriented helices for all particle sizes, as shown in Fig. 5.34(A), (E), and (I). Under an external magnetic field applied along the octahedron height, the magnetization of the smaller octahedra ( $h = 100\text{--}220\text{ nm}$ ) gradually rotates towards the field direction without developing any non-trivial magnetization textures [Fig. 5.34(A)-(D)]. A similar smooth transformation from a zero-field non-collinear to a field-induced ferrimagnetic state was reported previously in a study of very small ( $h \sim 30\text{ nm}$ )  $\text{Cu}_2\text{OSeO}_3$  nanoparticles [41].

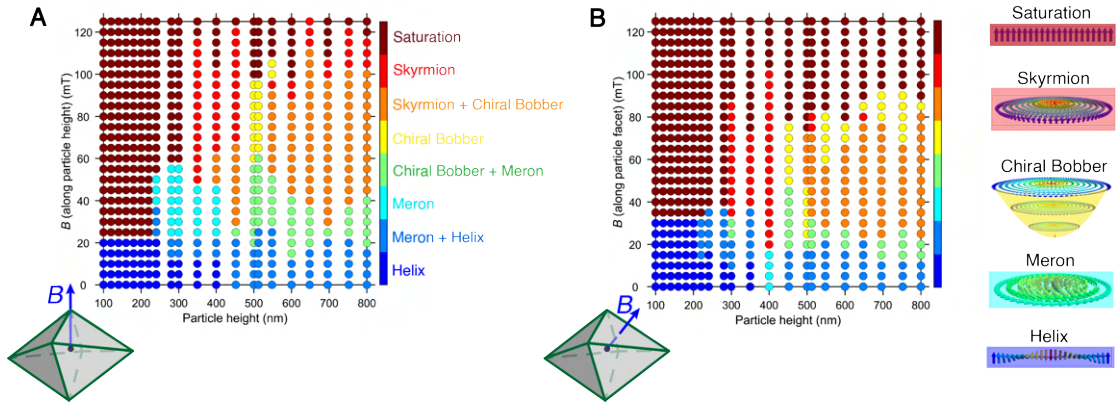


**Figure 5.35: Size dependent phase diagram of octahedral  $\text{Cu}_2\text{OSeO}_3$  particles.** Spin texture phase diagram as a function of height of the octahedron, as obtained from micromagnetic simulations. (A) The magnetic field was applied along the top vertex of the octahedron, that is along [001] whereas, in (B) the magnetic field was applied along one of the triangular facets, that is along [111]. The dotted lines represent the simulation points in the phase diagram. All the magnetic textures were identified manually.

In contrast, larger octahedra exhibit a variety of field-induced magnetic textures, including half-skyrmions (merons) in octahedra with  $220 < h < 350\text{ nm}$ , chiral bobbars ( $350 < h < 400\text{ nm}$ ) and skyrmion tubes ( $h > 400\text{ nm}$ ) in various (field-dependent) co-existent combinations. Representative simulations for particles with  $h = 350\text{ nm}$  and  $h = 600\text{ nm}$  are shown in Fig. 5.34E-L, wherein skyrmion and chiral bobber spin textures are stabilized. The field-induced transformation of the helical structure to the meron state in the particles allows a minimization of the Zeeman energy while preserving the periodicity of the magnetic texture, when formation of the complete skyrmion tube is unfavored by the confinement effect. The chiral bobber state, seen as a combination of a skyrmion tube and a Bloch point, is stabilized for the same critical particle size as the skyrmion state, suggesting similar formation mechanisms for these two textures. Our simulations suggest the stabilization of the chiral bobber state as an edge state of  $\text{Cu}_2\text{OSeO}_3$  in larger nanoparticles which is consistent with the generalized theory of chiral bobbars at the surface in cubic chiral magnets and experimental works on FeGe which hosts a helimagnetic ground state with a spiral pitch similar to  $\text{Cu}_2\text{OSeO}_3$  [5, 161, 228]. Recently, the

Laboratory for Neutron Scattering and Imaging (LNS), Paul Scherrer Institut (PSI), Villigen, Switzerland.

bobber phase induced by proximity effect was also evidenced in  $\text{Cu}_2\text{OSeO}_3$ /magnetic multi-layer heterostructure [158]. However, their unambiguous experimental evidence in bulk and nanostructured  $\text{Cu}_2\text{OSeO}_3$  is remaining as a challenging task which can be further addressed by real-space electron holography or resonant elastic x-ray scattering. Further, we find that in  $\text{Cu}_2\text{OSeO}_3$  nanocrystals the critical size for nucleation of a single skyrmion tube was found to be around 350 nm (Fig. 5.34F and G). The phase diagram summarizing these findings is shown in Fig. 5.35A.

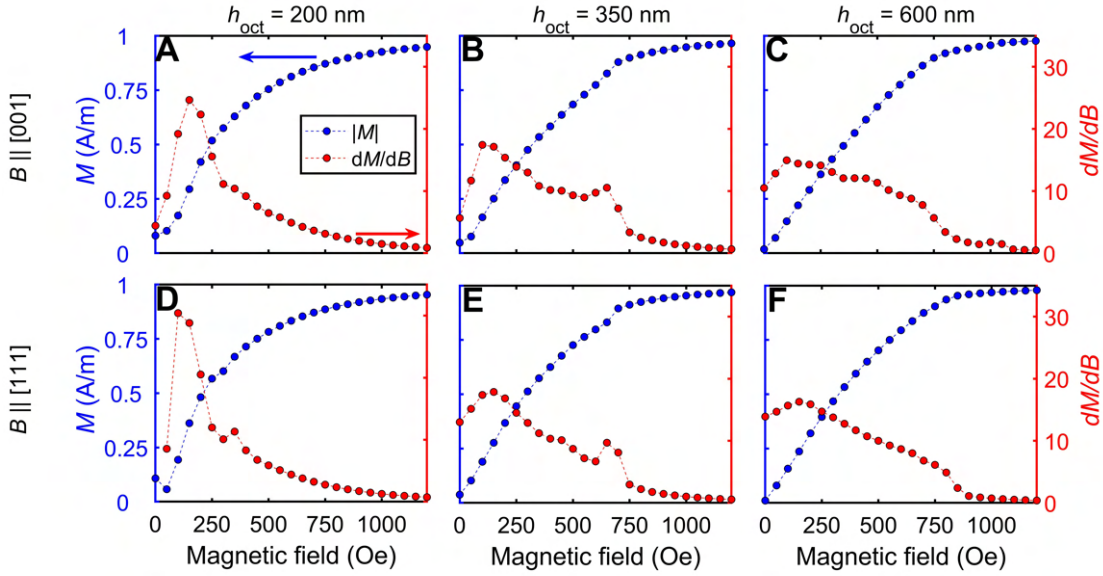


**Figure 5.36: Magnetization ( $M$ ) and  $dM/dB$  as obtained from the micromagnetic simulations.** For the three sizes shown in Fig. 5.34, evolution of the total magnetization as a function of magnetic field, as obtained from micromagnetic simulations. Total magnetization refers to the norm of the three spatial components. (A)-(C) represent when the magnetic field was applied along the top vertex of the octahedron ([100]), whereas (D)-(F) represent those along one of the facets ([111]).  $dM/dB$  clearly shows the metamagnetic-type transitions in individual nanoparticles (for example, panel B).

Similar simulations were done for the case when the magnetic field was oriented perpendicular to one of the octahedral triangular facets. The size-field phase diagram (Fig. 5.35B) appears qualitatively similar to Fig. 5.35A, with small differences in bobber and skyrmion stability regions. For each orientation of the magnetic field, a similar threshold volume of magnetic particle is identified below which topologically non-trivial magnetization configurations analogous to those found in the bulk are not expected to be stable. The field evolution of the magnetic texture is qualitatively reflected in the magnetization curves directly extracted from the micromagnetic simulations (Fig. 5.36). These findings agree with the experimental magnetometry and SANS data, and the expectation for other particle shapes considered in previous micromagnetic simulations [34, 41, 45, 46, 148, 150]. On the other hand, the present experimental data do not allow a straightforward identification of the different topological spin



### 5.10. Micromagnetic Simulations On $\text{Cu}_2\text{OSeO}_3$ Particles Based On Landau-Lifshitz-Gilbert equation

textures expected according to our simulations. Real-space imaging probes such as electron holography or Lorentz-transmission electron microscopy (LTEM) are needed to determine the detailed spin configurations at the single particle level (see Fig. 5.37).

The magnetization  $M$  component along the direction of the applied field was extracted from the simulations for both  $B \parallel [001]$  (along the particle height, as seen in Fig. 5.35A) and  $B \parallel [111]$  (along the particle facet, in Fig. 5.35B). Metamagnetic transitions seen in both  $M(B)$  and  $dM/dB$  graphs illustrate the evolution of magnetic textures shown in Fig. 5.34.

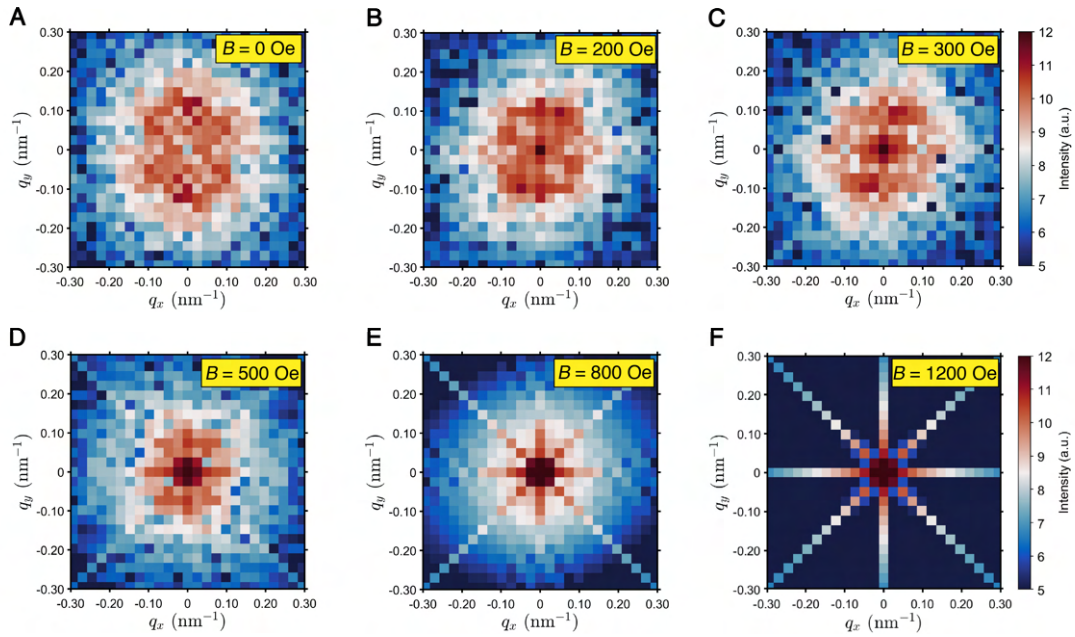


**Figure 5.37: FFT of the magnetic texture within each particle.** Magnetic field evolution of the Fast Fourier Transformation of the  $z$ -component of the magnetization,  $M_z \parallel \vec{B}$  projected onto the  $(q_x, q_y)$  plane for the 512 nm particle.

To distinguish between the possible signatures of new three-dimensional (3D) magnetic textures we have analysed results of the micromagnetic simulations of 512 nm particles via Fast-Fourier Transformation (FFT) of the magnetization component  $M_z \parallel \vec{B}$  projected onto the  $(q_x, q_y)$  plane. The simulation results are shown in Figure 5.37 as a function of the magnitude of the applied field covering the characteristic phases (see Fig. 5.35): helical ( $B = 0$  Oe), helical + meron (200 Oe), meron (300 Oe), skyrmion + chiral bobber (500 Oe), single skyrmion (800 Oe) and, finally, induced ferromagnetic (1200 Oe). The FFTs show maxima centered at  $|q| \sim 0.1 \text{ nm}^{-1}$  in all phases hosting multiple magnetization kinks (or magnetic quasiparticles) which corresponds well to the characteristic wavevector of magnetic modulations in  $\text{Cu}_2\text{OSeO}_3$ . These maxima are superimposed onto the broad halo originated from the magnetic form-factor scattering from the single magnetic kinks, especially pronounced in the case of the isolated skyrmion (800 Oe). The cross-shaped intensity distribution at 1200 Oe represents the canted moments at the edges of the octahedron in the field-induced ferromagnetic state. The accurate fitting of the small-angle scattering profiles and their comparison to

micromagnetic models would be a promising way to extract the 3D magnetic textures such as merons, vortices and chiral bobbles. However, we note that the present calculation is done for the nanoparticle and does not account for the powder averaging of the scattering pattern and for the magnetization distribution within separated particles, which would smear out the characteristic features of the form factor (see the detailed analysis of the particle size distribution in magnetic SANS in a recent preprint [2]). Therefore, the unique identification of these phases is more likely to be completed via real-space probes, or scattering experiments that can be performed on the single-crystal-particle level, such as small-angle electron diffraction or resonant x-ray scattering.

## 6 Anisotropic Exchange Interaction

After uncovering details of the novel *geometrical confinement effects* in  $\text{Cu}_2\text{OSeO}_3$ , in this chapter, we elucidate one further aspect of chiral magnetism in this system, that is the anisotropic exchange interaction (AEI) and its impact on the low temperature magnetic phase diagram. We will first outline the necessary motivation to study the AEI in this material. This will be followed by a concise description of the  $t$ -REXS experiment performed at VEKMAG endstation in BESSY-II, Berlin to probe the AEI. And finally, the implication of our results on the emergent low temperature magnetic phase diagram will be discussed.

### 6.1 Significance Of AEI in Skyrmion Hosting Helimagnets

The Bak-Jensen model involving competing interactions such as the Heisenberg exchange interaction, the antisymmetric Dzyaloshinskii-Moriya interaction (DMI), the anisotropic exchange interaction (AEI), and cubic anisotropy satisfactorily explains the ground state magnetic structures of  $B20$ -type magnets. The first three terms are responsible for the formation of helical ground state and its well-defined orientation with respect to the crystallographic directions [10, 48, 132]. The weak cubic anisotropy term is responsible for the helix orientation under an external magnetic field. But in reality these cubic anisotropy terms together with AEI are often neglected since their strength is limited in  $B20$  group of compounds, and thus in their experimental observations [177]. Among the  $B20$  family of compounds,  $\text{MnSi}$  was found to have negative anisotropic exchange interaction constant ( $F_{\text{AEI}}$ ), resulting in spiral propagation along [111]. For  $\text{FeGe}$ , there was a change in sign of  $F_{\text{AEI}}$  as a function of temperature, since at higher temperatures  $q$  is oriented along [100], while that for the lower temperatures is [111] [113]. Whereas, for solid solution of  $\text{Mn}_{1-x}\text{Fe}_x\text{Si}$  and  $\text{Fe}_{1-x}\text{Co}_x\text{Si}$ ,  $F_{\text{AEI}}$  is found to fluctuate around zero. While the multiferroic compound  $\text{Cu}_2\text{OSeO}_3$ , is crystallographically different compared to the other helimagnets from  $P2_13$  family, the helix propagation direction is found to be  $\{100\}$ , same as  $\text{Fe}_{0.85}\text{Co}_{0.15}\text{Si}$ . Recently, away from the high-temperature equilibrium skyrmion lattice (HT-SkL), there have been many reports of emergent magnetic phases in  $\text{Cu}_2\text{OSeO}_3$  such as a low temperature skyrmion lattice (LT-SkL), tilted conical (TC) phase etc [9, 33, 63, 157]. Cubic anisotropy has been proposed to be the main factor stabilizing

these low temperature phases. Also, in a Zn-doped  $\text{Cu}_2\text{OSeO}_3$  sample,  $F_{\text{AEI}}$  was found to change sign from positive to negative with reducing temperature [128]. But as shown before, these samples behave quite differently compared to pristine  $\text{Cu}_2\text{OSeO}_3$  [175]. However, the stronger cubic anisotropy prevents the spiral  $q$  reorientation along  $\langle 111 \rangle$ , demonstrating the complex competing landscape of magnetic interactions in this system. So a systematic isolation of the anisotropic interactions, followed by efficient quantification therefore becomes very important, in order to have a better understanding of the low temperature properties of pristine  $\text{Cu}_2\text{OSeO}_3$ . The conventional ferromagnetic resonance technique fails to address the AEI since a high magnetic field used to investigate the field-polarized state is irrelevant from the point of view of AEI. On the other hand, due to its high spatial resolution, REXS has been established as a powerful technique to study the skyrmion lattice and the other related phases in chiral magnets [194, 195, 209]. Recently, it has been successfully employed to estimate  $F_{\text{AEI}}$  in FeGe [193]. But before we give a detailed account of the experimental results, we would like to provide a theoretical outline for the modified  $q$  in presence of AEI.

To account for the modifications caused to the modulation vector in presence of AEI, analytical calculations were performed on the Bak-Jensen model, but including not only AEI but also easy-axis anisotropy [10]<sup>1</sup>. In the first step we will first calculate the corrections to  $q$  due to anisotropic interactions, followed by that from the easy-axis anisotropy. If  $\psi$  is the polar angle of  $q$  in the  $xy$ -plane, the AEI energy can then be expressed as:

$$E_{\text{AEI}} = \frac{F_{\text{AEI}}}{2} \int \left[ \sum_{v=x,y,z} \left( \frac{\partial S^v}{\partial x^v} \right)^2 \right] dV. \quad (6.1)$$

If  $t$  is denoted to be the coordinate along  $q$ , and  $\phi(t)$  is the magnetization angle within the spiral plane, then we can also write the following:

$$E_{\text{AEI}} \propto \frac{S^2 F_{\text{AEI}} \sin^2 2\psi}{4} \int \left( \frac{d\phi}{dt} \right)^2 \cos^2 \phi dt. \quad (6.2)$$

For a (nearly) proper screw spiral without anisotropic interactions,  $\cos^2 \phi$  becomes 1/2, and the expression simplifies into,

$$E_{\text{AEI}} \propto \frac{S^2 F_{\text{AEI}} \sin^2 2\psi}{8} \int \left( \frac{d\phi}{dt} \right)^2 dt. \quad (6.3)$$

Whereas, for the exchange interactions we have,

---

<sup>1</sup>The analytical expressions were provided by Dr. Oleg I. Utesov at the Petersburg Nuclear Physics Institute, Gatchina, St-Petersburg, Russia.

$$F_{\text{EX}} \propto \frac{S^2 \mathbb{J}}{2} \int \left( \frac{d\phi}{dt} \right)^2 dt. \quad (6.4)$$

Therefore, combining Eqn 6.3 and Eqn 6.4, we arrive at the  $\psi$ -dependence of  $q$  as:

$$q(\psi) = \frac{\mathbb{D}}{\mathbb{J} + (F_{\text{AEI}}/4) \sin^2(2\psi)} \approx \frac{\mathbb{D}}{\mathbb{J}} \left( 1 - \frac{F_{\text{AEI}} \sin^2 2\psi}{4\mathbb{J}} \right). \quad (6.5)$$

Now turning to easy-axis anisotropy part, with the polar angle  $\zeta$ , similar expression for energy can be written in the following form:

$$E_{\text{aniso}} \propto -Z S^2 \sin^2(\psi - \zeta) \int \cos^2 \phi dt. \quad (6.6)$$

where,  $Z$  is the uniaxial anisotropy constant. With a slight tedious calculations after implementing Eqn 6.6 into the Sine-Gordon equation, we arrive at the azimuthal angle dependence of modulation vector on  $\zeta$  as:

$$q' = q(\psi) \left[ 1 - 2\pi \frac{Z^2 \sin^4(\psi - \zeta)}{\mathbb{J}^2 q^4} \right]. \quad (6.7)$$

Combining Eqn 6.7 and Eqn 6.5, we obtain the final expression for corrections to modulation vector in presence of both anisotropic exchange interaction as well as uniaxial anisotropy

$$q' = \frac{\mathbb{D}}{\mathbb{J}} \left[ 1 - \frac{F_{\text{AEI}} \sin^2 2\psi}{4\mathbb{J}} - 2\pi \frac{\sin^4(\psi - \zeta) Z^2}{\mathbb{D}^4 / \mathbb{J}^2} \right]. \quad (6.8)$$

This is the master expression used to fit the azimuthal angular dependence of  $q$  in section 6.3. Since any material-specific parameters were not used for derivation of Eqn. 6.8, the obtained results remain valid for any helimagnets (which is stabilized by DM interaction) possessing a conical phase.

## 6.2 High-resolution $t$ -REXS Experiments at BESSY-II

For our experiments, a high quality  $\text{Cu}_2\text{OSeO}_3$  single crystal grown by CVT technique was oriented with [001] out of plane direction [47]. The details of the growth and the characterizations are outlined in section 4.1. A lamella (see Fig. 6.1B) was prepared using focused ion beam (FIB) milling from the very same crystal later used for our  $r$ -REXS experiments. The final thickness of the lamella was kept around 150 nm. This thin plate was placed behind an aperture of diameter  $10\mu\text{m}$  on a gold-coated  $\text{Si}_3\text{N}_4$  membrane. The whole assembly is finally transferred onto a copper frame held together by kapton tape (shown in Fig. 6.1C).

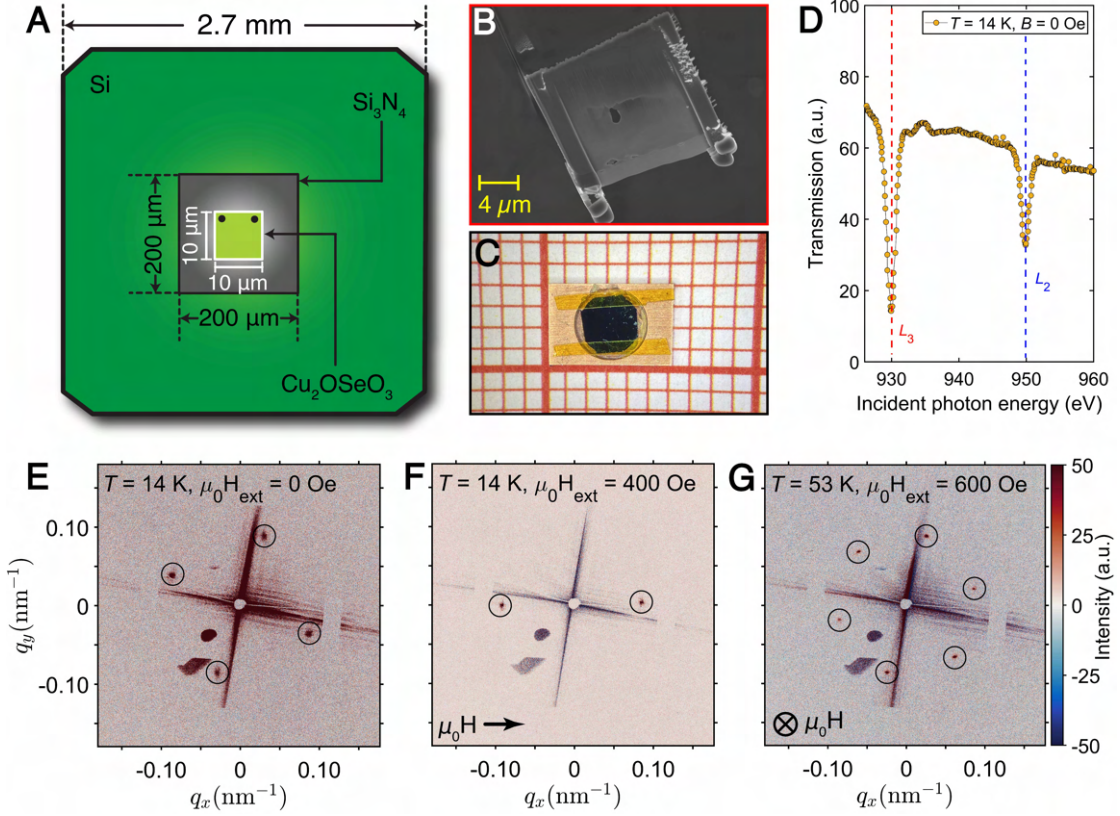


**Figure 6.1: Lamella preparation and initial characterizations at Cu- $L_3$  edge.** (A) Schematic sketch of the sample attached to a  $\text{Si}_3\text{N}_4$  membrane and the whole assembly fixed on a Si-frame. As expected from the scale of the final sample (usually in the range of tens of microns), fabrication is performed by cutting a larger crystal using focused ion beam (FIB) technique. (B) Actual image of the FIB cut lamella after transfer onto the  $\text{Si}_3\text{N}_4$  membrane. (C) Final image of the sample assembly. The Si-frame is supported on the larger Cu-frame using kapton tape. (D) Energy scan across  $L_3$  and  $L_2$  electronic transition edges for copper showing sharp resonant absorption. Probing a (E) two domain helical phase, (F) single domain conical phase and (G) a single domain skyrmion lattice phase at the  $L_3$  resonance edge of Cu. At zero magnetic field below  $T_{\text{HM}}$ ,  $\text{Cu}_2\text{OSeO}_3$  has three helical domains propagating along three principal cubic directions,  $\langle 100 \rangle$ . Since  $[001]$  crystallographic direction is pointing out of the sample plane, two in-plane helical domains are aligned along  $[100]$  and  $[010]$ , respectively. While an in-plane magnetic field is essential for stabilizing the conical phase, skyrmion lattice phase requires an out-of-plane magnetic field to form.

The  $t$ -REXS experiments were performed at the soft x-ray beamline PM2-VEKMAG (BESSY-II, Helmholtz-Zentrum Berlin for Materials and Energy, Germany) [140]. The vector magnet used for this work can produce a 9 T magnetic field along the x-ray beam, while 2 T and 1 T in the plane perpendicular to it. The scattered intensities were collected on a  $4096 \times 4096 \text{ pixel}^2$  CCD detector. Each detector image shown in this chapter was a sum of three exposures of 20s each.

Before proceeding with the actual experiment, the initial characterizations were carried out



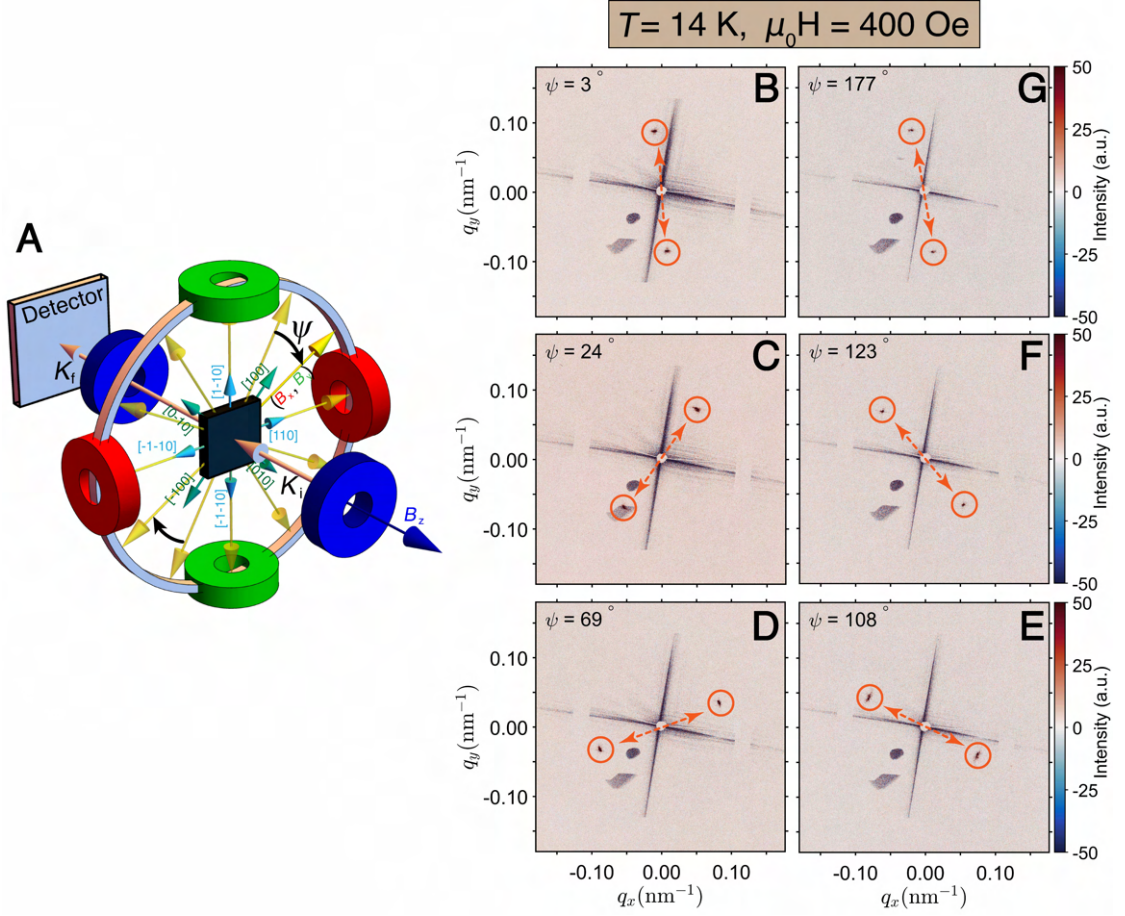


**Figure 6.2: Response of conical peaks due to in-plane magnetic field.** (A) The vector magnet setup at PM2-VEKMAG endstation in BESSY-II, Berlin. The vector magnet is capable of producing a 9 T magnetic field along the x-ray beam, while 2 T and 1 T in the plane perpendicular to it. For most of the experiment, the magnetic field was rotated in the  $(x, y)$ -plane, as shown in the sketch. The sample was a lamella shown in Fig. 6.1B. A CCD detector was mounted 66.5 cm behind the sample. According to the convention used, the vertical direction set to be  $\psi = 0$ . (B)-(G) show the detector images while magnetic field was oriented at different angles with respect to the vertical. These are indicated in each panel. The measurements were performed at the base temperature,  $T = 14 \text{ K}$ . Here, the magnetic field was first ramped up to 700 Oe, in order to achieve a field-polarized state, followed by ramping down to 400 Oe (inside conical phase) before acquiring the detector image. This sequence was repeated for each angle  $\psi$ . To observe the behaviour of conical peaks in all four quadrants,  $\psi$  was varied between  $0^\circ$  and  $180^\circ$ .

for the familiar phases in  $\text{Cu}_2\text{OSeO}_3$ . First an energy scan with a fixed photon helicity was performed across the electric dipole transitions for Cu, i.e. from far below  $L_3$  to far above  $L_2$ . Optimal  $L_3$  and  $L_2$  edges were found to be 929.5 eV and 949.8 eV, respectively. During the complete experiment, circularly polarized x-rays were used. First the sample was cooled down to the base temperature ( $T = 14 \text{ K}$ ) to study the zero-field helical state. In  $\text{Cu}_2\text{OSeO}_3$ ,

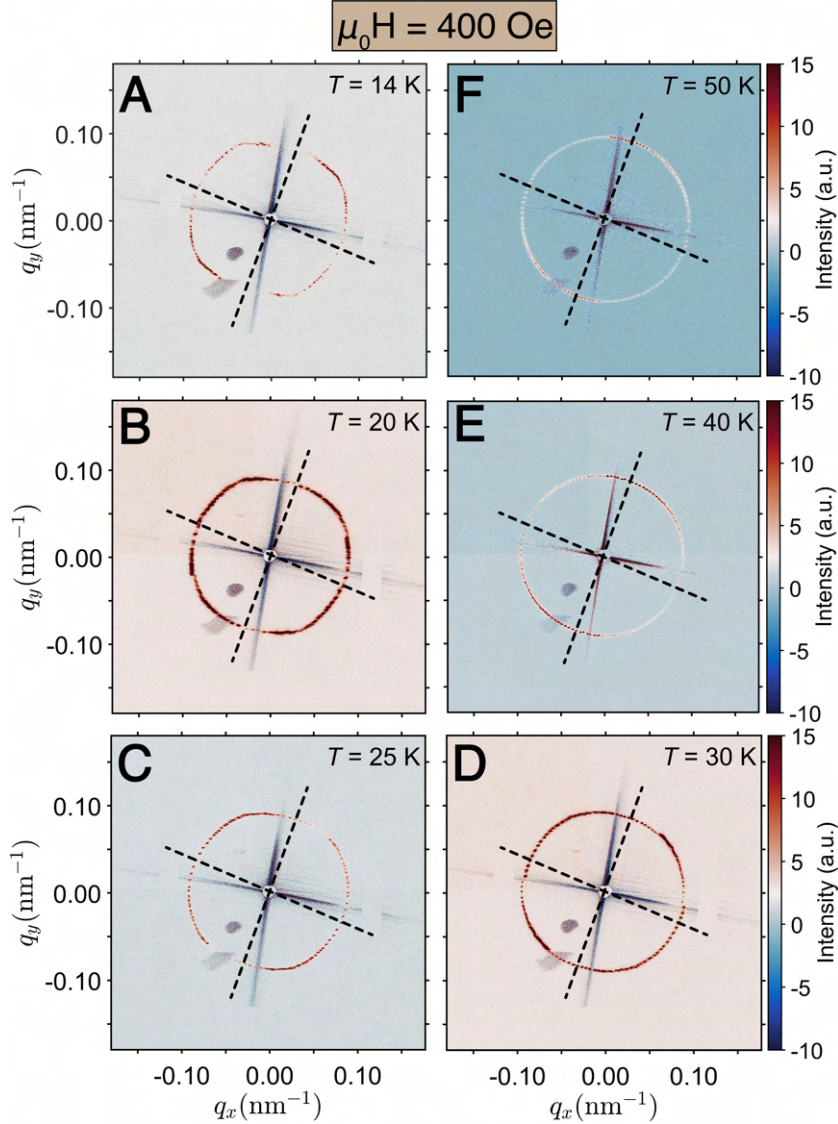


**Figure 6.3: Summed up intensity profile of the conical peaks in 2D reciprocal space at various temperatures.** The protocol described in Fig. 6.2 was repeated at six temperatures below  $T_c$ . The two dashed black lines are oriented along  $[100]$  and  $[010]$ , respectively (as shown in panel-E of Fig. 6.1). For simplicity, the colormap scale was kept the same for all panels. These summed up images outline the angular path traced by the conical peak as a function of  $\psi$ . As can be seen clearly, this is the result of competing interactions at various temperatures. The uniaxial anisotropy being stronger compared to the exchange anisotropy at 50 K, enforces the trajectory traced by the conical peaks to resemble an ellipse. But with gradual lowering of temperature, the exchange anisotropy begins to affect the profile more, resulting in more systematic behaviour with respect to easy in-plane crystallographic axes, that is the four  $\langle 100 \rangle$ s and  $\langle 110 \rangle$ s.

there exist three zero field helical domains along the three principal  $\langle 100 \rangle$  axes. Since the thin plate was prepared with  $[001]$  normal to sample plane, the remaining two  $\langle 100 \rangle$  domains lie



within the sample plane. In other words, [001] being out of scattering plane, the remaining two helical domains result in two Friedel pairs in the scattering plane. This is shown in Fig. 6.1E. The extracted real space pitch length of 68(2) nm also agrees quite well with the reported literature [3, 206]. Next we applied an in-plane magnetic field to reorient the helices into the conical phase, resulting in two spots on the detector plane, as shown in Fig. 6.1F. Finally with an out of plane magnetic field at  $T = 53$  K, we observe the familiar six spots pattern due to a well-ordered SkL phase. Thus the magnetic phases and the corresponding phase boundaries from our lamella match quite well with the numerous reports on this system [32, 169, 209].

### 6.3 Results And Discussions

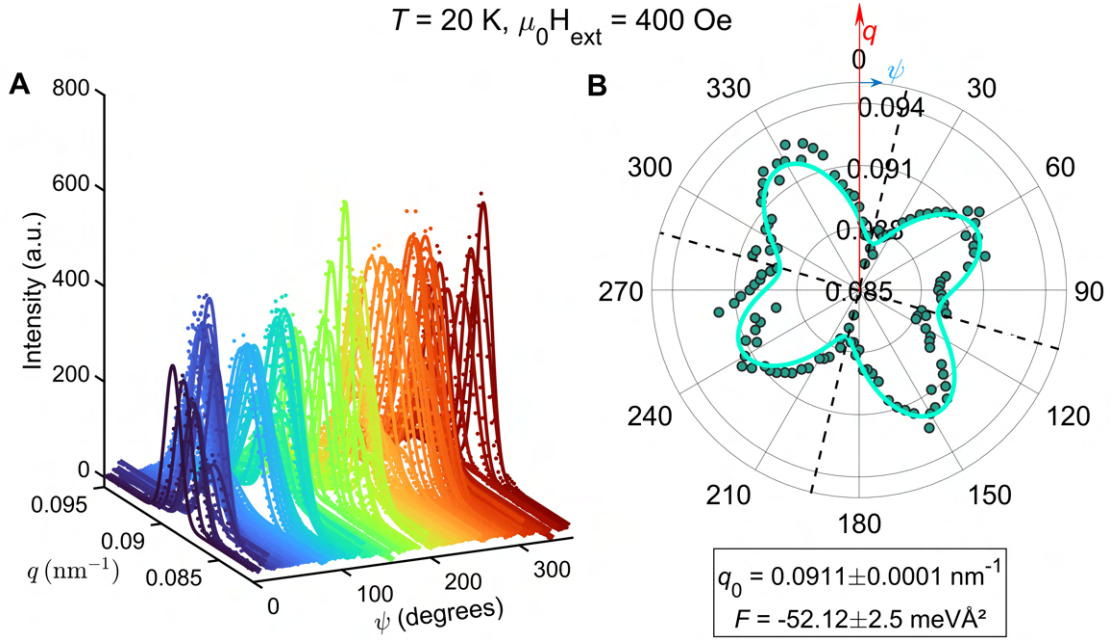


**Figure 6.4: Anisotropic exchange interaction constant for  $\text{Cu}_2\text{OSeO}_3$  at  $T = 20$  K.** The summed up images shown in Fig. 6.3 are now analysed individually for each  $\psi$ . Each detector image (for example the ones shown in Fig. 6.2) was analysed with help of a sector box of  $3^\circ$  angular width in order to obtain intensity vs  $q$  line plot. The resulting 1D data was fitted with a Gaussian function to extract the peak position and intensity. Panel-A represents the result of the fitting procedure for all  $\psi$ s. As shown in panel-B, the extracted peak position ( $q_{\text{max}}$ ) has a strong influence from the in-plane crystallographic directions. Finally the  $q_{\text{max}}$  is fitted with Eqn 6.8.

Utilizing the full capability of the magnet, we vectorially varied the magnetic field in the sample plane. In the conical phase, the cone propagation direction follows the magnetic field. Therefore, with a constant (magnitude) in-plane magnetic field we can decouple the changes caused by AEI to that coming from its magnetic field dependency. As shown in Fig. 6.2, Friedel pairs follow the in-plane magnetic field quite well. With the  $4096 \times 4096$  pixel<sup>2</sup> CCD detector, all four quadrants of the 2D reciprocal space around [000] central peak were

accessible, which was previously missing for the similar study performed on another cubic chiral magnet FeGe [193]. The lack of higher harmonics do indeed confirm the phase shown in Fig. 6.2 at  $T = 14$  K and  $B = 400$  Oe to be conical phase, without any distortion as found in chapter 7 for a bulk crystal. This state was prepared by the following procedure. First helical state was achieved by cooling the sample down to the target temperature ( $T = 14$  K, shown in Fig. 6.1E), followed by ramping up the magnetic field to 700 Oe to force the helices into the ferrimagnetic phase. Finally the field was slowly ramped down to 400 Oe in order to remain inside the conical phase for a particular  $\psi$ . After each acquisition, the magnetic field was once again ramped up to 700 Oe, followed by changing its in-plane direction,  $\psi$ . This protocol was repeated for each  $\psi$  ranging between 0 and  $180^\circ$  with a  $3^\circ$  step (shown in Fig. 6.2).

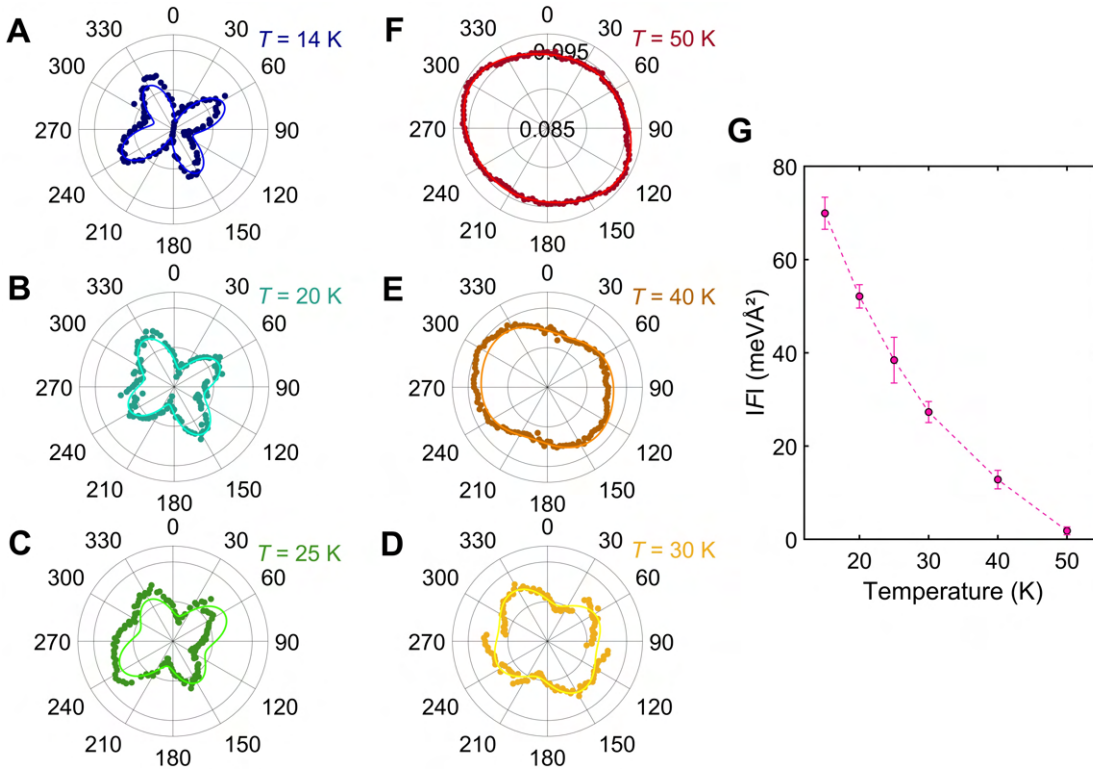


**Figure 6.5: AEI constant as a function of temperature.** As previously explained in Fig. 6.4, each azimuth was fitted with a Gaussian peak and the resultant was plotted for different temperatures on a polar grid. For simplicity, the radial ( $q$ ) scale for each plot from panel-A to panel-F was kept constant. Finally the  $q_{\text{max}}$  is fitted with Eqn 6.8 at all six temperatures. Panel-G shows the evolution of AEI constant with respect to temperature.

For a particular sample temperature, intensity corresponding to each of the Friedel pair for measured  $\psi$ s was extracted and summed up. The resultant is shown in Fig. 6.3. At  $T = 50$  K, the intensity profile appears almost circular but with a slight elliptic distortion. Temperature induced fluctuations, which are responsible for the stability of HT-SkL phase in cubic chiral magnets [134], also diminish the effects of AEI at this temperature. The observed ellipticity in the intensity profile at 50 K is the indication of uniaxial anisotropy, caused by strain coming

from the contacts made on the sample during FIB milling. While reducing temperature, the profile starts to develop subtle “features” along the marked crystallographic axes. At  $T = 25$  K (see Fig. 6.3C), the intensity profile deviates from the ellipticity seen at  $T = 50$  K and starts developing extra intensities along the in-plane  $\langle 110 \rangle$  directions. This is further pronounced at the base temperature of 14 K, as shown in Fig. 6.3A. Concomitantly,  $|q|$  along the  $\langle 100 \rangle$  directions is found to be the minimum.

In the next step, we look into the radial and angular details for each  $\psi$  manually using the ImageJ software [1, 35]. In order to simply contain a single Bragg peak, a sector box of  $3^\circ$  angular width was chosen around each. Also, both peaks from the Friedel pair were analysed separately, using mirror sectors. Thus, providing us information about  $|q|$  in all four quadrants simultaneously. The intensity as well as the centre of this averaged curve was fitted with help of a Gaussian peak. This is outlined in panel-A of Fig. 6.4. It is to be noted that due to tiny vibrations caused by external sources, the sample inside the vector magnet had to be re-centred after every 20-30 measurements. Therefore, intensity evolution of the peaks is inconclusive with respect to the crystallographic axes. On the other hand, as shown in panel-B, the extracted peak position  $|q| (I_{\max})|$  has a strong influence from it. This  $|q| (I_{\max})|$  is plotted in panel-B of Fig. 6.4. At the specified temperature,  $|q|$  varies between  $0.086 \text{ nm}^{-1}$  along  $[100]$  till  $0.092 \text{ nm}^{-1}$  along  $[110]$  in a monotonous fashion, as expected according to Eqn. 6.8. Finally the  $|q| (I_{\max})|$  was fitted with Eqn. 6.8 in order to obtain  $|F|$  at this temperature. As shown in Fig. 6.4B,  $F_{\text{AEI}}$  was found to be  $-52.12 \pm 2.5 \text{ meV\AA}^2$ . The uniaxial term in Eqn. 6.8 was fixed with the one obtained at  $T = 50$  K ( $1.61 \pm 0.01 \text{ meV\AA}^2$ ), since we did not observe any significant variation in it as a function of temperature. The same procedure was followed for the remaining temperatures, and the fitted curves are shown in Fig. 6.5A-F. The direct influence of AEI on  $|q| (I_{\max})|$  can be seen clearly in these panels. The resultant  $F_{\text{AEI}}$  from the fittings are shown in panel-B of Fig. 6.5. The constant of anisotropic exchange interaction was found to be  $-1.83 \pm 0.83 \text{ meV\AA}^2$  at 50 K, which monotonically reduces to  $-69.93 \pm 3.43 \text{ meV\AA}^2$  at 14 K. As opposed to *Moody et al.* [128], we did not observe any sign change of  $F_{\text{AEI}}$  as a function of temperature in the pristine  $\text{Cu}_2\text{OSeO}_3$ . The actual sign of the  $F_{\text{AEI}}$  suggests that the helix propagation should be along  $\langle 111 \rangle$ , similar to MnSi. But experimentally it has been shown not to change from  $\langle 100 \rangle$  axes even down to the lowest temperatures [3]. Concomitantly, the cubic anisotropy has been shown to increase rapidly with lowering temperatures [33]. From our results, it is safe to conclude that an increase of the cubic anisotropy is still larger than the change in  $F_{\text{AEI}}$ , such that the helices stay oriented along  $\langle 100 \rangle$ . We believe these results will be highly useful towards better understanding of microscopic hamiltonian in  $\text{Cu}_2\text{OSeO}_3$ , resulting in the LT-SkL phase and TC phase etc.



## 7 Surface Spiral State With Doubled Periodicity: An Open Question

The magnetic skyrmion lattice was first discovered in the archetypal helimagnet MnSi in 2009 [134]. Progressively over the next few years, other chiral cubic hosts such as FeGe [218],  $\text{Fe}_{1-x}\text{Co}_x\text{Si}$  [220], and  $\text{Cu}_2\text{OSeO}_3$  [169] were also found to host a SkL phase (HT-SkL) just below their transition temperature ( $T_c$ ). There was remarkable similarity among their magnetic field vs temperature ( $H - T$ ) phase diagram. Along with the SkL phase just below  $T_c$ , they also showed the same sequence of field-driven transitions, Helical  $\rightarrow$  Conical  $\rightarrow$  Field-polarized state. Although the absolute field values for the phase boundaries of these transitions were unique for each of these magnets ( $H_{c1}$  and  $H_{c2}$ ) [3, 17, 19, 208]. Recently, the magnetic behaviour of the chiral insulating host,  $\text{Cu}_2\text{OSeO}_3$  has been shown to be different compared to the itinerant skyrmion hosts of the  $B20$  family. Together with the familiar HT-SkL phase,  $\text{Cu}_2\text{OSeO}_3$  was found to host a LT-SkL phase (and a tilted conical phase) away from the ferromagnetic transition [33], and only along  $\langle 100 \rangle$  cubic axes. Thus resulting in quite distinct magnetic phase diagrams along  $\langle 100 \rangle$ ,  $\langle 110 \rangle$ , and  $\langle 111 \rangle$  crystallographic axes (see Fig. 5.2). This LT-SkL phase does not require any thermal Gaussian fluctuations in order to be stabilized. Instead, the formation and stabilization of this isolated SkL phase is a consequence of temperature induced increase in the magneto-crystalline anisotropy of this system [63]. Thus one needs to re-examine these magnetic phases more thoroughly, in order to uncover any novel mechanisms in this material.

### 7.1 Description Of The High-resolution $r$ -REXS Experiments

Motivated by this argument, we utilized high resolution resonant elastic x-ray scattering (REXS) experiments to revisit various magnetic phases and their transformation to each other. The experiment was performed at BL-29 Boreas at the ALBA synchrotron facility in Barcelona. Unlike chapter 6, here we employed REXS in reflection geometry ( $r$ -REXS). Recently,  $r$ -REXS has been proved to be a suitable probe to uncover subtle features in  $\text{Cu}_2\text{OSeO}_3$  [31, 221, 222, 223, 224]. The surface sensitivity of  $r$ -REXS provides us with an added layer of information, which remains invisible to other scattering probes, such as SANS. As calculated by van der Laan *et al.*, the penetration depth of x-rays at the resonant edge is about 100 nm in  $\text{Cu}_2\text{OSeO}_3$  [198].

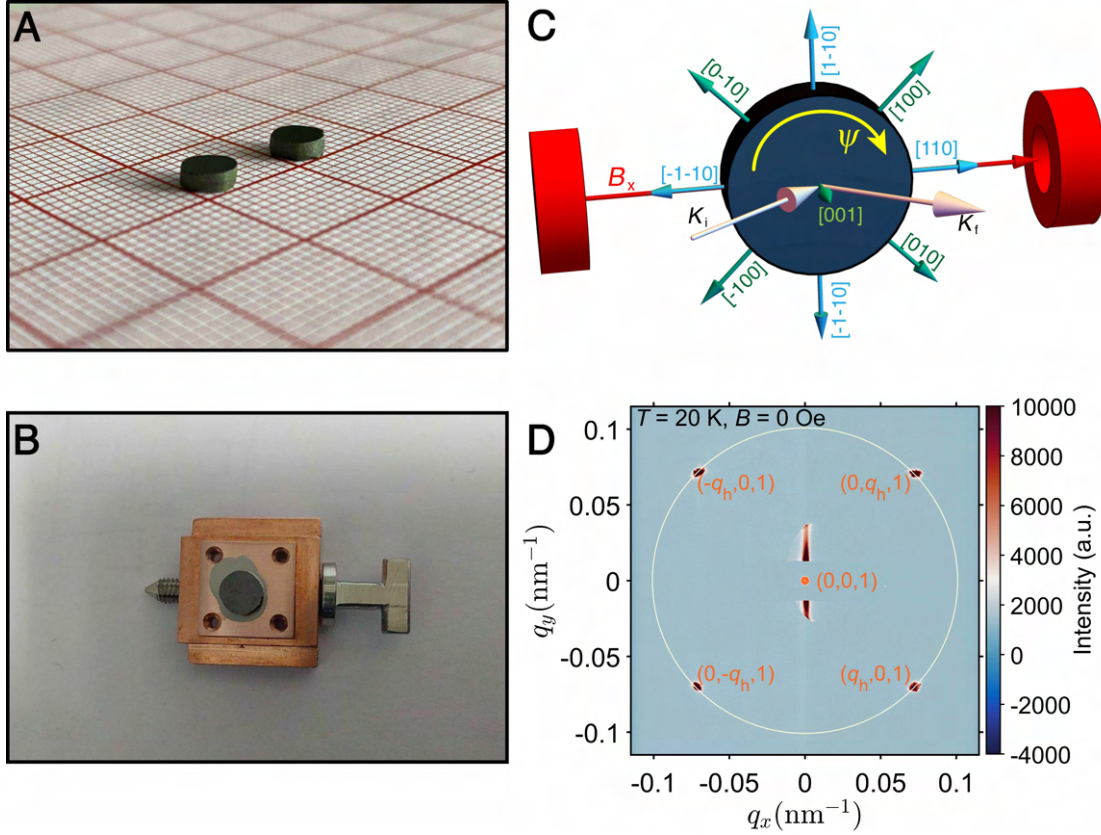


**Figure 7.1: Setup of the *r*-REXS experiment at BL29 BOREAS.** (A) Optical image of the disk-shaped  $\text{Cu}_2\text{OSeO}_3$  single crystal used for the experiments. The single crystal was grown by CVT technique, oriented along  $[001]$  and finally cut into two disks as shown in the picture. One flat facet of each disk was mirror-polished with  $\leq 5$  nm surface roughness. One of these two disks was mounted on a sample holder, as shown in (B). (C) Shows the experimental scattering geometry used at BL-29 Boreas for our experiment. Since the disk sample was oriented with  $[001]$  out of the plane, an in-plane azimuthal rotation provided us access to the remaining two  $\langle 100 \rangle$  domains along with two  $\langle 110 \rangle$  domains. The incident angle was kept constant at about  $48^\circ$ . (D) Sample was cooled down to 20 K and scattering pattern was recorded without applying any field. Four orthogonal spots on the detector plane show up as a result of the two propagating helices along the two in-plane  $\langle 100 \rangle$  domains.

This makes *r*-REXS a truly surface sensitive technique. Only the  $(0,0,1)$  structural peak of  $\text{Cu}_2\text{OSeO}_3$  is accessible by *r*-REXS under resonant Cu- $L_3$  edge, at  $\theta - 2\theta \approx 48\text{-}96^\circ$ . For the experimental part, one single crystal grown by the CVT technique was oriented with  $[001]$  being surface-normal to the flat side (see Fig. 7.1A). In order to minimize demagnetization effects, this single crystal was cut into two disk shaped smaller crystals, and mechanically polished in order to remove any parasitic surface layer. One of the two disk-shaped samples was mounted on an azimuthally-rotatable sample holder (shown in Fig. 7.1B). With  $[001]$  out of the sample plane, we have access to remaining two  $\langle 100 \rangle$ s and two  $\langle 110 \rangle$ s in the sample plane, as shown in Fig. 7.1C. The sample was cooled down to base temperature ( $\sim 18$  K) in a



## 7.1. Description Of The High-resolution $r$ -REXS Experiments

cryomagnet, capable of producing a maximum 1.5 T in-plane magnetic field. At zero magnetic field below  $T_c$ , with our experimental geometry, two helical domains lie within the sample plane, locked along [010] and [100]. The resultant magnetic scattering shows up as four clear Bragg peaks on the detector plane, as shown in Fig. 7.1D. The corresponding azimuthal angle ( $\psi$ ) is set to be zero for this orientation (along [110]).

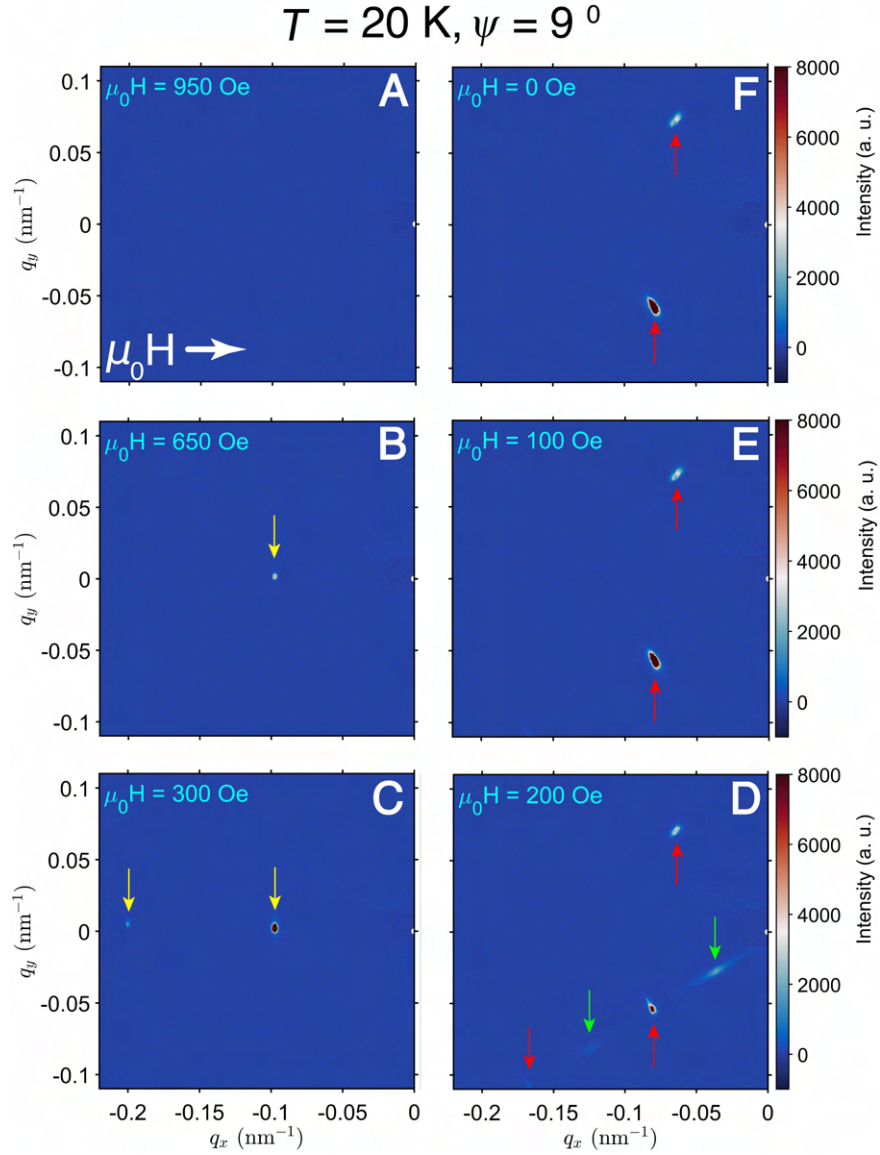


**Figure 7.2: Observation of SS-state in a field-driven sequence.** Detector image showing results of magnetic field scan. The applied in-plane magnetic field has been indicated in corresponding panels. Note that SS-state was observed *only* while ramping the magnetic field down to zero, from saturation. The angle  $\psi$  is tilted away from [110] direction by 9 degrees. Yellow, green, and red arrows point towards incommensurate Bragg peaks corresponding to conical state, SS-state, and helical state, respectively. Note the shift of beam centre to the edge of the detector.



## 7.2 Results And Discussions

Figure 7.2 shows results of the standard field-driven sequence at  $T = 20$  K. The sample was azimuthally rotated about  $9^\circ$  with respect to  $\psi = 0$ . With strong enough magnetic field (around 1000 Oe),  $\text{Cu}_2\text{OSeO}_3$  remains in a forced ferrimagnetic state, resulting in only magnetic scattering intensity at the commensurate  $q$  positions. But with magnetic field being ramped down, the system enters conical phase, with propagation direction locked along the external magnetic field. The scattering from the conical phase shows up as two horizontal spots on the detector. But since we cover only half of the 2D reciprocal space, we have access to only one Bragg peak (Fig. 7.2B). With further lowering of the magnetic field, we observe higher harmonic signal from the conical phase, quite possibly due to elliptic distortion, as shown in Panel-C of Fig. 7.2. As the magnetic field is decreased further towards zero, around 200 Oe, we observe the appearance of a new Bragg reflection at  $q_h/2$  along with its higher harmonic (see Fig. 7.2D). Finally, with lowering the magnetic field to zero, we re-enter helical phase with two domains oriented along the in-plane  $\langle 100 \rangle$  axes.

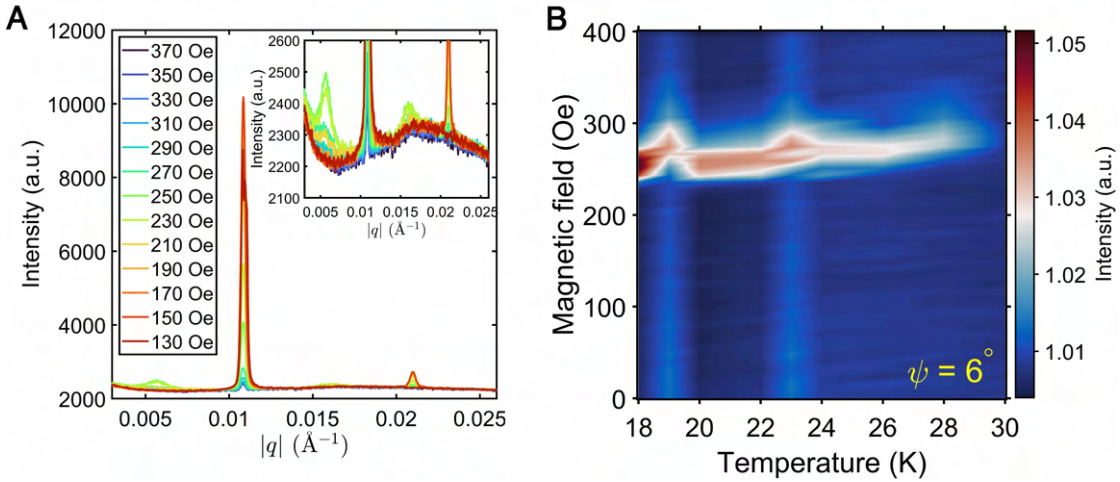


**Figure 7.3:  $H - T$  phase diagram of the surface spiral state.** A. Magnetic field dependency of both  $q$  and  $q/2$  peaks. The field was always applied in horizontal direction. B. Temperature and magnetic field dependent phase diagram constructed for a single azimuthal angle,  $\psi = 6^\circ$ .

The intensity evolution for all satellites as a function of magnetic field is shown in panel-A of Fig. 7.3. We also found similar absorption due to both  $q/2$  and  $q$  peaks. The broad Bragg peak from this new phase points towards this surface spiral state (SSS) being manifested in only few of the top sample layers. Through more detailed investigations, we uncovered the entire regime of stability for the SSS. We found that this new state existed only below  $T = 30$  K, and in a  $\sim 50$  Oe magnetic field window. The state could also survive  $\pm 5^\circ$  of azimuthal rotation around  $\psi = 0$ . From the data at hand, we propose the following explanations for the observation of the SSS.

A mechanism similar to the tilted spiral stabilization may also account for of the new metastable surface spiral state with the doubled period. Indeed, its emergence only for a narrow angular

range of  $\psi$  suggests that the balance between cubic and exchange anisotropies is required to achieve the stability of the state. However, the reason why the spiral pitch is doubled remains unclear at present. In principle, the helical state in cubic chiral magnets is well described by the Bak-Jensen model that determines the spiral periodicity  $\lambda = \mathbb{J}/\mathbb{D}$  as the main term, and the AEI responsible for the small anisotropic corrections, as discussed in the previous chapter. Hence, the doubling of the helical pitch at the surface is unexpected within this phenomenological model. Moreover, the phase is clearly different from the three-dimensional surface spirals (also called stacked spirals) that have been predicted by *Rybakov et al.* [162] and recently observed in FeGe thin plate [190]. Due to its anisotropic nature, and exact  $2\lambda$  periodicity, the SSS is clearly different compared to the stacked spirals. The theoretical and experimentally measured periods of these stacked spirals  $\lambda_{ss}$  are field-dependent and have a period of  $1.1\lambda \leq \lambda_{ss} \leq 1.8\lambda$ .

Interestingly, the surface spiral state did not show up in the  $t$ -REXS experiment (discussed in Chapter 6). Two possible reasons can be considered. Firstly, this state is clearly metastable and might be easily destroyed by the tensile strain observed in the lamella. Another possibility is that the state requires co-existence of three helical domains, one of which has a wavevector parallel to the out-of-plane [001] axis. Stability of this helical (conical) domain is suppressed in a thin plate sample [162, 195]. At present these two scenarios cannot be distinguished and require a separate study of a strain-free  $\text{Cu}_2\text{OSeO}_3$  lamella.

Emergence of the new surface state challenges existing theories of cubic chiral magnets and calls for further theoretical and experimental efforts to understand the complex landscape of magnetic interactions in  $\text{Cu}_2\text{OSeO}_3$ . AEI should not be neglected when considering complex magnetic behaviour of other chiral magnets beyond symmetric exchange, DMI, and cubic anisotropy. For example, it may be involved to explain the low-temperature helical pitch and SkL shortening and deformation in Co-Zn-Mn alloys [96, 155, 192] and emergence of the enigmatic low- $T$   $B$ -phase in MnSi [141].



# Higher Order Spin Texture In A **Part III** Complex Cubic Magnet



## 8 $\text{Co}_5\text{TeO}_8$ : Structural Complexity Meets Topology

The Dzyaloshinskii-Moriya interaction (DMI) has been the key ingredient in the formation of the helical ground state, and thus the skyrmion lattice phase of chiral magnets. In the DMI-stabilized magnets, the typical helix pitch length varies as the ratio between ferromagnetic exchange and DM vector. This signifies the consequences of lattice symmetry on the macroscopic magnetic properties. One of the best examples of this is the  $\beta$ -Mn type chiral cubic structure (belongs to either  $P4_132$  or  $P4_332$  space group) [186], which shows a diverse class of magnetic orders such as helix [73], skyrmion lattice [94, 131], spin glass [145], even magnetism without long range order [176], mainly dependent on the variation of Mn content within the unit cell. In this chapter, we outline the complex incommensurate magnetism of one such compound,  $\text{Co}_5\text{TeO}_8$ , by combining static magnetization, dynamic AC susceptibility with wide angle neutron diffraction as well as small angle neutron scattering measurements. We also propose a stabilization mechanism for the participating magnetic phases, through detailed *ab initio* calculations based on quantum chemistry principles.

### 8.1 Topological Hedgehog Magnetic Structures

The Bak-Jensen model correctly predicts the similar phase diagram for the skyrmion hosting  $B20$  magnets together with  $\text{Cu}_2\text{OSeO}_3$ , even for substituted systems such as  $\text{Mn}_{1-x}\text{Fe}_x\text{Si}$  and  $\text{Fe}_{1-x}\text{Co}_x\text{Si}$ . But with substituting Si with Ge in MnSi, dramatic changes in the phase diagram are observed (see Fig. 8.1E). First of these being the gradual increase in the transition temperature ( $T_N$ ). In the crystal lattice, when Ge replaces Si, the interatomic distances increase. Thus in the Stoner criterion, this leads to reduction of transfer integral and finally bandwidth, resulting in a higher  $T_N$ . In fact,  $T_N$  changes by more than a factor of five between the two extreme members of the family (MnSi:  $\sim 30$  K, and MnGe:  $\sim 170$  K). Second is the change in magnetic spin texture with Ge substitution. The parent system, MnSi hosts helical ground state along with a skyrmion lattice (SkL) phase, as shown in Fig. 8.1E. But with gradual Ge substitution, we observe three critical concentration ranges. For  $0 \leq x \leq 0.35$ , the typical helical+SkL phases, while at the other extreme end, that is for  $0.7 \leq x \leq 1$ , the cubic triple- $q$  hedgehog lattice (Fig. 8.1C) is formed as the zero field state. In the intermediate Ge concentration, that

is when  $0.35 < x < 0.7$ , a tetrahedral quadrupole- $q$  state (shown in Fig. 8.1D) is formed at zero magnetic field. Third, while looking at the phase diagram shown in Fig. 8.1E, one does not fail to notice the increased magnetic field strength required for the ferromagnetic transition, with Ge substitution. As evidenced from Fig. 8.1F, the magnetic phase diagram consists of only one transition, that is unwinding of a hedgehog lattice into a forced field-polarized state. Thus the phase boundaries shown in Fig. 8.1E directly estimates the energy scale required for untwisting either of the two hedgehog lattices into a ferromagnetic phase. These magnetic point defects serve as singularities in the continuum field of magnetization distribution, effectively acting as monopoles and anti-monopoles.

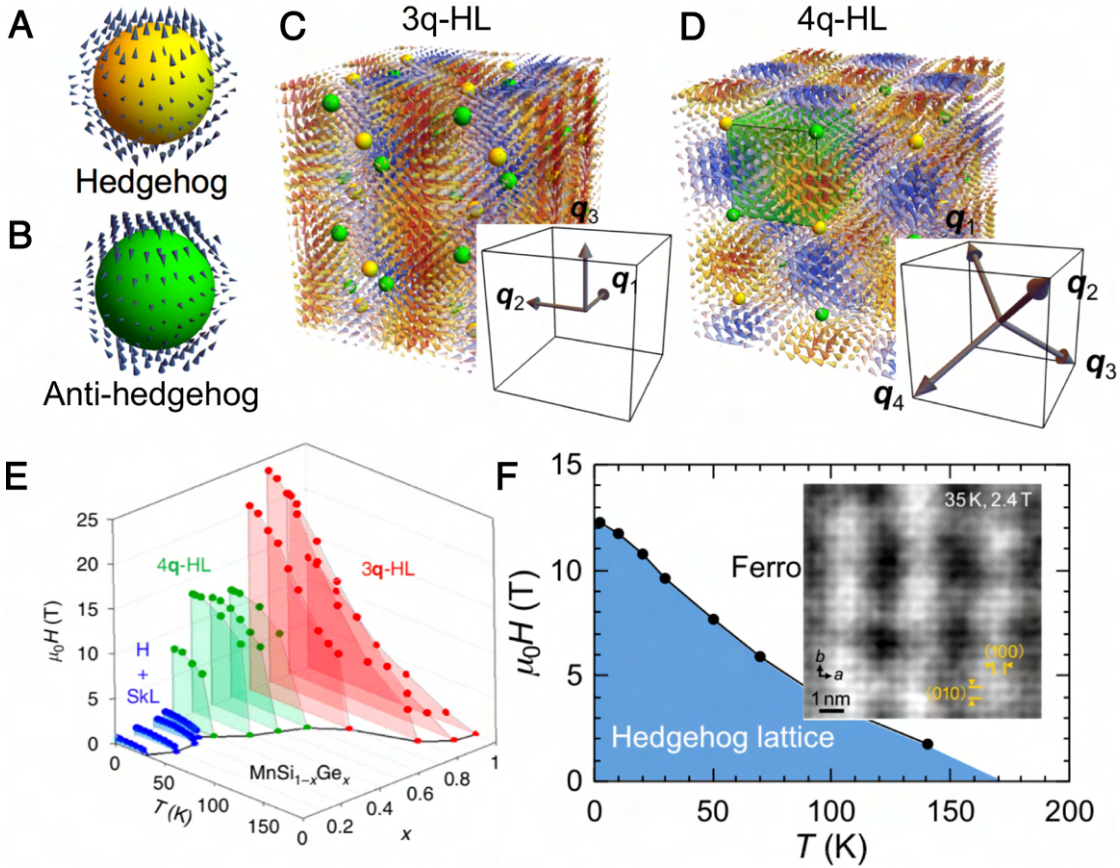


**Figure 8.1: Cubic and tetrahedral hedgehog lattice in  $\text{MnSi}_{1-x}\text{Ge}_x$ .** Magnetization configuration of (A) hedgehog and (B) anti-hedgehog. A magnetic configuration consisting of hedgehogs and anti-hedgehogs for (C) cubic 3- $q$  and (D) tetrahedral 4- $q$  spin structure. (E) shows the boundaries between incommensurate phases and field-polarized state in various compositions of  $\text{MnSi}_{1-x}\text{Ge}_x$  solid solution. (F) shows the phase diagram for  $\text{MnGe}$ . The inset shows Lorentz transmission electron microscopy (LTEM) image for the cubic 3- $q$  hedgehog lattice. The three-dimensional spin structure while projected onto a two-dimensional plane, produces the observed square contrast pattern. This figure is adapted from Ref. [187].

The topological nature of the 4- $q$  as well as the 3- $q$  hedgehog lattice is evidenced by the finite topological Hall signal observed in the electrical transport measurements [54]. The unwinding



of the topologically non-trivial hedgehog lattice into topologically trivial ferromagnetic phase involves annihilation of hedgehog–antihedgehog pairs. This highly non-trivial phase transition aptly results in gigantic responses in various experimental probes [53, 54, 87, 88, 103]. The origin of these responses are ascribed to critical fluctuations of the underlying hedgehog lattices [78, 79, 80, 225, 226]. Since the strength of DMI in this material is almost comparable to other  $B20$  materials, the appearance of small period helices is not supported by the DMI-based theoretical description applicable for other  $B20$  materials [55, 106]. Thus, in order to account for the short period magnetic texture, various other theoretical approaches have been proposed, such as a frustration mechanism [214], a biquadratic interaction based on the Ruderman-Kittel-Kasuya-Yosida (RKKY) interaction [143], as well as the topological-chiral interaction [61]. Since both the  $3-q$  and the  $4-q$  topological phases appear for different concentrations of Ge in  $\text{MnSi}_{1-x}\text{Ge}_x$  series, one requires external pressure to achieve the topological transition among them. As will be shown towards the end of this chapter, in  $\text{Co}_5\text{TeO}_8$ , this topological phase transition can be achieved rather trivially, paving the path for novel data storage devices.

## 8.2 Micro Crystal Synthesis And Characterizations

*Solid State Synthesis Route:* The synthesis approach for  $\text{Co}_5\text{TeO}_8$  was two-fold. In the first step, pure phase polycrystalline sample was synthesized using conventional solid-state reactions. Stoichiometric amounts of  $\text{CoCO}_3$  (Aldrich, 99.999%) and  $\text{TeO}_2$  (Aldrich, 99.999%) were thoroughly mixed using a mortar. The resultant mixture was transferred to a platinum crucible and placed inside a high-temperature muffle furnace. The temperature of the furnace was slowly raised to  $1000^\circ\text{C}$  at a rate of  $100^\circ\text{C}$  per hour. The furnace was then dwelled for an hour at that temperature. Then the furnace temperature was increased to  $1100^\circ\text{C}$  at slower rate of  $50^\circ\text{C}$  per hour. The powder was then sintered at this temperature for about 3 days, followed by quenching to room temperature. The quenching process was necessary to avoid co-crystallization of  $\text{Co}_3\text{O}_4$  spinel. Powder XRD pattern collected at room temperature confirmed the resultant product to be pure phase  $\text{Co}_5\text{TeO}_8$ . This whole process is sketched in panel-A of Fig. 8.2. The SEM image shown in Fig. 8.2B confirms the  $\text{Co}_5\text{TeO}_8$  micro crystals to have mostly octahedral morphology, with clear triangular facets along  $[111]$ . The typical size of these crystals was found to be around  $10\text{-}15\ \mu\text{m}$ .

In the second step, larger single crystal growth of  $\text{Co}_5\text{TeO}_8$  was attempted several times using various synthetic routes. For the chemical vapor transport (CVT) growth,  $1\text{-}2\ \text{g}$  of polycrystalline sample prepared in the previous step was used as the source material. Various transport agents, such as  $\text{HCl}$ ,  $\text{Cl}_2$ , and  $\text{HBr}$  were tried. No reaction was found to take place between the reactant and the transport agents. The reaction of Co with quartz also presented a huge challenge during the growth. The flux method was also employed to try the growth as well. About  $1\ \text{g}$  of  $\text{Co}_5\text{TeO}_8$  polycrystalline sample was taken in an alumina crucible and mixed with either  $\text{CoCl}_2 \cdot 6\text{H}_2\text{O}$ ,  $\text{CaCO}_3$ , or  $\text{Co}(\text{NO}_3)_3 \cdot 6\text{H}_2\text{O}$  thoroughly before trying the flux growth method. All the trials resulted in co-crystallization of either  $\text{Co}_3\text{O}_4$ , or  $\text{CoO}$ , or  $\text{Co}_3\text{TeO}_6$  or

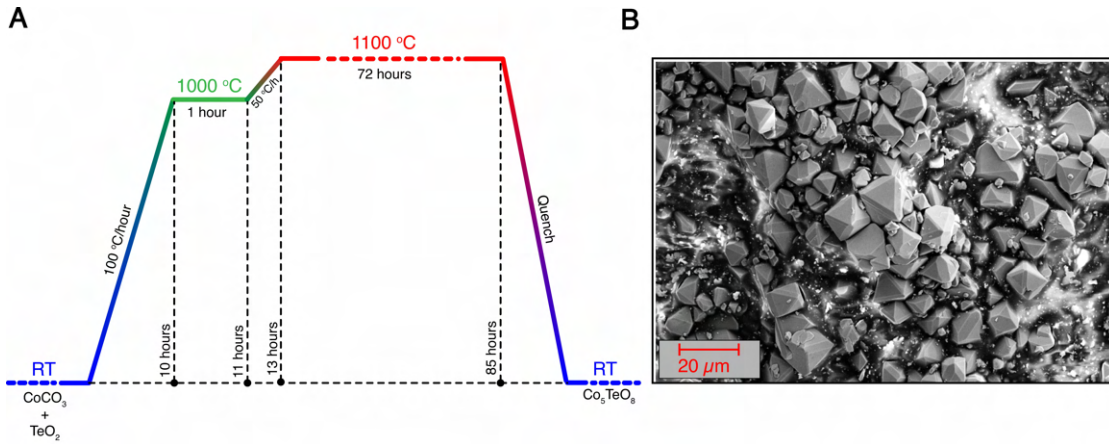


**Figure 8.2: Solid state synthesis of  $\text{Co}_5\text{TeO}_8$ .** (A) Temperature-time schematic diagram showing the synthesis method employed for the preparation of  $\text{Co}_5\text{TeO}_8$  polycrystalline sample. A muffle furnace was used for this purpose. (B) SEM micrograph showing highly faceted well-crystalline  $\text{Co}_5\text{TeO}_8$  particles.

$\text{Co}_2\text{Te}_3\text{O}_8$  or a combination of two or more. Growths were also tried in inert atmosphere as well as under flowing  $\text{N}_2$ , or  $\text{O}_2$  gases. All of the above mentioned methods did not succeed in producing larger single crystal of  $\text{Co}_5\text{TeO}_8$ . As it will be shown later part of this thesis (Section 8.6), conclusive results from neutron scattering experiments can be obtained using the polycrystalline sample.

*Single crystal & Powder x-ray diffraction:* Single crystal XRD measurement was performed on one grain of  $\text{Co}_5\text{TeO}_8$  with an approximate size of  $15\mu\text{m}$ . The resultant reciprocal space maps for  $\ell=0$  and  $\ell=1$  are shown in panel-A and B of Fig. 8.3. Appearance of the forbidden (001) reflection is due to the anomalous Templeton scattering, since the data was collected over a period of 13 hours. For reference, frame acquisition for  $\sim 10\text{mins}$ , gives decent refinement results. Rietveld refinement was performed on a polycrystalline sample, and the lattice parameters as well as atomic coordinates match quite well with the single crystal data (see Panel-C of Fig. 8.3).

Atoms	$x$	$y$	$z$	Occupancy	U	Wyckoff site
Co1	0.50027	0.50027	0.50027	1.00	0.016	8c
Co2	0.38622	0.13622	0.37500	1.00	0.016	12d
Te	0.12500	0.12500	0.12500	1.00	0.015	4a
O1	0.37120	0.37120	0.37120	1.00	0.017	8c
O2	0.11630	-0.10130	0.12310	1.00	0.017	24e

**Table 8.1:** Atomic site information for  $\text{Co}_5\text{TeO}_8$ , as obtained from single crystal x-ray diffraction experiments.

The crystallographic structure of  $\text{Co}_5\text{TeO}_8$  is shown in panel-D of Fig. 8.3. There exists two inequivalent Co-sites at 8c and 12d positions, which with neighbouring oxygen atoms, form

tetrahedra and octahedra, respectively. Te atoms exist at the 4a sites with octahedrally coordinated environment. A summary of the unit cell information is provided in Table 8.1.

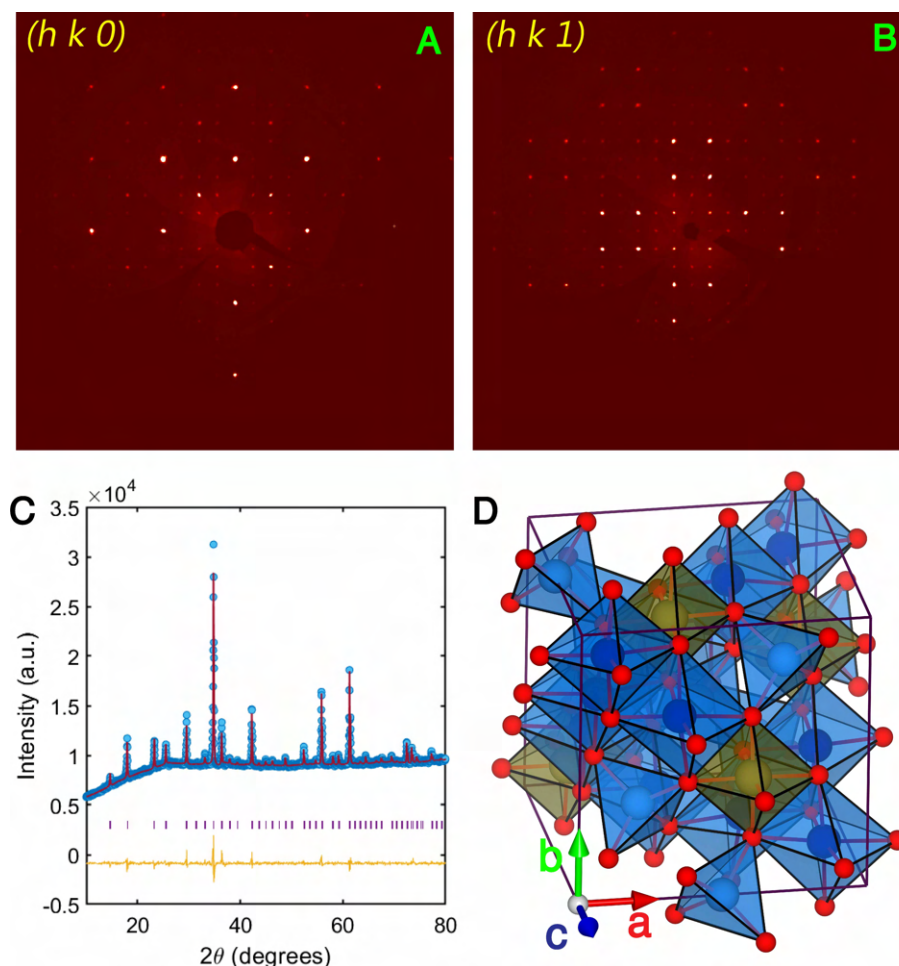


**Figure 8.3: XRD analysis of  $\text{Co}_5\text{TeO}_8$ .** (A) and (B) show reciprocal space map of  $\text{Co}_5\text{TeO}_8$  obtained from the single crystal x-ray diffraction experiment. (C) Rietveld refinement results of the powder x-ray diffraction pattern from the polycrystalline sample. (D) The crystal structure of  $\text{Co}_5\text{TeO}_8$  visualized with VESTA [127].

In order to determine the Co oxidation state more precisely, we performed Electron energy loss spectroscopy (EELS) on a thin plate (similar to the one shown in Panel-B of Fig. 6.1, with thickness  $\sim 150$  nm) cut from a single crystal  $\text{Co}_5\text{TeO}_8$  using FIB milling (not shown here). We used incident energy from below  $L_3$  till above  $L_2$ . Several line scans were performed on a  $8 \times 5 \mu\text{m}^2$  area. Our results showed that the oxidation state of Co was found to be 2+ throughout the thin plate.

### 8.3 Magnetic Phase Diagram Construction Through Magnetization & Susceptibility Measurements

Following the structural analysis, the magnetic properties of  $\text{Co}_5\text{TeO}_8$  were measured. DC magnetization as well as AC susceptibility measurements were performed using the VSM and ACMS-II option of a commercial Quantum Design (QD) 14T Physical Property Measurement System (PPMS). The polycrystalline sample was enclosed in a standard polypropylene holder provided by QD. The results from our extensive characterizations will be discussed as follows: we will first show the magnetization measurements performed as a function of temperature, followed by the ones as a function of magnetic field. Finally the complementary results from AC susceptibility temperature scans will be presented.

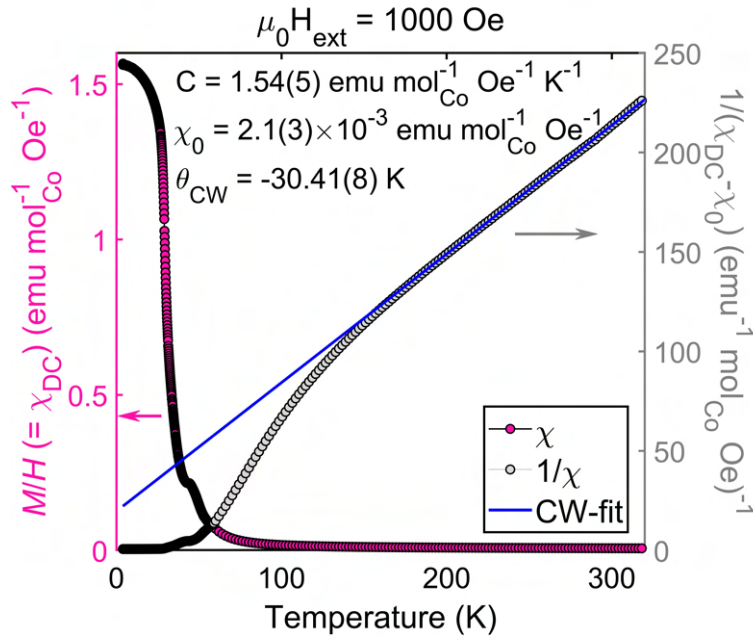


**Figure 8.4: Static magnetization of  $\text{Co}_5\text{TeO}_8$  at a constant applied magnetic field.** DC magnetization measured for  $\text{Co}_5\text{TeO}_8$  sample in presence of 1000 Oe external magnetic field. The inverse of  $\chi_{\text{DC}}$  was fitted with Curie-Weiss law between 180 K and 310 K. In order to have a more reliable results, the fitting range was varied within  $\pm 10$  K.

Temperature dependent magnetization measurements were carried out for  $\text{Co}_5\text{TeO}_8$  in a wide range, between 320 K and 5 K. As shown in Fig. 8.4, with an appearance of a tiny kink, a magnetic transition is observed around 45 K. Below this temperature, the moment value increases sharply, before attaining a maximum value of about  $\sim 1.6 \text{ emu mol}_{\text{Co}}^{-1} \text{ Oe}^{-1}$  at 5 K. Above the transition temperature ( $T_N$ ), the magnetic moment value decreases monotonically with increasing temperature. In order to gain further insight into the intrinsic magnetism of  $\text{Co}_5\text{TeO}_8$ , data obtained above  $T_N$ , deep inside the paramagnetic phase was fitted with a Curie-Weiss function. The Curie-Weiss temperature was obtained to be  $-30.41(8)$  K, which suggests a antiferromagnetic type dominant magnetic interaction in this system. From the

### 8.3. Magnetic Phase Diagram Construction Through Magnetization & Susceptibility Measurements

observed Curie constant, we estimate the effective moment to be  $3.51 \mu_B/\text{Co}$ , which is lower than the spin-only value of  $3.87 \mu_B/\text{Co}$  for  $\text{Co}^{2+}$ .

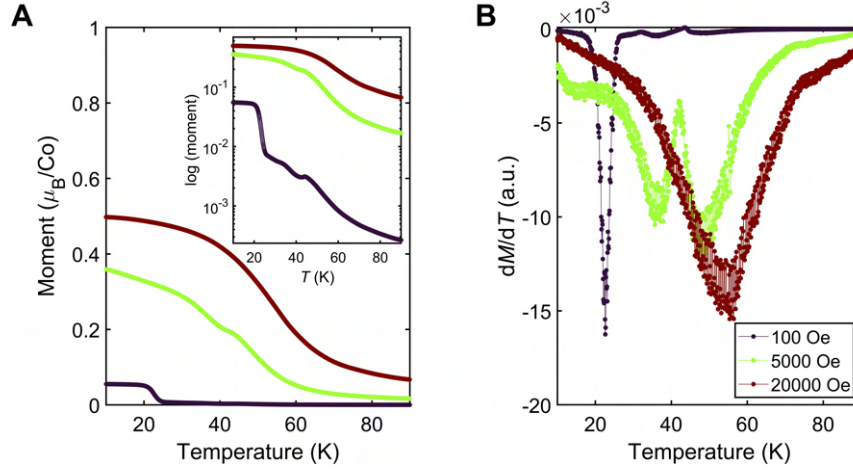


**Figure 8.5: Subtle variations in the temperature induced transitions in  $\text{Co}_5\text{TeO}_8$  for a few selected magnetic fields.** (A) VSM temperature scans for  $\text{Co}_5\text{TeO}_8$  in the presence of three different magnetic fields. The inset highlights the evolution of  $M$  as a function of  $T$  on a logarithmic scale. For the low field measurement, the clear signature of temperature induced transitions can be observed. This is further evidenced by  $dM/dT$ , as shown in panel-B. The sharp transitions at low fields evolve into smeared high-field crossovers.

We now illustrate the temperature dependent magnetization behaviour in a smaller window. As shown in Fig. 8.5, a series of magnetic transitions are observed, as the temperature is lowered from the paramagnetic regime. These transitions which are observed with a 100 Oe applied field, smear out with a higher magnetic field, for example, 5000 Oe. Finally with the application of an even greater magnetic field, 20000 Oe, we see only one dip in the  $dM/dT$  curve. This provides us with the first evidence of complicated magnetism in this system. Also, the magnetism is governed by at least three distinct energy scales which will ultimately determine the magnetic phase diagram.

We now illustrate the effect of gradual changes in the  $M$  vs  $T$  curves for more number of applied magnetic fields. As can be seen clearly, with increasing field strength, the transition observed at around 28 K, shifts towards higher temperatures. This is corroborated by the  $dM/dT$  curves as well. Concomitantly, the shoulder seen between 30-35 K flattens out, leading to complete suppression of it around 1500 Oe. Whereas the cusp marking the onset of  $T_N$  slowly flattens out while moving towards lower temperatures. Finally when the magnetic field is higher than  $\sim 1$  T,  $T_N$  is observed to move towards higher temperatures. Figure .8.6 highlights all the temperature-dependent transitions which can be tracked by static magnetization measurements.

After the detailed temperature scans with different magnetic field strength, we now turn our attention towards tracking the magnetic field induced phases in  $\text{Co}_5\text{TeO}_8$  below  $T_N$ . As



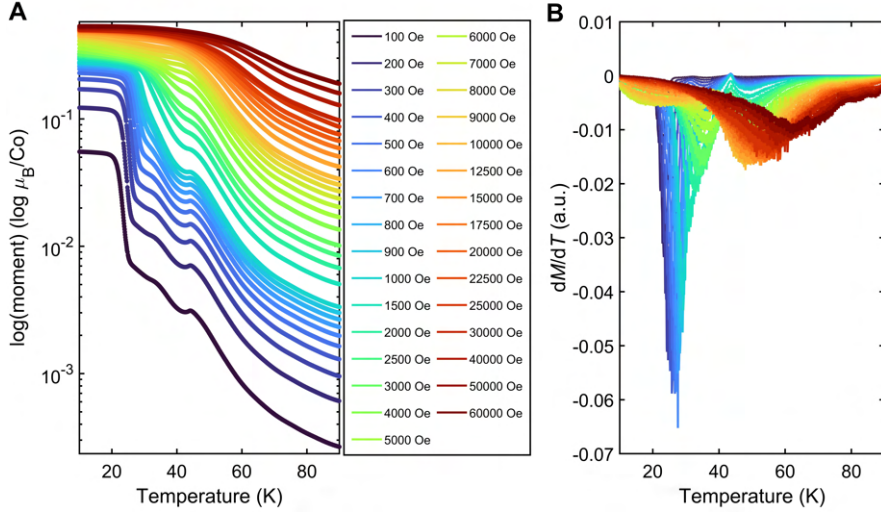


**Figure 8.6: Temperature dependent static magnetization for  $\text{Co}_5\text{TeO}_8$  under various strength of magnetic fields.** The data shown in Fig. 8.5 was extended to many different fields and the resultant temperature scans are shown in panel-A. Systematic changes can be seen in the temperature scans from low to high magnetic fields. Note the logarithmic y-scale. (B) Shows the derivative with respect to temperature, which have been used to construct the magnetic phase diagram later.

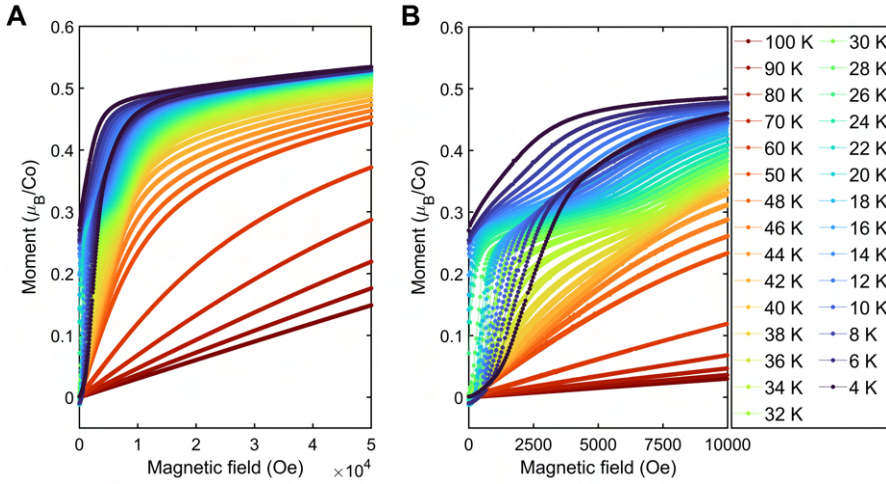


**Figure 8.7: Static isothermal magnetization measured above and below  $T_N$  for  $\text{Co}_5\text{TeO}_8$ .** (A) Shows the evolution of isothermal magnetization as a function of magnetic field. These measurements were performed from well-below till well-above  $T_N$ . (B) Shows the magnified region below 1 T for panel-A. Clear sign of metamagnetic-type transitions are visible, while ramping the magnetic field both up and down direction, with a significant remanent magnetization.

shown in panel-A of Fig. 8.7, above  $T_N$ , deep inside the paramagnetic phase, the  $M$  as a function of  $H$  increases linearly, without developing any features, which is the typical response expected in the paramagnetic phase. Magnetic isotherms at lower temperatures show a



### 8.3. Magnetic Phase Diagram Construction Through Magnetization & Susceptibility Measurements

pronounced hysteresis, with remanent magnetization reaching up to 60% of the high-field value (for example at  $T = 5$  K and  $\mu_0 H = 5$  T). This is shown in panel-B of Fig. 8.7. With lowered temperatures, sharp metamagnetic-type transitions can also be observed.

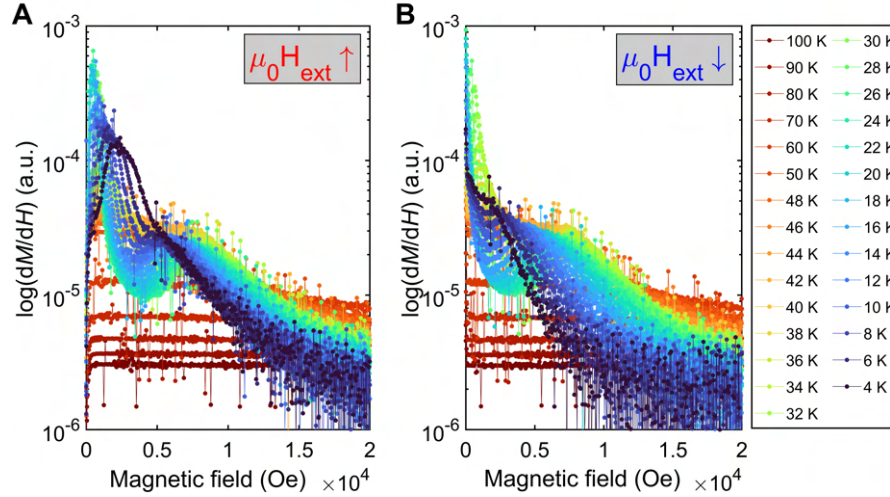


**Figure 8.8:  $dM/dH$  for  $\text{Co}_5\text{TeO}_8$  signalling field-induced metamagnetic-type phase transitions.** Derivative of the isothermal magnetization shown in Fig. 8.7. In order to distinguish between the hysteresis,  $dM/dH$  has been plotted in two different panels. Panel-(A) shows the results while magnetic field was ramped up. Derivative with respect to ramping down magnetic field is shown in panel-(B). In order to highlight the tiny changes in the slope, both panels have been shown in logarithmic scale.

The appearance of metamagnetic-type transitions are crucial from the viewpoint of chiral magnetism [33, 187, 229]. As shown in panel-A and B of Fig. 8.8, a “valley” feature appears in the  $dM/dH$  curves at intermediate temperatures. Analysis of the data collected at higher temperatures confirms the absence of any field-induced phases where the measurements were performed. Magnetic isotherms at temperatures just below  $T_N$ , shows a shoulder-type feature which gradually turns into the “valley” feature, before turning into a broad feature at the lowest temperatures. Magnetic hysteresis is also clearly evident while comparing panel-A and B.

Now we look into the details of magnetic isotherms just below  $T_N$  down to the sharp transition observed in the temperature dependent magnetization data. At  $T = 44$  K, even though the  $M(H)$  curve appears not to host any field-induced metamagnetic phases, the  $dM/dH$  shows a clear appearance of a broad region in magnetic field suggesting clear existence of a second field-induced phase. While we go down in temperature, this flat region slowly starts developing to a more pronounced phase boundaries as can be seen in panel-B of Figure. 8.9. That also suggests a well-stabilized field induced phase where spin reorientation in and out of which could be energetically expensive, for example (but not limited to) a topological phase. The inset shows the analysis performed at  $T = 32$  K. The field-induced phase boundaries extracted at this temperature will be used later in section 8.6.

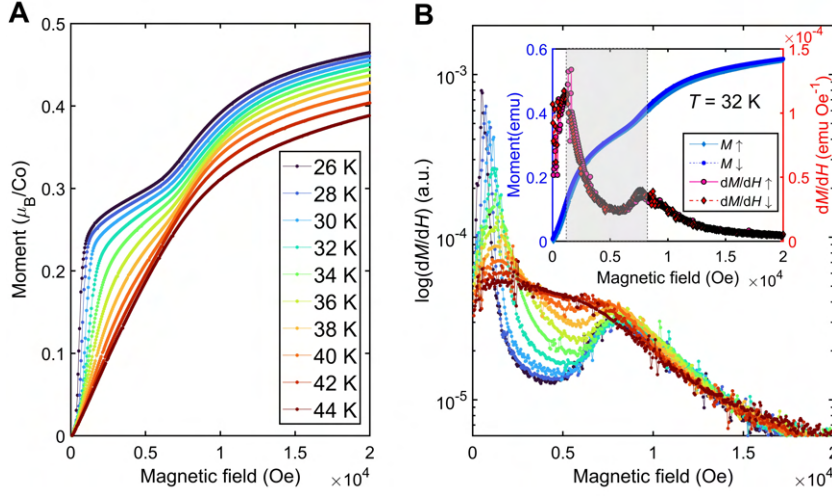


**Figure 8.9: Magnetic field-induced metamagnetic phase transitions at selected temperatures below  $T_N$ .** (A) Measured isothermal magnetization below transition temperature, where clear field-induced magnetic states can be found. The relevance of these temperatures will be discussed in section 8.6. (B) Magnetization derivative with respect to magnetic field outlines the phase boundaries between different metamagnetic phases. In skyrmion hosting cubic helimagnets this “valley” region has been ascribed to the SkL phase. Inset shows the  $M$  as well as the corresponding  $dM/dB$  at  $T = 32$  K. This will be highly relevant in section 8.6, when we try to make a connection with the magnetic spin structure in this chiral host.

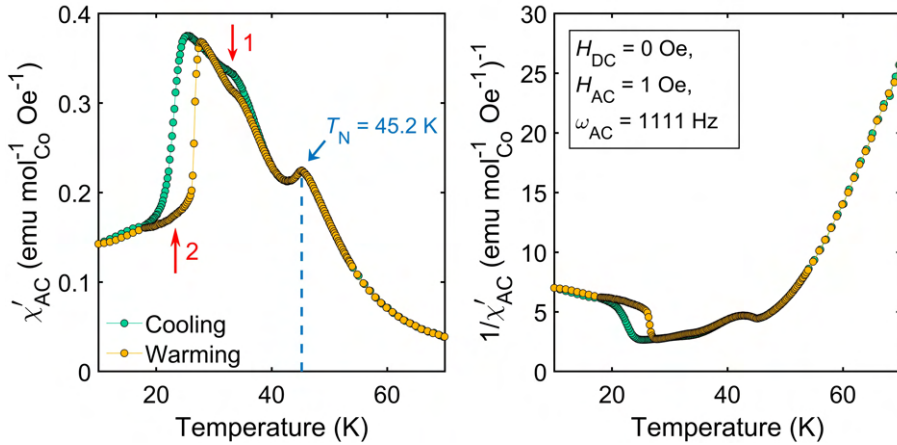


**Figure 8.10: Probing zero-field magnetic transitions in  $\text{Co}_5\text{TeO}_8$  using AC susceptibility measurements.** Temperature-induced transitions in  $\text{Co}_5\text{TeO}_8$  were probed by more sensitive AC susceptibility measurements. In panel-(A), we show the real part of AC magnetic susceptibility ( $\chi'_{AC}$ ) measured under zero-field cooling (ZFC) and zero-field cooled warming (ZFCW) conditions. Both hysteresis regions are properly marked. The inverse  $\chi'$  is shown in panel-(B). As mentioned in this panel, external DC magnetic field was set to be zero for these measurements. While for the AC part, the excitation field and frequency were set to be 1 Oe and 1111 Hz respectively.

### 8.3. Magnetic Phase Diagram Construction Through Magnetization & Susceptibility Measurements

To look into the details of temperature-induced transitions, dynamic AC susceptibility measurements were performed on the same sample.  $H_{AC}$  and  $\omega_{AC}$  were fixed at 1 Oe and 1111 Hz respectively. As compared with the magnetization data, we now see a clear peak in  $\chi'$ . Results of the zero-field cooling and zero-field cooled warming protocols are shown in panel-A of Fig. 8.10. Two hysteresis regions have been marked, which will again have relevance in section 8.6. We also observed practically no observable changes in the frequency dependent  $\chi' - T$  data. This could mean that the characteristic frequency scale for the magnetic texture below  $T_N$  (will be discussed in section 8.6) could be out of the window of AC susceptibility measurements.

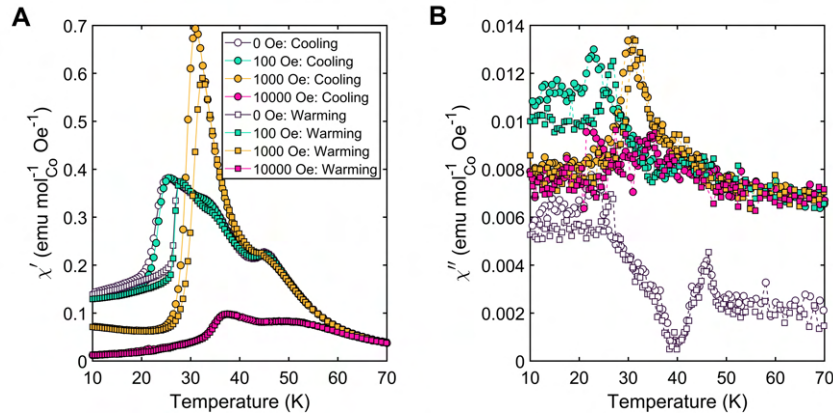


**Figure 8.11: Behaviour of various temperature driven transitions probed by  $\chi_{AC}$ .** AC susceptibility temperature scans were measured for few other applied constant DC magnetic fields. DC fields were chosen such a way that they reflect the complex temperature-driven transitions in the system. Panel-(A) shows the real part of these temperature scans, while imaginary parts are shown together in panel-(B).

$\chi' - T$  scans were performed in presence of fixed external DC magnetic fields and shown in Fig. 8.11. The imaginary part of the 0 Oe scan shows a small yet clear sign of a peak signalling a dissipative transition between the paramagnetic and the ordered phase. Between 0 Oe and 100 Oe, there is practically no difference between the  $\chi' - T$  curves delineating any low lying magnetic phases. But at 1000 Oe, the first hysteresis region has completely vanished while the second hysteresis region has shifted up in the temperature scale. The dissipative nature of this hysteresis region is clear from panel-B of Fig. 8.11. While with 10000 Oe of magnetic field, both transitions have smoothened out without any sign of noticeable hysteresis. These findings corroborate the magnetization results previously obtained and signifies a great agreement between the static and dynamic measurements.

We now discuss the  $\chi' - T$  data for the remaining constant DC magnetic fields. As shown in panel-A of Fig. 8.12, we see a gradual change in the phase boundaries, which is backed up by the derivatives with respect to the temperature ( $dM/dT$ ) shown in Fig. 8.12B. With higher applied constant magnetic fields, the first hysteresis region vanishes, and concomitantly  $\chi'$  acquires a larger value. Such behaviour observed in  $\chi'$  points towards non-trivial response in

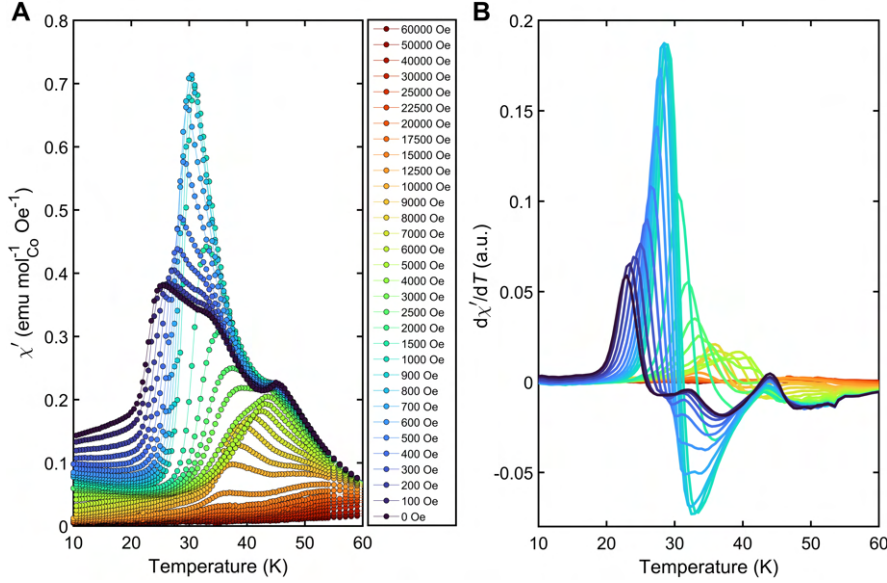


**Figure 8.12: All AC susceptibility temperature scans at different applied DC fields for  $\text{Co}_5\text{TeO}_8$ .** In order to extract the boundaries of participating magnetic phases, AC susceptibility temperature scans were performed in presence of a few constant DC magnetic fields, between 0 Oe and 60000 Oe. The real part of the susceptibility and its corresponding derivative with respect to temperature have been shown in panel-(A) and (B), respectively. For all scans, AC field was fixed at 1 Oe, whereas AC frequency were fixed at 1111 Hz.

the susceptibility measurements while the system enters the low temperature phase directly from the one close to  $T_N$ .

Electrical capacitance data was measured using a custom setup inserted in a Physical Property Measurement System (PPMS). For the experimental part, a pellet was made by pressing the polycrystalline sample and magnetic field dependence of the capacitance was measured below  $T_N$ . As seen from panel-A and B of Fig. 8.13, sharp changes are observed in the magnetic field-dependence of the electrical capacitance data. Only at the lowest temperature ( $T = 10$  K), the capacitance at intermediate magnetic fields is higher compared to the zero-field value. The apparent differences observed in the magnetic field values of  $C(H)$  and  $dM/dH$  values could be a result of demagnetization factor originating from two different geometries employed for both experiments. As shown in Fig. 8.13C, there are two distinct regions in the  $C(H)$  curve, where the capacitance varies linearly with magnetic field. At the highest temperature, the inflection point signifies the change in net capacitance of the magnetic phases. Comparing these capacitance data with the corresponding data from magnetization measurements, a clear signal of the intertwined nature of the magnetic and electric order parameter emerge.

Finally, we combine all our results from static as well as dynamic measurements to formulate the magnetic phase diagram of  $\text{Co}_5\text{TeO}_8$ . This is shown in Figure. 8.14. Note that the boundaries obtained from  $M - T$  data has not been shown in the phase diagram, since most of them

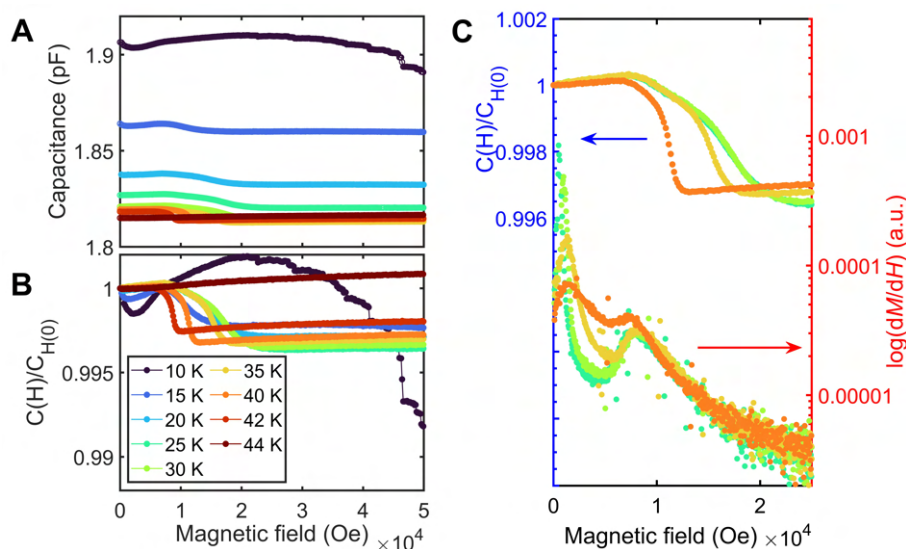


**Figure 8.13: Electrical capacitance as a function of magnetic field for  $\text{Co}_5\text{TeO}_8$ .** Capacitance measurements were performed using a firm pellet made out of polycrystalline  $\text{Co}_5\text{TeO}_8$  sample. The results of magnetic field scans are shown in panel-A. In order to highlight the tiny changes observed in the field scans, all data were normalized with respect to the zero-field value. This is shown in panel-B. The sharp changes observed at specific magnetic field values also coincide with the data obtained from the static magnetization measurements (see Fig. 8.8).

overlap with the ones obtained from  $\chi' - T$  data. The phases have been labelled as unknowns due to the inability of magnetometry methods to correctly identify the real magnetic structure of the phases. For proper identification of these phases, real space probes such as Lorentz TEM (LTEM), or reciprocal space probes such as resonant elastic x-ray scattering (REXS), wide angle neutron diffraction and small angle neutron scattering (SANS) methods can be used. Out of all these probes, SANS is useful only if the magnetic structure of these phase are incommensurate in nature. But from the phase diagram, it is immediately clear that the magnetic energy landscape in  $\text{Co}_5\text{TeO}_8$  is highly non-trivial and would require careful characterization tools in order to be fully resolved.

## 8.4 Heat Capacity Of $\text{Co}_5\text{TeO}_8$

Heat capacity measurements were performed on a robust pellet made out of the polycrystalline  $\text{Co}_5\text{TeO}_8$  sample. The pellet was mounted onto a typical  $3 \times 3 \text{ mm}^2$  sapphire plate. Apiezon N grease was used to make good thermal contact between the sample and the platform. The settings is the same as can be seen in Fig. 5.24A.

First, we performed heat capacity measurements on the  $\text{Co}_5\text{TeO}_8$  pellet without applying any magnetic field. Heat capacity was measured while warming up the sample gradually between 2.1 K and 95 K using the short-pulse protocol. More description about the method can be found in section 5.7. The results from the heat capacity measurements are shown in



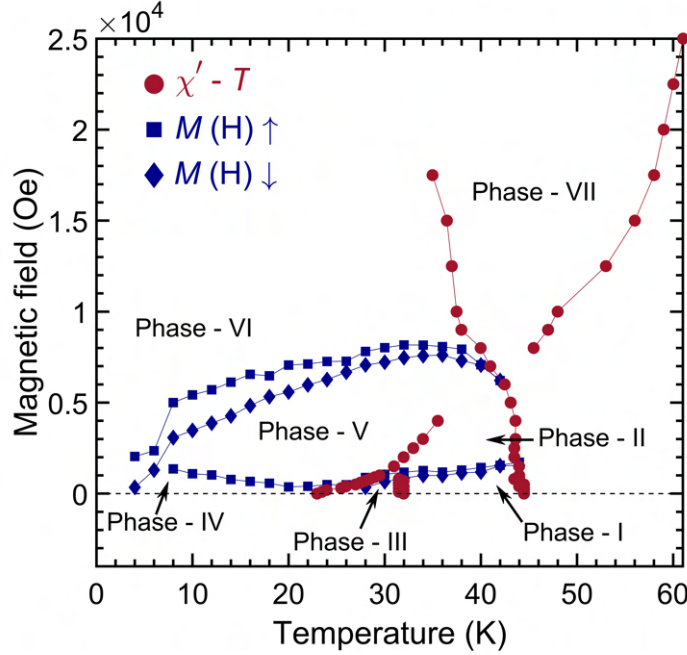


**Figure 8.14: Magnetic phase diagram of  $\text{Co}_5\text{TeO}_8$  as inferred from magnetization and susceptibility measurements.** Magnetic phase diagram of  $\text{Co}_5\text{TeO}_8$  has been constructed using magnetization and susceptibility measurements. The diamond symbols signify the phase boundaries extracted from magnetic field scans while the field was ramped down.

Fig. 8.15. For comparison, zero-field AC susceptibility data is also shown. A small kink in the heat capacity curve is seen at  $T_N$ . There was no signature of a first or second order transition seen at both temperatures marked with dashed lines.

From the low temperature regime ( $T < 20$  K) of  $\text{Co}_5\text{TeO}_8$ , electronic contribution to the heat capacity was extracted using Sommerfeld's relation (shown in Fig. 8.16). The extracted coefficients are typical examples of those obtained from insulating materials. In panel-B of Fig. 8.16, we show the high temperature heat capacity of  $\text{Co}_5\text{TeO}_8$ .  $C_p$  varies linearly over all the measured temperatures. It could be that the material at 100 K is still influenced heavily by the magnetic transition at  $T_N$  and thus not entirely inside the non-linear regime yet.

Next, the magnetic field dependence of  $C_p$  was measured, and the results are shown in Fig. 8.17. Even though both static magnetization and dynamic susceptibility measurements show cascade of transitions, heat capacity measurements do not show any sign of magnetic transitions, neither at  $T_N$ , nor at the second hysteresis region. In fact, with higher magnetic fields, the small kink previously observed at  $T_N$  was smeared. This is shown in panel-B of Fig. 8.17.

Since the short-pulse technique could not produce any of the phase boundaries, we used the long-pulse technique to probe the same. Details about the protocol itself, along with other technical details can be found in section 5.7. Here we applied a 50% heat pulse to probe the



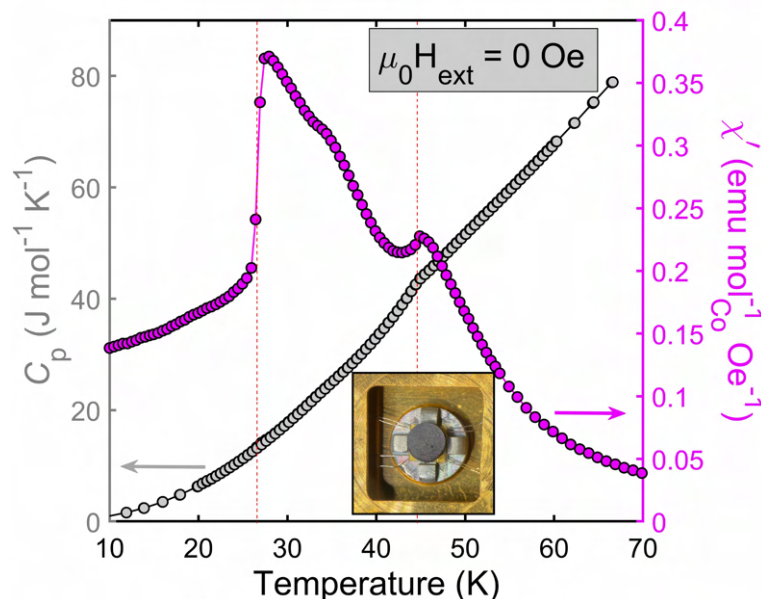


**Figure 8.15: Heat capacity of  $\text{Co}_5\text{TeO}_8$  measured with short heat pulses and zero magnetic field.** Nature of the zero-field phase transitions were also probed by heat capacity measurements. As shown in the inset, a firm pellet was pressed from the polycrystalline sample and mounted on the platform using grease.  $C_p$  vs  $T$  was measured for  $\text{Co}_5\text{TeO}_8$  between 2.1 K and 68 K covering the magnetically ordered regime. For comparison purpose, zero-field AC susceptibility scan, measured under ZFCW condition, is also shown.

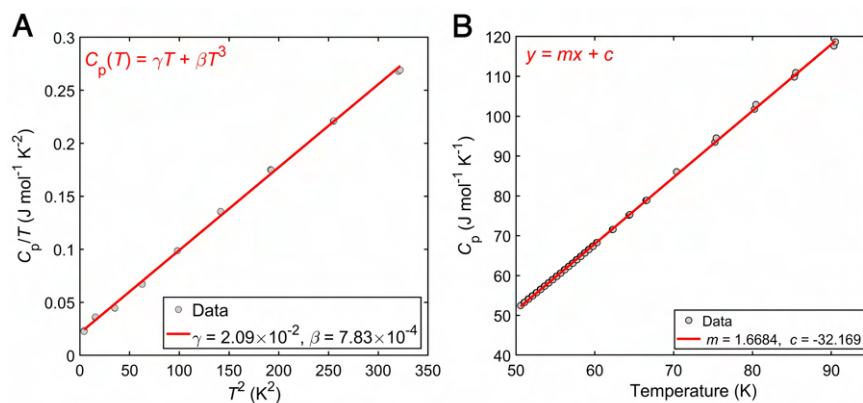


**Figure 8.16: Low temperature thermodynamic quantities of  $\text{Co}_5\text{TeO}_8$ .**  $C_p(T)$  for  $T < 20$  K regime of the zero-field heat capacity measurement (shown in fig. 8.15) was used to extract the Sommerfeld coefficient, as shown in panel-(A). Panel-B highlights the unexpected linearity observed in  $C_p$  till the highest measured temperature of 90 K.

transition regions. The temperature-time evolution of the sample is shown in panel-(A) and (C) of Fig. 8.18. Unlike  $\text{Cu}_2\text{OSeO}_3$ , we still were not able to observe any conclusive signature of a phase transition in this system (see panel-(B) and (D) of Fig. 8.18). We also tried to set the

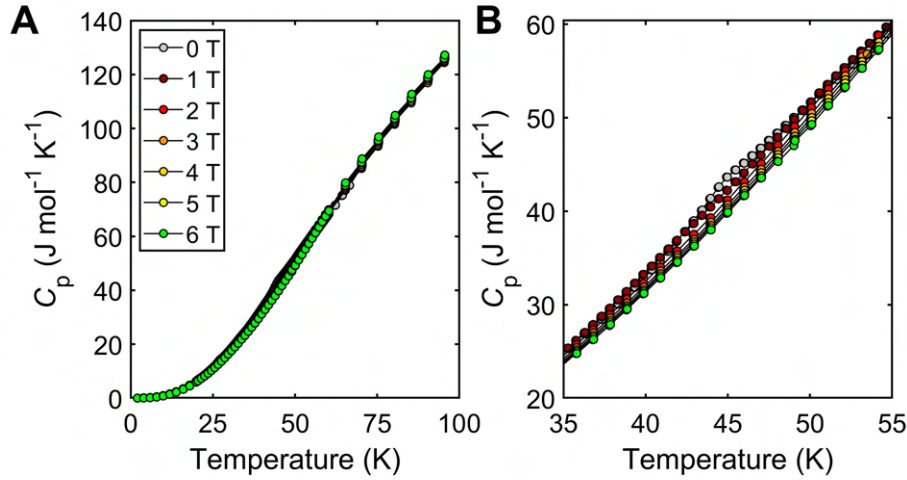


**Figure 8.17:  $\text{Co}_5\text{TeO}_8$  specific heat extracted from short heat pulses for increasing magnetic fields.** After the zero-field heat capacity measurement, finite magnetic field dependent heat capacity measurements were also performed using the same short pulse technique. Panel-(A) shows measured heat capacity, whereas panel-(B) shows the region around  $T_N$  highlighting the absence of any first or second order transitions.

equilibrium temperature close to  $T_N$  and reduce the heat pulse width. But similar outcomes were still obtained. Trying to vary the time constant of the pulse also did not result in anything significantly better.

We also varied the equilibrium sample + platform temperature to check for signatures of phase transitions across the magnetic phase diagram of  $\text{Co}_5\text{TeO}_8$ . As can be seen in Fig. 8.19, even this process did not result in any sharp or smeared peaks.

Finally, we performed heat capacity measurements at various field strengths using the long-pulse technique. The small kink seen at  $T_N$  was slowly smeared out, similar to the one shown in Fig. 8.17. In conclusion, even though there are a number of transitions clearly evident from both static magnetization as well as dynamic susceptibility measurements, we did not observe any signatures of these transitions across the magnetic phase diagram using both the short-pulse as well as the long-pulse technique.

## 8.5 Powder Neutron Diffraction

In order to resolve the zero-field magnetic states of  $\text{Co}_5\text{TeO}_8$  (shown in the complicated phase diagram of Fig. 8.14), powder neutron diffraction measurements were performed at the thermal neutron beamline, HRPT of SINQ, located at PSI. Neutrons of wavelength  $2.45 \text{ \AA}$  were used for all measurements. Since there was no magnetic field applied, goal of the experiment was to resolve the phases labelled as Phase-I, Phase-III and Phase-IV in Fig. 8.14. About 2g of  $\text{Co}_5\text{TeO}_8$  powder was enclosed in a standard vanadium can (as shown in panel-B of Fig. 8.21)

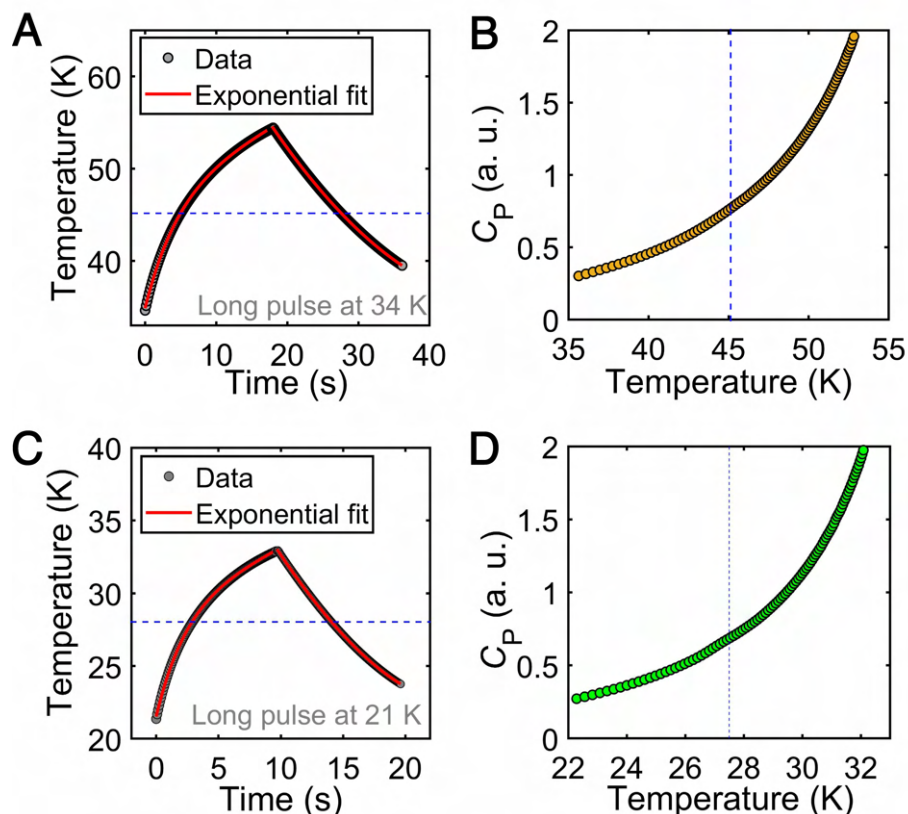
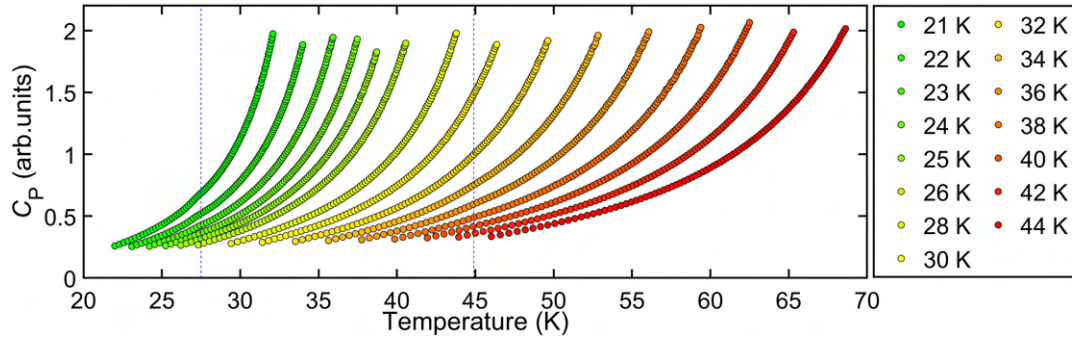


**Figure 8.18: Probing various temperature-driven transitions using long heat pulses.** Long heat pulses were also used in order to check for any sharp  $1^{st}$  order transitions in  $\text{Co}_5\text{TeO}_8$ . Shown in panel-A is the heat pulse which was applied in order to increase the sample temperature by 50 % from the equilibrium temperature of 36 K. The blue line indicates the location of  $T_N$ . Corresponding heat capacity data is shown in panel-(B). Similar measurements were performed in order to check for the nature of the low temperature hysteresis region (as indicated in Fig. 8.10). The results are shown in panel-(C) and (D). The blue line in panel-C stands for the middle of the low temperature hysteresis region.

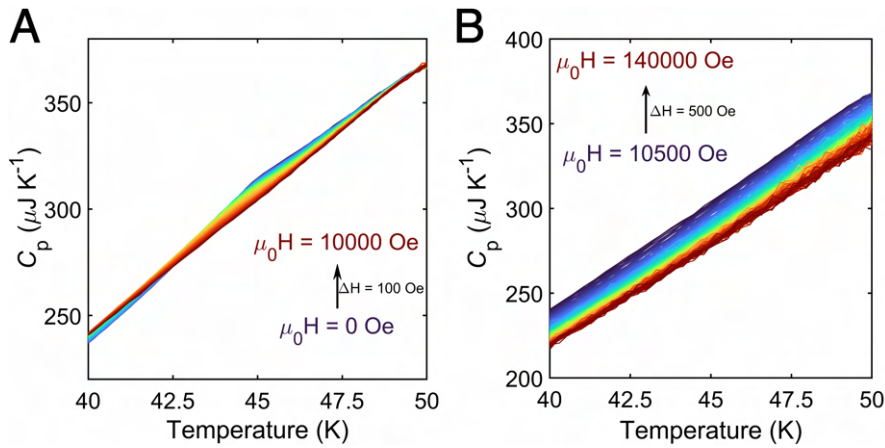
and installed inside a cryostat.

Diffraction data was first collected at  $T = 80$  K in the paramagnetic phase. Similar to the XRD data collected at room temperature, no additional phases were found. This is shown in Panel-A of Fig. 8.21. A comparison has been made with the pattern collected at  $T = 43$  K, just below  $T_N$  (Fig. 8.10). As shown in panel-B of Fig. 8.21, we observe two satellites decorating the  $q = (1,1,1)$  nuclear peak. These peaks are labelled as  $(1,1,1 \pm \delta)$ , where  $\delta$  was found to be  $0.0818 \pm 0.0045 \text{ \AA}^{-1}$ . In real space this would correspond to  $7.68 \pm 0.42 \text{ nm}$ . The temperature dependent variation observed in susceptibility measurements (as shown in Fig. 8.10) are thus attributed to incommensurate magnetism in this compound.

In order to check the temperature evolution of the satellites, NPD measurements were performed at various points in the phase diagram between 1 K and 80 K. The results are outlined in



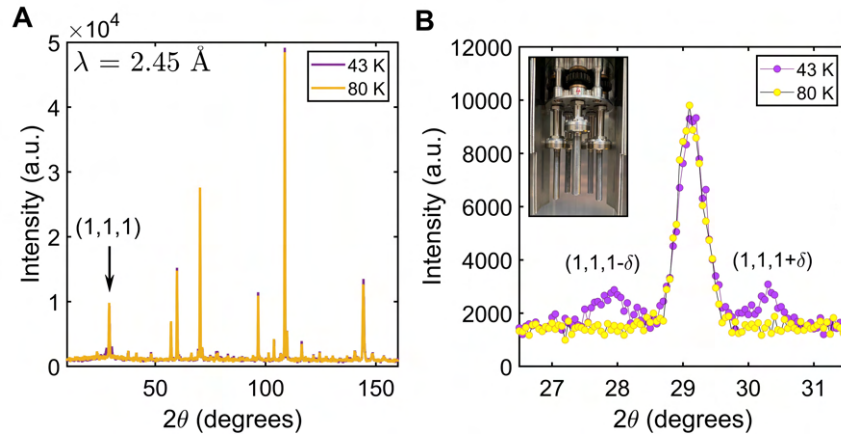
**Figure 8.19: Further probing of the transitions using long heat pulses.** All the zero field transitions for  $\text{Co}_5\text{TeO}_8$  as seen by static magnetization and AC susceptibility measurements were probed by long heat pulses, but with different equilibrium starting temperatures as indicated. Each time a long heat pulse was applied in order to raise the temperature of the sample by 50% from the equilibrium value.



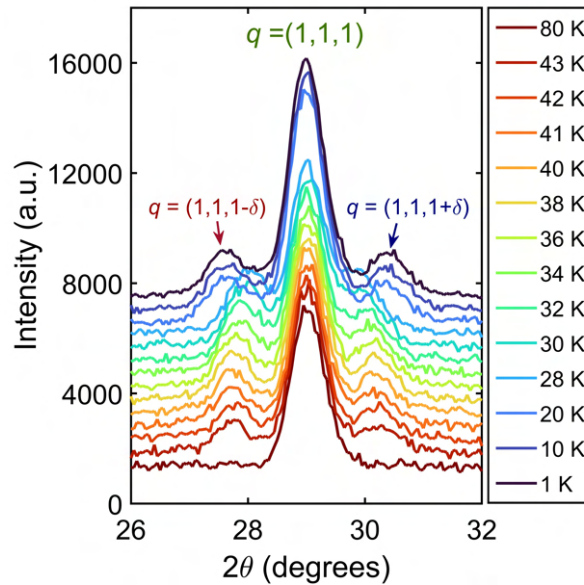
**Figure 8.20: Magnetic field dependent specific heat of  $\text{Co}_5\text{TeO}_8$  measured using long pulses.** Long heat pulse was also used to extract heat capacity as a function of magnetic field, similar to the process shown in Fig. 5.25 of Chapter. 5. Until 1 T, magnetic field was sequentially varied with a 100 Oe step (panel-A), followed by a 500 Oe step till the maximum field of 14 T (panel-B). As clearly shown, no evidence for any field-induced transitions were found.

Fig. 8.22. As can be clearly seen, with reducing the temperature towards the second hysteresis region (see again Fig. 8.10A), the satellites move closer to the central (1,1,1) Bragg peak. The significant temperature-dependent variation in the  $|q|$  transforms the actual satellites to more “shoulder-like” peaks. Whereas, below the hysteresis region, the satellites make a sudden jump to a higher  $\delta$  and continue to move further away from (1,1,1) peak.

A combined analysis was performed for the set of three peaks obtained at all temperatures, with three different Gaussian functions. While approaching the second hysteresis region, the intensities of both satellites were found to increase by a factor of  $\sim 250\%$ . Concomitantly, the



**Figure 8.21: Powder neutron diffraction results obtained from  $\text{Co}_5\text{TeO}_8$ .** (A) Powder neutron diffraction pattern of  $\text{Co}_5\text{TeO}_8$  in a wide  $2\theta$  range. (B) Shows the magnified region around (111) nuclear peak. A comparison of intensity between paramagnetic phase (80 K) and slightly below ordering temperature (43 K) shows the appearance of two peaks corresponding to zero field incommensurate magnetic phase. Inset shows one of the vanadium cans containing polycrystalline  $\text{Co}_5\text{TeO}_8$  sample used for the experiments.



**Figure 8.22: Temperature evolution of the magnetic satellites as obtained via neutron diffraction measurements.** Variation in  $q$  for the (1,1,1) as well as the (1,1,1 $\pm\delta$ ) peaks as seen from the experiments performed at HRPT, PSI. Note that a constant offset was applied to each data set in order to emphasize on the temperature dependence of the satellite peaks.

(1,1,1) peak intensity was found to decrease by  $\sim 18\%$ . Since there were no other satellites observed in the pattern, this variation is attributed to a redistribution of diffraction intensity to other commensurate peaks. Indeed, slight change in Bragg peak intensity can be seen for other



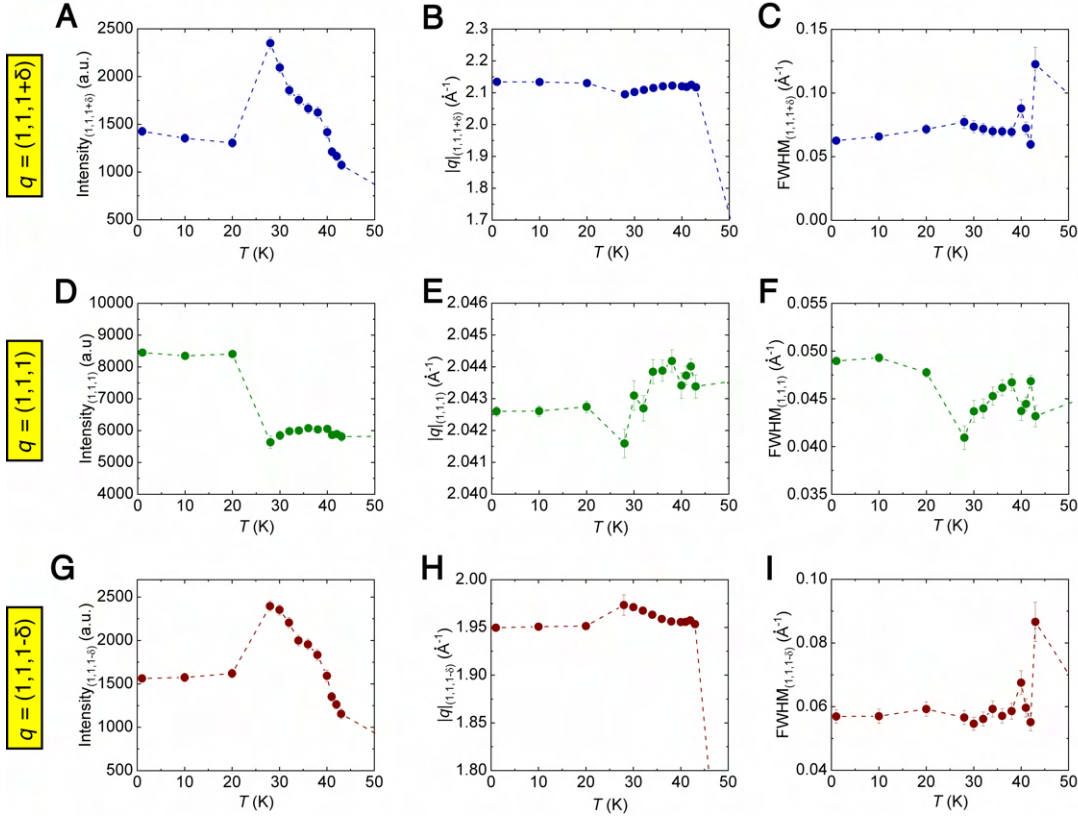


**Figure 8.23: Analysis of (111) Bragg peak and its incommensurate satellites in  $\text{Co}_5\text{TeO}_8$ .** Temperature dependence of (111) Bragg peak and its corresponding magnetic satellites were analysed individually. Panel-(A) shows the result of intensity evolution, panel-B shows the position and panel-C shows FWHM extracted from the fit for the right satellite. Whereas panel-(D) to (F) show the results for the main peak and (G) to (I) for the left satellite.

nuclear peaks (see Fig. 8.21A). Below the hysteresis region, a slightly asymmetric behaviour was observed for the satellites, while the intensity remains almost the same for the (1,1,1) Bragg peak. We also observe a small kink in the satellite intensities at near the first hysteresis region. For  $|q|$  as a function of temperature for (1,1,1+ $\delta$ ) peak, we observe that it changes from  $2.1171 \pm 0.0065 \text{ \AA}^{-1}$  at 43 K to  $2.0953 \pm 0.0028 \text{ \AA}^{-1}$  at 28 K, while for the (1,1,1- $\delta$ ) peak the same goes from  $1.9534 \pm 0.0025 \text{ \AA}^{-1}$  at 43 K till  $1.9735 \pm 0.0107 \text{ \AA}^{-1}$  at 28 K. As can be seen from Fig. 8.23,  $|q|$  does not change drastically for (1,1,1) Bragg peak. To conclude, we assign the cascade of transitions observed in our AC susceptibility measurements to occurrence and therefore temperature-induced fine changes associated with the incommensurate magnetic order. Around the first hysteresis region, with changes observed only in intensity of Bragg peaks, but not in  $|q|$  suggests a tiny reorientation of the magnetic moments. Small angle neutron scattering studies can provide further details about the microscopic magnetism in this system.



## 8.6 Reciprocal Space Magnetic Structure Using SANS

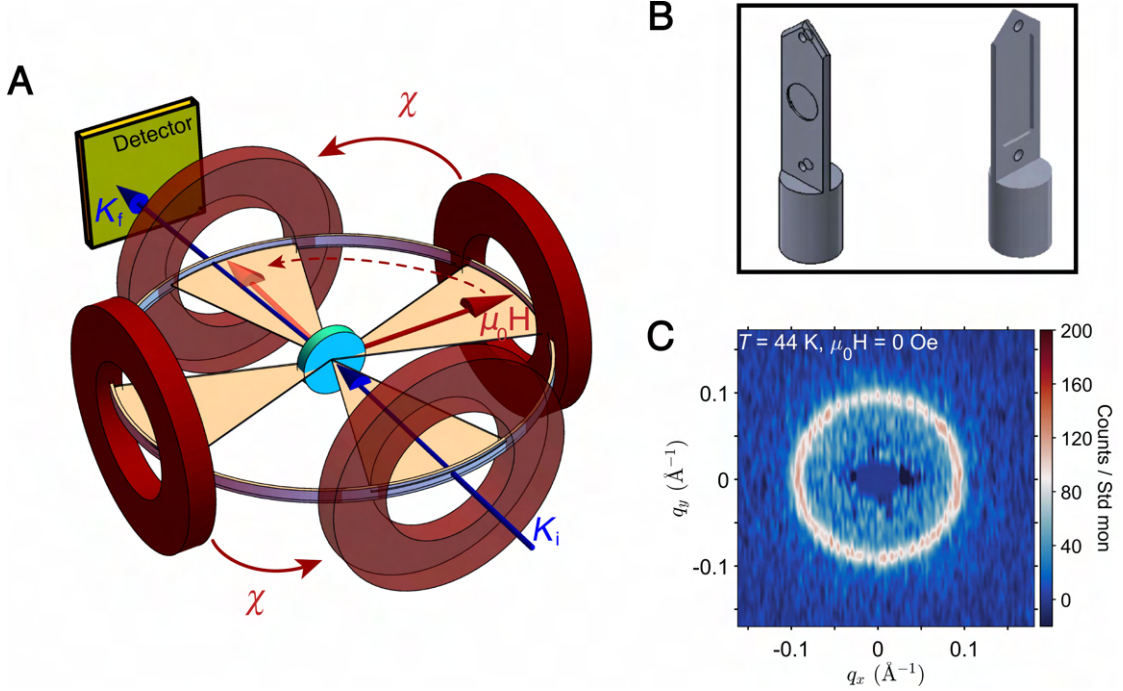


**Figure 8.24: SANS experimental configuration for  $\text{Co}_5\text{TeO}_8$  at the SANS-I instrument, PSI.** Schematics of the sample environment used for our SANS experiment is shown in panel-A. The MA-7 magnet window is about 45 degrees in each quadrant, as shown. This magnet is capable of producing 6.8 T in-plane field. The direction of the applied magnetic field can be changed by a  $90^\circ$  in-plane rotation. Thus switching between the  $\mu_0 \vec{H} \perp \vec{K}_i$  ( $\chi = 0^\circ$ ) and  $\mu_0 \vec{H} \parallel \vec{K}_i$  ( $\chi = 90^\circ$ ) configurations. Both these geometries were used during our SANS experiments. (B) In order to restrict any sample movements, the polycrystalline sample was loaded onto the custom made Al-holder shown in panel-B. (C) Clear magnetic scattering from the sample was observed even without applying any external field. This scattering pattern was recorded at  $T = 44$  K, just below  $T_N$ . The zero-field magnetic phase shows up as a sphere of intensity (due to the polycrystallinity) in reciprocal space, correspondingly as a ring on the detector plane.

*Experimental setup:* In order to resolve the magnetic structure of  $\text{Co}_5\text{TeO}_8$ , as a function of both temperature and magnetic field, small angle neutron scattering (SANS) experiments were carried out. For this purpose, we used the SANS-I instrument of Swiss Spallation Neutron Source (SINQ) located at the Paul Scherrer Institute (PSI). A custom made Aluminium frame was used as the sample holder (as shown in Fig. 8.24B). Polycrystalline sample in form of a pellet was tightly packed inside the small cavity, which can be seen in the picture. This design ensured extra stability to the pellet compared to other standard sample holders. The whole sample + holder unit was then installed inside an Oxford cryostat containing the MA7 magnet (from the SINQ instrumentation support group). Figure 8.24A shows the schematics of the magnet with sample installed inside. The measurements are performed in either of the  $45^\circ$  openings in each of the four quadrants, while the remaining  $180^\circ$  are the dark angles.

This Helmholtz magnet is capable of producing 6.8 T horizontal magnetic field. For all of our experiments, neutrons with wavelength 5 Å with a FWHM spread  $\Delta\lambda/\lambda = 10\%$  were used. The incoming neutron beam was collimated by a distance of 8m before the sample, whereas the scattered neutrons were collected with by a two-dimensional multidetector placed 3.5m behind the sample. All the data analysis were performed using the GRAS<sub>ans</sub>P software [42].

At first, the sample was cooled down to 50 K, in order to record a paramagnetic background. Followed by collection of scattering data just below  $T_N$ . As shown in Fig. 8.24C, a “ring-like” scattering pattern is obtained at  $T = 44$  K. The radius of this ring (that is  $|q|$ ) was found to be  $0.0903 \pm 0.0002 \text{ \AA}^{-1}$  (correspondingly  $6.96 \pm 0.02$  nm in real space), which matches closely with the value obtained from our neutron diffraction measurements (see section 8.5). With this quick verification, now we can try to resolve the magnetic structure from various phases in Co<sub>5</sub>TeO<sub>8</sub>.

### Results and discussions

The whole measurement protocol was two-fold. I. Re-verify the temperature scans performed with neutron diffraction experiments, but with finer steps. II. Resolve the field-induced phases shown in Fig. 8.14. Both transverse as well as longitudinal geometries were used to collect scattering patterns for the latter. Although, in scope of this thesis, we will focus only on the results obtained in the geometry where the magnetic field was applied perpendicular to the neutron beam.

*SANS experiments as a function of temperature:* First we focus on the temperature dependent scattering from Co<sub>5</sub>TeO<sub>8</sub>. These results are summarized in Figure. 8.25. As can be seen in panel-A, above  $T_N$ , no magnetic scattering was observed. Instead weak low- $q$  scattering could be due to pronounced paramagnetic fluctuations [82]. Just below  $T_N$ , a sphere of intensity develops around (0,0,0) central peak, due to powder averaging. This sphere shows up as a ring on the detector plane (see Fig. 8.24C or Fig. 8.25B). The  $|q|$  associated with this ring of intensity corresponds to the one obtained from the diffraction experiments. Upon lowering the temperature from  $T_N$ , the radius of the ring starts to shrink to lower  $qs$ , before completely vanishing just below the second hysteresis region. Concomitantly, a new ring appears at a higher  $|q|$ , as shown in Panel-E and F of Fig. 8.25. Around the second hysteresis region, inside a window of about 4 K, both these rings coexist with each other. This information was invisible to the wide angle diffraction discussed in the previous section.

From the analysis of the scattering pattern obtained from driving the system across the hysteresis region, important information is extracted. Below the hysteresis, both upon cooling as well as warming, the magnitude of the modulation vector remains constant. Whereas above hysteresis, the  $|q|$  is never recovered until the system reaches  $T_N$ . It attains a value slightly lower than that obtained upon cooling. The total intensity concentrated inside the sector shows clear sign of hysteresis, and also points towards a reorientation transition. Similarity between the sector box intensity and  $\chi'$  data suggests that the changes observed in the macroscopic

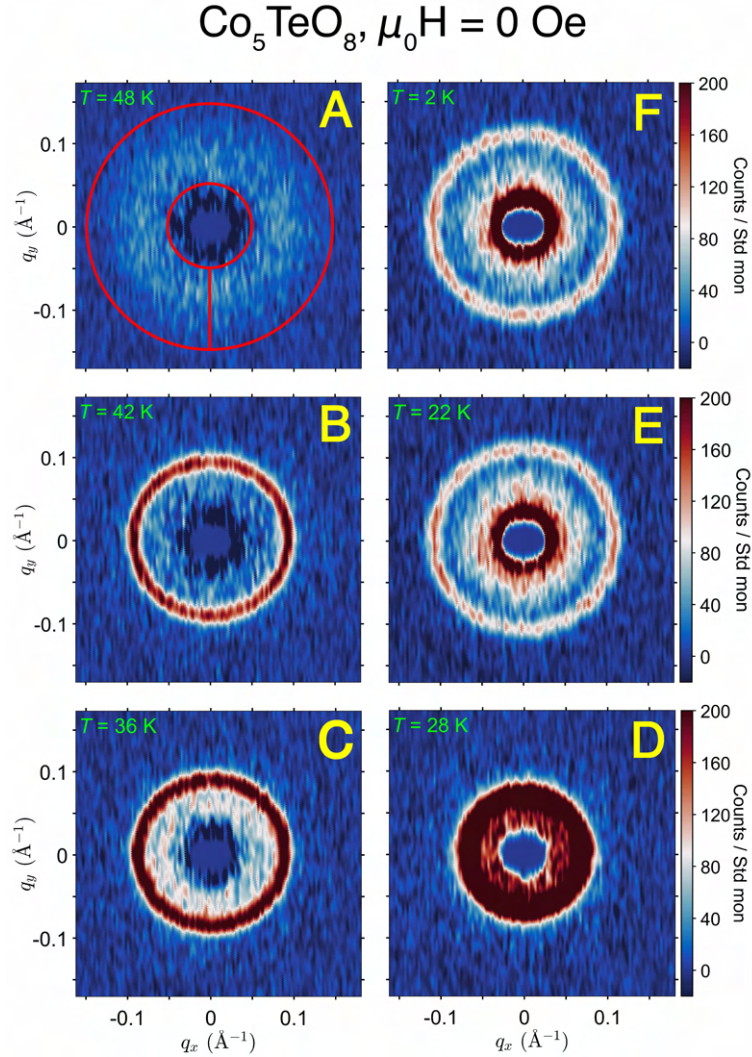


**Figure 8.25: SANS patterns for  $\text{Co}_5\text{TeO}_8$  as a function of temperature.** (A) Above no magnetic scattering was found. The observed scattering could be due to pronounced paramagnetic fluctuations. (B)-(E) show magnetic scattering obtained from  $\text{Co}_5\text{TeO}_8$  as a function of temperature. The corresponding temperatures are mentioned in each panel. Note that without any applied magnetic field, the SANS intensity correlates with the zero-field susceptibility measurements (shown in Fig. 8.10). In order to estimate the total radial intensity evolution as a function of  $|q|$ , an isotropic sector was chosen such that it contains the maximum of the intensity. Centres of these detector images have been masked. For simplicity, the colormap limit was kept the same for all detector images shown.

magnetic behaviour is driven by the microscopic reorientation of the incommensurate spin structure. Around the transition temperature, we see a clear two-peak structure in the total radial intensity evolution. As the temperature is gradually reduced, the inner ring broadens in  $q$ -space, while attaining a lower average  $q$ . The flattened intensity as a function of  $q$  (between  $0.04$  and  $0.085 \text{ \AA}^{-1}$ ) is evident from the results obtained at  $20 \text{ K}$  (see panel-C of Fig. 8.26).

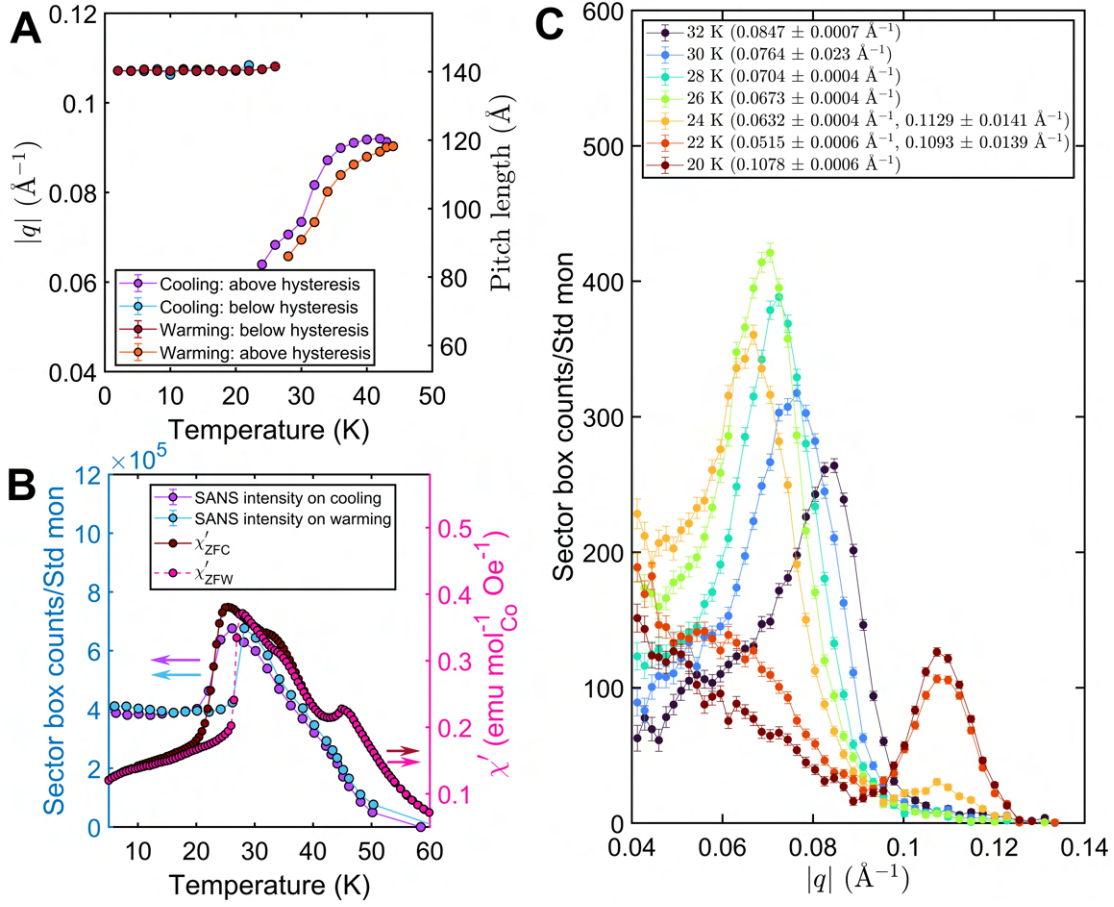


**Figure 8.26: Analysis of temperature dependent SANS patterns for  $\text{Co}_5\text{TeO}_8$ .** SANS scattering pattern as a function of temperature were analysed using the sector box shown in Panel-A of Fig. 8.25. (A) Shows the extracted  $|q|$  (along with the corresponding real space pitch length) at all temperatures. The intensity evolution of the ring is shown in Panel-B. Below the second hysteresis region, ring intensity was found to be constant over all measured temperatures. For comparison, real part of zero-field AC susceptibility scan is shown. (C) Shows the total radial intensity evolution as a function of  $|q|$ , as extracted from the sector shown in Fig. 8.25.

*SANS experiments as a function of magnetic field:* Now we turn our attention towards various field-induced phases in the magnetic phase diagram of  $\text{Co}_5\text{TeO}_8$  (Fig. 8.14). First, let us discuss the result of “field-training” procedure before analysing the finer steps. As described earlier, due to powder averaging, the incommensurate magnetic propagation vectors lie on a spherical manifold with constant radius in reciprocal space. This appears as a ring on the detector plane, as shown in Figure 8.27A. If the propagation vectors respond to a change in external magnetic field, by performing the field-training procedure, SANS intensity can be concentrated into a smaller reciprocal space volume. The procedure was decisive in determining key aspects of *geometrical confinement effects* in our recent work, outlined in Section 5.9 [11].

We chose 2.5 T magnetic field since no scattering was observed on the detector at this point.



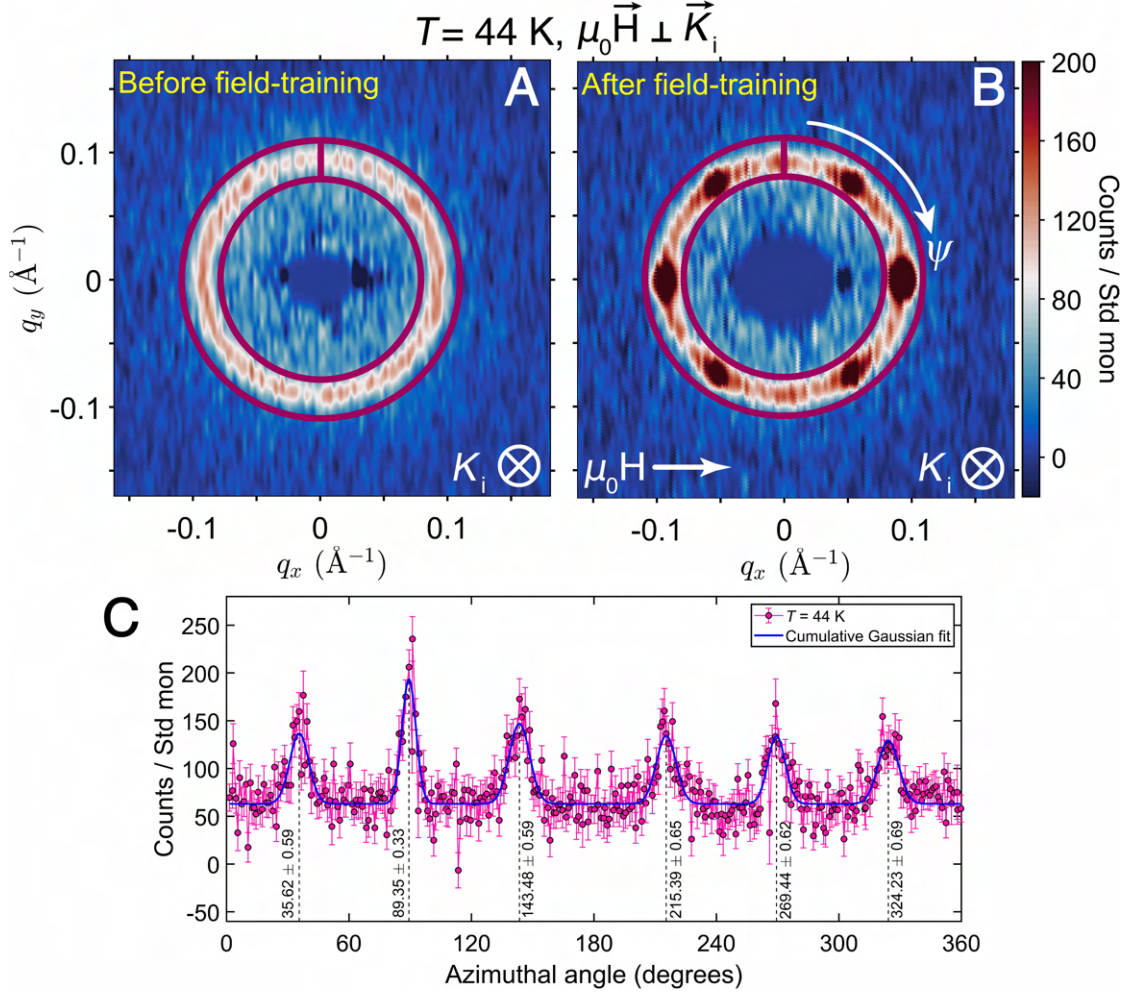


**Figure 8.27: High magnetic field-training of  $\text{Co}_5\text{TeO}_8$  just below  $T_N$  in transverse geometry.** (A) Shows the detector image before the field-training, same as panel-C of Fig. 8.24, while panel-B is the detector image obtained after field-training procedure. For this procedure, magnetic field was ramped up to 2.5 T at a rate of 100 Oe/s in a transverse geometry, held there for few minutes, followed by ramping down to 0 Oe at the same ramping rate. (C) Shows the integrated intensity inside the sector box shown in panel-B, as a function of azimuthal angle. This data was analysed with six independent Gaussian functions and the resultant cumulative fit is shown.

The result of the field-training procedure at 44 K for  $\text{Co}_5\text{TeO}_8$  is shown in panel-B of Fig. 8.27. SANS intensity concentrated at six angular Bragg peaks superimposed on a ring-like background is observed. This is further strengthened by the sector box averaging as a function of the azimuthal angle ( $\psi$ ), which is shown in Fig. 8.27C. The exact positions of these peaks were obtained by fitting six independent Gaussian functions, and are outlined in Fig. 8.27C. Clearly, the scattering is not a result expected from a standard SkL phase, and the reasoning is two-fold. (I) The SANS pattern lacks the inherent hexagonal symmetry expected due to

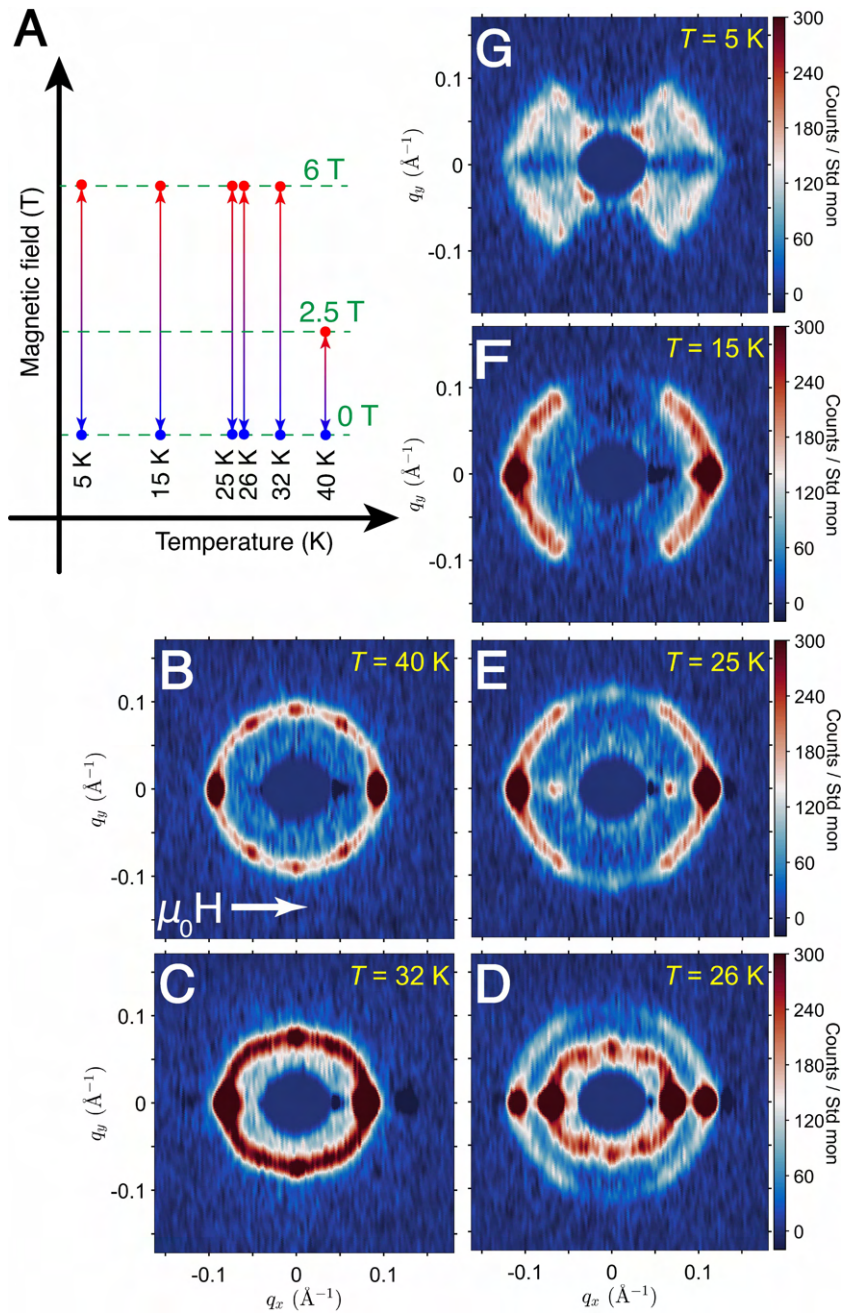


**Figure 8.28: Effects of Field-training procedure across the magnetic phase diagram of  $\text{Co}_5\text{TeO}_8$ .** (A) Schematics of the field-training procedure used at various temperatures. For temperatures less than 32 K, magnetic field was ramped up to the maximum available value, 6 T. The resultant scattering patterns are shown in panel-(B) to (G). For simplicity, the color scale is kept the same for all patterns.

scattering from a triple- $q$  SkL. (II) The scattering pattern shown in Fig. 8.27C is a consequence of the measurement performed in a transverse magnetic field, which for a conventional planar 3- $q$  SkL should just be a two-spot pattern concentrated at the north-south pole of the image.



More discussions about the phases will follow in the later part of this section. But from the initial assessment of the field-training procedure shows that magnetic modulation vectors are quite responsive to the external field and the resultant spin configuration is highly non-trivial.

The field-training procedure was extended to lower temperatures in the magnetic phase diagram of  $\text{Co}_5\text{TeO}_8$ . The results are shown in Fig. 8.28. If one refers to the phase diagram shown in Fig. 8.14, in case the field-training is performed before the appearance of Phase-VI, the maximum magnetic field required for obtaining pattern with no incommensurate magnetic scattering would be 2.5 T. But the appearance of Phase-VI significantly complicates the  $H - T$  diagram. The appearance of intensity minima at 32 K, 26 K, and 25 K on the 6 T background subtracted detector images clearly signals towards the non-vanishing incommensurate scattering even at these high magnetic fields. Above the appearance of Phase-VI, the field-training produces similar patterns, in accordance with the magnetic phase diagram. Performing field-training close to the second hysteresis region concentrates the scattering signal from the co-existing textures. The inner patterns are reminiscent of that obtained at higher temperatures, for example at 44 K. Whereas, the outer pattern appears more conical-type with some residual angular scattering. From the angular as well as the radial spread of the scattering pattern at the lowest measured temperature, it would be safe to assume that a complex arrangement of magnetic domains influence the scattering signal.

Now, we illustrate the magnetic field dependency of scattering patterns for  $\text{Co}_5\text{TeO}_8$ . In the first step, the zero-field state will be a ring of intensity on the detector plane. That is, we start with the magnetic order shown in Fig. 8.29A. Since the field is applied in the transverse direction to the incoming neutrons, the propagating magnetic order gradually reorients from a 3D spherical manifold to 1D line, oriented along the field. Thus the scattering pattern manifests as two peaks corresponding to a conical-type magnetic order (shown in panel-D of Fig. 8.29). With increasing the field even further, this peak gets suppressed and eventually vanishes. We did not observe any scattering signal above 1.5 T. Since the magnetization data obtained at 44 K clearly points towards unsaturated moments (for example, see Fig. 8.9), this phase can not be assigned to a field-polarized state. Instead, we postulate this state to be a field-induced intermediate state where scattering is concentrated at the commensurate peaks. But resolving this commensurate state is out of the scope of SANS experiments. When the magnetic field is ramped down to zero, it produces the familiar six Bragg spots on a background ring of intensity. This is marked by white arrows in Panel-F of Fig. 8.29. The evolution of the modulation vector was tracked by the sector box shown in Panel-A of Fig. 8.29. The results from the analysis of this radial dependency are shown in panel-G. The maxima observed in the sector box intensity corresponds to the magnetic field-induced transition from Phase-I to Phase-II (see Fig. 8.14). Correspondingly this maximum is complimented by a weak change in the slope of the  $|q|$  vs  $H$  curve. Note that such increasing  $|q|$  with higher magnetic fields is highly unusual in case of chiral skyrmion hosts. Similar behaviour has been found in polar hexagonal magnet  $\text{Y}_3\text{Co}_8\text{Sn}_4$ , where a higher order four-spin interaction has been proposed to stabilize the noncollinear magnetic structure [180]. This kind of magnetic field dependence on  $|q|$  is also reported for hexagonal frustrated magnet  $\text{Gd}_2\text{PdSi}_3$  [111]. It

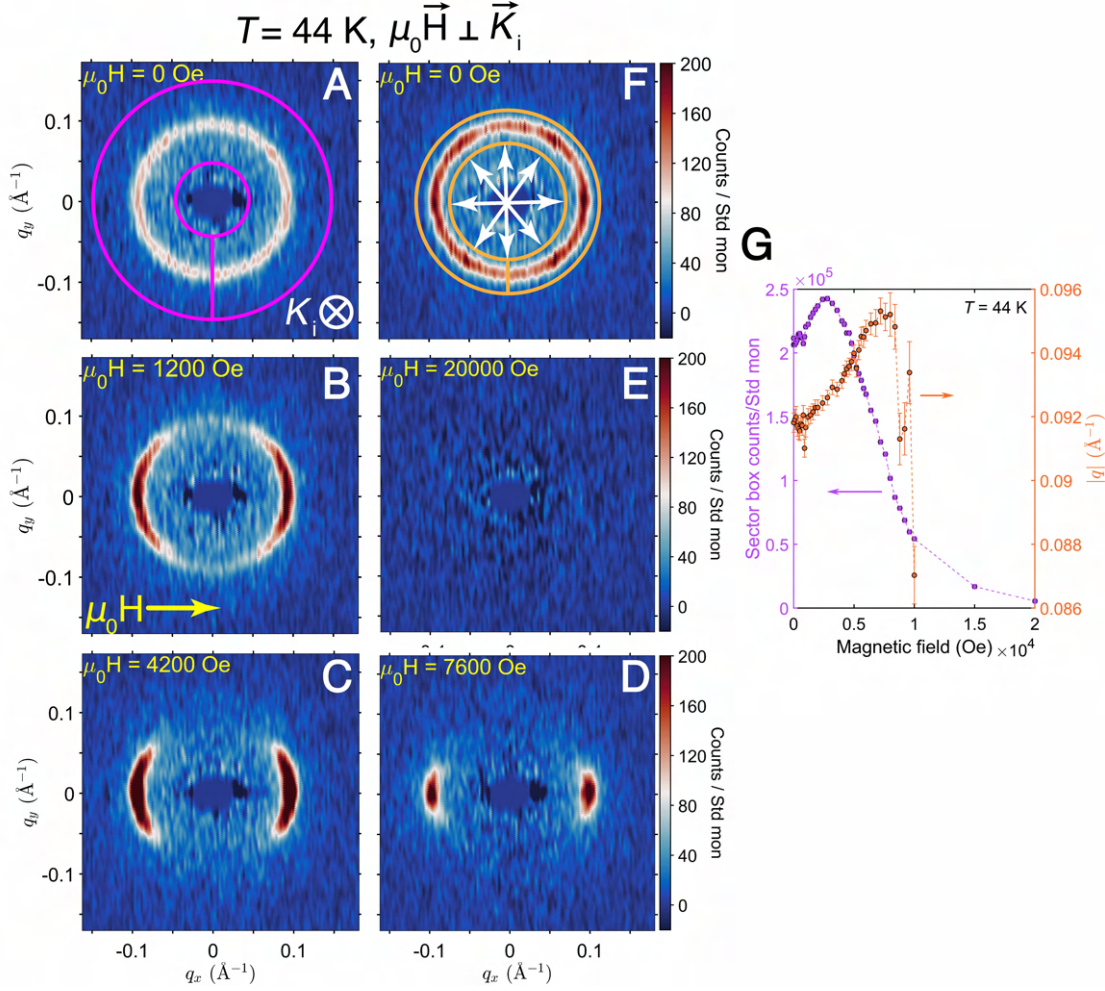


**Figure 8.29: Magnetic field dependent SANS patterns of  $\text{Co}_5\text{TeO}_8$  at  $T = 44$  K.** In the same transverse field geometry, scattering was recorded at the mentioned temperature. Panel-A shows the ring of scattering mentioned earlier. Magnetic order follows the increasing field strength and orients along with it (in Panel-B and C). In panel-D the two horizontal spots signal the formation of conical order, which subsequently transforms into a commensurate magnetic order shown in panel-E. Panel-F is the same as the panel-A in Fig. 8.27. The difference is that the sample was field-trained several times to concentrate more intensities on the Bragg spots. (G) shows the results of the analysis performed on the specified sector boxes shown in panel-A and F.

would imply that the stabilization mechanism of spin textures in  $\text{Co}_5\text{TeO}_8$  is beyond the most common DMI-based theories and other novel interactions need to be considered to explain these magnetic structures suitably. More details about this will follow in Section 8.7.

In the second step, we now analyse the magnetic field dependent evolution of incommensurate satellites created as a result of field-training at 28 K. This state is shown in panel-A of Fig. 8.30. Note that following the creation of the initial magnetic state at 28 K (as a result of the field-

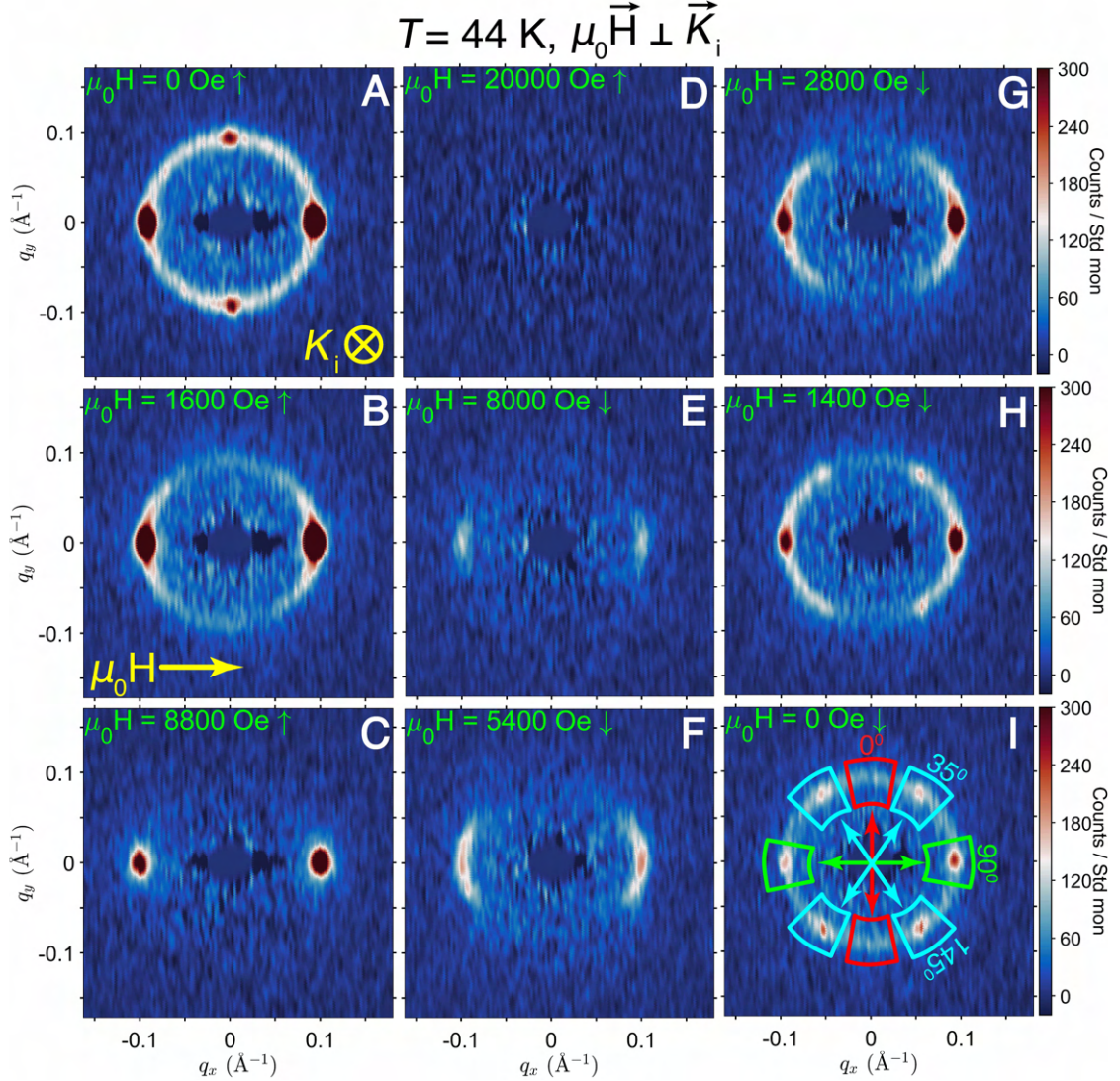


**Figure 8.30: Field evolution of incommensurate satellites at 44 K with zero-field state produced at 28 K.** As shown in panel-A, the four-spot zero-field state was produced at 28 K. With increasing magnetic field, scattering pattern follows the previous measurement and transforms into conical phase, as shown in panel-B and C. (D) At 2 T no scattering was observed at the corresponding  $|q|$  position. (E)-(G) Show the development of conical order with ramping down the magnetic field. (H) Shows the increment in scattering intensity at the angular spots. (I) Scattering pattern for the zero-field state after the field-training is complete. The angular positions of the sector boxes indicated in panel-I represent sector box corresponding to that particular position as well as the one which is situated diametrically opposite to it.

training procedure), the actual field dependent measurements were performed at 44 K. We see a considerable intensity focused at the north-south pole of the detector image. Magnetic order follows the field direction and gets concentrated along the horizontal direction, before all scattering signal is lost at 2 T. While ramping down, the opposite behaviour is observed,



but now the satellites form a six-spot pattern, unlike the initial scattering pattern. The sector boxes in panel-I of Fig. 8.30 are chosen such a way that to enclose all the Bragg peaks due to incommensurate phase(s).

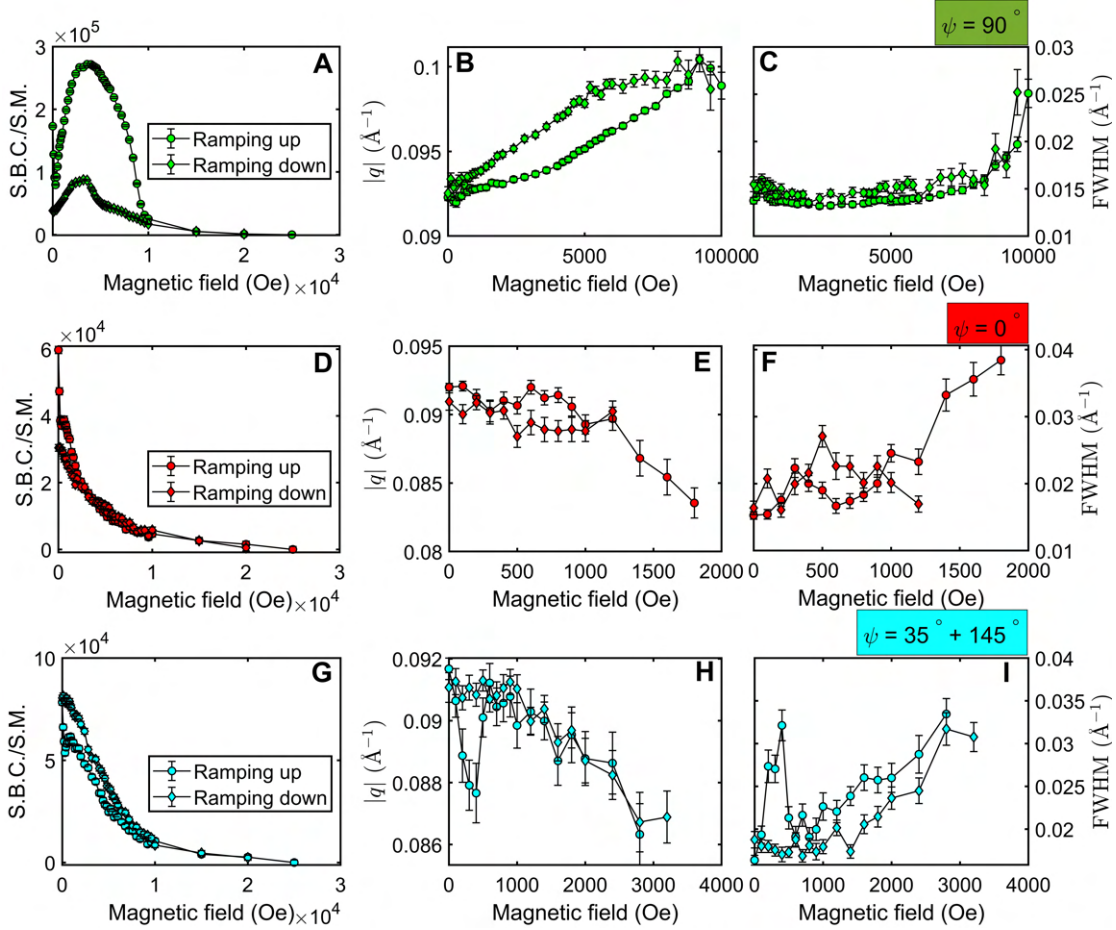


**Figure 8.31: Sector box analysis of scattering pattern at  $T = 44$  K for  $\text{Co}_5\text{TeO}_8$ .** Analysis of the sector boxes shown in panel-I of Fig. 8.30. Panel-A, B and C show the results of magnetic field dependent behaviour of the total intensity,  $|q|$ , and FWHM, respectively, for the  $90^\circ$  sector boxes. Panel (D)-(F) represent the same for  $0^\circ$  sector boxes. And finally, (G)-(I) show the same for both diagonal boxes.

Since the zero-field state was created due to field-training at 28 K, we start the field-ramping procedure with four Bragg peaks on the detector plane, instead of a uniformly distributed ring of intensity. But when the magnetic order starts to follow the field direction, the reorientation of modulation vectors is quite sharp and results in a pronounced maximum in the sector box intensity, as shown in panel-A of Fig. 8.31. Additionally, we also observed a pronounced maximum while ramping down the magnetic field, signalling the transition from Phase-II to Phase-I, as labelled in Fig. 8.14. Whereas smooth monotonous changes are observed for the rest of the sector boxes. Also, after the field-training procedure, the intensity of the  $90^\circ$  sector box was found to be smaller than the initial value, with a concomitant increased

intensity inside the other sector boxes. This fact is justified on the basis that the six-spot pattern is formed by reorientation of the conical type magnetic order.  $|q|$  still appears to be increasing with magnetic field, with a slight change in slope signalling the transition between Phase-I and Phase-II. The sharp changes seen in the behaviour of  $|q|$  for  $35^\circ + 145^\circ$  sector boxes is consequence of sharp reorientation of the modulation vector from  $0^\circ$  to  $90^\circ$ . The results thus obtained from our SANS analysis agrees quite well with the corresponding macroscopic magnetization data at 44 K. Which proves that not only the temperature-driven behaviour, but also magnetic field induced responses are consequences of incommensurate vector reorientation in  $\text{Co}_5\text{TeO}_8$ .

In order to track the changes occurring to the modulation vectors as a function of magnetic field, similar measurements were performed at  $T = 32$  K (Fig. 8.32). Since the zero-field state was now prepared at 44 K, it shows the appearance of familiar six Bragg spots, similar to which is seen earlier in Fig. 8.27. Magnetic field dependency revealed that even a 6 T magnetic field is not enough to suppress the incommensurate scattering. The response of the satellites was found to be quite anisotropic with respect to each other. Since the stability of each of the participating phases is enhanced, there are correspondingly sharper changes observed in the analysis.

With increasing the magnetic field strength, these spots start to expand quite anisotropically. In their respective regions of stability, satellites contained inside the  $90^\circ$  sector box and  $35^\circ + 145^\circ$  sector boxes behave quite similarly, including the magnetic field induced hysteresis region. We observed that unlike at  $T = 44$  K, while ramping up the magnetic field from zero,  $|q|$  does not increase linearly, but remains at a constant value (see panel-B and H of Fig. 8.33). But on the other hand, it decreases linearly before entering the magnetic field induced hysteresis region (panel-B of Fig. 8.33). This signifies the importance of magnetic history in this sample. Steep changes observed in the intensity both for  $90^\circ$  and  $(35^\circ + 145^\circ)$  sector boxes coincide perfectly with the phase boundaries extracted from magnetization measurements at 32 K (see Fig. 8.9 and Fig. 8.14). Increased stability of Phase-V is concluded from the concomitant enhanced plateau shown in panel-A and G.

Combining each result, we can now summarize all our findings from the SANS experiment. First, the field-training procedure does in fact produces a eight spot pattern, not six (see Fig. 8.34A). The weak intensity observed at the north-south position is enhanced while performing the same field-training sequence at lower temperatures. For the remaining six Bragg peaks seen in the same pattern, one possible three-dimensional magnetic structure is shown in panel-B of Fig. 8.34 (the Phase-I in Fig. 8.14). This is the so-called 4- $q$  hedgehog magnetic texture previously observed in  $\text{MnSi}_{1-x}\text{Ge}_x$  (for  $0.3 \leq x \leq 0.6$ ) [54]. But unlike these cases, the scattering in  $\text{Co}_5\text{TeO}_8$  is dominated by sharp Bragg peaks. In the same solid solution of  $\text{MnSi}_{1-x}\text{Ge}_x$  (but now  $0.7 \leq x \leq 1$ ), existence of cubic 3- $q$  hedgehog structure is also proposed. The modulation vectors for this kind of hedgehog lattices are shown in panel-C of Fig. 8.34. This is one of the candidate spin structures which could produce the observed scattering at the north-south pole positions (corresponding to Phase-II in Fig. 8.14). The other two planar

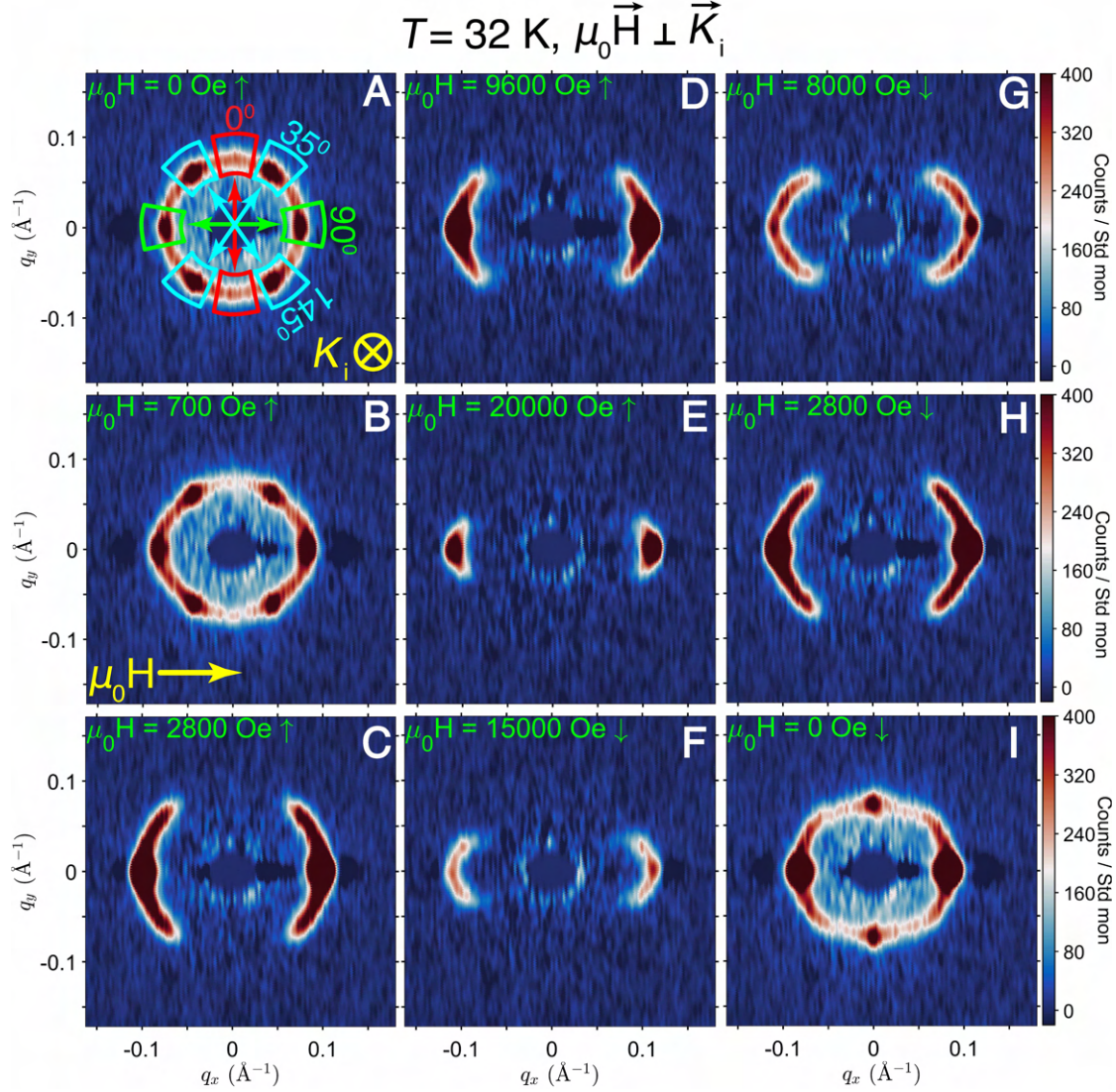


**Figure 8.32: Systematic magnetic field scan in transverse geometry at  $T = 32 \text{ K}$ .** Scattering patterns for various magnitude of magnetic field. The actual field value is mentioned in the corresponding panel. The sector boxes still carry the same meaning. One key difference with respect to the patterns shown in Fig. 8.31 is that here conical-type magnetic order still persists even at 6 T.

possibilities are 3- $q$  SkL and 2- $q$  square-SkL, shown in panel-D and E of Fig. 8.34, respectively.

*Wide angle rocking scan of the Ewald's sphere:* In order to verify the presence of tetrahedral 4- $q$  hedgehog lattice, as well as to uniquely determine the magnetic structure of Phase-II (among the three possible cases shown in Panels C-E of Fig. 8.34), a wide angle rocking scan (just below  $T_N$ ) was performed in zero applied magnetic field. Prior to the scan, sample was first field-trained at 2.5 T external magnetic field. The resultant is shown in Fig. 8.35B. This



## 8.6. Reciprocal Space Magnetic Structure Using SANS

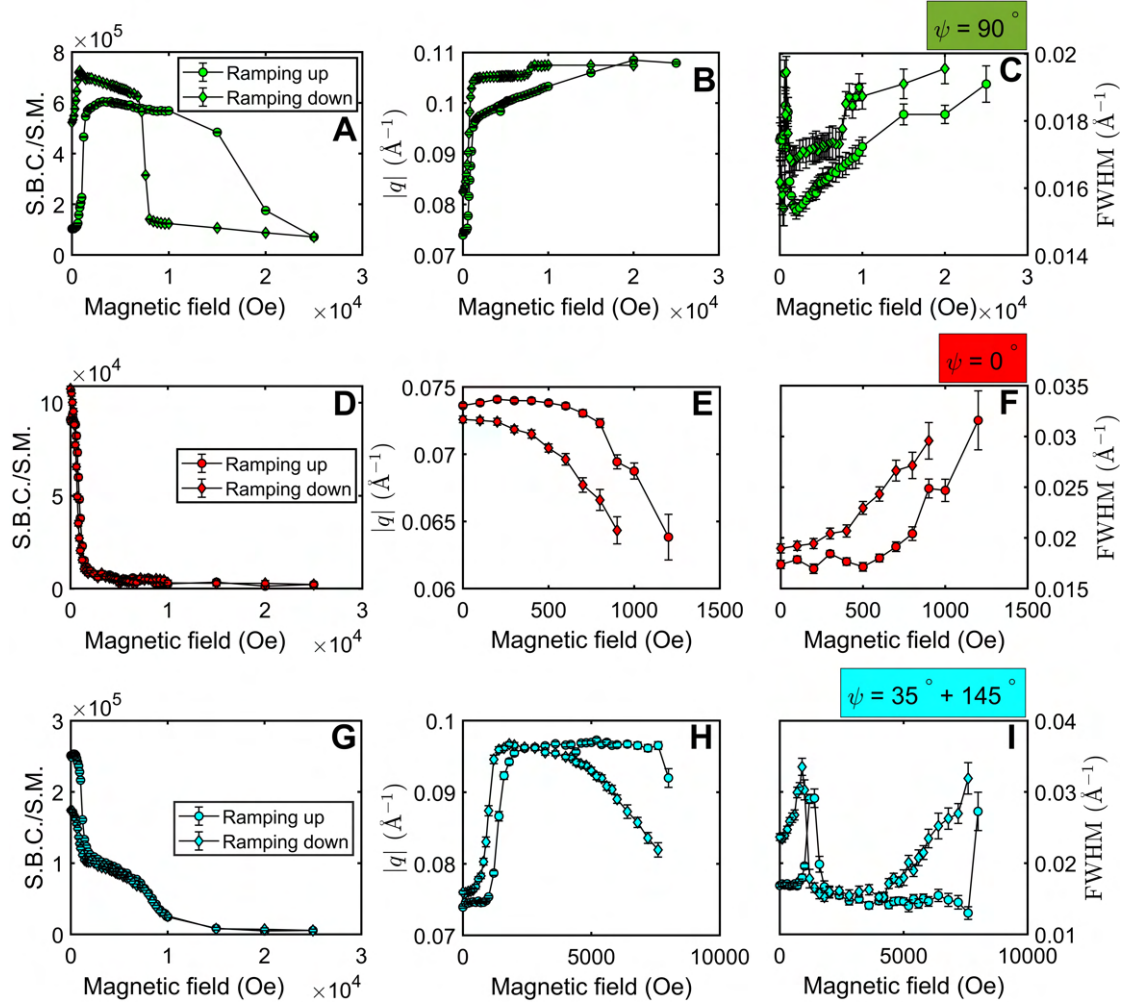


**Figure 8.33: Detailed analysis of scattering pattern at  $T = 32$  K for  $\text{Co}_5\text{TeO}_8$ .** Analysis for the sector boxes chosen in Fig. 8.32. Panels-A to I carry the same meaning as explained in the caption of Fig. 8.31.

scattering pattern represents  $\phi = 0^\circ$  configuration. The sample was then rotated around this position in an angular width of  $\pm 100^\circ$ .

Since the axis of rotation in Fig. 8.35B is oriented in north-south direction, one does not expect any change in the intensity of the Bragg peaks observed at those positions. As shown in panel-C of Fig. 8.35, this is precisely what is obtained from the experiment. Whereas, due to the manifold of  $q$  vectors, corresponding to both 4- $q$  as well as 3- $q$  hedgehog lattice, a periodic behaviour is expected from the  $I(\phi)$  scan for the other angular sector boxes. For the Bragg peaks arising at  $\psi = 35^\circ + 145^\circ$  (along with their mirror sectors), two peaks are observed at  $\pm 90^\circ$ , as shown in Fig. 8.35D. The scattering at these angles are predominantly attributed to the 4- $q$  hedgehog lattice, along with a small contribution from the 3- $q$  hedgehog lattice. For the same sectors, a slight asymmetric behaviour in  $I(\phi)$  is observed around  $\phi = 0$ , while

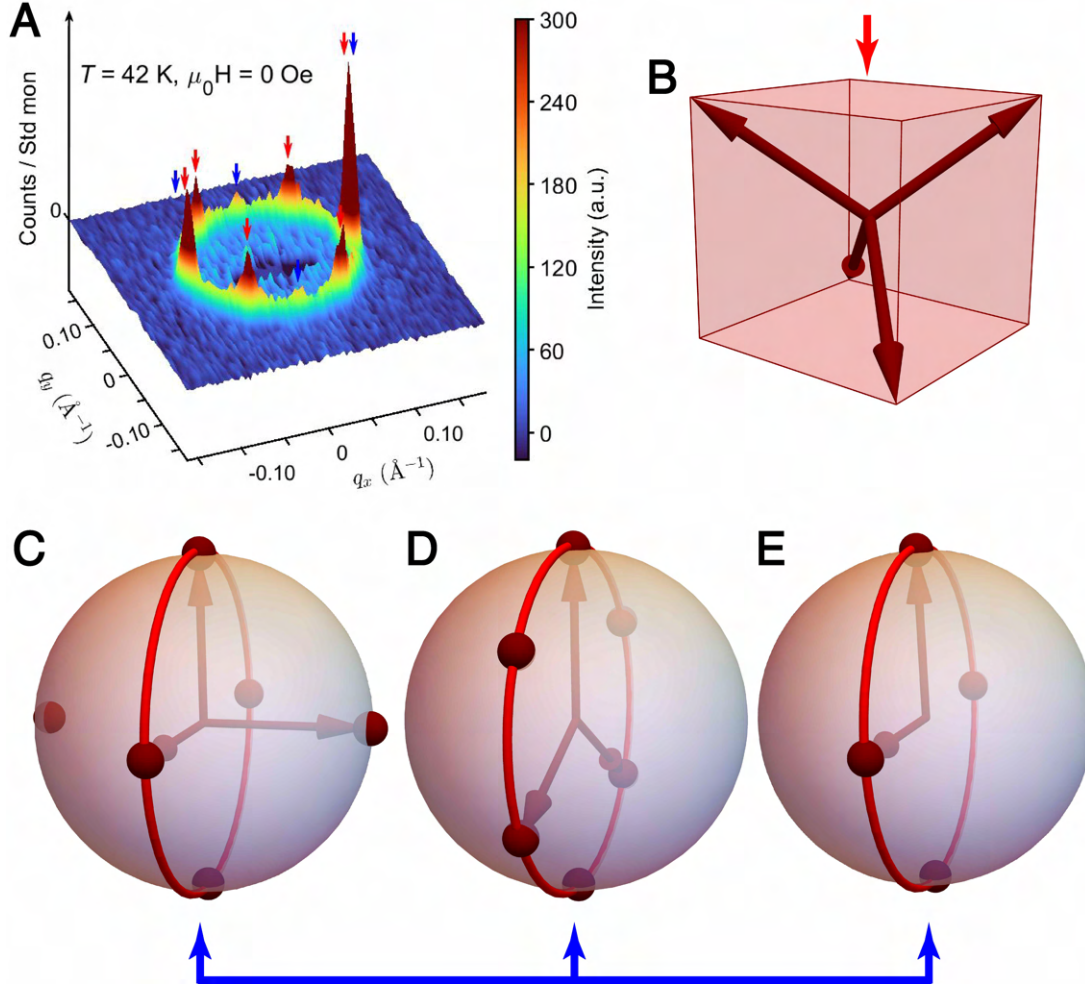


**Figure 8.34: Arrangement of propagation vectors corresponding to the proposed spin structure in  $\text{Co}_5\text{TeO}_8$ .** (A) The 2D detector image is now plotted in 3D to emphasize on the peaks observed at the north-south pole, that is at positions  $(0, \pm q_y)$ . (B)-(E) shows the proposed propagation vectors which could explain the observed scattering pattern. The coloured arrows represent possible contribution to the scattering signal.

attaining a constant scattering. This is an outcome of the  $q$  vector arrangement shown in Fig. 8.35A. Finally, for the conical Bragg peaks, that is when  $\psi = 90^\circ + 270^\circ$ , scattering is found to be dominated by five well-defined peaks (see Fig. 8.35E). These peaks are fitted with five independent Gaussian functions and the resultant is shown in panel-E of Figure 8.35. The  $\phi$  dependence of the total scattering can be well-explained with an easy correspondence with the schematics shown in Fig. 8.35A. While the peaks observed around  $\phi = \pm \sim 90^\circ$  originate mainly due to the 3- $q$  hedgehog lattice, those appearing around  $\sim 54^\circ$  are attributed to the 4- $q$  hedgehog lattice. Finally, around  $\phi = 0^\circ$ , scattering due to both magnetic structures are expected to contribute to the intensity, as shown in panel-E of Fig. 8.35. Thus, in the magnetic phase diagram of  $\text{Co}_5\text{TeO}_8$  (Fig. 8.14), we confirm Phase-I and Phase-II to be 4- $q$  tetrahedral hedgehog lattice and 3- $q$  cubic hedgehog lattice, respectively.

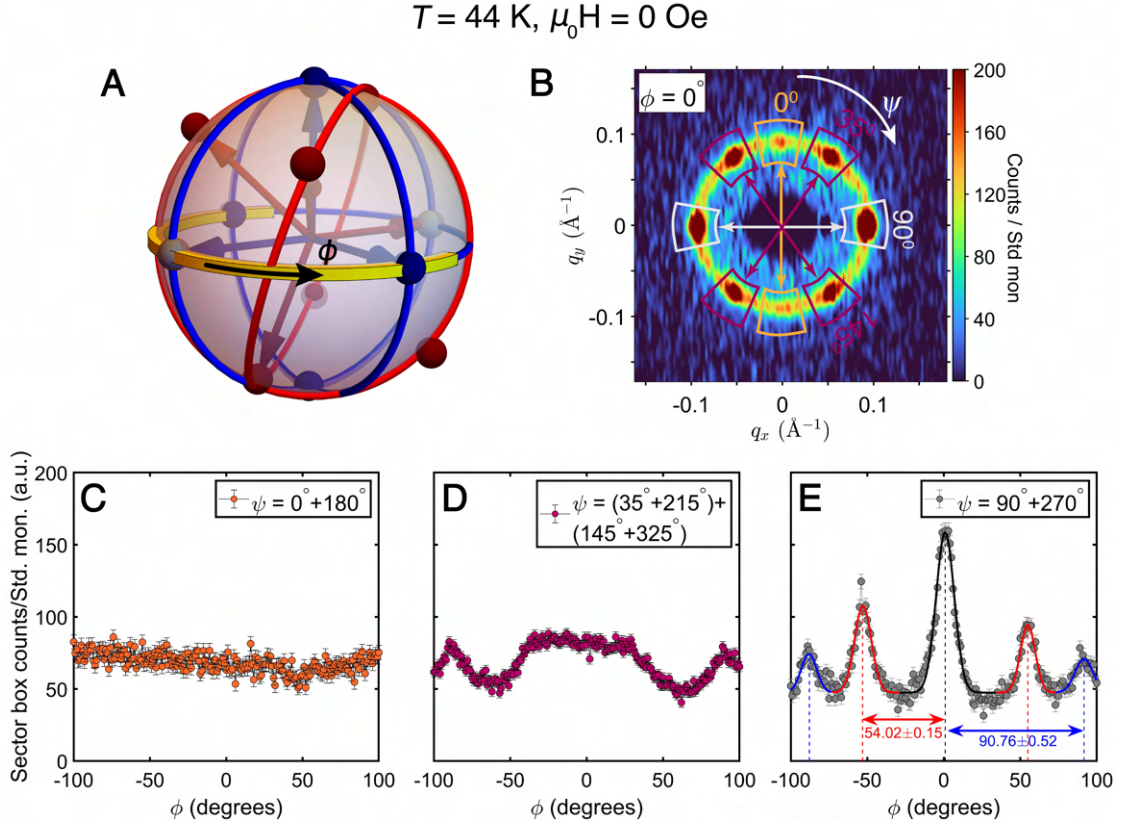


**Figure 8.35: Wide angle rocking scan of  $\text{Co}_5\text{TeO}_8$  without external magnetic field.** (A) propagation vectors of the 4- $q$  tetrahedral and the 3- $q$  cubic hedgehog lattice plotted around the Brillouin zone centre. The red and blue rings represent the manifold of  $q$  vectors for the 4- $q$  and 3- $q$  hedgehog lattice, respectively. The yellow arc is a schematic illustration of the angular coverage of the measurement, that is -100 till +100 with a step size of  $1^\circ$ . (B) shows the detector image of the field-trained pattern for  $\phi = 0$  configuration, that is  $\mu_0 \vec{H} \perp \vec{k}_i$ , that is when both grey spheres lie on the detector plane. The angular positions of sector boxes indicated in panel B represent sector boxes corresponding to that particular position, as well as the one which is situated diametrically opposite to it. (C)-(E) represent angular dependence of the sector box intensity as obtained by rocking the sample in the illustrated geometry. The  $I(\phi)$  profile thus obtained from the  $90^\circ + 270^\circ$  sector boxes was fitted with five independent Gaussian functions.

*Topological nature of the participating phases:* As shown by *Y. Fujishiro et. al.*, a finite topological Hall effect is associated with the quadrupole- $q$  hedgehog lattice in  $\text{MnSi}_{1-x}\text{Ge}_x$  [54]. By similar analogy, we expect a possible topological nature of the 4- $q$  spin structure proposed in  $\text{Co}_5\text{TeO}_8$  as well. Similar to the tetrahedral 4- $q$  hedgehog lattice, the cubic triple- $q$  hedgehog lattice observed in  $\text{MnSi}_{1-x}\text{Ge}_x$  also exhibits a finite topological Hall effect [54]. But the crucial difference among these two spin structures being the change in sign of the topological Hall effect as a function of magnetic field. While for cubic 3- $q$  hedgehog lattice, the sign flips from negative to positive with increasing magnetic field, the opposite behaviour is observed for the tetrahedral 4- $q$  hedgehog lattice [54]. This subtle difference may be attributed to

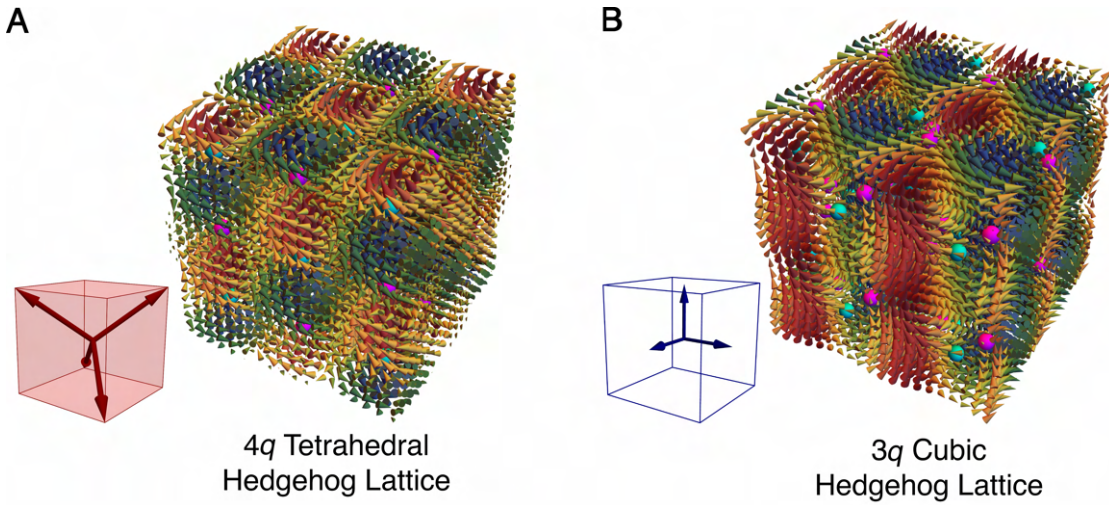


**Figure 8.36: Magnetic structure of both hedgehog lattices.** Spin structure of (A) tetrahedral 4- $q$  hedgehog lattice and (B) cubic 3- $q$  hedgehog lattice. Arrangement of corresponding propagation vectors characterizing each hedgehog lattice has also been shown. Cyan and magenta spheres represent hedgehogs and anti-hedgehogs, respectively.

the static and fluctuating effects originating due to the emergent magnetic field [39, 88, 89]. The source of this emergent magnetic field being hedgehogs (which act as monopoles) and anti-hedgehogs (anti-monopoles) in the lattice, resulting in non-trivial thermodynamic and electrical responses [53, 54, 87, 88, 103]. Similar magneto-electric responses are also expected from the dynamics of hedgehogs and anti-hedgehogs in the insulating  $\text{Co}_5\text{TeO}_8$ . In order to tune the observed topological spin texture in  $\text{MnSi}_{1-x}\text{Ge}_x$  solid solution, one needs to tune the lattice constant, which could be highly non-trivial at times. Whereas, a topological transition among the proposed tetrahedral 4- $q$  and cubic 3- $q$  spin structure in  $\text{Co}_5\text{TeO}_8$  is observed at a rather small magnetic field of  $\sim 1000$  Oe. It would be worthwhile checking if the proposed magnetic structures in  $\text{Co}_5\text{TeO}_8$  may be distinguished by their topological properties or not.

## 8.7 Estimation Of Exchange Couplings Through Quantum Chemical Approaches

Even if they are fundamentally different compared to each other,  $\text{Co}_5\text{TeO}_8$  shares striking similarities in terms of magnetic texture with one of  $B20$  materials,  $\text{MnGe}$  (or rather a solid solution containing Si) [54]. Both systems host ultra-short magnetic textures ( $< 10\text{nm}$ ). From the experimental side,  $\text{MnGe}$  is proposed to have gigantic DMI values, which could even be comparable to the leading order ferromagnetic exchange interactions [55, 106]. This is clearly not feasible. Whereas, theoretical calculations set an estimation of DMI constant which is of the same order as for the other  $B20$  materials. These contrasting results lead to the proposal of several other stabilization mechanisms based on I. Ruderman-Kittel-Kasuya-Yosida (RKKY) interaction [143], II. Frustration arising due to AFM interactions [214], and III.



## 8.7. Estimation Of Exchange Couplings Through Quantum Chemical Approaches

Orbital motion of electrons giving rise to non-coplanar spin arrangement, giving rise to the so called topological-chiral interaction [61]. In order to avoid such complicated scenarios, and to provide a simple solution to the stabilization mechanism behind the observed magnetic spin texture, we calculated the strength of leading order exchange couplings using *ab initio* quantum chemistry methods.

*Description of the method:* We perform many-body wavefunction calculations on electrostatically embedded finite-size models carved from the experimentally resolved crystal structure<sup>1</sup>. As shown in Figure (structure), the crystal structure consists of two distinct Co atoms that are six-fold and four-fold coordinated by O atoms. The finite-size models adopted in our calculations comprise a central unit hosting either one or two octahedra (tetrahedra) treated with multireference or multiconfigurational wavefunctions, surrounded by the nearest-neighbor octahedra (tetrahedra). These latter octahedra (tetrahedra) account for the charge distribution in the vicinity of the central unit and are treated at the Hartree-Fock level. The crystalline environment is restored by embedding each model in an array of point charges fitted to recreate the long-range Madelung electrostatic potential [104]. Electron correlation effects in the central units are described at the complete-active-space self-consistent-field (CASSCF) and multi-reference configuration interaction (MRCI) levels of theory [67], including spin-orbit interactions. MRCI calculations involve single and double excitations from the  $3d$  valence shells of  $\text{Co}^{2+}$  ions and the  $p$  valence shells of the bridging ligands. We remark that embedded finite-size model approaches have proven effective to describe electronic excitations and magnetic interactions in a rich variety of strongly correlated insulators [38, 121], including  $d$ -electron lattices [25, 24, 97, 130], owing to their localized nature.

$$\mathcal{H} = \mathcal{H}^{\text{I}} + \mathcal{H}^{\text{II}}, \quad (8.1)$$

where,  $\mathcal{H}^{\text{I}}$  encodes the contribution of the interactions within sites of spin  $\vec{S}_i$  while  $\mathcal{H}^{\text{II}}$  encodes the coupling between the  $i^{\text{th}}$  and  $j^{\text{th}}$  nearest-neighbor sites bearing spin  $\vec{S}_i$  and  $\vec{S}_j$ , respectively. The intra-site contribution,  $\mathcal{H}^{\text{I}}$ , takes the form

$$\mathcal{H}^{\text{I}} = \sum_i \mathcal{A} \vec{S}_i^2, \quad (8.2)$$

where  $\mathcal{A}$  is the single-ion anisotropy. The inter-site contribution,  $\mathcal{H}^{\text{II}}$ , reads

$$\mathcal{H}^{\text{II}} = \mathbb{J}_1 \sum_{i<j} (\vec{S}_i \cdot \vec{S}_j) + \mathbb{J}_2 \sum_{i<j} (\vec{S}_i \cdot \vec{S}_j)^2 + \sum_{i<j} \vec{D} \cdot \vec{S}_i \times \vec{S}_j, \quad (8.3)$$

with  $\mathbb{J}_1$  and  $\mathbb{J}_2$  being the bilinear and biquadratic isotropic exchange couplings, respectively,

<sup>1</sup>This work was performed in collaboration with Dr. Ravi Yadav from the group of Chair of Computational Condensed Matter Physics (C3MP) at EPFL.

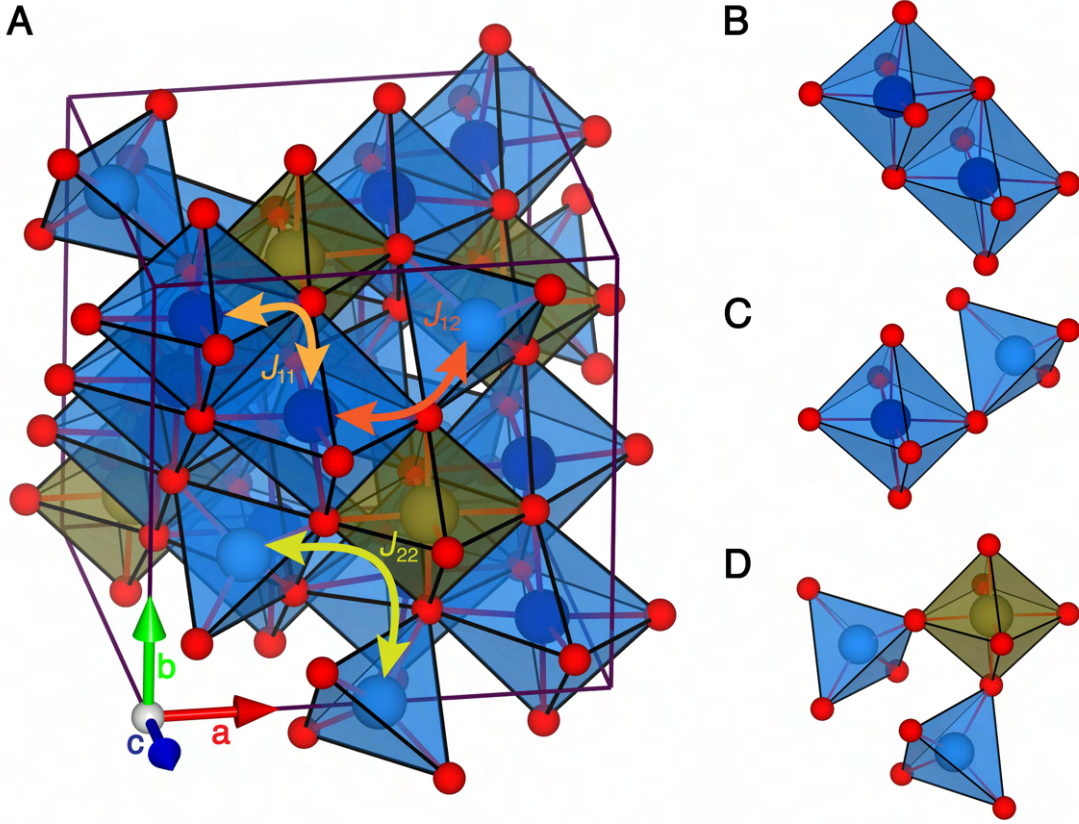


**Figure 8.37: Manifold of nearest-neighbor exchange interaction.** A. Crystal structure of  $\text{Co}_5\text{TeO}_8$ . There are two inequivalent Co atoms in the unit cell, crystallizing in an octahedral and tetrahedral coordination environment with nearest oxygen atoms. The leading order exchanges have been labelled. (B)-(D) illustrate these leading order exchange pathways more clearly.

and  $\vec{D}$  is the antisymmetric Dzyaloshinskii-Moriya interaction [132].

We determine the intra-site interactions appearing in  $\mathcal{H}^{\text{I}}$ , i.e., the single-ion anisotropy  $\mathcal{A}$ , relying on the one-site model. The single-ion anisotropy quantifies the zero-field splitting of the ground state that stems from spin-orbit and crystal-field effects. To assess this quantity, we rely on the methodology developed in Ref. [125] taking advantage of the multiplet structure and corresponding wavefunctions. In brief, the mixing of the low-lying  $^4T_1$  states with the higher-lying states is treated perturbatively and the spin-orbit wavefunctions related to the high-spin configuration are projected onto the space spanned by the  $^4T_1$   $|S, M_s\rangle$  states. The orthonormalized projections of the low-lying quartet wavefunctions,  $\tilde{\psi}_k$ , and the corresponding eigenvalues,  $E_k$ , are used to construct the effective Hamiltonian  $\tilde{\mathcal{H}}_{\text{eff}} = \sum_k E_k |\tilde{\psi}_k\rangle \langle \tilde{\psi}_k|$ . A one-to-one correspondence between  $\tilde{\mathcal{H}}_{\text{eff}}$  and the model Hamiltonian  $\tilde{H}_{\text{mod}} = S \cdot \vec{\mathcal{A}} \cdot S$  leads to the  $\vec{\mathcal{A}}$  tensor, which is then diagonalized to obtain the axial parameter,  $\mathcal{A}$ .

Finally, we determine the inter-site interactions appearing in the spin Hamiltonian  $\mathcal{H}^{\text{II}}$ , i.e.,



### 8.7. Estimation Of Exchange Couplings Through Quantum Chemical Approaches

Co-sites	$\mathbb{J}_1$	$\mathbb{J}_2$	$\mathbb{D}_x$	$\mathbb{D}_y$	$\mathbb{D}_z$	$ \mathbb{D}/\mathbb{J} $
Co <sub>1</sub> -Co <sub>1</sub>	0.116 meV	-0.0084 meV	-0.011 meV	0.073 meV	0.0656 meV	0.84
Co <sub>2</sub> -Co <sub>2</sub>	0.088 meV	-0.0011 meV	0.002 meV	0.003 meV	0.001 meV	0.03
Co <sub>1</sub> -Co <sub>2</sub>	0.208 meV	-0.0032 meV	0.003 meV	0.001 meV	0.021 eV	0.102

**Table 8.2:** Exchange parameters for Co<sub>5</sub>TeO<sub>8</sub>, as obtained from the quantum chemistry calculations.

the bilinear and biquadratic isotropic exchange couplings  $\mathbb{J}_1$  and  $\mathbb{J}_2$ , respectively, together with the antisymmetric anisotropic vector,  $\vec{\mathbb{D}}$ . We rely on the two-site model shown in Figure 8.37. We map the resulting *ab initio* Hamiltonian onto the anisotropic biquadratic model Hamiltonian given in Equation 3, which involves sixteen spin-orbit states corresponding to one septet, one quintet, one triplet, and a singlet. The mapping is accomplished according to the procedure described in Ref. [24]. The resulting magnetic interactions are listed in Table 8.2. The dominant term among the inter-site interactions is the bilinear isotropic exchange coupling  $\mathbb{J}_1$ , the positive sign of which indicates an anti-parallel spin interaction between the  $S=3/2$  centers. We find that all leading order bilinear Heisenberg exchanges are AFM in nature, whereas biquadratic terms are always FM. Competition among these leading order exchanges could introduce frustration into the lattice, which may in turn stabilize the higher order spin structure observed in our experiments. Similar mechanism has recently been proposed to stabilize skyrmion textures in Gd<sub>2</sub>PdSi<sub>3</sub> [111], Gd<sub>3</sub>Ru<sub>4</sub>Al<sub>12</sub> [71], and Co<sub>7</sub>Zn<sub>7</sub>Mn<sub>6</sub> [191], to name a few. Finally, summarizing all the results, we firmly believe frustration arising due to competing AFM interactions could actually lead to the unusual behaviour seen in the experiments.

From the single site calculations, contrasting results for both inequivalent Co-sites in terms of single ion anisotropy values were obtained. For the octahedrally coordinated Co-ion  $\mathcal{A}$  is found to be -2.1 meV, whereas the same for tetrahedrally coordinated Co-ion is 3.1 meV. These result suggest that the former favours an easy axis configuration, whereas the latter favours an easy plane one. These results can be readily verified using single crystalline samples.



## Summary & Conclusions **Part IV**



## 9 Conclusions & Future Work

In this thesis, we have investigated two chiral magnets with different aspects of their macroscopic magnetic properties. The conclusions can be summarized as:

- I. Size-tailored octahedral  $\text{Cu}_2\text{OSeO}_3$  particles approaching nanoscale sizes were synthesized by a low-temperature process and shown to be chemically and structurally equivalent to bulk  $\text{Cu}_2\text{OSeO}_3$ . The chemical treatment is based on selenious acid leaching from a selenite precursor induced by an acid-base neutralization. We anticipate that the same chemistry can be used to grow other selenite materials. Likewise, it can be applied to selenates when exposed to a base by leaching of selenic acid. Selenates and selenites are an important class of materials with a large spectrum of applications involving optical properties, catalysis, and energy to name but a few. We proposed four distinct chemical mechanisms for transforming the starting material,  $\text{CuSeO}_3 \cdot 2\text{H}_2\text{O}$ , into the final product,  $\text{Cu}_2\text{OSeO}_3$ . From magnetometry and neutron scattering experiments, together with micromagnetic simulations, we explored the interplay between the particle geometry and chiral magnetic interactions in  $\text{Cu}_2\text{OSeO}_3$  and find that a diverse array of magnetic configurations with variable topology may be stabilized according to the particle size. Correspondingly, our results shed new and detailed light on the size dependence of the magnetic phase diagrams and magnetization textures in small  $\text{Cu}_2\text{OSeO}_3$  samples. This includes the discovery for the first time of a critical octahedral height  $S_c$  of 190 nm ( $3\lambda$ ) below which no standard experimental signature for skyrmion tubes is found. For other types of topological spin textures (e.g., merons and bobbles), expected to be stable for shorter octahedral heights, investigation using experimental techniques such as LTEM and electron holography is highly desired. Elucidation of the magnetic textures in the larger particles also calls for the further development of neutron and X-ray beam techniques aiming at the reconstruction of the real-space magnetization distribution inside the particle [44, 65].
- II. The observed quantization effect of confined chiral magnetic modulations was revealed previously in epitaxially grown MnSi [92, 210] and FeGe [90, 153] chiral magnet thin

films. In these systems, the periodicity of helical-like phases was found to either increase or decrease slightly with respect to the bulk so that a discrete integer or half-integer number of helical turns span between film surfaces. The present work extends observation of this phenomenon to small  $\text{Cu}_2\text{OSeO}_3$  particles, where for each of  $h = 73$  and  $338$  nm, we observe clear increases in  $\lambda$  so that a single and five helical turns span the octahedron, respectively. The discretization in  $\lambda$  is generally explained as enforced by boundary conditions due to the reduced dimensionality and the surface-induced magnetic anisotropy. In contrast to spanning flat surfaces, the confined low-temperature integer-turn helical-like states span the octahedral height or, more generally, the non-adjacent octahedral vertices where four octahedron edges meet. This shows that the boundary conditions enforced by the geometry of a vertex, itself a form of structural topological defect, become increasingly dominant in the limit of small particle volume, low temperature, and low field. Moreover, since in the vicinity of the particle vertices, edges, and surfaces, the symmetry of the magnetic interactions is naturally broken compared with the bulk, entirely new magnetic configurations without analogy to the bulk have the potential to emerge. Due to this key role of the geometry in generating the interactions that underlie the confined magnetic configurations, their robust stability can be anticipated, particularly in the genuine nanoparticle limit. The geometrical confinement effects reported here bring fresh insight for the future exploitation of chiral magnets with sizes approaching the nanoscale, in particular by defining relevant length-scales for their use in applications settings.

- III. The low temperature magnetic phase diagram of  $\text{Cu}_2\text{OSeO}_3$  showcases richer physics compared to the other  $P2_13$  skyrmion hosts. Based on the proposal of higher cubic anisotropies, this system is home to a low-temperature skyrmion lattice which is completely independent from the high-temperature one, seen in many chiral magnets. The role of anisotropic exchange interaction is often neglected in the stability and propagation of helices. But through our detailed experiments, we find that AEI can no longer be considered negligible. Our experiments show clear sign of increased magneto-crystalline anisotropy consistent with previous proposal. Next, we will quantify the anisotropy independently using other experimental probes, such as dynamic cantilever magnetometry. This will provide a separate assessment of the anisotropies in the system.
- IV. Through the high-resolution  $r$ -REXS experiments, we discovered something unusual and novel in  $\text{Cu}_2\text{OSeO}_3$ . The surface spiral state with doubled periodicity is exciting from both theory as well as experimental point of view. According to existing theory, there actually exists no energy minimum along  $\langle 110 \rangle$ , in the energy landscape of  $\text{Cu}_2\text{OSeO}_3$  [156]. Magnonic signature from the Brillouin light scattering experiments could provide some clue about the inelastic process associated with it. In order to explain this novel phase, we need to go beyond the existing theories and start including higher order corrections to the Hamiltonian, such as a Lifshitz invariant in order to reasonably explain the occurrence of this phase. This is beyond the scope of this thesis, but we are confident that future studies will solve this mysterious appearance of the



---

novel phase.

- V. The chiral compound,  $\text{Co}_5\text{TeO}_8$  was synthesized in micro crystal form and detailed structural and magnetic characterizations were performed. As expected, we found a racemic mixture of two different chiralities in the sample. But distinction in magnetic properties due to left- or right-handedness of the crystal structure is not possible at the moment. We observed consistent magnetic properties from magnetization, and susceptibility measurements. The results of electrical capacitance measurements also showed features consistent with the ones from bulk magnetization data. Magnetic phase diagram was constructed based on all the experimental probes outlined in this thesis. The incredible complexity of it due to the role of complicated crystallographic lattice in this compound. Wide angle neutron diffraction and small angle neutron scattering experiments were performed at various points in the magnetic phase diagram. We could identify a higher order  $4q$  spin texture propagating in all three dimension. We also propose other topological/non-topological phases as candidates for different part of the phase diagram. Topological  $4q$  as well cubic  $3q$  spin textures have been observed in solid solution of Mn-Si-Ge series, but a single form of magnetic texture being stable for each stoichiometry [54]. Whereas, we observe magnetic field-induced transformation between the  $4q$  state to other non-trivial phases, which itself is exciting from both experimental as well as theoretical point of view. Resolving the spin texture in real space using Lorentz TEM or electron holography or in reciprocal space using Resonant elastic x-ray scattering is highly desired. Finally, with help *ab initio* calculations, we methodically propose a frustration-based mechanism which may stabilize different phases in this chiral cubic insulator. In the past, discovery of such compounds with exotic magnetic textures has boosted intense fundamental research from the community. We expect nothing less from this complex magnet.



# Bibliography

- [1] Abràmoff, M. D., Magalhães, P. J., and Ram, S. J. (2004). Image processing with ImageJ. *Biophotonics international*, 11(7):36–42.
- [2] Adams, M. P., Michels, A., and Kachkachi, H. (2022). Magnetic neutron scattering from spherical nanoparticles with Néel surface anisotropy: Atomistic simulations. *arXiv preprint arXiv:2205.07552*.
- [3] Adams, T., Chacon, A., Wagner, M., Bauer, A., Brandl, G., Pedersen, B., Berger, H., Lemmens, P., and Pfleiderer, C. (2012). Long-wavelength helimagnetic order and skyrmion lattice phase in  $\text{Cu}_2\text{OSeO}_3$ . *Phys. Rev. Lett.*, 108:237204.
- [4] Adams, T., Mühlbauer, S., Pfleiderer, C., Jonietz, F., Bauer, A., Neubauer, A., Georgii, R., Böni, P., Keiderling, U., Everschor, K., Garst, M., and Rosch, A. (2011). Long-Range Crystalline Nature of the Skyrmion Lattice in MnSi. *Phys. Rev. Lett.*, 107:217206.
- [5] Ahmed, A. S., Rowland, J., Esser, B. D., Dunsiger, S. R., McComb, D. W., Randeria, M., and Kawakami, R. K. (2018). Chiral bobbbers and skyrmions in epitaxial FeGe/Si(111) films. *Phys. Rev. Materials*, 2:041401.
- [6] Ahrens, J., Geveci, B., and Law, C. (2005). Paraview: An end-user tool for large data visualization. *The visualization handbook*, 717(8).
- [7] Als-Nielsen, J. and McMorrow, D. (2011). *Elements of modern X-ray physics*. John Wiley & Sons.
- [8] Amato, A., Luetkens, H., Sedlak, K., Stoykov, A., Scheuermann, R., Elender, M., Raselli, A., and Graf, D. (2017). The new versatile general purpose surface-muon instrument (gps) based on silicon photomultipliers for  $\mu$  sr measurements on a continuous-wave beam. *Review of Scientific Instruments*, 88(9):093301.
- [9] Aqeel, A., Sahliger, J., Taniguchi, T., Mändl, S., Mettus, D., Berger, H., Bauer, A., Garst, M., Pfleiderer, C., and Back, C. H. (2021). Microwave Spectroscopy of the Low-Temperature Skyrmion State in  $\text{Cu}_2\text{OSeO}_3$ . *Phys. Rev. Lett.*, 126:017202.
- [10] Bak, P. and Jensen, M. H. (1980). Theory of helical magnetic structures and phase transitions in MnSi and FeGe. *Journal of Physics C: Solid State Physics*, 13(31):L881.

## Bibliography

---

- [11] Baral, P. R., Ukleev, V., LaGrange, T., Cubitt, R., Živković, I., Rønnow, H. M., White, J. S., and Magrez, A. (2022). Tuning topological spin textures in size-tailored chiral magnet insulator particles. *The Journal of Physical Chemistry C*, 126(28):11855–11866.
- [12] Baral, P. R., Ukleev, V., Yu, L., Cubitt, R., Rønnow, H., White, J., and Magrez, A. (2020). Institut Laue-Langevin (ILL) doi:10.5291/ILL-DATA.5-31-2696.
- [13] Barron, L. D. (1986). True and false chirality and parity violation. *Chemical physics letters*, 123(5):423–427.
- [14] Barron, L. D. (2012). From cosmic chirality to protein structure: Lord Kelvin's legacy. *Chirality*, 24(11):879–893.
- [15] Battle, X. and Labarta, A. (2002). Finite-size effects in fine particles: magnetic and transport properties. *Journal of Physics D: Applied Physics*, 35(6):R15.
- [16] Bauer, A., Garst, M., and Pfleiderer, C. (2013). Specific Heat of the Skyrmion Lattice Phase and Field-Induced Tricritical Point in MnSi. *Phys. Rev. Lett.*, 110:177207.
- [17] Bauer, A., Garst, M., and Pfleiderer, C. (2016). History dependence of the magnetic properties of single-crystal  $\text{Fe}_{1-x}\text{Co}_x\text{Si}$ . *Phys. Rev. B*, 93:235144.
- [18] Bauer, A., Neubauer, A., Franz, C., Münzer, W., Garst, M., and Pfleiderer, C. (2010). Quantum phase transitions in single-crystal  $\text{Mn}_{1-x}\text{Fe}_x\text{Si}$  and  $\text{Mn}_{1-x}\text{Co}_x\text{Si}$ : Crystal growth, magnetization, ac susceptibility, and specific heat. *Phys. Rev. B*, 82:064404.
- [19] Bauer, A. and Pfleiderer, C. (2012). Magnetic phase diagram of MnSi inferred from magnetization and ac susceptibility. *Phys. Rev. B*, 85:214418.
- [20] Bedanta, S., Barman, A., Kleemann, W., Petravic, O., and Seki, T. (2013). Magnetic nanoparticles: a subject for both fundamental research and applications. *Journal of nanomaterials*, 2013.
- [21] Beille, J., Voiron, J., and Roth, M. (1983). Long period helimagnetism in the cubic B20  $\text{Fe}_x\text{Co}_{1-x}\text{Si}$  and  $\text{Co}_x\text{Mn}_{1-x}\text{Si}$  alloys. *Solid State Communications*, 47(5):399–402.
- [22] Belemuk, A. M. and Stishov, S. M. (2020). Vollhardt invariance in chiral magnets. *Phys. Rev. B*, 101:144426.
- [23] Bogdanov, A. N. and Yablonskii, D. (1989). Thermodynamically stable “vortices” in magnetically ordered crystals. the mixed state of magnets. *Zh. Eksp. Teor. Fiz*, 95(1):178.
- [24] Bogdanov, N. A., Maurice, R., Rousochatzakis, I., van den Brink, J., and Hozoi, L. (2013). Magnetic State of Pyrochlore  $\text{Cd}_2\text{Os}_2\text{O}_7$  Emerging from Strong Competition of Ligand Distortions and Longer-Range Crystalline Anisotropy. *Phys. Rev. Lett.*, 110:127206.
- [25] Bogdanov, N. A., van den Brink, J., and Hozoi, L. (2011). Ab initio computation of  $d$ - $d$  excitation energies in low-dimensional Ti and V oxychlorides. *Phys. Rev. B*, 84:235146.

- [26] Bordács, S., Butykai, A., Szigeti, B. G., White, J. S., Cubitt, R., Leonov, A. O., Widmann, S., Ehlers, D., von Nidda, H.-A. K., Tsurkan, V., et al. (2017). Equilibrium skyrmion lattice ground state in a polar easy-plane magnet. *Scientific Reports*, 7(1):1–11.
- [27] Bos, J.-W. G., Colin, C. V., and Palstra, T. T. M. (2008). Magnetoelectric coupling in the cubic ferrimagnet  $\text{Cu}_2\text{OSeO}_3$ . *Phys. Rev. B*, 78:094416.
- [28] Bradlyn, B., Cano, J., Wang, Z., Vergniory, M. G., Felser, C., Cava, R. J., and Bernevig, B. A. (2016). Beyond dirac and weyl fermions: Unconventional quasiparticles in conventional crystals. *Science*, 353(6299):aaf5037.
- [29] Brown, G. E. and Rho, M. (2010). *The multifaceted skyrmion*. World Scientific.
- [30] Bunsen, R. (1852). Vulkanische exhalation. *J. prakt. Chem*, 56:53.
- [31] Burn, D., Brearton, R., Ran, K., Zhang, S., van der Laan, G., and Hesjedal, T. (2021). Periodically modulated skyrmion strings in  $\text{Cu}_2\text{OSeO}_3$ . *npj Quantum Materials*, 6(1):1–8.
- [32] Burn, D. M., Wang, S., Wang, W., van der Laan, G., Zhang, S., Du, H., and Hesjedal, T. (2020). Field and temperature dependence of the skyrmion lattice phase in chiral magnet membranes. *Phys. Rev. B*, 101:014446.
- [33] Chacon, A., Heinen, L., Halder, M., Bauer, A., Simeth, W., Mühlbauer, S., Berger, H., Garst, M., Rosch, A., and Pfleiderer, C. (2018). Observation of two independent skyrmion phases in a chiral magnetic material. *Nature Physics*, 14(9):936–941.
- [34] Chui, C., Ma, F., and Zhou, Y. (2015). Geometrical and physical conditions for skyrmion stability in a nanowire. *AIP Advances*, 5(4):047141.
- [35] Collins, T. J. (2007). ImageJ for microscopy. *Biotechniques*, 43(S1):S25–S30.
- [36] Das, B., Balasubramanian, B., Skomski, R., Mukherjee, P., Valloppilly, S. R., Hadjipanayis, G. C., and Sellmyer, D. J. (2018). Effect of size confinement on skyrmionic properties of MnSi nanomagnets. *Nanoscale*, 10(20):9504–9508.
- [37] De Bergevin, F. and Brunel, M. (1981). Diffraction of x-rays by magnetic materials. I. general formulae and measurements on ferro- and ferrimagnetic compounds. *Acta Crystallographica Section A: Crystal Physics, Diffraction, Theoretical and General Crystallography*, 37(3):314–324.
- [38] de PR Moreira, I. and Illas, F. (2006). A unified view of the theoretical description of magnetic coupling in molecular chemistry and solid state physics. *Physical Chemistry Chemical Physics*, 8(14):1645–1659.
- [39] Deutsch, M., Makarova, O. L., Hansen, T. C., Fernandez-Diaz, M. T., Sidorov, V. A., Tsvyashchenko, A. V., Fomicheva, L. N., Porcher, F., Petit, S., Koepf, K., Rößler, U. K., and Mirebeau, I. (2014). Two-step pressure-induced collapse of magnetic order in the MnGe chiral magnet. *Phys. Rev. B*, 89:180407.

## Bibliography

---

- [40] Devi, M. M., Jha, M., Ganguli, A. K., and Chakraverty, S. (2017). Efficient synthesis and characterization of  $\text{Cu}_2\text{OSeO}_3$  nanoparticles via hydrothermal route. *Materials Research Express*, 4(11):115007.
- [41] Devi, M. M., Koshibae, W., Sharma, G., Tomar, R., Gaikwad, V. M., Varma, R. M., Nair, M. N., Jha, M., Sarma, D., Chatterjee, R., et al. (2019). The limit to realize an isolated magnetic single skyrmionic state. *Journal of Materials Chemistry C*, 7(5):1337–1344.
- [42] Dewhurst, C. (2020). GRASP User Manual, Technical Report No. ILL03DE01T, Institut Laue- Langevin, Grenoble (2003), available at: [www.ill.fr/lss/grasp](http://www.ill.fr/lss/grasp).
- [43] Domb, C. (2000). *Phase transitions and critical phenomena*. Elsevier.
- [44] Donnelly, C. and Scagnoli, V. (2020). Imaging three-dimensional magnetic systems with x-rays. *Journal of Physics: Condensed Matter*, 32(21):213001.
- [45] Du, H., Che, R., Kong, L., Zhao, X., Jin, C., Wang, C., Yang, J., Ning, W., Li, R., Jin, C., et al. (2015a). Edge-mediated skyrmion chain and its collective dynamics in a confined geometry. *Nature Communications*, 6(1):1–7.
- [46] Du, H., Liang, D., Jin, C., Kong, L., Stolt, M. J., Ning, W., Yang, J., Xing, Y., Wang, J., Che, R., et al. (2015b). Electrical probing of field-driven cascading quantized transitions of skyrmion cluster states in MnSi nanowires. *Nature Communications*, 6(1):1–7.
- [47] Dyadkin, V., Prša, K., Grigoriev, S. V., White, J. S., Huang, P., Rønnow, H. M., Magrez, A., Dewhurst, C. D., and Chernyshov, D. (2014). Chirality of structure and magnetism in the magnetoelectric compound  $\text{Cu}_2\text{OSeO}_3$ . *Phys. Rev. B*, 89:140409.
- [48] Dzyaloshinsky, I. (1958). A thermodynamic theory of “weak” ferromagnetism of antiferromagnetics. *Journal of physics and chemistry of solids*, 4(4):241–255.
- [49] Effenberger, H. and Pertlik, F. (1986). Die kristallstrukturen der kupfer (ii)-oxo-selenite  $\text{Cu}_2\text{O}(\text{SeO}_3)$  (kubisch und monoklin) und  $\text{Cu}_4\text{O}(\text{SeO}_3)_3$  (monoklin und triklin). *Monatshefte für Chemie/Chemical Monthly*, 117(8):887–896.
- [50] Fernández-Pacheco, A., Streubel, R., Fruchart, O., Hertel, R., Fischer, P., and Cowburn, R. P. (2017). Three-dimensional nanomagnetism. *Nature Communications*, 8(1):1–14.
- [51] Franke, K. J. A., Huddart, B. M., Hicken, T. J., Xiao, F., Blundell, S. J., Pratt, F. L., Crisanti, M., Barker, J. A. T., Clark, S. J., Štefančíč, A. c. v., Hatnean, M. C., Balakrishnan, G., and Lancaster, T. (2018). Magnetic phases of skyrmion-hosting  $\text{GaV}_4\text{S}_{8-y}\text{Se}_y$  ( $y = 0, 2, 4, 8$ ) probed with muon spectroscopy. *Phys. Rev. B*, 98:054428.
- [52] Fujima, Y., Abe, N., Tokunaga, Y., and Arima, T. (2017). Thermodynamically stable skyrmion lattice at low temperatures in a bulk crystal of lacunar spinel  $\text{GaV}_4\text{Se}_8$ . *Phys. Rev. B*, 95:180410.



- 
- [53] Fujishiro, Y., Kanazawa, N., Kurihara, R., Ishizuka, H., Hori, T., Yasin, F. S., Yu, X., Tsukazaki, A., Ichikawa, M., Kawasaki, M., et al. (2021). Giant anomalous Hall effect from spin-chirality scattering in a chiral magnet. *Nature Communications*, 12(1):1–6.
  - [54] Fujishiro, Y., Kanazawa, N., Nakajima, T., Yu, X., Ohishi, K., Kawamura, Y., Kakurai, K., Arima, T., Mitamura, H., Miyake, A., et al. (2019). Topological transitions among skyrmion- and hedgehog-lattice states in cubic chiral magnets. *Nature Communications*, 10(1):1–8.
  - [55] Gayles, J., Freimuth, F., Schena, T., Lani, G., Mavropoulos, P., Duine, R. A., Blügel, S., Sinova, J., and Mokrousov, Y. (2015). Dzyaloshinskii-Moriya Interaction and Hall Effects in the Skyrmion Phase of  $\text{Mn}_{1-x}\text{Fe}_x\text{Ge}$ . *Phys. Rev. Lett.*, 115:036602.
  - [56] Geim, A. K. and Novoselov, K. S. (2010). The rise of graphene. In *Nanoscience and technology: a collection of reviews from nature journals*, pages 11–19. World Scientific.
  - [57] Gilbert, D. A., Grutter, A. J., Neves, P. M., Shu, G.-J., Zimanyi, G., Maranville, B. B., Chou, F.-C., Krycka, K., Butch, N. P., Huang, S., and Borchers, J. A. (2019). Precipitating ordered skyrmion lattices from helical spaghetti and granular powders. *Phys. Rev. Materials*, 3:014408.
  - [58] Göbel, B., Mertig, I., and Tretiakov, O. A. (2021). Beyond skyrmions: Review and perspectives of alternative magnetic quasiparticles. *Physics Reports*, 895:1–28.
  - [59] Grenier, S. and Joly, Y. (2014). Basics of resonant elastic X-ray scattering theory. In *Journal of Physics: Conference Series*, volume 519, page 012001. IOP Publishing.
  - [60] Grigoriev, S., Potapova, N., Siegfried, S.-A., Dyadkin, V., Moskvina, E., Dmitriev, V., Menzel, D., Dewhurst, C., Chernyshov, D., Sadykov, R., et al. (2013). Chiral properties of structure and magnetism in  $\text{Mn}_{1-x}\text{Fe}_x\text{Ge}$  compounds: When the left and the right are fighting, who wins? *Physical Review Letters*, 110(20):207201.
  - [61] Grytsiuk, S., Hanke, J.-P., Hoffmann, M., Bouaziz, J., Gomonay, O., Bihlmayer, G., Lounis, S., Mokrousov, Y., and Blügel, S. (2020). Topological–chiral magnetic interactions driven by emergent orbital magnetism. *Nature Communications*, 11(1):1–7.
  - [62] Hahn, T., Shmueli, U., and Arthur, J. W. (1983). *International tables for crystallography*, volume 1. Reidel Dordrecht.
  - [63] Halder, M., Chacon, A., Bauer, A., Simeth, W., Mühlbauer, S., Berger, H., Heinen, L., Garst, M., Rosch, A., and Pfleiderer, C. (2018). Thermodynamic evidence of a second skyrmion lattice phase and tilted conical phase in  $\text{Cu}_2\text{OSeO}_3$ . *Phys. Rev. B*, 98:144429.
  - [64] Hasan, M. Z. and Kane, C. L. (2010). *Colloquium: Topological insulators*. *Reviews of Modern Physics*, 82(4):3045.
  - [65] Heacock, B., Sarenac, D., Cory, D., Huber, M., MacLean, J., Miao, H., Wen, H., and Pushin, D. (2020). Neutron sub-micrometre tomography from scattering data. *IUCr*, 7(5):893–900.

## Bibliography

---

- [66] Heinze, S., Von Bergmann, K., Menzel, M., Brede, J., Kubetzka, A., Wiesendanger, R., Bihlmayer, G., and Blügel, S. (2011). Spontaneous atomic-scale magnetic skyrmion lattice in two dimensions. *Nature Physics*, 7(9):713–718.
- [67] Helgaker, T., Jorgensen, P., and Olsen, J. (2014). *Molecular electronic-structure theory*. John Wiley & Sons.
- [68] Hicken, T. J., Holt, S. J. R., Franke, K. J. A., Hawkhead, Z., Štefančič, A., Wilson, M. N., Gomilšek, M., Huddart, B. M., Clark, S. J., Lees, M. R., Pratt, F. L., Blundell, S. J., Balakrishnan, G., and Lancaster, T. (2020). Magnetism and néel skyrmion dynamics in  $\text{GaV}_4\text{S}_{8-y}\text{Se}_y$ . *Phys. Rev. Research*, 2:032001.
- [69] Hicken, T. J., Wilson, M. N., Franke, K. J. A., Huddart, B. M., Hawkhead, Z., Gomilšek, M., Clark, S. J., Pratt, F. L., Štefančič, A., Hall, A. E., Ciomaga Hatnean, M., Balakrishnan, G., and Lancaster, T. (2021). Megahertz dynamics in skyrmion systems probed with muon-spin relaxation. *Phys. Rev. B*, 103:024428.
- [70] Hill, J. and McMorro, D. (1996). Resonant exchange scattering: polarization dependence and correlation function. *Acta Crystallographica Section A: Foundations of Crystallography*, 52(2):236–244.
- [71] Hirschberger, M., Nakajima, T., Gao, S., Peng, L., Kikkawa, A., Kurumaji, T., Kriener, M., Yamasaki, Y., Sagayama, H., Nakao, H., et al. (2019). Skyrmion phase and competing magnetic orders on a breathing kagomé lattice. *Nature Communications*, 10(1):1–9.
- [72] Holt, S., Štefančič, A., Loudon, J., Lees, M., and Balakrishnan, G. (2021). Investigations of the size distribution and magnetic properties of nanoparticles of  $\text{Cu}_2\text{OSeO}_3$ . *Materials Research Express*, 8(11):116101.
- [73] Hori, T., Shiraishi, H., and Ishii, Y. (2007). Magnetic properties of  $\beta$ -MnCoZn alloys. *Journal of magnetism and magnetic materials*, 310(2):1820–1822.
- [74] Hsu, P.-J., Kubetzka, A., Finco, A., Romming, N., Von Bergmann, K., and Wiesendanger, R. (2017). Electric-field-driven switching of individual magnetic skyrmions. *Nature Nanotechnology*, 12(2):123–126.
- [75] Huang, P., Schönenberger, T., Cantoni, M., Heinen, L., Magrez, A., Rosch, A., Carbone, F., and Rønnow, H. M. (2020). Melting of a skyrmion lattice to a skyrmion liquid via a hexatic phase. *Nature Nanotechnology*, 15(9):761–767.
- [76] Ishiwata, S., Nakajima, T., Kim, J.-H., Inosov, D. S., Kanazawa, N., White, J. S., Gavalano, J. L., Georgii, R., Seemann, K. M., Brandl, G., Manuel, P., Khalyavin, D. D., Seki, S., Tokunaga, Y., Kinoshita, M., Long, Y. W., Kaneko, Y., Taguchi, Y., Arima, T., Keimer, B., and Tokura, Y. (2020). Emergent topological spin structures in the centrosymmetric cubic perovskite  $\text{SrFeO}_3$ . *Phys. Rev. B*, 101:134406.

- 
- [77] Ishiwata, S., Tokunaga, M., Kaneko, Y., Okuyama, D., Tokunaga, Y., Wakimoto, S., Kakurai, K., Arima, T., Taguchi, Y., and Tokura, Y. (2011). Versatile helimagnetic phases under magnetic fields in cubic perovskite  $\text{SrFeO}_3$ . *Phys. Rev. B*, 84:054427.
- [78] Ishizuka, H. and Nagaosa, N. (2018). Spin chirality induced skew scattering and anomalous Hall effect in chiral magnets. *Science Advances*, 4(2):eaap9962.
- [79] Ishizuka, H. and Nagaosa, N. (2020). Anomalous electrical magnetochiral effect by chiral spin-cluster scattering. *Nature Communications*, 11(1):1–6.
- [80] Ishizuka, H. and Nagaosa, N. (2021). Large anomalous Hall effect and spin Hall effect by spin-cluster scattering in the strong-coupling limit. *Phys. Rev. B*, 103:235148.
- [81] Iwasaki, J., Mochizuki, M., and Nagaosa, N. (2013). Current-induced skyrmion dynamics in constricted geometries. *Nature Nanotechnology*, 8(10):742–747.
- [82] Janoschek, M., Garst, M., Bauer, A., Krautscheid, P., Georgii, R., Böni, P., and Pfleiderer, C. (2013). Fluctuation-induced first-order phase transition in Dzyaloshinskii-Moriya helimagnets. *Phys. Rev. B*, 87:134407.
- [83] Janson, O., Rousochatzakis, I., Tsirlin, A. A., Belesi, M., Leonov, A. A., Rößler, U. K., Van Den Brink, J., and Rosner, H. (2014). The quantum nature of skyrmions and half-skyrmions in  $\text{Cu}_2\text{OSeO}_3$ . *Nature Communications*, 5(1):1–11.
- [84] Jiang, J., Liu, Z., Sun, Y., Yang, H., Rajamathi, C., Qi, Y., Yang, L., Chen, C., Peng, H., Hwang, C., et al. (2017). Signature of type-II Weyl semimetal phase in  $\text{MoTe}_2$ . *Nature Communications*, 8(1):1–6.
- [85] Jin, C., Li, Z.-A., Kovács, A., Caron, J., Zheng, F., Rybakov, F. N., Kiselev, N. S., Du, H., Blügel, S., Tian, M., et al. (2017). Control of morphology and formation of highly geometrically confined magnetic skyrmions. *Nature Communications*, 8(1):1–9.
- [86] Kakihana, M., Aoki, D., Nakamura, A., Honda, F., Nakashima, M., Amako, Y., Nakamura, S., Sakakibara, T., Hedo, M., Nakama, T., et al. (2018). Giant hall resistivity and magnetoresistance in cubic chiral antiferromagnet  $\text{EuPtSi}$ . *Journal of the Physical Society of Japan*, 87(2):023701.
- [87] Kanazawa, N., Kitaori, A., White, J. S., Ukleev, V., Rønnow, H. M., Tsukazaki, A., Ichikawa, M., Kawasaki, M., and Tokura, Y. (2020). Direct Observation of the Statics and Dynamics of Emergent Magnetic Monopoles in a Chiral Magnet. *Phys. Rev. Lett.*, 125:137202.
- [88] Kanazawa, N., Nii, Y., Zhang, X.-X., Mishchenko, A., De Filippis, G., Kagawa, F., Iwasa, Y., Nagaosa, N., and Tokura, Y. (2016a). Critical phenomena of emergent magnetic monopoles in a chiral magnet. *Nature Communications*, 7(1):1–7.
- [89] Kanazawa, N., Onose, Y., Arima, T., Okuyama, D., Ohoyama, K., Wakimoto, S., Kakurai, K., Ishiwata, S., and Tokura, Y. (2011). Large topological hall effect in a short-period helimagnet  $\text{MnGe}$ . *Phys. Rev. Lett.*, 106:156603.

## Bibliography

---

- [90] Kanazawa, N., White, J. S., Rønnow, H. M., Dewhurst, C. D., Fujishiro, Y., Tsukazaki, A., Kozuka, Y., Kawasaki, M., Ichikawa, M., Kagawa, F., and Tokura, Y. (2016b). Direct observation of anisotropic magnetic field response of the spin helix in FeGe thin films. *Phys. Rev. B*, 94:184432.
- [91] Kaneko, K., Frontzek, M. D., Matsuda, M., Nakao, A., Munakata, K., Ohhara, T., Kakihana, M., Haga, Y., Hedo, M., Nakama, T., et al. (2019). Unique helical magnetic order and field-induced phase in trillium lattice antiferromagnet EuPtSi. *Journal of the Physical Society of Japan*, 88(1):013702.
- [92] Karhu, E. A., Kahwaji, S., Robertson, M. D., Fritzsche, H., Kirby, B. J., Majkrzak, C. F., and Monchesky, T. L. (2011). Helical magnetic order in MnSi thin films. *Phys. Rev. B*, 84:060404.
- [93] Karube, K., Shibata, K., White, J. S., Koretsune, T., Yu, X. Z., Tokunaga, Y., Rønnow, H. M., Arita, R., Arima, T., Tokura, Y., and Taguchi, Y. (2018a). Controlling the helicity of magnetic skyrmions in a  $\beta$ -Mn-type high-temperature chiral magnet. *Phys. Rev. B*, 98:155120.
- [94] Karube, K., White, J., Reynolds, N., Gavilano, J., Oike, H., Kikkawa, A., Kagawa, F., Tokunaga, Y., Rønnow, H. M., Tokura, Y., et al. (2016). Robust metastable skyrmions and their triangular-square lattice structural transition in a high-temperature chiral magnet. *Nature Materials*, 15(12):1237–1242.
- [95] Karube, K., White, J. S., Morikawa, D., Dewhurst, C. D., Cubitt, R., Kikkawa, A., Yu, X., Tokunaga, Y., hisa Arima, T., Rønnow, H. M., Tokura, Y., and Taguchi, Y. (2018b). Disordered skyrmion phase stabilized by magnetic frustration in a chiral magnet. *Science Advances*, 4(9):eaar7043.
- [96] Karube, K., White, J. S., Ukleev, V., Dewhurst, C. D., Cubitt, R., Kikkawa, A., Tokunaga, Y., Rønnow, H. M., Tokura, Y., and Taguchi, Y. (2020). Metastable skyrmion lattices governed by magnetic disorder and anisotropy in  $\beta$ -Mn-type chiral magnets. *Phys. Rev. B*, 102:064408.
- [97] Katukuri, V. M., Stoll, H., van den Brink, J., and Hozoi, L. (2012). Ab initio determination of excitation energies and magnetic couplings in correlated quasi-two-dimensional iridates. *Physical Review B*, 85(22):220402.
- [98] Kawassiadis, C. T., Manoussakis, G., and Tossidis, J. (1967). Study of selenous acid dissociation in mixed aqueous-alcoholic solvents. *Journal of Inorganic and Nuclear Chemistry*, 29(2):401–405.
- [99] Kelvin, L. W. T. (1904). *Baltimore lectures on molecular dynamics and the wave theory of light*. CUP Archive.
- [100] Kézsmárki, I., Bordács, S., Milde, P., Neuber, E., Eng, L., White, J., Rønnow, H. M., Dewhurst, C., Mochizuki, M., Yanai, K., et al. (2015). Néel-type skyrmion lattice with confined orientation in the polar magnetic semiconductor GaV<sub>4</sub>S<sub>8</sub>. *Nature Materials*, 14(11):1116–1122.

- 
- [101] Khanh, N. D., Nakajima, T., Yu, X., Gao, S., Shibata, K., Hirschberger, M., Yamasaki, Y., Sagayama, H., Nakao, H., Peng, L., et al. (2020). Nanometric square skyrmion lattice in a centrosymmetric tetragonal magnet. *Nature Nanotechnology*, 15(6):444–449.
  - [102] Kindervater, J., Adams, T., Bauer, A., Haslbeck, F. X., Chacon, A., Mühlbauer, S., Jonietz, F., Neubauer, A., Gasser, U., Nagy, G., Martin, N., Häußler, W., Georgii, R., Garst, M., and Pfleiderer, C. (2020). Evolution of magnetocrystalline anisotropies in  $\text{Mn}_{1-x}\text{Fe}_x\text{Si}$  and  $\text{Mn}_{1-x}\text{Co}_x\text{Si}$  as inferred from small-angle neutron scattering and bulk properties. *Phys. Rev. B*, 101:104406.
  - [103] Kitaori, A., Kanazawa, N., Ishizuka, H., Yokouchi, T., Nagaosa, N., and Tokura, Y. (2021). Enhanced electrical magnetochiral effect by spin-hedgehog lattice structural transition. *Phys. Rev. B*, 103:L220410.
  - [104] Klintenberg, M., Derenzo, S., and Weber, M. (2000). Accurate crystal fields for embedded cluster calculations. *Computer physics communications*, 131(1-2):120–128.
  - [105] Kodama, R. (1999). Magnetic nanoparticles. *Journal of magnetism and magnetic materials*, 200(1-3):359–372.
  - [106] Koretsune, T., Nagaosa, N., and Arita, R. (2015). Control of Dzyaloshinskii-Moriya interaction in  $\text{Mn}_{1-x}\text{Fe}_x\text{Ge}$ : a first-principles study. *Scientific Reports*, 5(1):1–10.
  - [107] Kosterlitz, J. M. and Thouless, D. J. (1973). Ordering, metastability and phase transitions in two-dimensional systems. *Journal of Physics C: Solid State Physics*, 6(7):1181.
  - [108] Kresse, G. and Furthmüller, J. (1996). Efficient iterative schemes for ab initio total-energy calculations using a plane-wave basis set. *Phys. Rev. B*, 54:11169–11186.
  - [109] Kresse, G. and Hafner, J. (1993). Ab initio molecular dynamics for liquid metals. *Phys. Rev. B*, 47:558–561.
  - [110] Kruchkov, A., White, J., Bartkowiak, M., Živković, I., Magrez, A., and Rønnow, H. (2018). Direct electric field control of the skyrmion phase in a magnetoelectric insulator. *Scientific Reports*, 8(1):1–7.
  - [111] Kurumaji, T., Nakajima, T., Hirschberger, M., Kikkawa, A., Yamasaki, Y., Sagayama, H., Nakao, H., Taguchi, Y., hisa Arima, T., and Tokura, Y. (2019). Skyrmion lattice with a giant topological hall effect in a frustrated triangular-lattice magnet. *Science*, 365(6456):914–918.
  - [112] Kurumaji, T., Nakajima, T., Ukleev, V., Feoktystov, A., Arima, T.-h., Kakurai, K., and Tokura, Y. (2017). Néel-type skyrmion lattice in the tetragonal polar magnet  $\text{VOSe}_2\text{O}_5$ . *Phys. Rev. Lett.*, 119:237201.
  - [113] Lebech, B., Bernhard, J., and Freltoft, T. (1989). Magnetic structures of cubic FeGe studied by small-angle neutron scattering. *Journal of Physics: Condensed Matter*, 1(35):6105.

## Bibliography

---

- [114] Leonov, A. O., Togawa, Y., Monchesky, T. L., Bogdanov, A. N., Kishine, J., Kousaka, Y., Miyagawa, M., Koyama, T., Akimitsu, J., Koyama, T., Harada, K., Mori, S., McGrouther, D., Lamb, R., Krajnak, M., McVitie, S., Stamps, R. L., and Inoue, K. (2016). Chiral surface twists and skyrmion stability in nanolayers of cubic helimagnets. *Phys. Rev. Lett.*, 117:087202.
- [115] Levatić, I., Šurija, V., Berger, H., and Živković, I. (2014). Dissipation processes in the insulating skyrmion compound  $\text{Cu}_2\text{OSeO}_3$ . *Phys. Rev. B*, 90:224412.
- [116] Li, W., Jin, C., Che, R., Wei, W., Lin, L., Zhang, L., Du, H., Tian, M., and Zang, J. (2016a). Emergence of skyrmions from rich parent phases in the molybdenum nitrides. *Phys. Rev. B*, 93:060409.
- [117] Li, Y., Adroja, D., Biswas, P. K., Baker, P. J., Zhang, Q., Liu, J., Tsirlin, A. A., Gegenwart, P., and Zhang, Q. (2016b). Muon Spin Relaxation Evidence for the U(1) Quantum Spin-Liquid Ground State in the Triangular Antiferromagnet  $\text{YbMgGaO}_4$ . *Phys. Rev. Lett.*, 117:097201.
- [118] Liu, Z., Yang, L., Wu, S.-C., Shekhar, C., Jiang, J., Yang, H., Zhang, Y., Mo, S.-K., Hussain, Z., Yan, B., et al. (2016). Observation of unusual topological surface states in half-heusler compounds  $\text{LnPtBi}$  (Ln= Lu, Y). *Nature Communications*, 7(1):1–7.
- [119] Lv, B. Q., Weng, H. M., Fu, B. B., Wang, X. P., Miao, H., Ma, J., Richard, P., Huang, X. C., Zhao, L. X., Chen, G. F., Fang, Z., Dai, X., Qian, T., and Ding, H. (2015). Experimental Discovery of Weyl Semimetal TaAs. *Phys. Rev. X*, 5:031013.
- [120] Maisuradze, A., Guguchia, Z., Graneli, B., Rønnow, H. M., Berger, H., and Keller, H. (2011).  $\mu\text{SR}$  investigation of magnetism and magnetoelectric coupling in  $\text{Cu}_2\text{OSeO}_3$ . *Phys. Rev. B*, 84:064433.
- [121] Malrieu, J. P., Caballol, R., Calzado, C. J., De Graaf, C., and Guihery, N. (2014). Magnetic interactions in molecules and highly correlated materials: physical content, analytical derivation, and rigorous extraction of magnetic hamiltonians. *Chemical reviews*, 114(1):429–492.
- [122] Malta, J., Paixão, J., Gonçalves, A., et al. (2019). Synthesis and magnetic studies of nanocrystalline  $\text{Cu}_2\text{OSeO}_3$ , a chiral topological magnet. *Journal of Magnetism and Magnetic Materials*, 474:122–126.
- [123] Matatagui, D., Kolokoltsev, O., Qureshi, N., Mejía-Uriarte, E., and Saniger, J. (2015). A magnonic gas sensor based on magnetic nanoparticles. *Nanoscale*, 7(21):9607–9613.
- [124] Matsuno, J., Ogawa, N., Yasuda, K., Kagawa, F., Koshibae, W., Nagaosa, N., Tokura, Y., and Kawasaki, M. (2016). Interface-driven topological Hall effect in  $\text{SrRuO}_3$ - $\text{SrIrO}_3$  bilayer. *Science Advances*, 2(7):e1600304.
- [125] Maurice, R., Bastardis, R., Graaf, C. d., Suaud, N., Mallah, T., and Guihery, N. (2009). Universal theoretical approach to extract anisotropic spin hamiltonians. *Journal of Chemical Theory and Computation*, 5(11):2977–2984.



- [126] Milde, P., Köhler, D., Seidel, J., Eng, L. M., Bauer, A., Chacon, A., Kindervater, J., Mühlbauer, S., Pfeiderer, C., Buhrandt, S., Schütte, C., and Rosch, A. (2013). Unwinding of a Skyrmion Lattice by Magnetic Monopoles. *Science*, 340(6136):1076–1080.
- [127] Momma, K. and Izumi, F. (2008). VESTA: a three-dimensional visualization system for electronic and structural analysis. *Journal of Applied crystallography*, 41(3):653–658.
- [128] Moody, S., Nielsen, P., Wilson, M., Venero, D. A., Štefančič, A., Balakrishnan, G., and Hatton, P. (2021). Experimental evidence of a change of exchange anisotropy sign with temperature in Zn-substituted  $\text{Cu}_2\text{OSeO}_3$ . *Physical Review Research*, 3(4):043149.
- [129] Moreau-Luchaire, C., Moutafis, C., Reyren, N., Sampaio, J., Vaz, C., Van Horne, N., Bouzehouane, K., Garcia, K., Deranlot, C., Warnicke, P., et al. (2016). Additive interfacial chiral interaction in multilayers for stabilization of small individual skyrmions at room temperature. *Nature Nanotechnology*, 11(5):444–448.
- [130] Moreira, I. d. P. R., Illas, F., Calzado, C. J., Sanz, J. F., Malrieu, J.-P., Amor, N. B., and Maynau, D. (1999). Local character of magnetic coupling in ionic solids. *Phys. Rev. B*, 59:R6593–R6596.
- [131] Morikawa, D., Yu, X., Karube, K., Tokunaga, Y., Taguchi, Y., Arima, T.-h., and Tokura, Y. (2017). Deformation of topologically-protected supercooled skyrmions in a thin plate of chiral magnet  $\text{Co}_8\text{Zn}_8\text{Mn}_4$ . *Nano Letters*, 17(3):1637–1641.
- [132] Moriya, T. (1960). Anisotropic superexchange interaction and weak ferromagnetism. *Phys. Rev.*, 120:91–98.
- [133] Müller, G. P., Hoffmann, M., Dißelkamp, C., Schürhoff, D., Mavros, S., Sallermann, M., Kiselev, N. S., Jónsson, H., and Blügel, S. (2019). Spirit: Multifunctional framework for atomistic spin simulations. *Phys. Rev. B*, 99:224414.
- [134] Mühlbauer, S., Binz, B., Jonietz, F., Pfeiderer, C., Rosch, A., Neubauer, A., Georgii, R., and Böni, P. (2009). Skyrmion Lattice in a Chiral Magnet. *Science*, 323(5916):915–919.
- [135] Nagaosa, N. and Tokura, Y. (2013). Topological properties and dynamics of magnetic skyrmions. *Nature Nanotechnology*, 8(12):899–911.
- [136] Naya, C. and Sutcliffe, P. (2018). Skyrmions in models with pions and rho mesons. *Journal of High Energy Physics*, 2018(5):1–14.
- [137] Nayak, A. K., Kumar, V., Ma, T., Werner, P., Pippel, E., Sahoo, R., Damay, F., Rößler, U. K., Felser, C., and Parkin, S. S. (2017). Magnetic antiskyrmions above room temperature in tetragonal heusler materials. *Nature*, 548(7669):561–566.
- [138] Ni, Y., Li, H., Jin, L., and Hong, J. (2009). Synthesis of 1D  $\text{Cu}(\text{OH})_2$  nanowires and transition to 3D  $\text{CuO}$  microstructures under ultrasonic irradiation, and their electrochemical property. *Crystal growth & design*, 9(9):3868–3873.

## Bibliography

---

- [139] Niitsu, K., Liu, Y., Booth, A. C., Yu, X., Mathur, N., Stolt, M. J., Shindo, D., Jin, S., Zang, J., Nagaosa, N., et al. (2022). Geometrically stabilized skyrmionic vortex in FeGe tetrahedral nanoparticles. *Nature Materials*, 21(3):305–310.
- [140] Noll, T., Radu, F., et al. (2016). The mechanics of the VEKMAG experiment. *Proc. of MEDSI2016, Barcelona, Spain*, pages 370–373.
- [141] Ohkuma, M., Mito, M., Pardo, M., Kousaka, Y., Iwasaki, S., Ohishi, K., Akimitsu, J., Inoue, K., Laliena, V., and Campo, J. (2022). New magnetic intermediate state, “b-phase,” in the cubic chiral magnet MnSi. *APL Materials*, 10(4):041104.
- [142] Okamura, Y., Yamasaki, Y., Morikawa, D., Honda, T., Ukleev, V., Nakao, H., Murakami, Y., Shibata, K., Kagawa, F., Seki, S., Arima, T., and Tokura, Y. (2017). Directional electric-field induced transformation from skyrmion lattice to distinct helices in multiferroic  $\text{Cu}_2\text{OSeO}_3$ . *Phys. Rev. B*, 95:184411.
- [143] Okumura, S., Hayami, S., Kato, Y., and Motome, Y. (2020). Magnetic hedgehog lattices in noncentrosymmetric metals. *Phys. Rev. B*, 101:144416.
- [144] Omrani, A. A., White, J. S., Prša, K., Živković, I., Berger, H., Magrez, A., Liu, Y.-H., Han, J. H., and Rønnow, H. M. (2014). Exploration of the helimagnetic and skyrmion lattice phase diagram in  $\text{Cu}_2\text{OSeO}_3$  using magnetoelectric susceptibility. *Phys. Rev. B*, 89:064406.
- [145] Paddison, J. A., Stewart, J. R., Manuel, P., Courtois, P., McIntyre, G. J., Rainford, B. D., and Goodwin, A. L. (2013). Emergent frustration in Co-doped  $\beta$ -Mn. *Physical Review Letters*, 110(26):267207.
- [146] Panella, J. R., Trump, B. A., Marcus, G. G., and McQueen, T. M. (2017). Seeded chemical vapor transport growth of  $\text{Cu}_2\text{OSeO}_3$ . *Crystal Growth & Design*, 17(9):4944–4948.
- [147] Parkin, S. S. P., Hayashi, M., and Thomas, L. (2008). Magnetic Domain-Wall Racetrack Memory. *Science*, 320(5873):190–194.
- [148] Pathak, S. A. and Hertel, R. (2021). Three-dimensional chiral magnetization structures in FeGe nanospheres. *Phys. Rev. B*, 103:104414.
- [149] Peng, L., Takagi, R., Koshibae, W., Shibata, K., Nakajima, K., Arima, T.-h., Nagaosa, N., Seki, S., Yu, X., and Tokura, Y. (2020). Controlled transformation of skyrmions and antiskyrmions in a non-centrosymmetric magnet. *Nature Nanotechnology*, 15(3):181–186.
- [150] Pepper, R. A., Beg, M., Cortés-Ortuño, D., Kluyver, T., Bisotti, M.-A., Carey, R., Vousden, M., Albert, M., Wang, W., Hovorka, O., et al. (2018). Skyrmion states in thin confined polygonal nanostructures. *Journal of Applied Physics*, 123(9):093903.
- [151] Perdew, J. P., Burke, K., and Ernzerhof, M. (1996). Generalized Gradient Approximation Made Simple. *Phys. Rev. Lett.*, 77:3865–3868.

- [152] Platzman, P. and Tzoar, N. (1970). Magnetic scattering of x-rays from electrons in molecules and solids. *Physical Review B*, 2(9):3556.
- [153] Porter, N. A., Spencer, C. S., Temple, R. C., Kinane, C. J., Charlton, T. R., Langridge, S., and Marrows, C. H. (2015). Manipulation of the spin helix in FeGe thin films and FeGe/Fe multilayers. *Phys. Rev. B*, 92:144402.
- [154] Prasai, N., Trump, B. A., Marcus, G. G., Akopyan, A., Huang, S. X., McQueen, T. M., and Cohn, J. L. (2017). Ballistic magnon heat conduction and possible Poiseuille flow in the helimagnetic insulator  $\text{Cu}_2\text{OSeO}_3$ . *Phys. Rev. B*, 95:224407.
- [155] Preißinger, M., Karube, K., Ehlers, D., Szigeti, B., Krug von Nidda, H.-A., White, J., Ukleev, V., Rønnow, H., Tokunaga, Y., Kikkawa, A., et al. (2021). Vital role of magnetocrystalline anisotropy in cubic chiral skyrmion hosts. *npj Quantum Materials*, 6(1):1–9.
- [156] Qian, F., Bannenberg, L. J., Wilhelm, H., Chaboussant, G., Debeer-Schmitt, L. M., Schmidt, M. P., Aqeel, A., Palstra, T. T. M., Brück, E., Lefering, A. J. E., Pappas, C., Mostovoy, M., and Leonov, A. O. (2018). New magnetic phase of the chiral skyrmion material  $\text{Cu}_2\text{OSeO}_3$ . *Science Advances*, 4(9):eaat7323.
- [157] Qian, F., Wilhelm, H., Aqeel, A., Palstra, T. T. M., Lefering, A. J. E., Brück, E. H., and Pappas, C. (2016). Phase diagram and magnetic relaxation phenomena in  $\text{Cu}_2\text{OSeO}_3$ . *Phys. Rev. B*, 94:064418.
- [158] Ran, K., Liu, Y., Guang, Y., Burn, D. M., van der Laan, G., Hesjedal, T., Du, H., Yu, G., and Zhang, S. (2021). Creation of a chiral bobber lattice in helimagnet-multilayer heterostructures. *Phys. Rev. Lett.*, 126:017204.
- [159] Romming, N., Hanneken, C., Menzel, M., Bickel, J. E., Wolter, B., von Bergmann, K., Kubetzka, A., and Wiesendanger, R. (2013). Writing and Deleting Single Magnetic Skyrmions. *Science*, 341(6146):636–639.
- [160] Rößler, U. K., Leonov, A. A., and Bogdanov, A. N. (2011). Chiral skyrmionic matter in non-centrosymmetric magnets. In *Journal of Physics: Conference Series*, volume 303, page 012105. IOP Publishing.
- [161] Rybakov, F. N., Borisov, A. B., Blügel, S., and Kiselev, N. S. (2015). New type of stable particlelike states in chiral magnets. *Phys. Rev. Lett.*, 115:117201.
- [162] Rybakov, F. N., Borisov, A. B., Blügel, S., and Kiselev, N. S. (2016). New spiral state and skyrmion lattice in 3d model of chiral magnets. *New Journal of Physics*, 18(4):045002.
- [163] Sanchez, D. S., Belopolski, I., Cochran, T. A., Xu, X., Yin, J.-X., Chang, G., Xie, W., Manna, K., Süß, V., Huang, C.-Y., et al. (2019). Topological chiral crystals with helicoid-arc quantum states. *Nature*, 567(7749):500–505.
- [164] Schäfer, H. (1962). *Chemische Transportreaktionen: der Transport anorganischer Stoffe über die Gasphase und seine Anwendungen*. Number 76. Verlag Chemie.

## Bibliography

---

- [165] Schröter, N., Pei, D., Vergniory, M. G., Sun, Y., Manna, K., De Juan, F., Krieger, J., Süß, V., Schmidt, M., Dudin, P., et al. (2019). Chiral topological semimetal with multifold band crossings and long Fermi arcs. *Nature Physics*, 15(8):759–765.
- [166] Schwarze, T., Waizner, J., Garst, M., Bauer, A., Stasinopoulos, I., Berger, H., Pfleiderer, C., and Grundler, D. (2015). Universal helimagnon and skyrmion excitations in metallic, semiconducting and insulating chiral magnets. *Nature Materials*, 14(5):478–483.
- [167] Seki, S., Ishiwata, S., and Tokura, Y. (2012a). Magnetoelectric nature of skyrmions in a chiral magnetic insulator  $\text{Cu}_2\text{OSeO}_3$ . *Phys. Rev. B*, 86:060403.
- [168] Seki, S., Kim, J.-H., Inosov, D. S., Georgii, R., Keimer, B., Ishiwata, S., and Tokura, Y. (2012b). Formation and rotation of skyrmion crystal in the chiral-lattice insulator  $\text{Cu}_2\text{OSeO}_3$ . *Phys. Rev. B*, 85:220406.
- [169] Seki, S., Yu, X. Z., Ishiwata, S., and Tokura, Y. (2012c). Observation of skyrmions in a multiferroic material. *Science*, 336(6078):198–201.
- [170] Shibata, K., Yu, X., Hara, T., Morikawa, D., Kanazawa, N., Kimoto, K., Ishiwata, S., Matsui, Y., and Tokura, Y. (2013). Towards control of the size and helicity of skyrmions in helimagnetic alloys by spin–orbit coupling. *Nature Nanotechnology*, 8(10):723–728.
- [171] Shirane, G., Shapiro, S. M., and Tranquada, J. M. (2002). *Neutron scattering with a triple-axis spectrometer: basic techniques*. Cambridge University Press.
- [172] Skyrme, T. H. R. (1962). A unified field theory of mesons and baryons. *Nuclear Physics*, 31:556–569.
- [173] Soumyanarayanan, A., Raju, M., Gonzalez Oyarce, A., Tan, A. K., Im, M.-Y., Petrović, A., Ho, P., Khoo, K., Tran, M., Gan, C., et al. (2017). Tunable room-temperature magnetic skyrmions in Ir/Fe/Co/Pt multilayers. *Nature Materials*, 16(9):898–904.
- [174] Squires, G. L. (1996). *Introduction to the theory of thermal neutron scattering*. Courier Corporation.
- [175] Štefančič, A., Moody, S., Hicken, T., Birch, M., Balakrishnan, G., Barnett, S., Crisanti, M., Evans, J., Holt, S., Franke, K., et al. (2018). Origin of skyrmion lattice phase splitting in Zn-substituted  $\text{Cu}_2\text{OSeO}_3$ . *Physical Review Materials*, 2(11):111402.
- [176] Stewart, J., Rainford, B., Eccleston, R., and Cywinski, R. (2002). Non-Fermi-liquid behavior of electron-spin fluctuations in an elemental paramagnet. *Physical Review Letters*, 89(18):186403.
- [177] Sucksmith, W. and Thompson, J. E. (1954). The magnetic anisotropy of cobalt. *Proceedings of the Royal Society of London. Series A. Mathematical and Physical Sciences*, 225(1162):362–375.

- [178] Tabata, C., Matsumura, T., Nakao, H., Michimura, S., Kakihana, M., Inami, T., Kaneko, K., Hedo, M., Nakama, T., and Ōnuki, Y. (2019). Magnetic field induced triple- $q$  magnetic order in trillium lattice antiferromagnet EuPtSi studied by resonant x-ray scattering. *Journal of the Physical Society of Japan*, 88(9):093704.
- [179] Takagi, R., Matsuyama, N., Ukleev, V., Yu, L., White, J. S., Francoual, S., Mardegan, J. R., Hayami, S., Saito, H., Kaneko, K., et al. (2022). Square and rhombic lattices of magnetic skyrmions in a centrosymmetric binary compound. *Nature Communications*, 13(1):1–7.
- [180] Takagi, R., White, J. S., Hayami, S., Arita, R., Honecker, D., Rønnow, H. M., Tokura, Y., and Seki, S. (2018). Multiple- $q$  noncollinear magnetism in an itinerant hexagonal magnet. *Science Advances*, 4(11):eaau3402.
- [181] Tang, J., Wu, Y., Kong, L., Wang, W., Chen, Y., Wang, Y., Soh, Y., Xiong, Y., Tian, M., and Du, H. (2021). Two-dimensional characterization of three-dimensional magnetic bubbles in Fe<sub>3</sub>Sn<sub>2</sub> nanostructures. *National science review*, 8(6):nwaa200.
- [182] Tanigaki, T., Shibata, K., Kanazawa, N., Yu, X., Onose, Y., Park, H. S., Shindo, D., and Tokura, Y. (2015). Real-space observation of short-period cubic lattice of skyrmions in MnGe. *Nano Letters*, 15(8):5438–5442.
- [183] Templeton, D. H. and Templeton, L. K. (1994). Tetrahedral anisotropy of x-ray anomalous scattering. *Phys. Rev. B*, 49:14850–14853.
- [184] Thole, B. T., van der Laan, G., Fuggle, J. C., Sawatzky, G. A., Karnatak, R. C., and Esteve, J.-M. (1985). 3d x-ray-absorption lines and the  $3d^9 4f^{n+1}$  multiplets of the lanthanides. *Phys. Rev. B*, 32:5107–5118.
- [185] Togawa, Y., Koyama, T., Takayanagi, K., Mori, S., Kousaka, Y., Akimitsu, J., Nishihara, S., Inoue, K., Ovchinnikov, A. S., and Kishine, J. (2012). Chiral Magnetic Soliton Lattice on a Chiral Helimagnet. *Phys. Rev. Lett.*, 108:107202.
- [186] Tokunaga, Y., Yu, X., White, J., Rønnow, H. M., Morikawa, D., Taguchi, Y., and Tokura, Y. (2015). A new class of chiral materials hosting magnetic skyrmions beyond room temperature. *Nature Communications*, 6(1):1–7.
- [187] Tokura, Y. and Kanazawa, N. (2020). Magnetic skyrmion materials. *Chemical Reviews*, 121(5):2857–2897.
- [188] Topping, C. and Blundell, S. (2018). AC susceptibility as a probe of low-frequency magnetic dynamics. *Journal of Physics: Condensed Matter*, 31(1):013001.
- [189] Tucker, G. S., White, J. S., Romhányi, J., Szaller, D., Kézsmárki, I., Roessli, B., Stuhr, U., Magrez, A., Groitl, F., Babkevich, P., Huang, P., Živković, I., and Rønnow, H. M. (2016). Spin excitations in the skyrmion host Cu<sub>2</sub>OSeO<sub>3</sub>. *Phys. Rev. B*, 93:054401.

## Bibliography

---

- [190] Turnbull, L. A., Littlehales, M. T., Wilson, M. N., Birch, M. T., Popescu, H., Jaouen, N., Verezhak, J. A. T., Balakrishnan, G., and Hatton, P. D. (2022). X-ray holographic imaging of magnetic surface spirals in FeGe lamellae. *Phys. Rev. B*, 106:064422.
- [191] Ukleev, V., Karube, K., Derlet, P., Wang, C., Luetkens, H., Morikawa, D., Kikkawa, A., Mangin-Thro, L., Wildes, A., Yamasaki, Y., et al. (2021a). Frustration-driven magnetic fluctuations as the origin of the low-temperature skyrmion phase in  $\text{Co}_7\text{Zn}_7\text{Mn}_6$ . *npj Quantum Materials*, 6(1):1–8.
- [192] Ukleev, V., Pschenichnyi, K. A., Utesov, O., Karube, K., Mühlbauer, S., Cubitt, R., Tokura, Y., Taguchi, Y., White, J. S., and Grigoriev, S. V. (2022). Spin wave stiffness and damping in a frustrated chiral helimagnet  $\text{Co}_8\text{Zn}_8\text{Mn}_4$  as measured by small-angle neutron scattering. *Phys. Rev. Research*, 4:023239.
- [193] Ukleev, V., Utesov, O., Yu, L., Luo, C., Chen, K., Radu, F., Yamasaki, Y., Kanazawa, N., Tokura, Y., Arima, T.-h., and White, J. S. (2021b). Signature of anisotropic exchange interaction revealed by vector-field control of the helical order in a FeGe thin plate. *Phys. Rev. Research*, 3:013094.
- [194] Ukleev, V., Yamasaki, Y., Morikawa, D., Karube, K., Shibata, K., Tokunaga, Y., Okamura, Y., Amemiya, K., Valvidares, M., Nakao, H., Taguchi, Y., Tokura, Y., and Arima, T. (2019). Element-specific soft x-ray spectroscopy, scattering, and imaging studies of the skyrmion-hosting compound  $\text{Co}_8\text{Zn}_8\text{Mn}_4$ . *Phys. Rev. B*, 99:144408.
- [195] Ukleev, V., Yamasaki, Y., Utesov, O., Shibata, K., Kanazawa, N., Jaouen, N., Nakao, H., Tokura, Y., and Arima, T.-h. (2020). Metastable solitonic states in the strained itinerant helimagnet FeGe. *Phys. Rev. B*, 102:014416.
- [196] Van Arkel, A. and de Boer, J. H. (1925). Darstellung von reinem Titanium-, Zirkonium-, Hafnium- und Thoriummetall. *Zeitschrift für anorganische und allgemeine Chemie*, 148(1):345–350.
- [197] van der Laan, G. and Thole, B. T. (1991). Strong magnetic x-ray dichroism in 2p absorption spectra of 3d transition-metal ions. *Phys. Rev. B*, 43:13401–13411.
- [198] van der Laan, G., Zhang, S., and Hesjedal, T. (2021). Depth profiling of 3D skyrmion lattices in a chiral magnet-A story with a twist. *AIP Advances*, 11(1):015108.
- [199] Vansteenkiste, A., Leliaert, J., Dvornik, M., Helsen, M., Garcia-Sanchez, F., and Van Waeyenberge, B. (2014). The design and verification of MuMax3. *AIP Advances*, 4(10):107133.
- [200] Vivas, L. G., Yanes, R., Berkov, D., Erokhin, S., Bersweiler, M., Honecker, D., Bender, P., and Michels, A. (2020). Toward understanding complex spin textures in nanoparticles by magnetic neutron scattering. *Phys. Rev. Lett.*, 125:117201.



- [201] Vollhardt, D. (1997). Characteristic Crossing Points in Specific Heat Curves of Correlated Systems. *Phys. Rev. Lett.*, 78:1307–1310.
- [202] Wang, L., Feng, Q., Kim, Y., Kim, R., Lee, K. H., Pollard, S. D., Shin, Y. J., Zhou, H., Peng, W., Lee, D., et al. (2018a). Ferroelectrically tunable magnetic skyrmions in ultrathin oxide heterostructures. *Nature Materials*, 17(12):1087–1094.
- [203] Wang, X., Yuan, H., and Wang, X. (2018b). A theory on skyrmion size. *Communications Physics*, 1(1):1–7.
- [204] Weng, H., Fang, C., Fang, Z., Bernevig, B. A., and Dai, X. (2015). Weyl Semimetal Phase in Noncentrosymmetric Transition-Metal Monophosphides. *Phys. Rev. X*, 5:011029.
- [205] White, J. S., Živković, I., Kruchkov, A. J., Bartkowiak, M., Magrez, A., and Rønnow, H. M. (2018). Electric-Field-Driven Topological Phase Switching and Skyrmion-Lattice Metastability in Magnetoelectric  $\text{Cu}_2\text{OSeO}_3$ . *Phys. Rev. Applied*, 10:014021.
- [206] White, J. S., Levatić, I., Omrani, A., Egetenmeyer, N., Prša, K., Živković, I., Gavilano, J. L., Kohlbrecher, J., Bartkowiak, M., Berger, H., et al. (2012). Electric field control of the skyrmion lattice in  $\text{Cu}_2\text{OSeO}_3$ . *Journal of Physics: Condensed Matter*, 24(43):432201.
- [207] White, J. S., Prša, K., Huang, P., Omrani, A. A., Živković, I., Bartkowiak, M., Berger, H., Magrez, A., Gavilano, J. L., Nagy, G., Zang, J., and Rønnow, H. M. (2014). Electric-Field-Induced Skyrmion Distortion and Giant Lattice Rotation in the Magnetoelectric Insulator  $\text{Cu}_2\text{OSeO}_3$ . *Phys. Rev. Lett.*, 113:107203.
- [208] Wilhelm, H., Baenitz, M., Schmidt, M., Rößler, U. K., Leonov, A. A., and Bogdanov, A. N. (2011). Precursor phenomena at the magnetic ordering of the cubic helimagnet FeGe. *Phys. Rev. Lett.*, 107:127203.
- [209] Wilson, M. N., Birch, M. T., Štefančič, A., Twitchett-Harrison, A. C., Balakrishnan, G., Hicken, T. J., Fan, R., Steadman, P., and Hatton, P. D. (2020). Stability and metastability of skyrmions in thin lamellae of  $\text{Cu}_2\text{OSeO}_3$ . *Phys. Rev. Research*, 2:013096.
- [210] Wilson, M. N., Karhu, E. A., Lake, D. P., Quigley, A. S., Meynell, S., Bogdanov, A. N., Fritzsche, H., Rößler, U. K., and Monchesky, T. L. (2013). Discrete helicoidal states in chiral magnetic thin films. *Phys. Rev. B*, 88:214420.
- [211] Xia, Y. and Yang, P. (2003). Guest editorial: chemistry and physics of nanowires.
- [212] Xu, S.-Y., Belopolski, I., Alidoust, N., Neupane, M., Bian, G., Zhang, C., Sankar, R., Chang, G., Yuan, Z., Lee, C.-C., Huang, S.-M., Zheng, H., Ma, J., Sanchez, D. S., Wang, B., Bansil, A., Chou, F., Shibaev, P. P., Lin, H., Jia, S., and Hasan, M. Z. (2015). Discovery of a Weyl fermion semimetal and topological Fermi arcs. *Science*, 349(6248):613–617.
- [213] Yang, L., Liu, Z., Sun, Y., Peng, H., Yang, H., Zhang, T., Zhou, B., Zhang, Y., Guo, Y., Rahn, M., et al. (2015). Weyl semimetal phase in the non-centrosymmetric compound TaAs. *Nature Physics*, 11(9):728–732.

## Bibliography

---

- [214] Yang, S.-G., Liu, Y.-H., and Han, J. H. (2016). Formation of a topological monopole lattice and its dynamics in three-dimensional chiral magnets. *Phys. Rev. B*, 94:054420.
- [215] Yang, S.-H., Naaman, R., Paltiel, Y., and Parkin, S. S. (2021). Chiral spintronics. *Nature Reviews Physics*, 3(5):328–343.
- [216] Yasuda, K., Wakatsuki, R., Morimoto, T., Yoshimi, R., Tsukazaki, A., Takahashi, K., Ezawa, M., Kawasaki, M., Nagaosa, N., and Tokura, Y. (2016). Geometric Hall effects in topological insulator heterostructures. *Nature Physics*, 12(6):555–559.
- [217] Yu, X., DeGrave, J. P., Hara, Y., Hara, T., Jin, S., and Tokura, Y. (2013). Observation of the magnetic skyrmion lattice in a MnSi nanowire by Lorentz TEM. *Nano Letters*, 13(8):3755–3759.
- [218] Yu, X., Kanazawa, N., Onose, Y., Kimoto, K., Zhang, W., Ishiwata, S., Matsui, Y., and Tokura, Y. (2011). Near room-temperature formation of a skyrmion crystal in thin-films of the helimagnet FeGe. *Nature Materials*, 10(2):106–109.
- [219] Yu, X., Koshibae, W., Tokunaga, Y., Shibata, K., Taguchi, Y., Nagaosa, N., and Tokura, Y. (2018). Transformation between meron and skyrmion topological spin textures in a chiral magnet. *Nature*, 564(7734):95–98.
- [220] Yu, X., Onose, Y., Kanazawa, N., Park, J. H., Han, J., Matsui, Y., Nagaosa, N., and Tokura, Y. (2010). Real-space observation of a two-dimensional skyrmion crystal. *Nature*, 465(7300):901–904.
- [221] Zhang, S., Bauer, A., Burn, D., Milde, P., Neuber, E., Eng, L., Berger, H., Pfleiderer, C., Van Der Laan, G., and Hesjedal, T. (2016a). Multidomain skyrmion lattice state in  $\text{Cu}_2\text{OSeO}_3$ . *Nano Letters*, 16(5):3285–3291.
- [222] Zhang, S., van der Laan, G., Müller, J., Heinen, L., Garst, M., Bauer, A., Berger, H., Pfleiderer, C., and Hesjedal, T. (2018a). Reciprocal space tomography of 3D skyrmion lattice order in a chiral magnet. *Proceedings of the National Academy of Sciences*, 115(25):6386–6391.
- [223] Zhang, S. L., Bauer, A., Berger, H., Pfleiderer, C., van der Laan, G., and Hesjedal, T. (2016b). Resonant elastic x-ray scattering from the skyrmion lattice in  $\text{Cu}_2\text{OSeO}_3$ . *Phys. Rev. B*, 93:214420.
- [224] Zhang, S. L., van der Laan, G., Wang, W. W., Haghighirad, A. A., and Hesjedal, T. (2018b). Direct observation of twisted surface skyrmions in bulk crystals. *Phys. Rev. Lett.*, 120:227202.
- [225] Zhang, X.-X., Mishchenko, A. S., De Filippis, G., and Nagaosa, N. (2016c). Electric transport in three-dimensional skyrmion/monopole crystal. *Phys. Rev. B*, 94:174428.
- [226] Zhang, X.-X. and Nagaosa, N. (2017). Ultrasonic elastic responses in a monopole lattice. *New Journal of Physics*, 19(4):043012.

- [227] Zheng, F., Li, H., Wang, S., Song, D., Jin, C., Wei, W., Kovács, A., Zang, J., Tian, M., Zhang, Y., Du, H., and Dunin-Borkowski, R. E. (2017). Direct Imaging of a Zero-Field Target Skyrmion and Its Polarity Switch in a Chiral Magnetic Nanodisk. *Phys. Rev. Lett.*, 119:197205.
- [228] Zheng, F., Rybakov, F. N., Borisov, A. B., Song, D., Wang, S., Li, Z.-A., Du, H., Kiselev, N. S., Caron, J., Kovács, A., et al. (2018). Experimental observation of chiral magnetic bobbars in B20-type FeGe. *Nature Nanotechnology*, 13(6):451–455.
- [229] Živković, I., Pajić, D., Ivek, T., and Berger, H. (2012). Two-step transition in a magneto-electric ferrimagnet  $\text{Cu}_2\text{OSeO}_3$ . *Physical Review B*, 85(22):224402.
- [230] Živković, I., White, J., Rønnow, H. M., Prša, K., and Berger, H. (2014). Critical scaling in the cubic helimagnet  $\text{Cu}_2\text{OSeO}_3$ . *Physical Review B*, 89(6):060401.





# Priya Ranjan Baral

## Curriculum Vitae

I am a graduate student pursuing a PhD in physics at École polytechnique fédérale de Lausanne (EPFL), Switzerland. This is where I get to work on a multidisciplinary project (which includes physics, chemistry and material science) based on magnetic Skyrmions. The freedom I have received so far at EPFL nourished my collaboration as well as leadership skills. With the experience I have gained through my PhD journey, I am ready to tackle my next real world challenges from an application perspective, naturally in industry. And when I am not thinking about Skyrmions, I spend my time hiking on Swiss mountains, playing badminton or cooking.

### Personal Details

- **Date of Birth** : 2<sup>nd</sup> April 1993
- **Nationality** : Indian
- **Address** : EPFL SB IPHYS-CGF C3MP LQM, PH D2 445 (Bâtiment PH), Station 3, CH-1015, Lausanne
- **Languages** : English, Hindi, and Odia (Fluent), French (Basic)

### Research Experience

- Dec 2017–Till  
date ○ **Doctoral Assistant**, *Physics of skyrmion hosting nano-structures*, C3MP, EPFL, Supervisors : Dr. Arnaud Magrez & Prof. Oleg V Yazyev.  
*Magnetic skyrmions is a class of several nontrivial spin configurations in chiral magnets. They require very little energy cost to be moved with electric currents in metallic environment, making them promising information carriers for future memory devices and ultradense data storage, while skyrmion phases in bulk materials are interesting from a fundamental point of view in exploring topological states of matter ...*
- June-2017–Nov  
2017 ○ **Project Assistant**, *Error correction during DNA replication*, IISER-Thiruvananthapuram, Supervisor : Dr. Mamata Sahoo.  
*The cloning of a DNA molecule, known as DNA replication, is mediated by a lot of enzymes starting from Helicase to Nuclease and Topoisomerase and so on. Though all these enzymes play equally important roles in the whole process, the main enzyme-of-interest is DNA polymerase ...*
- May 2016–May  
2017 ○ **Research Fellow**, *Magnetic features of Iron based intermetallic compound*, IISER-Thiruvananthapuram, Supervisor : Dr. R C Nath.  
*Published in Physical Review B*

### Education

#### Academic Qualifications

- Dec 2017 -  
present ○ **Doctoral Assistant**, *École polytechnique fédérale de Lausanne (EPFL)*, Lausanne, CH.  
Topological Aspects Of Non-centrosymmetric Magnets
- 2011–2016 ○ **BS-MS Dual Degree**, *Indian Institute of Science Education and Research*, Thiruvananthapuram, Kerala, IN, *First Class*.  
Physics Major & Chemistry Minor

### Technical and Personal skills

- **Material Synthesis**: Solid state, Hydrothermal, Reflux, CVT, Flux, Bridgman, FIB.
- **Characterization**: Powder-XRD, Single crystal-XRD, Synchrotron XRD, Raman, SEM, TEM, XRF, EDX
- **Advanced Measurements** : SQUID, PPMS, LTEM, Neutron diffraction, Inelastic neutron scattering, Small angle neutron scattering, Resonant soft X-ray scattering, muon spin resonance ( $\mu$ SR)
- **Softwares**: MATLAB, Mathematica, LaTeX, OriginLab, FullProf Suite, Office365, MuMax3, ImageJ, Adobe illustrator

*Doctoral Assistant, Chair of Computational Condensed Matter Physics,  
École polytechnique fédérale de Lausanne, Switzerland*

☎ +41 78 747 20 98 • ☎ +41 21 69 33391 • ✉ [priya.baral@epfl.ch](mailto:priya.baral@epfl.ch)  
🌐 [www.linkedin.com/in/priyaranjan-baral-26976372](http://www.linkedin.com/in/priyaranjan-baral-26976372)

## Conferences and Workshops

- PSI Condensed Matter Summer Camp 2020.
- Main organiser of the **Summer school on Quantum Magnetism - 2019**.
- Represented EPFL at the **Global Young Scientists Summit (GYSS) - 2019**.
- **Sinergia Nanoskymionics Young Researchers' Workshop**, May 2018.
- **Study of Matter Using Intense Radiation Sources and Under Extreme Conditions** from 3-6<sup>th</sup> November 2016 at UGC-DAE CSR, University Campus, Khandwa Road, Indore.
- Workshop on **Gravitational Waves and the LIGO- India Project: Great opportunities for Young Scientists and Engineers** on 2<sup>nd</sup> June 2016 at Science and Technology Museum, Thiruvananthapuram.
- **International Symposium on Clusters, Cluster-Assemblies and Nano materials (ISCAN-2016)**.

## Publications

- Tuning topological spin textures in size-tailored chiral magnet insulator particles.  
**P. R. Baral**, V. Ukleev, T. LaGrange, R. Cubitt, I. Živković, H. M. Rønnow, J. S. White, Arnaud Magrez  
*Journal of Physical Chemistry C, ACS*, <https://doi.org/10.1021/acs.jpcc.2c03600>
- Self-flux-grown  $\text{Ba}_4\text{Fe}_4\text{ClO}_{9.5-x}$  crystals exhibiting structures with tunable modulation.  
A. Arakcheeva, D. W. Bi, **P. R. Baral**, and A. Magrez  
*CrystEngComm*, DOI: <https://doi.org/10.1039/D1CE01657A>
- Accuracy and speed of elongation in a minimal model of DNA replication.  
M. Sahoo, Arsha N., **P. R. Baral**, and S. Klumpp  
*Physical Review E*, DOI : [10.1103/PhysRevE.104.034417](https://doi.org/10.1103/PhysRevE.104.034417)
- $\text{Ba}_5(\text{IO}_6)_2$ : crystal structure evolution from room temperature to 80 K.  
D. W. Bi, **P. R. Baral**, and A. Magrez  
*Acta Crystallographica Section E*, DOI : [10.1107/S2056989021004990](https://doi.org/10.1107/S2056989021004990)
- Cluster spin-glass behaviour and memory effect in  $\text{Cr}_{0.5}\text{Fe}_{0.5}\text{Ga}$ .  
Pallab Bag, **P. R. Baral**, and R. Nath  
*Physical Review B*, DOI : [10.1103/PhysRevB.98.144436](https://doi.org/10.1103/PhysRevB.98.144436)
- Synthesis and physical properties of spin-1 honeycomb lattice  $\text{Pb}_6\text{Ni}_9(\text{TeO}_6)_5$ .  
**P. R. Baral**, N. Ahmed, J. Kumar, S. Nair, and R. Nath  
*Journal of Alloys and Compounds*, DOI : [http://doi.org/10.1016/j.jallcom.2017.04.010](https://doi.org/10.1016/j.jallcom.2017.04.010)

## Awards and Achievements

- Teaching Assistant for Solid State Physics-I (2-times), Solid State Physics-II (4-times), and General Physics - Mechanics (2-times) at EPFL.
- Supervised five Travaux pratiques (TP4) students and three summer interns.
- Currently funded via "Nano-skyrmionics" project approved by SNSF (Grant no - 171003).
- India-UK Commonwealth Scholarship-2017.
- **INSPIRE fellowship** awarded by Department of Science and Technology (DST, Govt. of India) from 2011-2016.
- Other scholarships from Government of India.
- **Elite Q&A expert** for *Advanced Physics* at the online platform, Chegg-India.
- All the national level entrance examinations.

## References

- **Prof. Oleg V. Yazyev**,  
*Chair of Computational Condensed Matter Physics*,  
École polytechnique fédérale de Lausanne,  
E-mail: oleg.yazyev@epfl.ch
- **Dr. Arnaud Magrez**,  
*Head, Crystal Growth Facility*,  
École polytechnique fédérale de Lausanne,  
E-mail: arnaud.magrez@epfl.ch
- **Prof. Henrik M. Rønnow**,  
*Director, Laboratory for Quantum Magnetism & IPHYS*,  
École polytechnique fédérale de Lausanne,  
E-mail: henrik.ronnow@epfl.ch

Doctoral Assistant, Chair of Computational Condensed Matter Physics,  
École polytechnique fédérale de Lausanne, Switzerland

☎ +41 78 747 20 98 • 📞 +41 21 69 33391 • ✉ [priya.baral@epfl.ch](mailto:priya.baral@epfl.ch)  
🌐 [www.linkedin.com/in/priyaranjan-baral-26976372](https://www.linkedin.com/in/priyaranjan-baral-26976372)